# Physics of Inhomogeneous Nematic Liquid Crystals: Colloidal Dispersions and Multiple Scattering of Light

Habilitationsschrift zur Erlangung
der Lehrbefugnis für das Fach Theoretische Physik
an der Universität Stuttgart

vorgelegt von
Holger Stark
geboren in Stuttgart

Institut für Theoretische und Angewandte Physik
der Universität Stuttgart
Juni 1999

# Contents

# Introduction

In 1888, Reinitzer [292] was the first to recognize that apart from the familiar states of matter – solid, liquid, and gas – there exists a fourth state of aggregation. In particular, certain organic molecules do not show a single transition from solid to liquid, but rather a cascade of transitions involving what we now call liquid crystalline phases. With fluids they share the ability to flow, however, they also exhibit anisotropies in their dielectric, magnetic, and optical properties reminiscent of crystals. This work deals with the nematic phase which possesses the simplest liquid crystalline order. For example, rod-like organic molecules align on average parallel to each other forming a long-range orientational order whereas their centers of mass are disordered as in a conventional fluid. The mean orientation of the molecules is indicated by a unit vector, named director. It coincides with the optical axis of the birefringent nematic phase.

The energetic ground state of a nematic liquid crystal is represented by a spatially uniform director field. The present work addresses inhomogeneities in the nematic order which are induced either by bounding surfaces and external fields or by strong thermal fluctuations of the director. In the first half of this century, the elastic theory for long-wavelength distortions of the director as an orientational order parameter was developed culminating in the Oseen-Zöcher-Frank free energy [259, 407, 121]. Since the nematic state breaks the continuous rotational symmetry of the isotropic fluid, these distortions correspond to hydrodynamic Goldstone modes. Their dynamics is governed by an extension of the Navier-Stokes equations, first formulated by Ericksen [102] and Leslie [204] and derived later by the Harvard group following rigorously the framework of hydrodynamics [117]. Furthermore, topological defects in the orientational order arise. As we will recognize in Part II, they provide a determining feature of inhomogeneous nematic liquid crystals.

Colloidal dispersions of particles in a solvent are part of our everyday life and an important state of matter for fundamental research. Motivated by experiments on inverted and multiple nematic emulsions [279], in Part II we investigate the properties of spherical particles suspended in a nematic environment. Due to the coupling of the liquid crystal molecules to the surface of the suspended objects, the director field is spatially non-uniform. After an introduction into the topic and a careful review of literature in Chapter 3, we study in Chapter 4, what I consider the paradigm for the understanding of nematic colloidal dispersions, *i.e.*, the director configuration around one single particle. As we explain in Chapter 5, its overall symmetry determines the long-range two-particle interaction mediated by the distorted director field. In Chapter 6, we calculate Stokes's friction force

experienced by a particle moving in a nematic environment, and in Chapter 7 we investigate how suspended particles behave when the surrounding liquid crystal is enclosed into a complex geometry. Finally, in Chapter 8 we demonstrate that surface-induced nematic order influences the two-particle interaction even above the nematic-isotropic phase transition. It can induce flocculation in an otherwise stabilized dispersion, addressing a key issue in colloid science.

Inhomogeneities in the nematic order are furthermore induced by thermal fluctuations of the director, *i.e.*, the local optical axis. Single light scattering from such fluctuations is well understood [146]. In Part III we use this scattering mechanism to test our generalized theory for the diffuse transport of light and its temporal correlations in random anisotropic media. Diffusing light constitutes a successful regime for accessing multiply scattered light in the limit where the photons behave like random walkers. It can even be used to monitor the dynamics of turbid systems [226]; a technique which is now called diffusing-wave spectroscopy [270]. In Chapter 9 we provide a review of all the fascinating facets of multiply scattered light, and we also introduce the basic theory of diffuse light transport in isotropic systems. In Chapter 10 we then generalize the theory to anisotropic media, namely, uniaxial nematic liquid crystals.

We begin with Part I, where we review the phenomenological description of the nematic phase. In Chapter 1 we introduce the total free energy from which a static director configuration is determined by minimization. We then access the properties of the hydrodynamic director modes on the basis of the Ericksen-Leslie equations governing the dynamics of the director. In Chapter 2 we provide the basic knowledge of topological point and line defects necessary for the understanding of director configuration around a single spherical particle.

# Part I

# Nematic Liquid Crystals

# Chapter 1

# Phenomenological Description

Typical liquid crystalline compounds consist of organic molecules. According to their elongated or disc-like shape one distinguishes between calamatic and discotic liquid crystals. Figure 1.1a) presents the molecular structure of the well-studied compound *N*-(*p*-methoxybenzylidene)-*p*-butylaniline (MBBA). Its approximate length and width are 20 Å and 5 Å. At sufficiently high temperatures, the liquid crystalline compound behaves like a conventional isotropic liquid; the molecules do not show any long-range positional and orientational order, as illustrated in the right box of Fig. 1.1b) for rod-like molecules. Cooling below the clearing point $T_c$, the liquid becomes turbid, which indicates a phase transition to the liquid crystalline state. Finally, below the melting point $T_m$ the system is solid. There exists a wealth of liquid crystalline phases [49, 76, 46]. Here we concentrate on the simplest, *i.e.*, the nematic phase, which consists of non-chiral molecules. Their centers of mass are disordered as in the isotropic liquid, whereas their main axes align themselves on average parallel to each other, so that they exhibit a long-range orientational order. The average direction is given by a unit vector $\boldsymbol{n}$, called *Frank director*. However, $\boldsymbol{n}$ merely characterizes an axis in space, *e.g.*, the optical axis of the birefringent nematic phase. As a result, all physical quantities, which we formulate in the following, have to be invariant under the inversion of the director ($\boldsymbol{n} \rightarrow -\boldsymbol{n}$). From the topological point of view, the order parameter space of the nematic phase is the projective plane $P^2 = S^2/Z_2$, *i.e.*, the unit sphere $S^2$ in three dimensions with opposite points identified [351]. Unlike the magnetization in ferromagnets, the nematic order parameter is not a vector. This statement can be understood from the following argument. Organic molecules often carry a permanent electric dipole moment along their main axis but so far no ferroelectric nematic phase with a spontaneous polarization has been found. Therefore, the same number of molecules that point into a certain direction in space also have to point into the opposite direction.

In *thermotropic* liquid crystals, the phase transitions are controlled by temperature. On the other hand, increasing the concentration of rod- or disc-like objects in a solvent can lead to the formation of what is called *lyotropic* liquid crystalline phases. The objects can be either large macromolecules, like the famous tobacco mosaic virus [119], or micelles, which form when amphiphilic molecules are dissolved, *e.g.*, in water.

All directions in the isotropic fluid are equivalent. The phase transition to the ne-

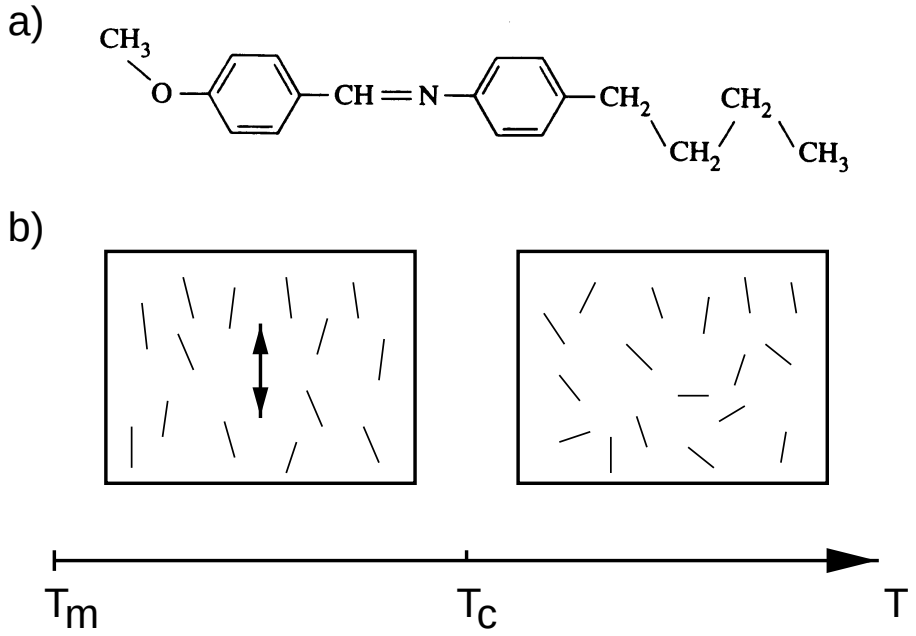


Figure 1.1: a) The compound MBBA b) The nematic liquid-crystalline phase below the clearing point $T_c$. The average direction of the molecules is indicated by the double arrow $\{\boldsymbol{n}, -\boldsymbol{n}\}$.

matic state breaks the continuous rotational symmetry of the isotropic liquid. As a result, domains with differently oriented directors appear like in a ferromagnet. These domains strongly scatter light and are one reason for the turbidity of the nematic phase. Hydrodynamic Goldstone modes appear in systems with a broken continuous symmetry [116, 46]. They are "massless", *i.e.*, their excitation does not cost any energy for vanishing wave number. In the nematic phase, the Goldstone modes correspond to thermal fluctuations of the director about its equilibrium value. Such fluctuations of the local optical axis also scatter light very strongly.

In the next three Sections 1.1-1.3 we will lay the basis for an understanding of the static and dynamical properties of the nematic phase, and we will apply it to director fluctuations in Section 1.4, which serves as a prerequisite for Part III of this work. Sections 1.1 and 1.2 also provide the necessary knowledge for Part II. There, we will determine the spatially non-uniform field of directors in complex geometries under the influence of surfaces and external fields and in the presence of topological defects. Furthermore, with the help of the dynamic theory in Section 1.3, we will calculate the Stokes drag of a particle in a nematic environment, and we will demonstrate that it is influenced by the presence of topological defects close to the particle.

## 1.1 Free Energy

Thermodynamics tells us that a complete knowledge of a system on a macrosopic level follows from the minimization of an appropriate thermodynamic potential [44]. We use the free energy, which consists of bulk and surface terms,

$$F_{\boldsymbol{n}} = F_{el} + F_{24} + F_H + F_S = \int d^3r \, (f_{el} + f_{24} + f_H) + \int dS f_S \ , \tag{1.1}$$

and discuss them in order.

The energetic ground state of a nematic liquid crystal is a spatially uniform director field; any deviation from it costs elastic energy. To describe slowly varying spatial distortions of the director field $\boldsymbol{n}(\boldsymbol{r})$, one expands the free energy density into the gradient of $\boldsymbol{n}(\boldsymbol{r})$, $\nabla_i n_j$, up to second order, and demands that the energy density obeys the local point symmetry $D_{\infty h}$ of the nematic phase. The point group $D_{\infty h}$ contains all the symmetry elements of a cylinder, *i.e.*, all rotations about an axis parallel to $\boldsymbol{n}(\boldsymbol{r})$, a mirror plane perpendicular to $\boldsymbol{n}(\boldsymbol{r})$, and an infinite number of two-fold axes also perpendicular to $\boldsymbol{n}(\boldsymbol{r})$. The result is the Oseen-Zöcher-Frank free energy density [259, 407, 121], which consists of two parts,

$$f_{el} = \frac{1}{2}[K_1(\mathrm{div}\boldsymbol{n})^2 + K_2(\boldsymbol{n}\cdot\mathrm{curl}\boldsymbol{n})^2 + K_3(\boldsymbol{n}\times\mathrm{curl}\boldsymbol{n})^2] \tag{1.2}$$

and

$$f_{24} = -\frac{K_{24}}{2}\mathrm{div}(\boldsymbol{n}\mathrm{div}\boldsymbol{n} + \boldsymbol{n}\times\mathrm{curl}\boldsymbol{n}) \ , \tag{1.3}$$

where $K_1$, $K_2$, $K_3$, and $K_{24}$ denote, respectively, the *splay*, *twist*, *bend*, and *saddle-splay* elastic constants. Figure 1.2 illustrates the characteristic deformations of the director field. The splay and bend distortions can be viewed, respectively, as part of a source or vortex field. In the twist deformation, the director rotates about an axis perpendicular to itself. In calamatic liquid crystals one usually finds the following relation, $K_3 \geq K_1 > K_2$. For example, in the compound pentylcyanobiphenyl (5CB), $K_1 = 0.42 \cdot 10^{-6}$ dyn, $K_2 = 0.23 \cdot 10^{-6}$ dyn, and $K_3 = 0.53 \cdot 10^{-6}$ dyn. In discotic liquid crystals, the relationship $K_2 > K_1 > K_3$ is predicted [329, 260, 340], which is in good agreement with experiments, where $K_2 \geq K_1 > K_3$ is observed [378, 153].

The saddle-splay term is a pure divergence. It can be transformed into integrals over all surfaces of the system,

$$F_{24} = -\frac{1}{2}K_{24}\int d\boldsymbol{S}\cdot(\boldsymbol{n}\mathrm{div}\boldsymbol{n} + \boldsymbol{n}\times\mathrm{curl}\boldsymbol{n}) \ , \tag{1.4}$$

where it prefers the formation of a saddle (see Fig. 1.2). A Cauchy relation for $K_{24}$ follows from the Maier-Saupe molecular approach [253],

$$K_{24} = (K_{11} + K_{22})/2 \ . \tag{1.5}$$

Exact measurements of $K_{24}$ are still missing but it is of the order of the bulk elastic constants $K_1$, $K_2$, and $K_3$ [63, 10, 62]. There is also the possibility of another surface

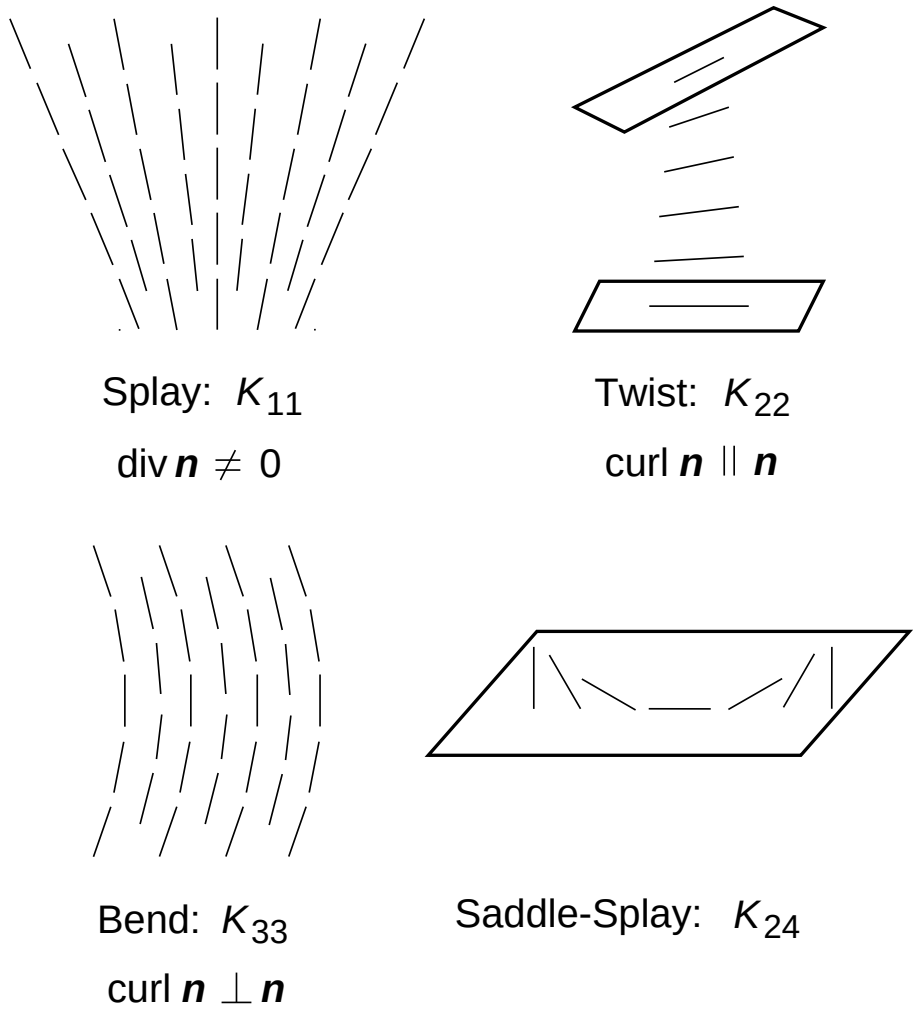


Figure 1.2: Illustration of the characteristic deformations in a nematic liquid crystal: *splay*, *twist*, *bend*, and *saddle-splay*.

term with a free energy density $K_{13}\,\mathrm{div}(\boldsymbol{n}\mathrm{div}\boldsymbol{n})$, which we will not consider in this work [253, 256, 17, 265, 266]. The controversy about it seems to be solved [267].

In the one-constant approximation, $K = K_1 = K_2 = K_3$, the Frank free energy takes the form

$$F_{el} = \frac{K}{2}\int d^3r(\nabla_i n_j)^2 + \frac{K-K_{24}}{2}\int d\boldsymbol{S}\cdot(\boldsymbol{n}\mathrm{div}\boldsymbol{n} + \boldsymbol{n}\times\mathrm{curl}\boldsymbol{n}) \ . \tag{1.6}$$

It is often used to obtain a basic understanding of a system without having to deal with effects due to the elastic anisotropy. The bulk term is equivalent to the non-linear sigma model in statistical field theory [406, 46] or the continuum description of the exchange interaction in a ferromagnet [245].

In nematic liquid crystals we can assume a linear relation between the magnetization $\boldsymbol{M}$ and an external magnetic field $\boldsymbol{H}$, $\boldsymbol{M} = \boldsymbol{\chi}\boldsymbol{H}$, where $\boldsymbol{\chi}$ stands for the tensor of the

magnetic susceptibility. The nematic phase represents a uniaxial system, for which the second-rank tensor $\boldsymbol{\chi}$ always takes the following form:

$$\boldsymbol{\chi} = \chi_\perp \mathbf{1} + \Delta\chi(\boldsymbol{n} \otimes \boldsymbol{n}) \ ; \tag{1.7}$$

$\mathbf{1}$ is the unit tensor, and $\otimes$ means dyadic product. We have introduced the magnetic anisotropy $\Delta\chi = \chi_\parallel - \chi_\perp$. It depends on the two essential magnetic susceptibilities $\chi_\parallel$ and $\chi_\perp$ for magnetic fields applied, respectively, parallel or perpendicular to the director. The general expression for the magnetic free energy density is $-\boldsymbol{H} \cdot \boldsymbol{\chi} \boldsymbol{H}/2$ [194]. A restriction to terms that depend on the director $\boldsymbol{n}$ yields

$$f_H = -\frac{\Delta\chi}{2}[(\boldsymbol{n} \cdot \boldsymbol{H})^2 - H^2] \ . \tag{1.8}$$

In usual nematics $\Delta\chi$ is positive and typically of the order of $10^{-7}$ [76]. For $\Delta\chi > 0$, the free energy density $f_H$ favors an alignment of the director $\boldsymbol{n}$ parallel to $\boldsymbol{H}$. By adding a term $-\Delta\chi H^2/2$ on the right-hand side of Eq. (1.8), we shift the reference point in order that the magnetic free energy of a completely aligned director field is zero. This will be useful in Chapter 4 where we calculate the free energy of an infinitely extended system. The balance between elastic and magnetic torques on the director defines an important length scale, the magnetic coherence length

$$\xi_H = \sqrt{\frac{K_3}{\Delta\chi H^2}} \ . \tag{1.9}$$

Suppose the director is planarly anchored at a wall, and a magnetic field is applied perpendicular to it. Then $\xi_H$ gives the distance from the wall that is needed to orient the director along the applied field [76]. The coherence length tends to infinity for $H \to 0$.

Finally, we employ the surface free energy of Rapini-Papoular to take into account the interaction of the director with boundaries:

$$f_S = \frac{W}{2}[1 - (\boldsymbol{n} \cdot \hat{\boldsymbol{\nu}})^2] \ . \tag{1.10}$$

The unit vector $\hat{\boldsymbol{\nu}}$ denotes some preferred orientation of the director at the surface, and $W$ is the coupling constant. It varies in the range $10^{-4} - 1$ erg/cm$^2$ as reviewed by Blinov *et al.* [29]. In Subsection 4.3.4 we will give a lower bound of $W$ for the interface of water and the liquid crystalline phase of 5CB in the presence of the surfactant sodium dodecyl sulfate, which was used in the experiment by Poulin *et al.* on nematic emulsions [279, 280]. From a comparison between the Frank free energy and the surface energy one arrives at the extrapolation length [76]

$$\xi_S = \frac{K_3}{W} \ . \tag{1.11}$$

It signifies the strength of the anchoring. Take a particle of radius $a$ in a nematic environment with an uniform director field at infinity. (We will investigate this case thoroughly

in Chapter 4.) The Frank free energy of this system is proportional to $K_3 a$ whereas the surface energy scales as $Wa^2$. At *strong* anchoring, *i.e.*, for $Wa^2 \gg K_3 a$ or $\xi_S \ll a$, the energy to turn the director away from its preferred direction $\hat{\boldsymbol{\nu}}$ at the whole surface would be much larger than the bulk energy. Therefore, it is preferable for the system that the director points along $\hat{\boldsymbol{\nu}}$. However, $\boldsymbol{n}$ can deviate from $\hat{\boldsymbol{\nu}}$ in an area of order $\xi_S a$. In Subsection 4.3.4 we will use this argument to explain a ring configuration around the particle. *Rigid* anchoring is realized for $\xi_S \to 0$. Finally, $\xi_S \gg a$ means *weak* anchoring, where the influence of the surface is minor. Since in our discussion we have always referred $\xi_S$ to the radius $a$, it is obvious that the strength of the anchoring is not an absolute quantity but depends on characteristic length scales of the system.

## 1.2 Routes towards the Director Field

The director field $\boldsymbol{n}(\boldsymbol{r})$ in a given geometry follows from a minimization of the total free energy $F_{\boldsymbol{n}} = F_{el} + F_{24} + F_H + F_S$ under the constraint that $\boldsymbol{n}$ is a unit vector:

$$\delta F_{\boldsymbol{n}} = 0 \qquad \text{with} \qquad \boldsymbol{n} \cdot \boldsymbol{n} = 1 \ . \tag{1.12}$$

Even in the one-constant approximation and under the assumption of rigid anchoring of the director at the boundaries, this is a difficult problem to solve because of the additional constraint. Typically, full analytical solutions only exist for one-dimensional problems, *e.g.*, for the description of the Fréedericksz transition [49, 76], or in two dimensions when certain symmetries are assumed [216]. To handle the constraint, one can use a Lagrange parameter or introduce an appropriate parametrization for the director, *e.g.*, a tilt ($\Theta$) and twist ($\Phi$) angle, so that the director in the local coordinate basis takes the form

$$\boldsymbol{n} = (\sin\Theta\cos\Phi, \sin\Theta\sin\Phi, \cos\Theta) \ . \tag{1.13}$$

If an accurate analytical determination of the director field is not possible, there are two strategies. First, an ansatz function is constructed that fulfills the boundary conditions and contains free parameters. Then, the director field follows from a minimization of the total free energy in the restricted space of functions with respect to the free parameters. In Section 4.2 we will see that this method is quite successful.

Secondly, one can look for numerical solutions of the Euler-Lagrange equations corresponding to the variational problem formulated in Eq. (1.12). They are equivalent to functional derivatives of $F_{\boldsymbol{n}}[\Theta, \Phi]$, where we use the tilt and twist angle of Eq. (1.13) to parametrize the director:

$$\frac{\delta F_{\boldsymbol{n}}}{\delta \Theta} = \frac{\delta F_{\boldsymbol{n}}}{\delta n_i}\frac{\partial n_i}{\partial \Theta} = 0 \tag{1.14}$$

$$\frac{\delta F_{\boldsymbol{n}}}{\delta \Phi} = \frac{\delta F_{\boldsymbol{n}}}{\delta n_i}\frac{\partial n_i}{\partial \Phi} = 0 \ . \tag{1.15}$$

Einstein's summation convention over repeated indices is used. To arrive at the equations above for $\Theta(\boldsymbol{r})$ and $\Phi(\boldsymbol{r})$, we have employed a chain rule for functional derivatives [335].

These chain rules are useful in numerical problems since they allow to write the Euler-Lagrange equations, which can be quite complex, in a more compact form. For example, the bulk and surface equations that are solved in Section 4.3 could only be calculated with the help of the algebraic program Maple after applying the chain rules.

Typically, we take a starting configuration for the director field and relax it on a grid via the Newton-Gauss-Seidel method [284]. It is equivalent to Newton's iterative way of determining the zeros of a function but now generalized to functionals. We illustrate it here for the tilt angle $\Theta$:

$$\Theta^{\text{new}}(\boldsymbol{r}) = \Theta^{\text{old}}(\boldsymbol{r}) - \frac{\delta F_{\boldsymbol{n}}/\delta\Theta(\boldsymbol{r})}{\text{“}\delta^2 F_{\boldsymbol{n}}/\delta\Theta^2(\boldsymbol{r})\text{”}} \quad . \tag{1.16}$$

There are two possibilities to implement the method numerically. If the grid for the numerical investigation is defined by the coordinate lines, one determines the Euler-Lagrange equations analytically. Then, they are discretized by the method of finite differences for a discrete set of grid points $\boldsymbol{r}$[284]. Finally, “$\delta^2 F_{\boldsymbol{n}}/\delta\Theta^2(\boldsymbol{r})$” is calculated as the derivative of $\delta F_{\boldsymbol{n}}/\delta\Theta(\boldsymbol{r})$ with respect to $\Theta(\boldsymbol{r})$ at the grid point $\boldsymbol{r}$. We put “$\delta^2 F_{\boldsymbol{n}}/\delta\Theta^2(\boldsymbol{r})$” into quotes because it is not the discretized form of a real second-order functional derivative, which would involve a delta function. If the geometry of the system is more complex, the method of finite elements is appropriate (see Chaper 7). In two dimensions, *e.g.*, the integration area is subdivided into *finite elements*, which in the simplest case are triangles. In doing so, the boundaries of the complex geometry are well approximated by polygons. The finite-element technique generally starts from an already discretized version of the total free energy $F_{\boldsymbol{n}}$ and then applies a numerical minimization scheme, *e.g.*, the Newton-Gauss-Seidel method. Both the first and second derivatives in Eq. (1.16) are performed with respect to $\Theta(\boldsymbol{r})$ at the grid point $\boldsymbol{r}$.

## 1.3 Hydrodynamic Equations

In the last section we concentrated on the static properties of the director field. In this section we review a set of dynamic equations coupling the flow of the liquid crystal to the dynamics of the Frank director. The set consists of a generalization of the Navier-Stokes equations for the fluid velocity $\boldsymbol{v}$ to uniaxial media and a dynamic equation for the director $\boldsymbol{n}$. We will not provide any detailed derivation of these equations, rather we will concentrate on the explanation of their meaning. The main problem is how to find a dynamic equation for the director. An early approach dates back to Oseen [259]. Ericksen [102, 103, 104, 105, 106] and Leslie [204, 205] considered the liquid crystal as a Cosserat continuum [108] whose constituents possess not only translational but also orientational degrees of freedom. Based on methods of rational thermodynamics [107], they derived an equation for the fluid velocity from the balance law for momentum density and an equation for the director, which they linked to the balance law for angular momentum. The full set of equations is commonly referred to as the *Ericksen-Leslie equations*. An alternative approach is due to the Harvard group [117, 46] which formulated equations

following rigorously the ideas of hydrodynamics [116, 46]. It only deals with hydrodynamic variables, *i.e.*, densities of conserved quantities, like mass, momentum, and energy, or broken-symmetry variables. Each one obeys a conservation law. As a result, hydrodynamic modes exist whose, in general, complex frequencies become zero for vanishing wave number. Excitations associated with broken-symmetry variables are called hydrodynamic *Goldstone* modes according to a concept introduced by Goldstone in elementary particle physics [139, 140]. The director is such a variable that breaks the continuous rotational symmetry of the isotropic fluid. In a completely linearized form the Ericksen-Leslie equations and the equations of the Harvard group are identical.

In the following, we review the Ericksen-Leslie equations and explain them step by step. In a symbolic notation, they take the form [49, 76]

$$0 = \operatorname{div} \boldsymbol{v} \tag{1.17}$$

$$\varrho \frac{\mathrm{d}\boldsymbol{v}}{\mathrm{d}t} = \operatorname{div} \boldsymbol{T} \qquad \text{with} \qquad \boldsymbol{T} = -p\,\mathbf{1} + \boldsymbol{T}^0 + \boldsymbol{T}' \tag{1.18}$$

$$\mathbf{0} = \boldsymbol{n} \times (\boldsymbol{h}^0 - \boldsymbol{h}') \ , \tag{1.19}$$

where the divergence of the stress tensor is defined by $(\operatorname{div} \boldsymbol{T})_i = \nabla_j T_{ij}$. The first equation states that we consider an incompressible fluid. We also assume constant temperature in what follows. The third equation balances all the torques on the director. We will discuss it below. The second formula stands for the generalized Navier-Stokes equations. Note that

$$\frac{\mathrm{d}}{\mathrm{d}t} = \frac{\partial}{\partial t} + \boldsymbol{v} \cdot \operatorname{grad} \tag{1.20}$$

means the total or material time derivative as experienced by a moving fluid element. It includes the *convective* part $\boldsymbol{v} \cdot \operatorname{grad}$. Besides the pressure $p$, the stress tensor consists of two terms:

$$T^0_{ij} = -\frac{\partial f_b}{\partial \nabla_j n_k} \nabla_i n_k \qquad \text{with} \qquad f_b = f_{el} + f_{24} + f_m \tag{1.21}$$

$$\begin{aligned} T'_{ij} = {} & \alpha_1 n_i n_j n_k n_l A_{kl} + \alpha_2 n_j N_i + \alpha_3 n_i N_j \\ & + \alpha_4 A_{ij} + \alpha_5 n_j n_k A_{ik} + \alpha_6 n_i n_k A_{jk} \ . \end{aligned} \tag{1.22}$$

In addition to $p$, $\boldsymbol{T}^0$ introduces a second, anisotropic contribution in the static stress tensor. It is due to elastic distortions in the director field, where $f_b$ denotes the sum of all free energy densities introduced in Section 1.1. The quantity $\boldsymbol{T}'$ stands for the viscous part of the stress tensor. In isotropic fluids, it is simply proportional to the symmetrized gradient of the velocity field,

$$A_{ij} = \frac{1}{2} \left( \nabla_i v_j + \nabla_j v_i \right) \ . \tag{1.23}$$

The conventional shear viscosity equals $\alpha_4/2$ in Eq. (1.22). The uniaxial symmetry of nematic liquid crystals allows for further contributions proportional to $\boldsymbol{A}$ which contain

the director $\boldsymbol{n}$. There are also two terms that depend on the time derivative of the director $\boldsymbol{n}$, *i.e.*, the second dynamic variable,

$$\boldsymbol{N} = \frac{\mathrm{d}\boldsymbol{n}}{\mathrm{d}t} - \boldsymbol{\omega} \times \boldsymbol{n} \qquad \text{with} \qquad \boldsymbol{\omega} = \frac{1}{2}\mathrm{curl}\boldsymbol{v} \ , \tag{1.24}$$

The vector $\boldsymbol{N}$ denotes the rate of change of $\boldsymbol{n}$ relative to the fluid motion, or more precisely, relative to a local fluid vortex characterized by the angular velocity $\boldsymbol{\omega} = \mathrm{curl}\boldsymbol{v}/2$. The viscosities $\alpha_1, \ldots, \alpha_6$ are referred to as the Leslie coefficients. We will gain more insight into $\boldsymbol{T}'$ at the end of this section.

Finally, Eq. (1.19) demands that the total torque on the director due to elastic distortions in the director field ($\boldsymbol{h}^0$) and due to viscous processes ($\boldsymbol{h}'$) is zero. The elastic and viscous curvature forces are

$$h_i^0 = \nabla_j \frac{\partial f_b}{\partial \nabla_j n_i} - \frac{\partial f_b}{\partial n_i} \tag{1.25}$$

$$h_i' = \gamma_1 N_i + \gamma_2 A_{ij} n_j \qquad \text{with} \qquad \gamma_1 = \alpha_3 - \alpha_2 \ \text{ and } \ \gamma_2 = \alpha_2 + \alpha_3 \ . \tag{1.26}$$

De Gennes calls $\boldsymbol{h}^0$ a molecular field reminiscent to a similar quantity in magnetism [76]. In Eq. (1.19) the curvature force $\boldsymbol{h}^0 - \boldsymbol{h}'$ is only defined within an additive expression $\lambda(\boldsymbol{r},t)\boldsymbol{n}(\boldsymbol{r},t)$. It has the meaning of a Lagrange-multiplier term, and $\lambda(\boldsymbol{r},t)$ is to be determined by the condition that the director is normalized to unity. In static equilibrium, we obtain $\boldsymbol{h}^0(\boldsymbol{r}) + \lambda(\boldsymbol{r})\boldsymbol{n}(\boldsymbol{r}) = 0$, *i.e.*, the Euler-Lagrange equation in the bulk which follows from minimizing the total free energy $F_{\boldsymbol{n}}$ introduced in Section 1.1. One can easily show that the saddle-splay energy $f_{24}$ does not contribute to $\boldsymbol{h}^0$. The first term of the viscous curvature force $\boldsymbol{h}'$ describes the viscous process due to the rotation of neighboring molecules with different angular velocities. The coefficient $\gamma_1$ is, therefore, a typical rotational viscosity. The second term quantifies torques on the director field exerted by a shear flow. An inertial term for the rotational motion of the molecules is not included in Eq. (1.19). One can show that it is of no relevance for the time scales of micro-seconds or larger. In the approach of the Harvard group, it does not appear since it results in a non-hydrodynamic mode.

The energy dissipated in viscous processes follows from the entropy production rate

$$T\frac{\mathrm{d}S}{\mathrm{d}t} = \int (\boldsymbol{T}' \cdot \boldsymbol{A} + \boldsymbol{h}' \cdot \boldsymbol{N})\, d^3r \ , \tag{1.27}$$

where $T$ is temperature, and $S$ is entropy. The first term describes dissipation by shear flow and the second one dissipation by rotation of the director. Each term in the entropy production rate is always written as a product of a generalized flux and its conjugate force. The true conjugate force to the flux $\boldsymbol{A}$ is the symmetrized viscous stress tensor $T_{ij}'^{\mathrm{sym}} = (T_{ij}' + T_{ji}')/2$. The flux $\boldsymbol{N}$ is conjugate to the generalized force $\boldsymbol{h}'$. Note, that $\boldsymbol{h}'$ corresponds to the dual form of the antisymmetric part of $\boldsymbol{T}'$, *i.e.*, $h_i' = \varepsilon_{ijk}(T_{jk}' - T_{kj}')/2$. The Harvard group calls $\boldsymbol{T}'^{\mathrm{sym}}$ and $\boldsymbol{h}'$ fluxes since they appear in the currents of the

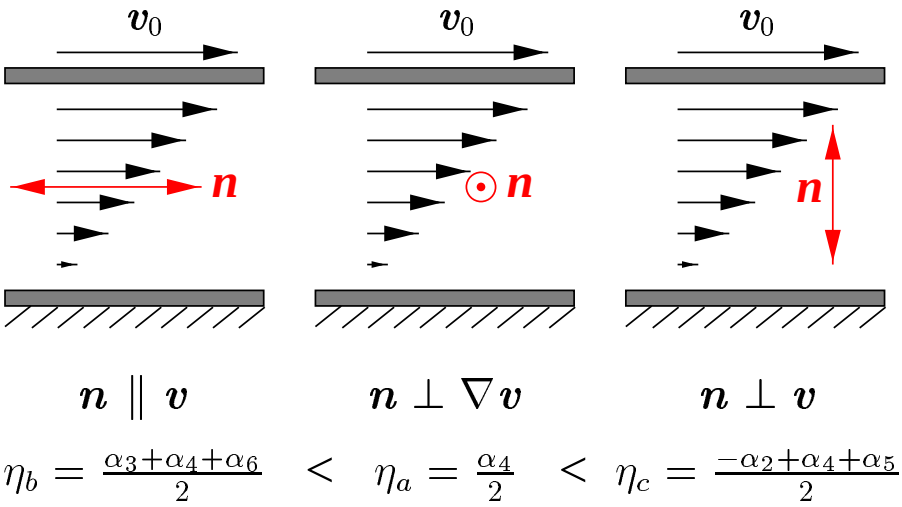


Figure 1.3: Definition of the three Mięsowicz viscosities in shear experiments.

respective balance laws for momentum and director [117, 46]. In hydrodynamics the viscous forces are assumed to be small, and they are written as linear functions of all the fluxes:

$$\begin{pmatrix} \boldsymbol{T}'^{\mathrm{sym}} \\ \boldsymbol{h}' \end{pmatrix} = \boldsymbol{\Gamma} \begin{pmatrix} \boldsymbol{A} \\ \boldsymbol{N} \end{pmatrix} \quad . \tag{1.28}$$

The matrix $\boldsymbol{\Gamma}$ must be compatible with the uniaxial symmetry of the nematic phase, and it must be invariant when $\boldsymbol{n}$ is changed into $-\boldsymbol{n}$. Furthermore, it has to obey Onsager's theorem [77], which demands a symmetric matrix $\boldsymbol{\Gamma}$ for zero magnetic field. Fulfilling all these requirements results in Eqs. (1.22) and (1.26). One additional, important Onsager relation is due to Parodi [263]:

$$\alpha_2 + \alpha_3 = \alpha_6 - \alpha_5 \quad . \tag{1.29}$$

It reduces the number of independent viscosities in a nematic liquid crystal to five. The Leslie coefficients of the compound 5CB are [58]

$$\begin{array}{llllll} \alpha_1 = -0.111\,\mathrm{P} & \alpha_2 = -0.939\,\mathrm{P} & \alpha_3 = -0.129\,\mathrm{P} \\ \alpha_4 = 0.748\,\mathrm{P} & \alpha_5 = 0.906\,\mathrm{P} & \alpha_6 = -0.162\,\mathrm{P} \quad . \end{array} \tag{1.30}$$

At the end, we explain two typical situations that help to clarify the meaning of the possible viscous processes in a nematic and how they are determined by the Leslie coefficients. In the first situation we perform typical shear experiments as illustrated in Fig. 1.3. The director field between the plates is spatially uniform, and the upper plate is moved with a velocity $v_0$ relative to the lower one. There will be a constant velocity gradient along the vertical $z$ direction. Three simple geometries exist with a symmetric orientation of the director; it is either parallel to the velocity field $\boldsymbol{v}$, or perpendicular to $\boldsymbol{v}$ and its gradient, or perpendicular to $\boldsymbol{v}$ and parallel to its gradient. The director can be firmly

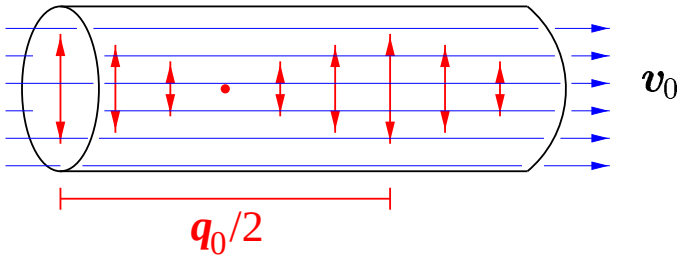


Figure 1.4: Permeation of a fluid through a helix formed by the nematic director.

aligned in one direction by applying a magnetic field strong enough to largely exceed the viscous torques. For all three cases, the shear forces $T'$ per unit area are calculated from the stress tensor $\boldsymbol{T}'$ of Eq. (1.22), yielding $T' = \eta_i v_0/d$, where $d$ is the seperation between the plates. The viscosities as a function of the Leslie coefficients for all three cases are given in Fig. 1.3. They are known as *Mięsowicz* viscosities after the scientist who first measured them [239, 240]. If one chooses a non-symmetric orientation for the director, the viscosity $\alpha_1$ is accessible in shear experiments, too [127].

The second situation describes a gedanken experiment illustrated in Fig. 1.4 [152]. Suppose the nematic director forms a helical structure with wave number $q_0$ inside a capillary. Such a configuration is found in cholesteric liquid crystals that form when the molecules are chiral. Strictly speaking, the hydrodynamics of a cholesteric is more complicated than the one of nematics [215]. However, for what follows we can use the theory formulated above. We assume that the velocity field in the capillary is spatially uniform and that the helix is not distorted by the fluid flow. Do we need a pressure gradient to press the fluid through the capillary, although there is no shear flow unlike a Poiseuille experiment? The answer is yes since the molecules of the fluid, when flowing through the capillary, have to rotate constantly to follow the director in the helix, which determines the average direction of the molecules. The dissipated energy follows from the second term of the entropy production rate in Eq. (1.27). The rate of change, $\boldsymbol{N} = \boldsymbol{v}_0 \cdot \mathrm{grad}\boldsymbol{n}$, is non-zero due to the convective time derivative. The energy dissipated per unit time and unit volume has to be matched by the work per unit time perfomed by the pressure gradient $p'$. One finally arrives at

$$p' = \gamma_1 q_0^2 v_0 \quad . \tag{1.31}$$

Obviously, the Gedanken experiment is determined by the rotational viscosity $\gamma_1$. It was suggested by Helfrich [152] who calls the motion through a fixed orientational pattern *permeation*. This motion is always dissipative because of the rotational viscosity of the molecules which have to follow the local director.

Of course, the gedanken experiment is not suitable for measuring $\gamma_1$. A more appropriate method is dynamic light scattering from director fluctuations, which we treat in the next section. The light scattering will then be described in Chapter 9. Together with the shear experiments it is in principle possible to measure all five indepent viscosities of a nematic liquid crystal.

## 1.4 Director Fluctuations

In this section we study thermal fluctuations of the director around its equilibrium value. We will proceed step by step, first deriving the static and then the dynamic properties of director modes. All the concepts of the previous sections will be applied. Our final goal is to arrive at the time autocorrelation function for director fluctuations, which is necessary for the understanding of light scattering in nematics. We will apply it in Part III.

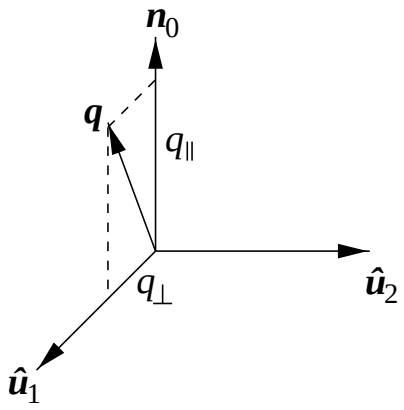


Figure 1.5: Definition of the basis vectors $\hat{\boldsymbol{u}}_1$ and $\hat{\boldsymbol{u}}_2$ relative to the equilibrium director $\boldsymbol{n}_0$ and a wave vector $q$.

We decompose the director in its equilibrium value $\boldsymbol{n}_0$ and the fluctuating part $\delta\boldsymbol{n}(\boldsymbol{r},t)$:

$$\boldsymbol{n}(\boldsymbol{r},t) = \boldsymbol{n}_0 + \delta\boldsymbol{n}(\boldsymbol{r},t) \ . \tag{1.32}$$

For small fluctuations, we have $\delta\boldsymbol{n}(\boldsymbol{r},t) \perp \boldsymbol{n}_0$ since $\boldsymbol{n}(\boldsymbol{r},t)$ is a unit vector. We expand $\delta\boldsymbol{n}(\boldsymbol{r},t)$ into plane waves,

$$\delta\boldsymbol{n}(\boldsymbol{r},t) = \int \frac{d^3q}{(2\pi)^3}\, \delta\boldsymbol{n}(\boldsymbol{q},t) \exp\left(i\boldsymbol{q}\cdot\boldsymbol{r}\right) \ , \tag{1.33}$$

and write $\delta\boldsymbol{n}(\boldsymbol{q},t)$ in the basis introduced in Fig. 1.5:

$$\delta\boldsymbol{n}(\boldsymbol{q},t) = \delta n_1(\boldsymbol{q},t)\hat{\boldsymbol{u}}_1(\boldsymbol{q}) + \delta n_2(\boldsymbol{q},t)\hat{\boldsymbol{u}}_2(\boldsymbol{q}) \ , \tag{1.34}$$

where the amplitudes $\delta n_\delta(\boldsymbol{q},t)$ $(\delta = 1,2)$ characterize the different director modes, *i.e.*, sinusoidal variations of the director in space. In our discussion we concentrate on the bulk properties of director fluctuations. Accordingly, the Frank free energy supplemented by the magnetic field term [see Eqs. (1.1), (1.2), and (1.8)] takes the form

$$F_{el}[\boldsymbol{n}(\boldsymbol{r},t)] + F_H[\boldsymbol{n}(\boldsymbol{r},t)] = \frac{1}{2}\sum_{\delta=1}^{2}\int \frac{d^3q}{(2\pi)^3}\, K_\delta(\boldsymbol{q})\, |\delta n_\delta(\boldsymbol{q},0)|^2 \tag{1.35}$$

with $\boldsymbol{q}$-dependent elastic constants

$$K_\delta(\boldsymbol{q}) = K_\delta q_\perp^2 + K_3 q_\parallel^2 + \Delta\chi H^2 \ , \tag{1.36}$$

where $q_\perp$ and $q_\parallel$ are the respective components of $\boldsymbol{q}$ perpendicular and parallel to $\boldsymbol{n}_0$. The saddle-splay term $F_{24}$ and the expression in the magnetic free energy $F_H$ that does not depend on the director are omitted. If we choose $q_\parallel = 0$, the director modes are pure splay $(\delta = 1)$ or twist $(\delta = 2)$ modes. For $q_\perp = 0$, we obtain two bend modes. The distortions corresponding to these modes are illustrated in Fig. 1.2. For a general wave vector $\boldsymbol{q}$, the modes contain a combination of bend and either splay or twist deformations.

The equipartition theorem states that each director mode has, on average, a thermal energy $k_{\rm B}T/2$. Application to the free energy of Eq. (1.35), yields the mean-square amplitude of each director mode[1] [76, 49]:

$$\langle\, |\delta n_\delta(\boldsymbol{q},t)|^2 \,\rangle = \frac{k_{\rm B}T}{K_\delta(\boldsymbol{q})} \ . \tag{1.37}$$

The spatial autocorrelation functions $\langle \delta n_\delta(\boldsymbol{r},0)\delta n_\delta(\boldsymbol{0},0)\rangle$ ($\delta = 1,2$) follow from Eq. (1.37) after a Fourier transformation. In the one-constant approximation ($K = K_i$), one finds [76]

$$\langle \delta n_\delta(\boldsymbol{r},0)\delta n_\delta(\boldsymbol{0},0)\rangle = \frac{k_{\rm B}T}{4\pi K r}\, \exp\left(-r/\xi_H\right) \ , \tag{1.38}$$

where $\xi_H$ is the magnetic coherence length, which we already encountered in Eq. (1.9). Here, $\xi_H$ gives the length scale over which director fluctuations are correlated. For typical magnetic fields of 1 T, $\Delta\chi = 10^{-7}$, and $K = 10^{-6}$ dyn, we obtain a coherence length of 3 $\mu$m. By the appropriate choice of the basis vectors $\hat{\boldsymbol{u}}_1$ and $\hat{\boldsymbol{u}}_2$, we have decoupled $\delta n_1(\boldsymbol{q},t)$ and $\delta n_2(\boldsymbol{q},t)$ from each other. Note that Eq. (1.38) is only valid for distances much larger than molecular dimensions.

Now we address the dynamics of director modes. We linearize the Ericksen-Leslie equations of the preceding section in $\delta\boldsymbol{n}(\boldsymbol{r},t)$ and $\boldsymbol{v}(\boldsymbol{r},t)$ and insert plane waves with a complex frequency $z$:

$$\begin{aligned} \delta\boldsymbol{n}(\boldsymbol{r},t) &= [\delta n_1(\boldsymbol{q},z)\hat{\boldsymbol{u}}_1(\boldsymbol{q}) + \delta n_2(\boldsymbol{q},z)\hat{\boldsymbol{u}}_2(\boldsymbol{q})]\, \exp(-zt + i\boldsymbol{q}\cdot\boldsymbol{r}) \\ \boldsymbol{v}(\boldsymbol{r},t) &= [v_1(\boldsymbol{q},z)\hat{\boldsymbol{u}}_1(\boldsymbol{q}) + v_2(\boldsymbol{q},z)\hat{\boldsymbol{u}}_2(\boldsymbol{q}) + v_\parallel(\boldsymbol{q},z)\boldsymbol{n}_0]\, \exp(-zt + i\boldsymbol{q}\cdot\boldsymbol{r}) \ . \end{aligned} \tag{1.39}$$

Since we consider an incompressible fluid, *i.e.*, $\mathrm{div}\boldsymbol{v} = 0$ or $iq_\perp v_1 = -iq_\parallel v_\parallel$, only the velocity components $v_1$ and $v_2$ are used. We arrive at two generalized eigenvalue problems [49]:

$$\boldsymbol{D}^{(\delta)}(\boldsymbol{q},z) \begin{pmatrix} \delta n_\delta(\boldsymbol{q},z) \\ v_\delta(\boldsymbol{q},z) \end{pmatrix} = \boldsymbol{0} \ , \tag{1.40}$$

where the dynamical matrices $\boldsymbol{D}^{(\delta)}(\boldsymbol{q},z)$ ($\delta = 1,2$) depend on the Frank constants $K_i$ and the Leslie viscosities $\alpha_i$. Again, through the choice of $\hat{\boldsymbol{u}}_1$ and $\hat{\boldsymbol{u}}_2$, we have decoupled $\delta n_1(\boldsymbol{q},z)$, $v_1(\boldsymbol{q},z)$ and $\delta n_2(\boldsymbol{q},z)$, $v_2(\boldsymbol{q},z)$ from each other. The solutions of Eq. (1.40) determine the eigenmodes in nematics. Their dispersion relations follow from $\det[\boldsymbol{D}^{(\delta)}] = 0$. Using $\varrho K/\eta^2 \ll 1$, where $\eta \approx 0.1$ P is a typical viscosity of nematics, and $\varrho = 1\,\mathrm{g/cm}^3$, one finds [117, 49, 46]:

$$z_{\mathrm{s}\delta} \approx \frac{K_\delta(\boldsymbol{q})}{\eta_\delta(\boldsymbol{q})} \qquad \text{and} \qquad z_{\mathrm{f}\delta} \approx \frac{\eta_{\mathrm{f}\delta}(\boldsymbol{q})}{\varrho} \ , \tag{1.41}$$

with viscosities of the s mode,

$$\eta_1(\boldsymbol{q}) = \gamma_1 - \frac{(\alpha_3 q_\perp^2 - \alpha_2 q_\parallel^2)^2}{\eta_b q_\perp^4 + \eta_c q_\parallel^4 + \eta_m q_\perp^2 q_\parallel^2} \qquad \text{and} \qquad \eta_2(\boldsymbol{q}) = \gamma_1 - \frac{\alpha_2^2 q_\parallel^2}{\eta_a q_\perp^2 + \eta_c q_\parallel^2} \ , \tag{1.42}$$

[1] Because we use a continuum of $\boldsymbol{q}$ vectors, the equipartition theorem gives $\langle\, \delta n_\delta(\boldsymbol{q},0)\, \delta n_\delta^*(\boldsymbol{q}',0)\,\rangle = [k_{\rm B}T/K_\delta(\boldsymbol{q})]\, \delta(\boldsymbol{q}-\boldsymbol{q}')$. Then we set $\langle\, |\delta n_\delta(\boldsymbol{q},t)|^2\,\rangle \equiv \int d^3q/(2\pi)^3\, \langle\, \delta n_\delta(\boldsymbol{q},0)\, \delta n_\delta^*(\boldsymbol{q}',0)\,\rangle$.

and of the f mode,

$$\begin{aligned} \eta_{\mathrm{f}1}(\boldsymbol{q}) &= \eta_b q_\perp^4 + \eta_c q_\parallel^4 + \eta_m q_\perp^2 q_\parallel^2 - (\alpha_3 q_\perp^2 - \alpha_2 q_\parallel^2)^2/\gamma_1 \\ \eta_{\mathrm{f}2}(\boldsymbol{q}) &= \eta_a q_\perp^2 + \eta_c q_\parallel^2 - \alpha_2^2 q_\parallel^2/\gamma_1 \ . \end{aligned} \tag{1.43}$$

The quantities $\eta_a$, $\eta_b$, and $\eta_c$ are the Mięsowicz viscosities introduced in Fig. 1.3, and

$$\eta_m = \alpha_1 + \eta_b + \eta_c \ . \tag{1.44}$$

The subscripts s and f denote 'slow' and 'fast' since $z_{\mathrm{s}\delta}/z_{\mathrm{f}\delta} \sim \varrho K/\eta^2 \ll 1$. Both modes are purely diffusive. The relaxation frequency $z_{\mathrm{s}\delta}$ involves the elastic constant $K_\delta(\boldsymbol{q})$ of Eq. (1.36) while $z_{\mathrm{f}\delta}$ does not. The slow modes, therefore, represent the relaxation of the orientational motion of the director. Their viscosities $\eta_\delta(\boldsymbol{q})$ are mainly determined by the rotational viscosity $\gamma_1$ with corrections such that $\eta_\delta(\boldsymbol{q}) < \gamma_1$. The fast mode, where no elastic torque is exerted on the molecules, is reminiscent of the diffusive transverse velocity mode in an isotropic fluid [116, 21, 46]. The interpretation of the nature of the eigenmodes is supported by investigating the ratios of the amplitudes:

$$\left(\frac{\delta n_\delta}{v_\delta}\right)_{\mathrm{s}} \sim \frac{\eta}{Kq} \qquad \text{and} \qquad \left(\frac{\delta n_\delta}{v_\delta}\right)_{\mathrm{f}} \sim \frac{\varrho}{\eta q} \ . \tag{1.45}$$

From these ratios we find

$$\left(\frac{\delta n_\delta}{v_\delta}\right)_{\mathrm{f}} \Bigg/ \left(\frac{\delta n_\delta}{v_\delta}\right)_{\mathrm{s}} \sim \frac{\varrho K}{\eta^2} \ll 1 \ , \tag{1.46}$$

so that the slow and fast modes are dominated by the respective amplitudes $\delta n_\delta$ or $v_\delta$.

Being familiar with the eigenmodes of nematics, we proceed to the calculation of the time autocorrelation function of the director. We first need to know how $\delta\boldsymbol{n}(\boldsymbol{q},t)$ and $\boldsymbol{v}(\boldsymbol{q},t)$ evolve when $\delta\boldsymbol{n}(\boldsymbol{q},t=0)$ and $\boldsymbol{v}(\boldsymbol{q},t=0)$ are given. We perform a Laplace transformation of the linearized Ericksen-Leslie equations using

$$\delta n_\delta(\boldsymbol{q},z) = \int_0^\infty dt\, \delta n_\delta(\boldsymbol{q},t) \exp(zt) \qquad \text{and} \qquad v_\delta(\boldsymbol{q},z) = \int_0^\infty dt\, v_\delta(\boldsymbol{q},t) \exp(zt) \tag{1.47}$$

and arrive at

$$\boldsymbol{D}^{(\delta)}(\boldsymbol{q},z) \begin{pmatrix} \delta n_\delta(\boldsymbol{q},z) \\ v_\delta(\boldsymbol{q},z) \end{pmatrix} = \frac{\partial}{\partial z}\left[\boldsymbol{D}^{(\delta)}(\boldsymbol{q},z)\right] \begin{pmatrix} \delta n_\delta(\boldsymbol{q},t=0) \\ v_\delta(\boldsymbol{q},t=0) \end{pmatrix} \ . \tag{1.48}$$

Solving for $\delta n_\delta(\boldsymbol{q},z)$ and applying the inverse Laplace transformation with the help of Cauchy's integral theorem, we obtain

$$\delta n_\delta(\boldsymbol{q},t) = \delta n_\delta(\boldsymbol{q},t=0)\, \exp(-z_{\mathrm{s}\delta} t) + \dots \ , \tag{1.49}$$

where we have concentrated on the essential term leaving out fast relaxing contributions and terms involving $v_\delta(\boldsymbol{q},t=0)$. So far we have considered variations in the thermal equilibrium value of the director $\boldsymbol{n}(\boldsymbol{q},t)$ and the velocity $\boldsymbol{v}(\boldsymbol{q},t)$. Due to Onsager's regression

hypothesis [258, 116, 21], we can employ Eq. (1.49) when calculating the time autocorrelation function of the fluctuating director component $\delta\boldsymbol{n}(\boldsymbol{q},t)$ about its thermal equilibrium value $\boldsymbol{n}_0$. We simply obtain

$$\langle\, \delta\boldsymbol{n}^*(\boldsymbol{q},t=0) \otimes \delta\boldsymbol{n}(\boldsymbol{q},t)\,\rangle = \sum_{\delta=1,2} \langle\, \delta n_\delta^*(\boldsymbol{q},t=0)\, \delta n_\delta(\boldsymbol{q},t)\rangle\, \hat{\boldsymbol{u}}_\delta(\boldsymbol{q}) \otimes \hat{\boldsymbol{u}}_\delta(\boldsymbol{q}) \tag{1.50}$$

with

$$\langle\, \delta n_\delta^*(\boldsymbol{q},t=0)\, \delta n_\delta(\boldsymbol{q},t)\rangle \approx \langle\, |\delta n_\delta(\boldsymbol{q},t=0)|^2\,\rangle\, \exp(-z_{\mathrm{s}\delta}t)\ . \tag{1.51}$$

We have neglected a contribution from the fast mode which is smaller than the leading term by a factor of the order of $(\varrho K/\eta^2)^2$. We have also used that $\langle\, \delta n_\delta^*(\boldsymbol{q},t=0)\, v_\delta(\boldsymbol{q},t=0)\rangle = 0$ since this correlation function should not change its value when $\delta n_\delta^*$ or $v_\delta$ are reversed. Hence, we realize that the time autocorrelation function of the director is dominated by the slow relaxing orientational mode. The mean-square amplitudes $\langle\, |\delta n_\delta(\boldsymbol{q},t=0)|^2\,\rangle$ have already been calculated via the equipartition theorem. Its value is stated in Eq. (1.37). With the result of Eqs. (1.50) and (1.51), which can also be derived with the help of the fluctuation-dissipation theorem [146, 116, 46], we are able to describe dynamic light scattering from director fluctuations in Chapter 10.

# Chapter 2

# Topological Defects

Topological defects [176, 234, 351, 46], which are a necessary consequence of broken continuous symmetry, exist in systems as disparate as superfluid helium 3 [375] and 4 [389], crystalline solids [348, 123, 250], liquid crystals [50, 187, 200], and quantum-Hall fluids[309]. They play an important if not determining role in such phenomena as response to external stresses [123, 250], the nature of phase transitions [46, 254, 345], or the approach to equilibrium after a quench into an ordered phase [39]; and they are the primary ingredient in such phases of matter as the Abrikosov flux-lattice phase of superconductors [2, 28] or the twist-grain-boundary phase of liquid crystals [293, 142, 143]. They even arise in certain cosmological models [53]. Topological defects are points, lines or walls in three-dimensional space where the order parameter of the system under consideration is not defined. The theory of homotopy groups [176, 234, 351, 46] provides a powerful tool to classify them. To identify, *e.g.*, line defects, homotopy theory considers closed loops in real space which are mapped into closed paths in the order parameter space. If a loop can be shrunk continuously to a single point, it does not enclose a defect. All other loops are divided into classes of paths which can be continuously transformed into each other. Then, each class stands for one type of line defect. All classes together, including the shrinkable loops, form the *first homotopy* or *fundamental group*. The group product describes the combination of defects. In the case of point singularities, the loops are replaced by closed surfaces, and the defects are classified via the *second homotopy group*.

In the next two section we deal with line and point defects in nematic liquid crystals whose order parameter space is the projective plane $P^2 = S^2/Z_2$, *i.e.*, the unit sphere $S^2$ with opposite points identified. They play a determining role for the behavior of colloidal dispersions in a nematic environment, which we will discuss in Part II. There exist several good reviews on defects in liquid crystals [176, 234, 351, 46, 50, 187, 200]. We will therefore concentrate on facts which are necessary for the understanding of colloidal dispersions. Furthermore, rather than being very formal, we choose a descriptive path for our presentation.

## 2.1 Line Defects = Disclinations

Line defects in nematic liquid crystals are also called *disclinations*. Homotopy theory tells us that the fundamental group $\pi_1(P^2)$ of the projective plane $P^2$ is the two-element group $Z_2$. Thus, there is only one class of stable disclinations. Figure 2.1 presents two typical examples. The defect line with the core is perpendicular to the drawing plane. The disclinations carry a winding number of strength + or $-1/2$, indicating a respective rotation of the director by + or $-360°/2$ when the disclination is encircled in the anticlockwise directon (see left part of Fig. 2.1). Note that the sign of the winding number is not fixed by the homotopy group. Both types of disclinations are topologically equivalent since there exists a continuous distortion of the director field which transforms one type into the other. Just start from the left disclination in Fig. 2.1 and rotate the director about the vertical axis through an angle $\pi$ when going outward from the core in any radial direction. You will end up with the right picture. The line defects in Fig. 2.1 are called *wedge* disclinations. In a Volterra process [176, 46] a cut is performed so that its limit, the disclination line, is perpendicular to the spatially uniform director field. Then the surfaces of the cut are rotated with respect to each other by an angle of $2\pi S$ about the disclination line, and material is either filled in ($S = +1/2$) or removed ($S = -1/2$). In *twist* disclinations the surfaces are rotated by an angle of $\pi$ about an axis perpendicular to the defect line. Disclinations of strength $\pm 1/2$ do not exist in a system with an vector order parameter since it lacks the inversion symmetry of the nematic phase with respect to the director. In addition, one finds $\pi_1(S^2) = 0$, *i.e.*, every disclination line of integral strength in a ferromagnet is unstable; "it escapes into the third dimension". The same applies to nematic liquid crystal as demonstrated by Cladis *et al.* [54, 390] and Bob Meyer [237] for $S = 1$.

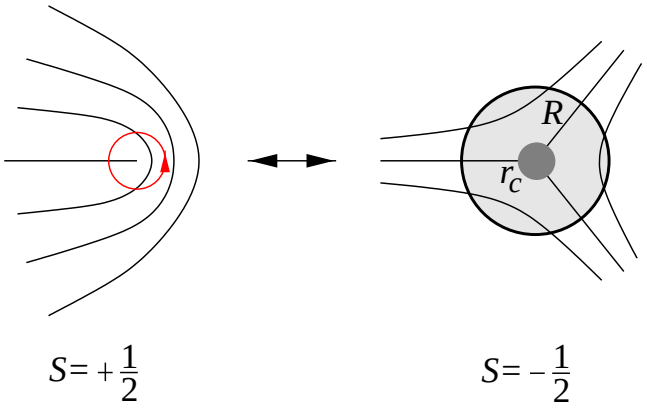


Figure 2.1: Disclinations of winding number $\pm 1/2$. For further explanations see text.

The director field around a disclination follows from the minimization of the Frank free energy (1.6) [176, 49, 76]. In the one-constant approximation the line energy $F_d$ of the disclination can be calculated as

$$F_d = \frac{\pi}{4} K \left( \frac{1}{2} + \ln \frac{R}{r_c} \right) \quad . \tag{2.1}$$

The surface term in Eq. (1.6) is neglected. The second term on the right-hand side of Eq. (2.1) stands for the elastic free energy per unit length around the line defect where $R$ is the radius of a circular cross section of the disclination (see Fig. 2.1). Since the energy

diverges logarithmically, one has to introduce a lower cut-off radius $r_c$, *i.e.*, the radius of the disclination core. Its line energy, given by the first term, is derived in the following way [176]. One assumes that the core of the disclination contains the liquid in the isotropic state with a free energy density $\varepsilon_c$ necessary to melt the nematic order locally. Splitting the line energy of the disclination as in Eq. (2.1) into the sum of a core and elastic part, $F_d = \pi r_c^2 \varepsilon_c + K\pi \ln(R/r_c)/4$, and minimizing it with respect to $r_c$, results in

$$\varepsilon_c = \frac{K}{8}\frac{1}{r_c^2} \quad , \tag{2.2}$$

so that we immediately arrive at Eq. (2.1). The right-hand side of Eq. (2.2) is equivalent to the Frank free energy density of the director field at a distance $r_c$ from the center of the disclination. Thus $r_c$ is given by the reasonable demand that the nematic state starts to melt when this energy density equals $\varepsilon_c$. With an estimate $\varepsilon_c = 10^{-7}\,\mathrm{erg/cm^3}$, which follows from a description of the nematic-isotropic phase transition by the Landau-de Gennes theory [199], and $K = 10^{-6}\,\mathrm{dyn}$, we obtain a core radius $r_c$ of the order of 10 nm. In the general case ($K_1 \neq K_2 \neq K_3$), an analytical expression for the elastic free energy does not exist. However, a rough approximation for the core energy per unit length, $F_c$, can be found by averaging over the Frank constants:

$$F_c = \frac{\pi}{8}\frac{K_1 + K_2 + K_3}{3} \quad . \tag{2.3}$$

In Section 4.3 we will make use of this form for $F_c$.

A more refined model of the disclination core is derived from Landau-de Gennes theory [73, 145, 323], which employs a traceless second-rank tensor $\boldsymbol{Q}$ as an order parameter (see Section 8.1). The tensor also describes biaxial liquid crystalline order. Investigations show that the core of a disclination should indeed be biaxial [218, 231, 315], with a core radius of the order of the biaxial correlation length $\xi_b$, *i.e.*, the length on which deviations from the uniaxial order exponentially decay to zero. Outside of the disclination core, the nematic order is essentially uniaxial. Therefore, the line energy of a disclination is still given by Eq. (2.1) with $r_c \sim \xi_b$, and with a core energy now determined by the energy difference between the biaxial and uniaxial state rather than the energy difference between the isotropic and nematic state.

## 2.2 Point Defects

Figure 2.2 presents typical point defects in a nematic liquid crystal known as *radial* and *hyperbolic hedgehogs*. Both director fields are rotationally symmetric about the vertical axis. The second homotopy group $\pi_2(P^2)$ of the projective plane $P^2$ is the set $Z$ of all integer numbers. They label every point defect by a topological charge $Q$. The result is the same as for the vector order parameter space $S^2$ since close to the point singularity the director field constitutes a unique vector field. For true vectors it is possible to distinguish between a radial hedgehog of positive and negative charge depending on their vector field

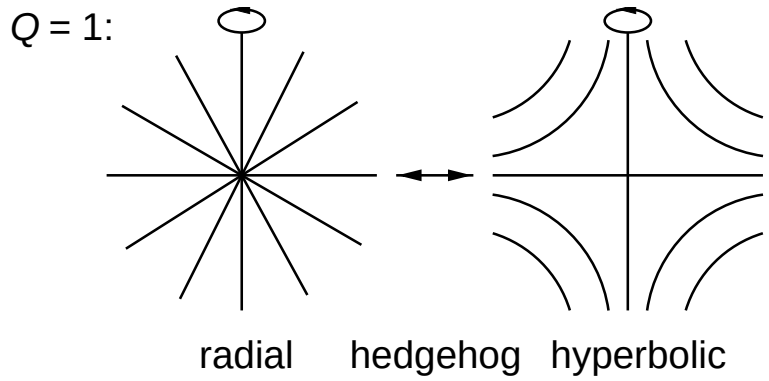


Figure 2.2: Radial and hyperbolic hedgehog of point charge $Q = 1$.

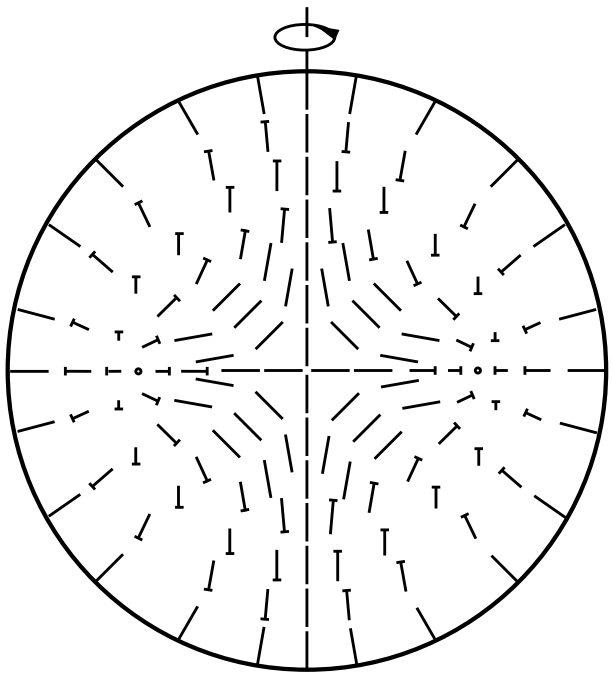

Figure 2.3: The hyperbolic hedgehog at the center is transformed into a radial point defect by a continuous distortion of the director field. Nails indicate directors tilted relative to the drawing plane.

that can either represent a source or a sink. In a nematic liquid crystal this distinction is not possible because $\boldsymbol{n}$ and $-\boldsymbol{n}$ describe the same state. Note, *e.g.*, that the directors close to a point defect are reversed if the defect is moved around a $\pm 1/2$ disclination line. Therefore, the sign of the charge $Q$ has no meaning in nematics, and by convention it is chosen positive. The charge $Q$ is determined by the number of times the unit sphere is wrapped by all the directors on a surface enclosing the defect core. An analytical expression for $Q$ is

$$Q = \left| \frac{1}{8\pi} \int dS_i \, \varepsilon_{ijk} \boldsymbol{n} \cdot (\nabla_j \boldsymbol{n} \times \nabla_k \boldsymbol{n}) \right| \quad , \tag{2.4}$$

where the integral is over any surface enclosing the defect core. Both the hedgehogs in Fig. 2.2 carry a topological charge $Q = 1$. They are topologically equivalent since they can be transformed into each other by a continuous distortion of the director field. Just start from the hyperbolic hedgehog and rotate the director about the vertical axis through an angle $\pi$ when going outward from the core in any radial direction. By this procedure, which is illustrated in Fig. 2.3 with the help of a nail picture, we end up with a radial hedgehog. The length of the nail is proportional to the projection of the director on the drawing plane, and the head of the nail is below the plane. Such a transition was observed by Lavrentovich and Terentjev in nematic drops with homeotropic, *i.e.*, perpendicular anchoring of the director at the outer surface [199].

In systems with vector symmetry, the combined topological charge of two hedgehogs with respective charges $Q_1$ and $Q_2$ is simply the sum $Q_1 + Q_2$. In nematics, where the sign of the topological charge has no meaning, the combined topological charge of two hedgehogs is either $|Q_1 + Q_2|$ or $|Q_1 - Q_2|$. It is impossible to tell with certainty which of these possible charges is the correct one by looking only at surfaces enclosing the individual hedgehogs. For example, the combined charge of two hedgehogs in the presence of a line defect depends on which path around the disclination the point defects are combined [351]. In Fig. 2.4 we illustrate how a radial and a hyperbolic hedgehog combine to a configuration with total charge $0 = |1 - 1|$. Since the distance $d$ of the defects is the only length scale in the system, dimensional arguments predict an interaction energy proportional to $Kd$ [261]. It grows linear in $d$ reminiscent to the interaction energy of quarks if one tries to separate them beyond distances larger than the diameter of a nucleus.

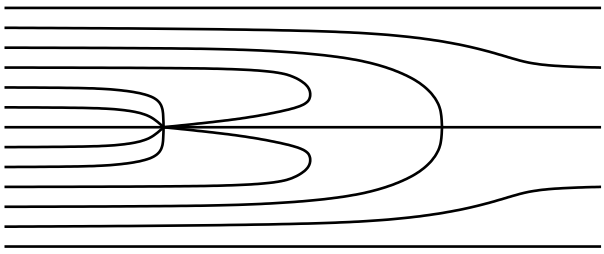

Figure 2.4: A radial (left) and a hyperbolic (right) hedgehog combine to a configuration with total charge $0 = |1 - 1|$.

The energies of the hedgehog configurations, shown in Fig. 2.2, are easily calculated from the Frank free energy $F_{el} + F_{24}$ [see Eqs. (1.2) and (1.3)]. The director fields of these configurations are $\boldsymbol{n} = (x, y, z)/r$ for the radial and $\boldsymbol{n} = (-x, -y, z)/r$ for the hyperbolic hedgehog, where $\boldsymbol{r} = (x, y, z)$ and $r = |\boldsymbol{r}|$. In a spherical region of radius $R$ with free

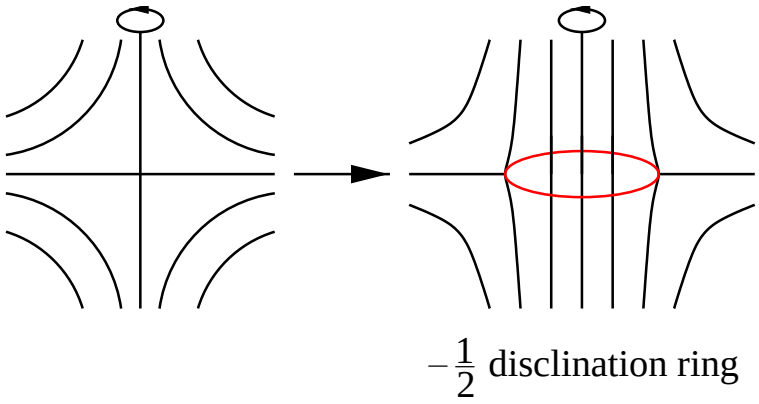


Figure 2.5: A hyperbolic hedgehog can be opened up to a $-1/2$ disclination ring.

boundary conditions at the outer surface, we obtain for their respective energies:

$$\begin{aligned} F_{\text{radial}} &= 4\pi(2K_1 - K_{24})R &&\rightarrow 4\pi(2K - K_{24})R \\ F_{\text{hyper}} &= \frac{4\pi}{15}(6K_1 + 4K_3 + 5K_{24})R &&\rightarrow \frac{4\pi}{3}(2K + K_{24})R \ , \end{aligned} \tag{2.5}$$

where the final expressions apply to the case of equal Frank constants. When $K_{24} = 0$, these energies reduce to those calculated in Ref. [199]. Note that the Frank free energy of point defects does not diverge in contrast to the distortion energy of disclinations in the preceding section. The hyperbolic hedgehog has lower energy than the radial hedgehog provided $K_3 < 6K_1 - 5K_{24}$ or $K > K_{24}$ for the one-constant approximation. Thus, if we concentrate on the bulk energies, *i.e.*, $K_{24} = 0$, the hyperbolic hedgehog is always energetically preferred, since $K_1$ is always of the same order as $K_3$. This seems to explain the observation of Lavrentovich and Terentjev, already mentioned [199], who found the configuration illustrated in Fig. 2.3 in a nematic drop with radial boundary conditions at the outer surface. However, a detailed explanation has to take into account the Frank free energy of the strongly twisted transition region between hyperbolic and radial hedgehog [199]. In Section 7.4 we will present a linear stability analysis for the radial hedgehog against twisting. In terms of the Frank constants, it provides a criterion for the twist transition to take place, and it shows that the twisting starts close to the defect core. If, in addition to the one-constant approximation, $K_{24}$ also fulfills the Cauchy relation (1.5), *i.e.*, $K = K_{24}$, the energies of the two hedgehog configurations in Eqs. (2.5) are equal, as one could have predicted from Eq. (1.6), which is then invariant with respect to rigid rotations of even a spatially varying $\boldsymbol{n}$.

The twisting of a hedgehog in a nematic drop takes place at a length scale of several microns [45, 199, 279]. However, point defect also possess a fine structure at smaller length scales, which has attracted a lot of attention. Figure 2.5 illustrates how a hyperbolic hedgehog opens up to a $-1/2$ disclination ring by filling in vertical lines of the director field. The farfield of the disclination ring is still given by the hedgehog so that the ring can be assigned the same topological point charge $Q = 1$. Similarly, a radial point defect is topologically

equivalent to a 1/2 disclination ring. Mineev pointed out that the characterization of a ring defect requires two parameters; the index of the line and the charge of the point defect [241]. The classification of ring defects within homotopy theory was developed by Garel [131] and Nakanishi *et al.* [251]. It can be asked whether it is energetically favorable for a hedgehog to open up to a disclination ring [244, 349]. One can obtain a crude estimate of the radius $R_0$ of the disclination ring with the help of Eqs. (2.1) and (2.5) for disclination and hedgehog energies. When $R_0 \gg r_c$, the director configuration of a charge 1 disclination ring is essentially that of a simple disclination line, discussed in the previous section. It extends up to distances of order $R_0$ from the ring center. Beyond this radius, the director configuration is approximately that of a hedgehog (radial or hyperbolic). Thus, we can estimate the energy of a disclination ring of radius $R_0$ centered in a spherical region of radius $R$ to be

$$F_{\rm ring} \approx 2\pi R_0 \left[\frac{\pi}{4} K \left(\frac{1}{2} + \ln \frac{R_0}{r_c}\right)\right] + 8\pi\alpha K (R - R_0) \ , \tag{2.6}$$

where $\alpha = 1$ for a radial hedgehog and $\alpha = 1/3$ for a hyperbolic hedgehog. We also set $K_{24} = 0$. Minimizing over $R_0$, we find

$$R_0 = r_c \exp\left[\frac{16}{\pi}\left(\alpha - \frac{3\pi}{32}\right)\right] \ . \tag{2.7}$$

Though admittedly crude, this approximation yields a result that has the same form as that calculated in Refs. [244, 349] using a more sophisticated ansatz for the director field. It has the virtue that it applies to both radial and hyperbolic far-field configurations. It predicts that the core of a radial hedgehog should be a ring with radius $R_0 \approx r_c e^{3.6}$, or $R_0 \approx 360\,\text{nm}$ for $r_c \approx 100\,\text{Å}$. The core of the hyperbolic hedgehog, on the other hand, will be a point rather than a ring because $R_0 \approx r_c e^{-0.2} \approx r_c$.

As in the case of disclinations, more refined models of the core of a point defect use the Landau-de Gennes free energy, which employs the second-rank tensor $\boldsymbol{Q}$ as an order paramter. Schopohl and Sluckin [316] chose a uniaxial $\boldsymbol{Q}$ but allowed the degree of orientational order, described by the Maier-Saupe parameter $S$ [49, 76], to continuously approach zero at the center of the defect. A stability analysis of the Landau-de Gennes free energy demonstrates that the radial hedgehog is either metastable or unstable against biaxial perturbations in the order parameter depending on the choice of the temperature and elastic constants [299, 133]. Penzenstadler and Trebin modeled a biaxial defect core [264]. They found that the core radius is of the order of the biaxial correlation length $\xi_b$, which for the compound MBBA gives approximately 25 nm. This is an order of magnitude smaller than the estimate above. The reason might be that the ansatz function used by Penzenstadler and Trebin does not include a biaxial disclination ring. Such a ring encircles a region of uniaxial order, as illustrated in the right part of Fig. 2.5, and it possesses a biaxial disclination core. Numerical studies indicate the existence of such a ring [331, 132] but a detailed analysis of the competition between a biaxial core and a biaxial disclination ring is still missing. We expect that Eq. (2.6) for a disclination ring and therefore Eq.

(2.7) for its radius can be justified within the Landau-de Gennes theory for $R_0 \gg r_c \sim \xi_b$. However, the Frank elastic constant and the core energy will be replaced by combinations of the Landau parameters. Since the ring radius $R_0$ varies exponentially with the elastic constants and the core energy, and since $r_c$ is only roughly defined, it is very difficult to predict with certainty even the order of magnitude of $R_0$. Further investigations are needed.

# Part II

# Colloidal Dispersions in Nematic Liquid Crystals

# Chapter 3

# Approaching Colloidal Dispersions

Our access to colloidal dispersions in nematic liquid crystals is threefold. We first motivate our investigation and shortly present the contents of the next chapters. Then, we give a historic account of the topic relating it to recent developments in the liquid crystal field and reviewing the work performed on colloidal dispersions in nematic liquid crystals. Finally, with nematic emulsions, we introduce one particular model system for such colloidal dispersions.

## 3.1 Motivation and Contents

Dispersions of particles in a host medium are part of our everyday life and an important state of matter for fundamental research. One distinguishes between emulsions, where surfactant-coated liquid droplets are dispersed in a fluid environment, colloidal suspensions, where the particles are solid, and aerosoles, with fluid or solid particles floating in a gaseous phase. Colloidal dispersions, whose particle size ranges from 10 nm to 10 $\mu$m, appear in food, with milk being the best-known fat-in-water emulsion, in drugs, cosmetics, paints, and ink. As such, they are of considerable technological importance. In nature, one is confronted by both the bothering and appealing side of fog, and one can look at the beautiful blue-greenish color of berg lakes in the Canadian Rockies, caused by light scattering from a fine dispersion of stone flower in water. The best-known example of an ordered colloid, a colloidal crystal, is the opal, formed from a uniform array of silica spheres compressed and fused over geological timescales. In fundamental research, colloidal dispersions are ideal systems to study Brownian motion and hydrodynamic interactions of suspended particles [306, 175]. They provide model systems [211, 134] for probing our understanding of melting and boiling, and for checking the Kosterlitz-Thouless-Halperin-Nelson-Young transition in two-dimensional systems [380, 401, 41]. The main interest in colloidal dispersions certainly focusses on the problem how to prevent the particles from flocculation, as stated by Russel, Saville, and Schowalter [306]:

> "Since all characteristics of colloidal systems change markedly in the transition from the dispersed to the aggregated state, the question of stability occupies a

central position in colloid science."

There exists a whole zoo of interactions between the particles whose delicate balance determines the stability of a colloidal dispersion. Besides the conventional van der Waals, screened Coulombic, and steric interactions [306], fluctuation-induced Casimir forces (*e.g.*, in binary fluids close to the critical point [181, 247]) and depletion forces in binary mixtures of small and large particles [306, 83, 82, 300] have attracted a lot of interest. Entropic effects play a major role in the three latter types of interactions. In a subtle effect, they also lead to an attraction between like-charged macroions [173, 67, 198] by Coulomb depletion [9].

The present work focusses on the interesting question of how particles behave when they are dispersed in a nematic liquid crystal. There arises an elastic distortion of the director field between the particles that induces additional long-range forces. They are of dipolar or quadrupolar type, depending on the symmetry of the director configuration around the particle [40, 288, 304, 279, 216]. The forces were confirmed by recent experiments in inverted nematic emulsions [279, 276, 280]. On the other hand, close to the suspended particles, topological point and line defects in the orientational order occur which strongly determine their behavior. For example, they give rise to a short-range repulsion [279, 280]. Colloidal dispersions in a nematic environment are therefore an ideal laboratory for studying the statics and dynamics of topological defects.

The following chapters deal with the physics of such dispersions. In Chapter 4 we investigate, what I consider the paradigm for their understanding, *i.e.*, the static properties of one particle. We concentrate on a radial anchoring of the director at its surface, for which we identify three different types of nematic environment; the dipole configuration, where the particle and a companion hyperbolic point defect form a tightly bound topologial dipole, the Saturn-ring configuration, where the particle is surrounded by a $-1/2$ disclination ring, and a structure with an equatorial surface ring, which appears for decreasing surface-anchoring strength. Secondly, in Chapter 5 we address two-particle interactions with the help of a phenomenological theory. Thirdly, we calculate the Stokes drag of one particle in Chapter 6. With its knowledge, one immediately has access to the diffusion constants for the Brownian motion of spherical objects via the Stokes-Einstein relation. In Chapter 7 we then turn our interest towards colloidal dispersions in complex geometries. In particular, we will consider particles, *e.g.*, droplets of water, in a large nematic drop. Finally, in Chapter 8 we investigate the effect of surface-induced nematic order on the stability of colloidal dispersions above the nematic-isotropic phase transition.

## 3.2 Historic Account

Liquid crystal emulsions, in which surfactant-coated drops, containing a liquid crystalline material, are dispersed in water, have been a particularly fruitful medium for studying topological defects for 30 years [235, 89, 45, 199, 187, 88]. The liquid crystalline drops typically range from $10\,\mu$m to $50\,\mu$m in diameter and are visible under a microscope. Changes in the Frank director $\boldsymbol{n}$ are easily studied under crossed polarizers. The isolated drops in

these emulsions provide an idealized spherical confining geometry for the nematic phase. With the introduction of polymer-dispersed liquid crystals as electrically controllable light shutters [85, 88], an extensive study of liquid crystals confined to complex geometries, like distorted drops in a polymer matrix or a random porous network in silica aerogel, was initiated [88, 66].

Here, we are interested in the inverse problem that is posed by particles suspended in a nematic solvent. Already in 1970, Brochard and de Gennes studied a suspension of magnetic grains in a nematic phase and determined the director field far away from a particle [40]. The idea was to homogeneously orient liquid crystals with a small magnetic anisotropy by a reasonable magnetic field strength through the coupling between the liquid-crystal molecules and the grains. The idea was realized experimentally by two groups [51, 115]. However, even in the highly dilute regime the grains cluster. Extending Brochard's and de Gennes' work, Burylov and Raikher studied the orientation of an elongated particle in a nematic phase [42]. Chaining of bubbles or microcrystallites was used to visualize the director field close to the surface of liquid crystals [289, 55]. A bistable liquid crystal display was introduced based on a dispersion of agglomerations of silica spheres in a nematic host [95, 183, 182, 138]. The system was called *filled nematics*. Chains and clusters were observed in the dispersion of latex particles in a lyotropic liquid crystal [278, 286, 287]. The radii of the particles were 60 and 120 nm. Therefore, details of the director field could not be resolved under the polarizing microscope.

Terentjev *et al.* started to investigate the director field around a sphere by both analytical and numerical methods, first concentrating on the Saturn-ring and surface-ring configuration [349, 185, 305, 325]. Experiments of Philippe Poulin and coworkers on inverted nematic emulsions, which we describe in the following section, clearly demonstrated the existence of a dipolar structure formed by a water droplet and a companion hyperbolic hedgehog [279, 276, 280, 281]. A similar observation at a nematic-isotropic interface was made by R. B. Meyer in 1972 [236]. Lately, Poulin, Mondain-Monval, *et al.* were able to identify the dipolar structure in suspensions of latex particles [277], and they could observe an equatorial ring configuration in the weak-anchoring limit of nematic emulsions [242]. Lubensky, Stark, and coworkers presented a thorough analytical and numerical analysis of the director field around a spherical particle [279, 216, 335]. It is discussed in the next chapter. Ramaswamy *et al.* [288] and Ruhwandl and Terentjev [304] determined the long-range quadrupolar interaction of particles surrounded by a ring disclination, whereas Lubensky *et al.* addressed both dipolar and quadrupolar forces [216] (see Chapter 5). Recently, Lev and Tomchuk studied aggregates of particles under the assumption of weak anchoring[207]. Work on the Stokes drag of a spherical object immersed into a uniformly aligned nematic was performed by Diogo [84], Roman and Terentjev [295], and Heuer, Kneppe, and Schneider [177, 155]. The calculations were extended to the Saturn-ring configuration by Ruhwandl and Terentjev [303] and to the dipolar structure by Ventzki and Stark [370], whose work is explored in detail in Chapter 6. Stark and Stelzer [339] numerically investigated multiple nematic emulsions [279] by means of finite elements. We discuss the results in Chapter 7. It is interesting to note that dipolar configurations also appear in two-dimensional systems including (1) free standing smectic films [209, 268],

where a circular region with an extra layer plays the role of the spherical particle, and (2) Langmuir films [111], in which a liquid-expanded inclusion in a tilted liquid-condensed region acts similarly. Pettey, Lubensky, and Link studied the dipolar structure in two dimensions theoretically [268]. In cholesteric liquid crystals particle-stabilized defect gels were found [402], and people start to investigate dispersion of particles in a smectic phase [122, 163, 27]. Finally, Meeker *et al.* reported a gel-like structure in nematic colloidal dispersions with a significant shear modulus [230].

With two excellent publications [319, 320], Ping Sheng initiated the interest in partially ordered nematic films above the nematic-isotropic phase transition temperature $T_c$ using the Landau-de Gennes approach. In 1981, Horn, Israelachvili, and Perez performed first measurements of liquid crystal-mediated forces between curved mica sheets [159]. Motivated by both works, Poniewierski and Sluckin refined Sheng's study [274]. Borštnik and Žumer explicitly considered two parallel plates immersed into a liquid crystal slightly above $T_c$ [36], and thoroughly investigated short-range interactions due to the surface-induced nematic order. An analog work was presented by de Gennes, however, assuming a surface-induced smectic order [75]. The effect of such a presmectic film was measured by Moreau, Richetti, and Barois [243]. Recent studies address short-range forces of spherical objects using either analytical methods [33], which we report in Chapter 8, or numerical calculations [128]. In Chapter 8 we also demonstrate that such forces can induce flocculation of colloidal particles above the nematic-isotropic phase transition [34, 35]. In a more general context, they were also suggested by Löwen [212, 213]. Muševič *et al.* probe these interactions with the help of an atomic force microscope [248, 249], whereas Böttger *et al.* [37] and Poulin *et al.* [275] are able to suspend solid particles in a liquid crystal above $T_c$. Even Casimir forces arising from fluctuations in the liquid-crystalline order parameter were investigated both in the nematic [5, 4, 346] and isotropic phase [405] of a liquid crystal.

## 3.3 Nematic Emulsions

Three years ago, Philippe Poulin succeeded in producing inverted and multiple nematic emulsions [279, 280]. The notion "inverted" refers to water droplets dispersed in a nematic solvent, in contrast to direct liquid-crystal-in-water emulsions. If the solvent itself forms drops surrounded by the water phase, one has multiple emulsions. We introduce them here since they initiated the theoretical work we report in the following chapters.

Philippe Poulin dispersed water droplets of 1 to 5 $\mu$m in diameter in a nematic liquid crystal host, pentylcyanobiphenyl (5CB), which formed larger drops ($\sim 50\,\mu$m diameter) surrounded by a continuous water phase. This isolated a controlled number of colloidal droplets in the nematic host which allowed to observe their structure readily. As a surfactant, a small amount of sodium dodecyl sulfate was used. It is normally ineffective at stabilizing water droplets in oil. Nevertheless, the colloidal water droplets remained stable for several weeks, which suggested that the origin of this stability is the surrounding liquid crystal – a hypothesis that was confirmed by the observation that droplets became unstable and coalesced in less than one hour after the liquid crystal was heated to the isotropic

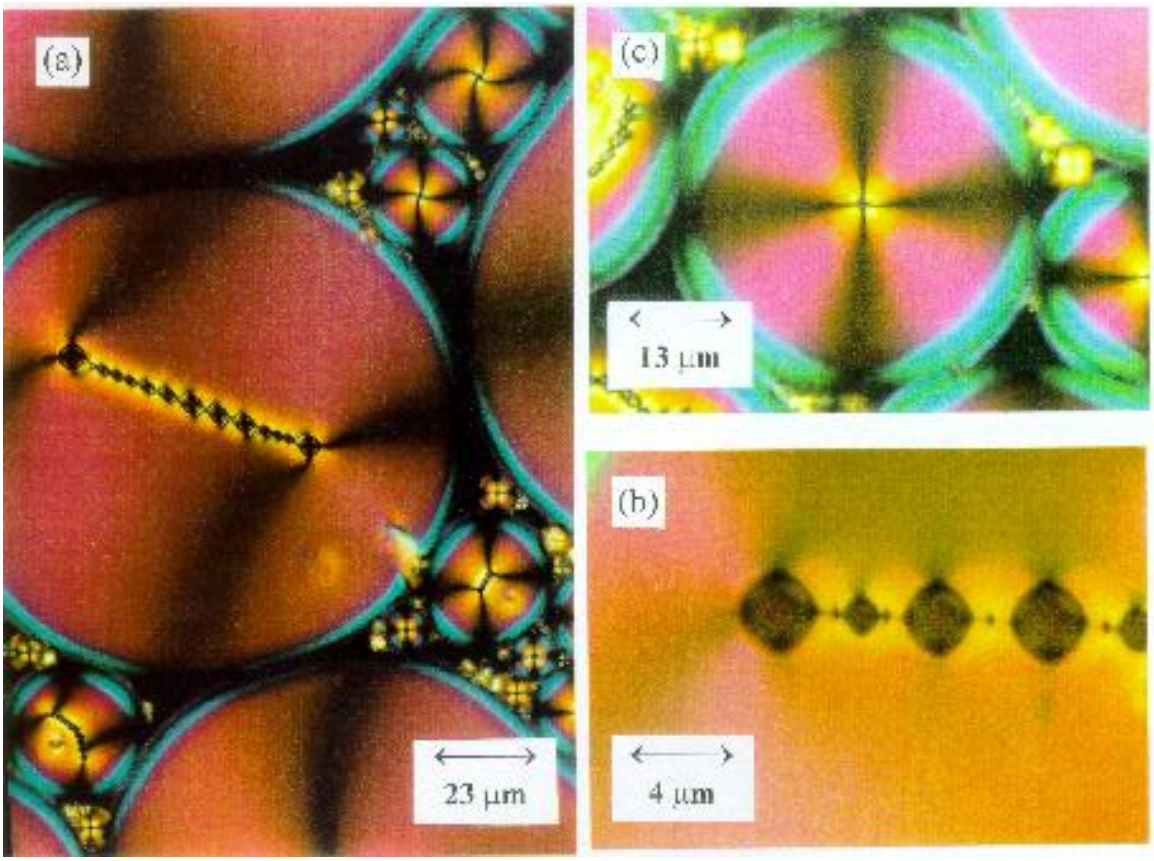


Figure 3.1: (a) Microscope image of a nematic multiple emulsion taken under crossed polarizers. (b) A chain of water droplets under high magnification. (c) A nematic drop containing a single water droplet .

phase. The surfactant also guaranteed a homeotropic, *i.e.*, normal boundary condition of the director at all the surfaces.

The multiple nematic emulsions were studied by observing them between crossed polarizers in a microscope. Under such conditions, an isotropic fluid will appear black, whereas regions in which there is the birefringent nematic will be colored. Thus the large nematic drops in a multiple emulsion appear predominately red in Fig. 3.1(a)[1], whereas the continuous water phase surrounding them is black. Dispersed within virtually all of the nematic drops are smaller colloidal water droplets, which also appear dark in the photo; the number of water droplets tends to increase with the size of the nematic drops. Remarkably, in all cases, the water droplets are constrained at or very near the center of the nematic drops. Moreover, their Brownian motion, usually observed in colloidal dispersions, has completely ceased. However, when the sample is heated to change the nematic into an isotropic fluid,

[1]Reprinted with permission from P. Poulin, H. Stark, T.C. Lubensky, and D.A. Weitz, Novel Colloidal Interactions in Anisotropic Fluids, Science **275**, 1770 (1997). Copyright 1997 American Association for the Advancement of Science .

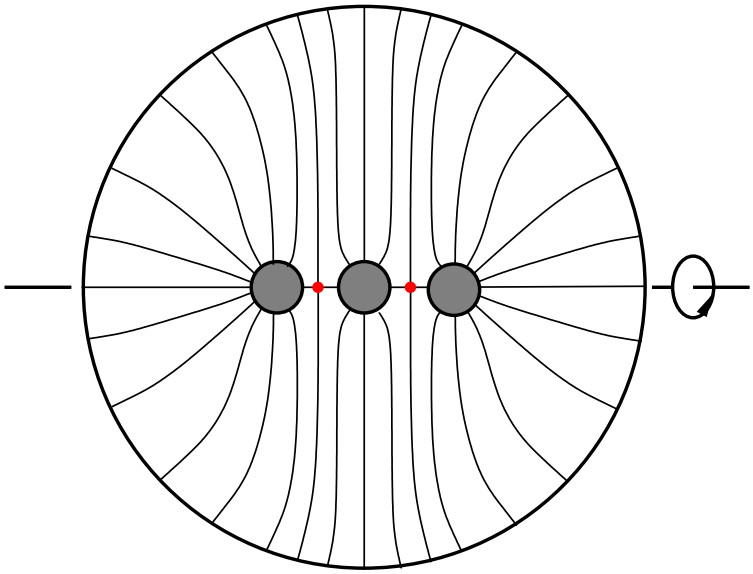

Figure 3.2: The director field lines of a nematic drop containing a string of three spherical particles.

the Brownian motion of the colloidal droplets is clearly visible in the microscope.

Perhaps the most striking observation in Fig. 3.1(a) is the behavior of the colloidal droplets when more than one of them cohabit the same nematic drop: the colloidal droplets invariably form linear chains. This behavior is driven by the nematic liquid crystal: the chains break, and the colloidal droplets disperse immediately upon warming the sample to the isotropic phase. However, although the anisotropic liquid crystal must induce an attractive interaction to cause the chaining, it also induces a shorter range repulsive interaction. A section of a chain of droplets under higher magnification [see Fig. 3.1(b)] shows that the droplets are prevented from approaching each other too closely, with the separation between droplets being a significant fraction of their diameter. A careful inspection of Fig. 3.1(b) even reveals black dots between the droplets which we soon will identify as topological point defects. The distance between droplets and these host-fluid defects increases with the droplet radius.

To qualitatively understand the observation, we start with one water droplet placed at the center of a large nematic drop. The homeotropic boundary condition enforces a radial director field between both spherical surfaces. It exhibits a distinctive four-armed star of alternating bright and dark regions under crossed polarizers that extend throughout the whole nematic drop as illustrated in Fig. 3.1(c). Evidently, following the explanations in Section 2.2 about point defects, the big nematic drop carries a topological point charge $Q = 1$ that is matched by the small water droplet which acts like a radial hedgehog. Each water droplet beyond the first added to the interior of the nematic drop must create orientational structure out of the nematic itself to satisfy the global constraint $Q = 1$. The simplest (though not the only [216]) way to satisfy this constraint is for each extra water

droplet to create a hyperbolic hedgehog in the nematic host. Note that from Fig. 2.4 we already know that a radial hedgehog (represented by the water droplet) and a hyperbolic point defect carry a total charge zero. Hence, $N$ water droplets in a large nematic drop have to be accompanied by $N-1$ hyperbolic hedgehogs. Figure 3.2 presents a qualitative picture of the director field lines for a string of three droplets. It is rotationally symmetric about the horizontal axis. Between the droplets, hyperbolic hedgehogs appear. They prevent the water droplets from approaching each other and from finally coalescing since this would involve a strong distortion of the director field . The defects therefore mediate a short-range repulsion between the droplets.

In the following chapters, we demonstrate the physical ideas which evolved from the experiments on multiple nematic emulsions. We will explain the chaining of droplets by introducing the topological dipole formed by one spherical particle and its companion hyperbolic defect. This leads us to the next chapter where we investigate the simplest situation, *i.e.*, one particle placed in a nematic solvent which is uniformly aligned at infinity.

# Chapter 4

# The Paradigm - One Particle

The multiple nematic emulsions that we introduced in Section 3.3 are already a complicated system. In this chapter we investigate thoroughly by both analytical and numerical means what I regard as the paradigm for the understanding of inverted nematic emulsions. We ask which director field configurations do occur when one spherical particle that prefers a radial anchoring of the director at its surface is placed into a nematic solvent uniformly aligned at infinity. This constitutes the simplest problem one can think of, and it is a guide to the understanding of more complex situations.

## 4.1 The Three Possible Configurations

If the directors are rigidly anchored at the surface, the particle carries a topological charge $Q = 1$. Because of the boundary conditions at infinity, the total charge of the whole system is zero; therefore, the particle must nucleate a further defect in its nematic environment. One possibility is a dipolar strucure where the particle and a hyperbolic hedgehog form a tightly bound object which we call *dipole* for short (see Fig. 4.1). As already explained in Fig. 2.4, the topological charges $+1$ of a radial hedgehog, represented by the particle, and of a hyperbolic point defect "add up" to a total charge of zero. In the *Saturn-ring* configuration, a $-1/2$ disclination ring encircles the spherical particle at its equator (see Fig. 4.1). Of course, the disclination ring can be moved upward or downward, and by shrinking it to the topologically equivalent hyperbolic hedgehog, the Saturn ring is continuously transformed into the dipole configuration. However, our calculations show that a non-symmetric position of the defect ring is never stable. When the surface anchoring strength $W$ is lowered (see Fig. 4.1), the core of the disclination ring prefers to sit directly at the surface of the particle. For sufficiently low $W$, the director field becomes smooth everywhere, and a ring of tangentially oriented directors is located at the equator of the sphere. In the case of tangential boundary conditions, there exists only one structure. It possesses two surface defects, called boojums, at the north and south pole of the particle [233, 45, 186, 377]. We will not investigate it further.

It is instructive to first consider the director field far away from the particle, which

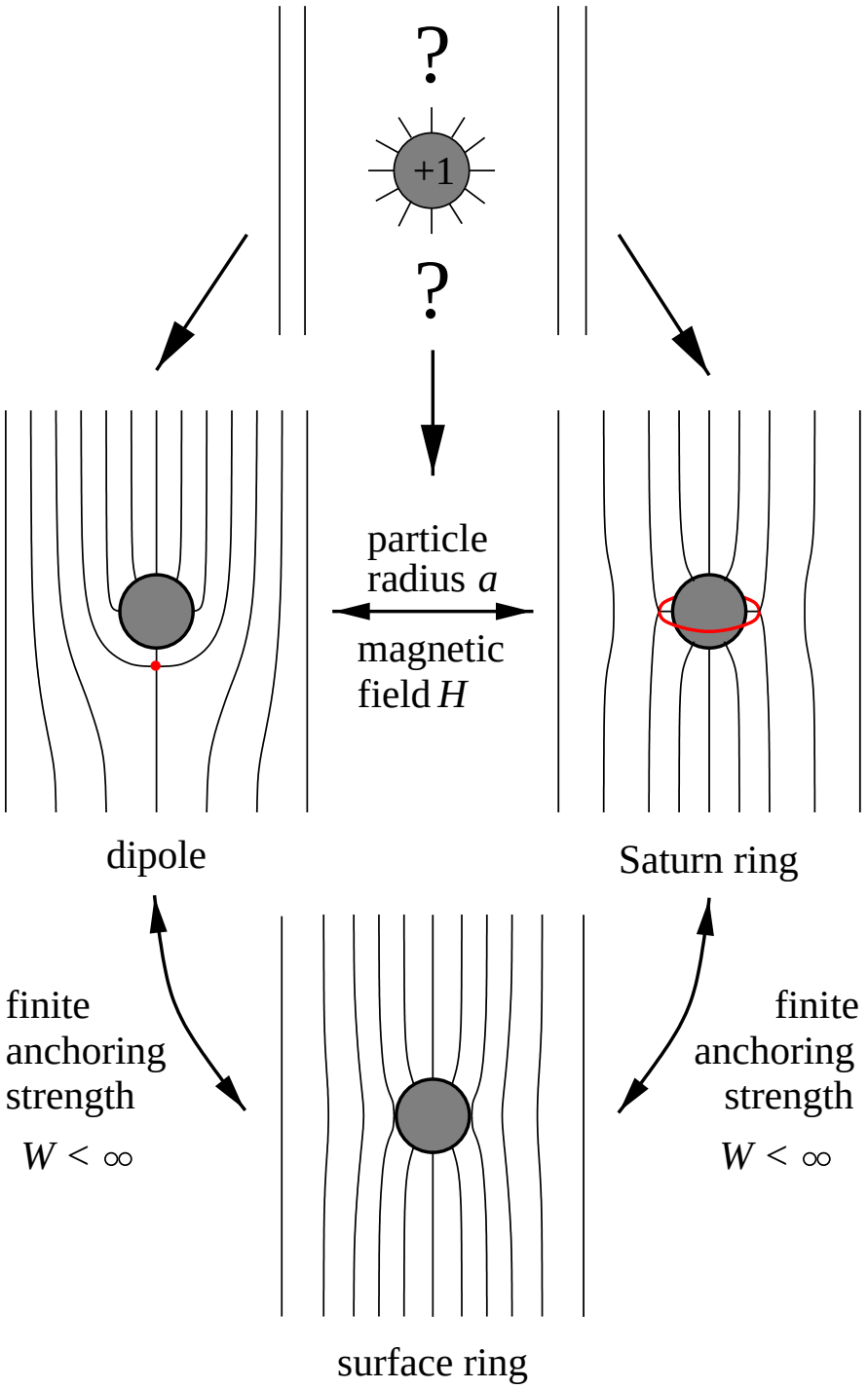


Figure 4.1: A spherical particle with a preferred homeotropic anchoring at its surface that is placed into a uniformly aligned nematic liquid crystal exhibits three possible structures: the dipole configuration where the particle is accompanied by a hyperbolic hedgehog, the Saturn-ring configuration where the particle is surrounded by a $-1/2$ disclination ring at the equator, and the surface-ring configuration.

crucially depends on the global symmetry of the system [40, 216]. With its knowledge, ansatz functions for the director configurations around a particle can be checked. Furthermore, the far field determines the long-range two-particle interaction. Let the director $\boldsymbol{n}_0$ at infinity point along the $z$ axis. Then, in the far field, the director is approximated by $\boldsymbol{n}(\boldsymbol{r}) \approx (n_x, n_y, 1)$ with $n_x, n_y \ll 1$. In leading order, the normalization of the director can be neglected, and the Euler-Lagrange equations for $n_x$ and $n_y$ arising from a minimization of the Frank free energy in the one-constant approximation are simply Laplace equations:

$$\nabla^2 n_\mu = 0 \ . \tag{4.1}$$

The solutions are the well-known multipole expansions of electrostatics that include monopole, dipole, and quadrupole terms. They are all present if the suspended particle has a general shape or if, *e.g.*, the dipole in Fig. 4.1 is tilted against $\boldsymbol{n}_0$. In the dipole configuration with its axial symmetry about $\boldsymbol{n}_0$, the monopole is forbidden, and we obtain

$$n_x = p\,\frac{x}{r_3} + 2c\,\frac{zx}{r^5} \qquad \text{and} \qquad n_y = p\,\frac{y}{r_3} + 2c\,\frac{zy}{r^5} \ , \tag{4.2}$$

where $r = (x^2 + y^2 + z^2)^{1/2}$. We use the expansion coefficients $p$ and $c$ to assign both a dipole ($\boldsymbol{p}$) and quadrupole ($\boldsymbol{c}$) moment to the configuration:

$$\boldsymbol{p} = p\,\boldsymbol{n}_0 \qquad \text{and} \qquad \boldsymbol{c} = c\,(\boldsymbol{n}_0 \otimes \boldsymbol{n}_0 - \mathbf{1}/3) \ . \tag{4.3}$$

The symbol $\otimes$ means tensor product, and $\mathbf{1}$ is the unit tensor of second rank. We adopt the convention that the dipole moment $\boldsymbol{p}$ points from the companion defect to the particle. Hence, if $p > 0$, the far field of Eqs. (4.2) belongs to a dipole configuration with the defect sitting below the particle (see Fig. 4.1). Note, that by dimensional analysis, $p \sim a^2$ and $c \sim a^3$, where $a$ is the radius of the sperical particle. Saturn-ring and surface-ring configurations possess a mirror plane perpendicular to the rotational axis. Therefore, the dipole term in Eqs. (4.2) is forbidden, *i.e.*, $p = 0$. We will show in Chapter 6 that the multipole moments $\boldsymbol{p}$ and $\boldsymbol{c}$ determine the long-range two-particle interaction. We will derive it on the basis of a phenomenological theory.

In the present chapter we investigate the dipole by both analytical and numerical means. First, we identify a twist transition which transforms it into a chiral object. Then, we study the transition from the dipole to the Saturn ring configuration, which is induced either by decreasing the particle radius or by applying a magnetic field. The role of metastability is discussed. Finally, we consider the surface-ring configuration and point out the importance of the saddle-splay free energy $F_{24}$. Lower bounds for the surface-anchoring strength $W$ are given.

## 4.2 An Analytical Investigation of the Dipole

Even in the one-constant approximation and for fixed homeotropic boundary conditions, analytical solutions of the Euler-Lagrange equations, arising from the minimization of

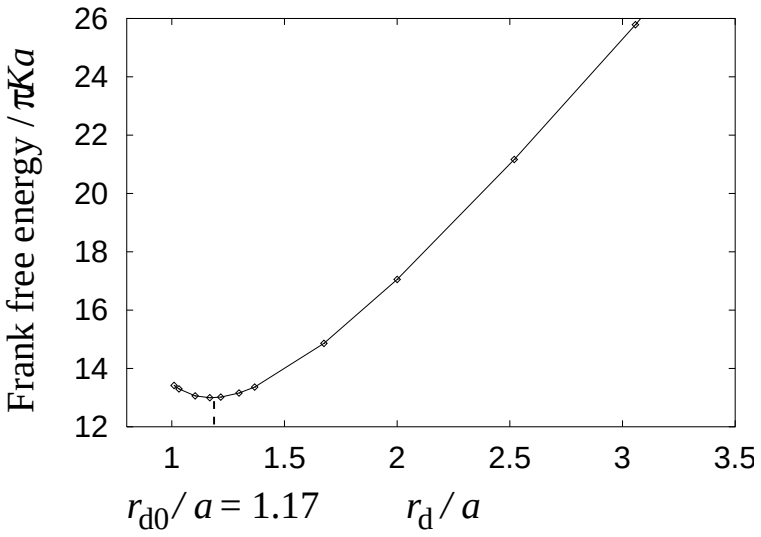


Figure 4.2: Frank free energy (in units of $\pi K a$) for the topological dipole as a function of the reduced distance $r_d/a$ from the particle center to the companion hedgehog.

the Frank free energy, cannot be found. The Euler-Lagrange equations are highly nonlinear due to the normalization of the director. In this section we investigate the dipole configuration with the help of ansatz functions that obey all boundary conditions and possess the correct far-field behavior. The free parameters in these ansatz functions are determined by minimizing the Frank free energy. We will see that this procedure already provides a good insight into our system.

We arrive at appropriate ansatz functions by looking at the electrostatic analog of our problem [279, 216], *i.e.*, a conducting sphere of radius $a$ and with a reduced charge $q$ which is exposed to an electric field of unit strength along the $z$ axis. The electric field is

$$\boldsymbol{E}(\boldsymbol{r}) = \boldsymbol{e}_z + qa^2 \frac{\boldsymbol{r}}{r^3} - a^3 \frac{r^2 \boldsymbol{e}_z - 3z\boldsymbol{r}}{r^5} \quad . \tag{4.4}$$

In order to enforce the boundary condition that $\boldsymbol{E}$ be normal to the surface of the sphere, an electric image dipole has to be placed at the center of the sphere. The ansatz function for the director field follows from a normalization: $\boldsymbol{n}(\boldsymbol{r}) = \boldsymbol{E}(\boldsymbol{r})/|\boldsymbol{E}(\boldsymbol{r})|$. An inspection of its far field gives

$$\boldsymbol{n}(\boldsymbol{r}) \approx \left( qa^2 \frac{x}{r^3} + 3a^3 \frac{xz}{r^5}, qa^2 \frac{y}{r^3} + 3a^3 \frac{yz}{r^5} \right) \quad , \tag{4.5}$$

in agreement with Eqs. (4.2). The electrostatic analog assigns a dipole moment $qa^2$ and a quadrupole moment $3a^3/2$ to the topological dipole. The zero of the electric field determines the location $-r_d \boldsymbol{e}_z$ of the hyperbolic hedgehog on the $z$ axis. Thus, $q$ or the distance $r_d$ from the center of the particle are the variational parameters of our ansatz functions. Note that for $q = 3$, the hedgehog just touches the sphere, and that for $q < 3$, a singular ring appears at the surface of the sphere. In Fig. 4.2 we plot the Frank free energy in

the one-constant approximation and in units of $\pi K a$ as a function of the reduced distance $r_d/a$. The saddle-splay term is not included, since for rigid anchoring it just provides a constant energy shift. There is a pronounced minimum at $r_{d0} = 1.17a$ corresponding to a dipole moment $p = qa^2 = 3.08a^2$. The minimum shows that the hyperbolic hedgehog sits close to the spherical particle. To check the magnitude of the thermal fluctuations of its radial position, we determine the curvature of the energy curve at $r_{d0}$; its approximate value amounts to $33\pi K/a$. According to the equipartition theorem, the average thermal displacement $\delta r_{d0}$ follows from the expression

$$\frac{\delta r_{d0}}{a} \approx \sqrt{\frac{k_B T}{33\pi K a}} \approx 2 \cdot 10^{-3} \ , \tag{4.6}$$

where the final estimate employs $k_B T \approx 4 \cdot 10^{-14}$ erg, $K \approx 10^{-6}$ dyn, and $a = 1\,\mu$m. These fluctuations in the length of the topological dipole are unobservably small. For angular fluctuations of the dipole, we find $\delta\theta \approx 10^{-2}$, *i.e*, still difficult to observe [216]. We conclude that the spherical particle and its companion hyperbolic hedgehog form a tightly bound object. Interestingly, we note that angular fluctuations in the 2D version of this problem diverge logarithmically with the sample size [268]. They are therefore much larger and have indeed been observed in free standing smectic films [209].

The droplet-defect dipole was observed by Philippe Poulin in inverted nematic emulsions [280]. In Fig. 4.3(top) we present how it looks like in a microscope under crossed polarizers, with one polarizer parallel to the dipole axis. In Fig. 4.3(bottom) we show a calculated image using the Jones matrix formalism [88] based on the director field of the electrostatic analog. Any refraction at the droplet boundary is neglected. The similarity of the two images is obvious and clearly confirms the occurrence of the dipole configuration.

The electric field ansatz is generalized by no longer insisting that it originates in a true electric field. This allows us to introduce additional variational paramters [216]. The Frank free energy at $r_{d0}$ is lowered, and the equilibrium separation amounts to $r_{d0} = 1.26a$. The respective dipole and quadrupole moments turn out to be $p = 2.20a^2$ and $c = -1.09a^2$. We are also able to construct ansatz functions for the dipole-Saturn ring transition utilizing the method of images for the related 2D problem and correcting the far field [216]. The results agree with the numerical study presented in the next section.

## 4.3 Results and Discussion of the Numerical Study

Before we present the results of our numerical study, we summarize the numerical method. Details can be found in [335].

### 4.3.1 Summary of Numerical Details

The numerical investigation is performed on a grid which is defined by modified spherical coordinates. Since the region outside the spherical particle is infinitely extended, we employ a radial coordinate $\rho = 1/r^2$. The exponent 2 is motivated by the far field of the dipole

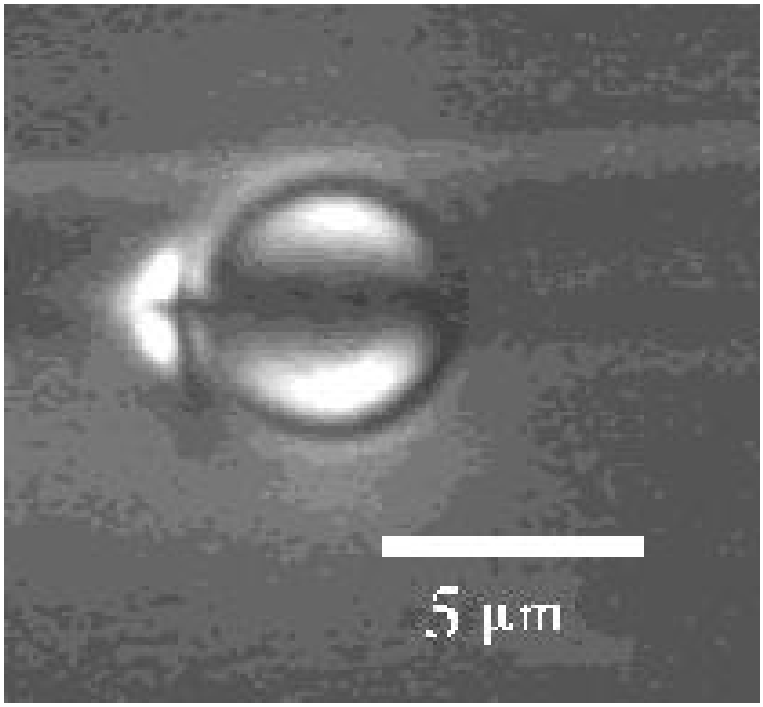


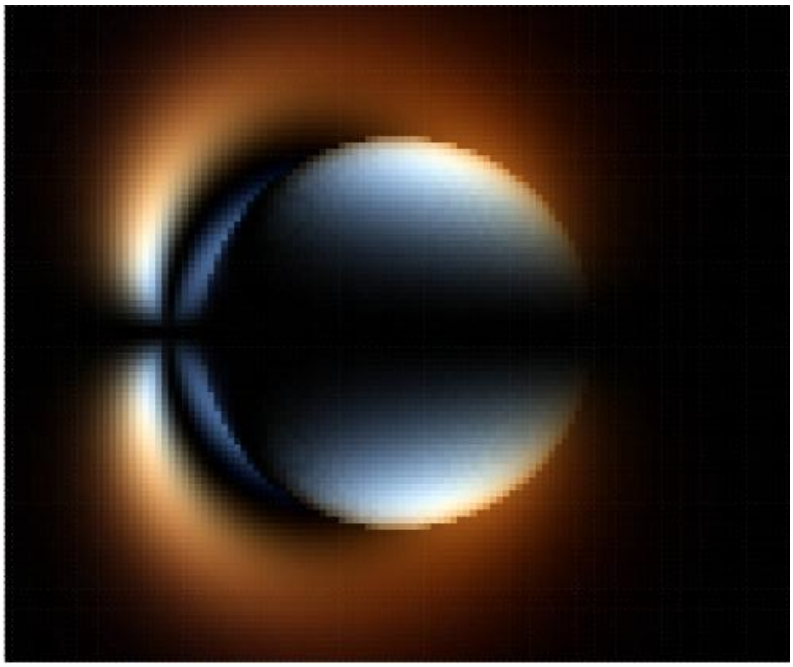

Figure 4.3: (top) Image of a single droplet with its companion defect as observed under crossed polarizers obtained by P. Poulin [280]. (bottom) Simulated image of the same configuration using the Jones matrix formalism [216]. The two pictures are very similar. From Ref. [216].

configuration. Such a transformation has two advantages. The exterior of the particle is mapped into a finite region, *i.e.*, the interior of the unit sphere ($\rho \leq 1$). Furthermore, equally spaced grid points along the coordinate $\rho$ result in a mesh size in real space which is small close to the surface of the particle. In this area the director field is strongly varying, and hence a good resolution for the numerical calculation is needed. On the other hand, the mesh size is large far away from the sphere where the director field is nearly homogeneous. Since our system is axially symmetric, the director field only depends on $\rho$ and the polar angle $\theta$. The director is expressed in the local coordinate basis $(\mathbf{e}_r, \mathbf{e}_\theta, \mathbf{e}_\phi)$ of the standard spherical coordinate system, and the director components are parametrized by a tilt $[\Theta(\rho,\theta)]$ and a twist $[\Phi(\rho,\theta)]$ angle: $n_r = \cos\Theta$, $n_\theta = \sin\Theta\cos\Phi$, and $n_\phi = \sin\Theta\sin\Phi$.

The total free energy $F_{\boldsymbol{n}}$ of Eq. (1.1) is expressed in the modified spherical coordinates. Then, the Euler-Lagrange equations in the bulk and at the surface are formulated with the help of the chain rules of Eqs. (1.14) and (1.15) and by utilizing the algebraic program Maple. A starting configuration of the director field is chosen and relaxed into a local minimum via the Newton-Gauss-Seidel method [284] which was implemented in a Fortran program.

So far we have described the conventional procedure of a numerical investigation. Now, we address the problem of how to describe disclination rings numerically. Figure 4.4 presents such a ring whose general position is determined by a radial ($r_d$) and an angular ($\theta_d$) coordinate. The free energy $F_{\mathbf{n}}$ of the director field follows from a numerical integration. This assigns some energy to the disclination ring which certainly is not correct since the numerical integration does not realize the large director gradients close to the defect core. To obtain a more accurate value for the total free energy $F$, we use the expression

$$F = F_{\boldsymbol{n}} - F_{\boldsymbol{n}}|_{\text{torus}} + F_{c/d} \times 2\pi r_d \sin\theta_d \ , \quad (4.7)$$

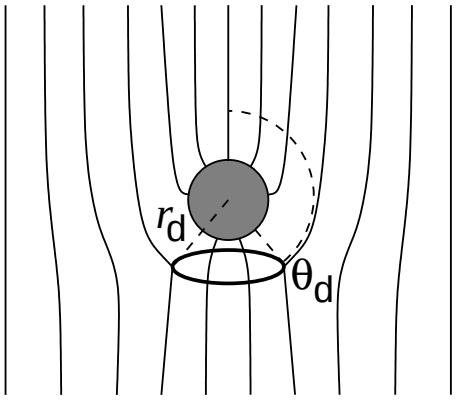


Figure 4.4: Coordinates $(r_d, \theta_d)$ for a $-1/2$ disclination ring with a general position around the spherical particle. From Ref. [335].

where $F_c$ and $F_d$ are the line energies of a disclination introduced in Eqs. (2.1) and (2.3). The quantity $F_{\boldsymbol{n}}|_{\text{torus}}$ denotes the numerically calculated free energy of a toroidal region of cross section $\pi R^2$ around the disclination ring. Its volume is $\pi R^2 \times 2\pi r_d \sin\theta_d$. The value $F_{\boldsymbol{n}}|_{\text{torus}}$ is replaced by the last term on the right-hand side of Eq. (4.7), which provides the correct free energy with the help of the line energies $F_c$ or $F_d$. We checked that the cross section $\pi R^2$ of the cut torus has to be equal or larger than $3\Delta\rho\Delta\theta/2$, where $\Delta\rho$ and $\Delta\theta$ are the lattice constants of our grid. For larger cross sections, the changes in the free energy $F$ for fixed core radius $r_c$ were less than 1 %, *i.e.*, $F$ became independent of $\pi R^2$. What is the result of this procedure? All lengths in the free energy $F_{\boldsymbol{n}}$ can be rescaled by the particle radius $a$. This would suggest

that the director configuration does not depend on the particle size. However, with the illustrated procedure a second length scale, *i.e.*, the core radius $r_c$ of a disclination, enters. All our results on disclination rings therefore depend on the ratio $a/r_c$. In discussing them, we assume $r_c \approx 10\,\mathrm{nm}$ [176] which then determines the radius $a$ for a given $a/r_c$.

### 4.3.2 Twist Transition of the Dipole Configuration

In this subsection we present our numerical study of the topological dipole. We always assume that the directors are rigidly anchored at the surface ($W \to \infty$) and choose a zero magnetic field. In Fig. 4.5 we plot the reduced distance $r_d/a$ of the hedgehog from the center of the sphere as a function of the reduced splay ($K_1/K_3$) and twist ($K_2/K_3$) constants. In the one-constant approximation, we find $r_d = 1.26 \pm 0.02$, where the mesh size of the grid determines the uncertainty in $r_d$. Our result is in excellent agreement with the generalized electric-field ansatz we introduced in the last section [216]. However, Ruhwandl and Terentjev using a Monte-Carlo minimization report a somewhat smaller value for $r_d$ [304]. In front of the thick line $r_d$ is basically constant. Beyond the line $r_d$ starts to grow which indicates a structural change in the director field illustrated in the nail picture of Fig. 4.6a). Around the hyperbolic hedgehog the directors develop a non-zero azimuthal component $n_\phi$, *i.e.*, they are tilted relative to the drawing plane. This introduces a twist into the dipole. It should be visible under a polarizing microscope when the dipole is viewed along its symmetry axis.

In Fig. 4.6b) we draw a phase diagram of the twist transition. As expected, it occurs when $K_1/K_3$ increases or when $K_2/K_3$ decreases, *i.e.*, when a twist deformation costs less energy than a splay distortion. The open circles are numerical results for the transition line which can well be fitted by the straight line $K_2/K_3 \approx K_1/K_3 - 0.04$. Interestingly, the small offset 0.04 means that $K_3$ does not play an important role. Typical calamitic liquid crystals like MBBA, 5CB, and PAA should show the twisted dipole configuration.

Since the twist transition breaks the mirror symmetry of the dipole, which then becomes a chiral object, we describe it by a Landau expansion of the free energy:

$$F = F_0 + a(K_1/K_3, K_2/K_3)[n_\phi^{\max}]^2 + c[n_\phi^{\max}]^4 \quad . \tag{4.8}$$

With the maximum azimuthal component $n_\phi^{\max}$ we have introduced a simple order parameter. Since the untwisted dipole possesses a mirror symmetry, only even powers of $n_\phi^{\max}$ are allowed. The phase transition line is determined by $a(K_1/K_3, K_2/K_3) = 0$. According to Eq. (4.8), we expect a power-law dependence of the order parameter with the exponent 1/2 in the twist region close to the phase transition. To test this idea, we choose a constant $K_2/K_3$ ratio and determine $n_\phi^{\max}$ for varying $K_1$. As the log-log plot in Fig. 4.7 illustrates, when approching the phase transition, the order parameter obeys the expected power law:

$$n_\phi^{\max} \sim (K_1/K_3 - 0.4372)^{1/2} \qquad \text{with} \qquad K_2/K_3 = 0.4 \quad . \tag{4.9}$$

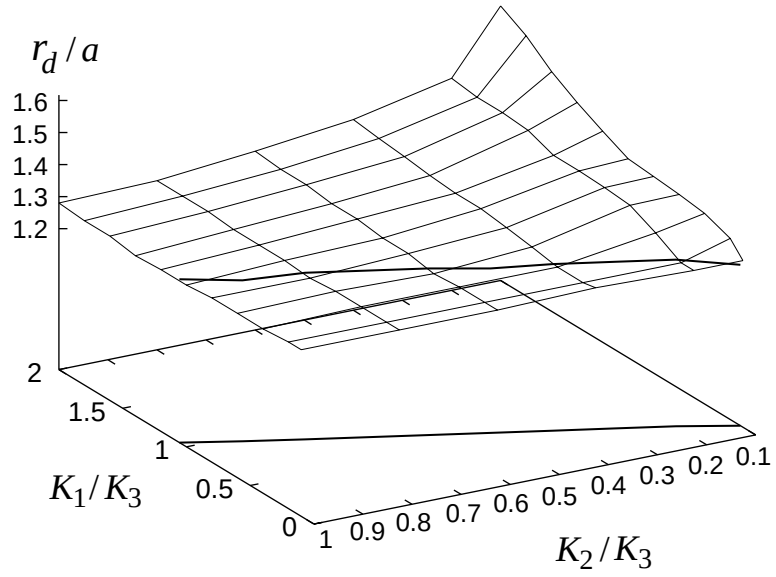


Figure 4.5: The reduced distance $r_d/a$ of the hyperbolic hedgehog from the center of the sphere as a function of the reduced splay ($K_1/K_3$) and twist ($K_2/K_3$) constants.

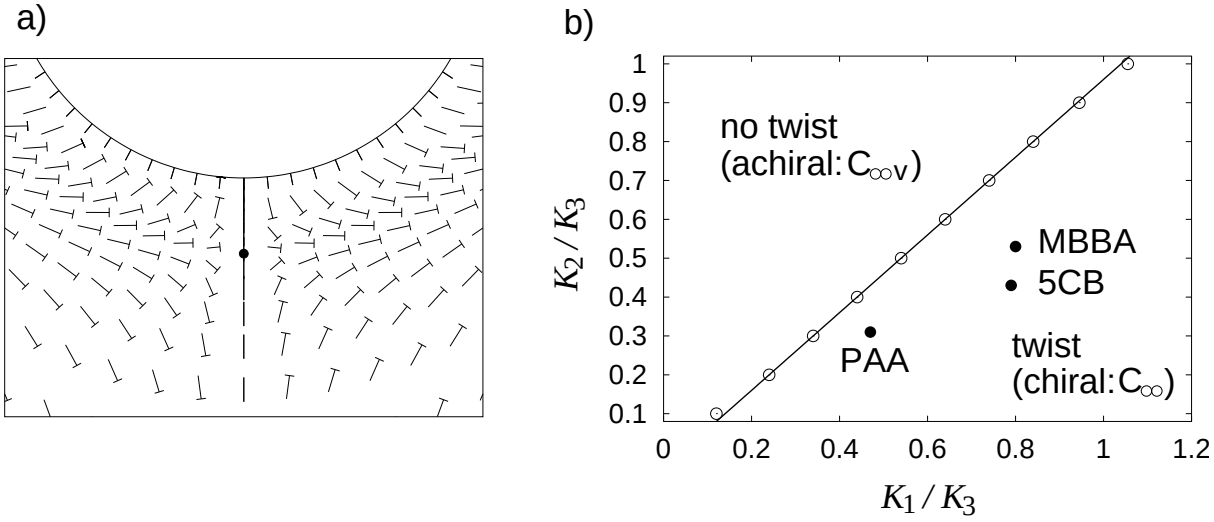


Figure 4.6: a) Nail picture of a close-up of the twisted dipole configuration. Around the hyperbolic hedgehog the directors are tilted relative to the drawing plane. From Ref. [335]. b) Phase diagram of the twist transition as a function of the reduced splay ($K_1/K_3$) and twist ($K_2/K_3$) constants. A full explanation is given in the text.

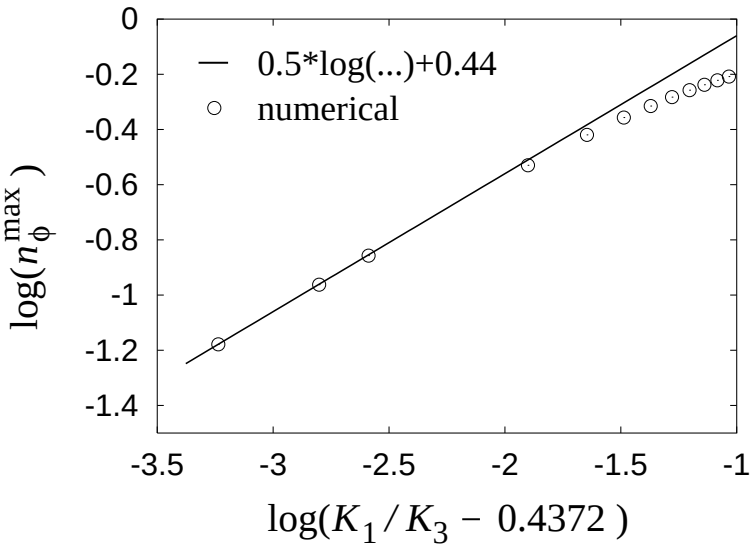


Figure 4.7: Log-log plot of the order parameter $n_\phi^{\max}$ versus $K_1/K_3$ close to the twist transition ($K_2/K_3 = 0.4$); $\circ$ ... numerical values, $-$ ... fit by a straight line.

### 4.3.3 Dipole versus Saturn Ring

There are two possibilities to induce a transition from the dipole to the Saturn-ring configuration; either by reducing the particle size or by applying, *e.g.*, a magnetic field. We always assume rigid anchoring in this subsection, set $K_{24} = 0$, and start with the first point.

#### Effect of particle size

In Fig. 4.8 we plot the free energy $F$ in units of $\pi K_3 a$ as a function of the angular coordinate $\theta_d$ of the disclination ring. For constant $\theta_d$, the free energy $F$ was chosen as the minimum over the radial coordinate $r_d$. The particle radius $a$ is the parameter of the curves, and the one-constant approximation is employed. Recall that $\theta_d = \pi/2$ and $\theta_d = \pi$ correspond, respectively, to the Saturn-ring or the dipole configuration. Clearly, for small particle sizes ($a = 180\,\mathrm{nm}$) the Saturn ring is the absolutely stable configuration, and the dipole enjoys some metastability. However, thermal fluctuations cannot induce a transition to the dipole since the potential barriers are much higher than the thermal energy $k_\mathrm{B}T$. *E.g.*, a barrier of $0.1\pi K_3 a$ corresponds to $1000\,k_\mathrm{B}T$ ($T = 300\,\mathrm{K}$, $a = 1\,\mu\mathrm{m}$). At $a \approx 270\,\mathrm{nm}$, the dipole assumes the global minimum of the free energy, and finally the Saturn ring becomes absolutely unstable at $a \approx 720\,\mathrm{nm}$. The scenario agrees with the results of Ref. [216] where an ansatz function for the director field was used. Furthermore, we stress that the particle sizes were calculated with the choice of 10 nm as the real core size of a line defect, and that our results depend on the line energy (2.1) of the disclination.

The reduced radial coordinate $r_d/a$ of the disclination ring as a function of $\theta_d$ is presented in Fig. 4.9. It was obtained by minimizing the free energy for fixed $\theta_d$. As long as the

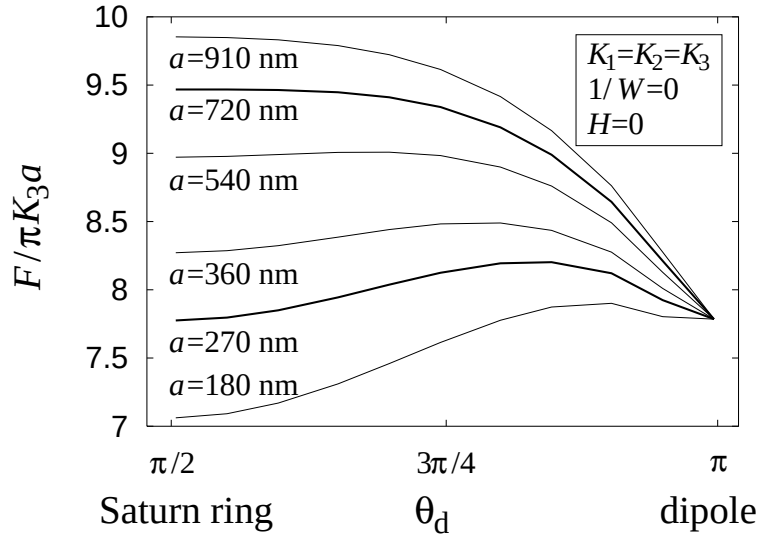


Figure 4.8: The free energy $F$ in units of $\pi K_3 a$ as a function of the angular coordinate $\theta_d$. The parameter of the curves is the particle size $a$. Further parameters are indicated in the inset.

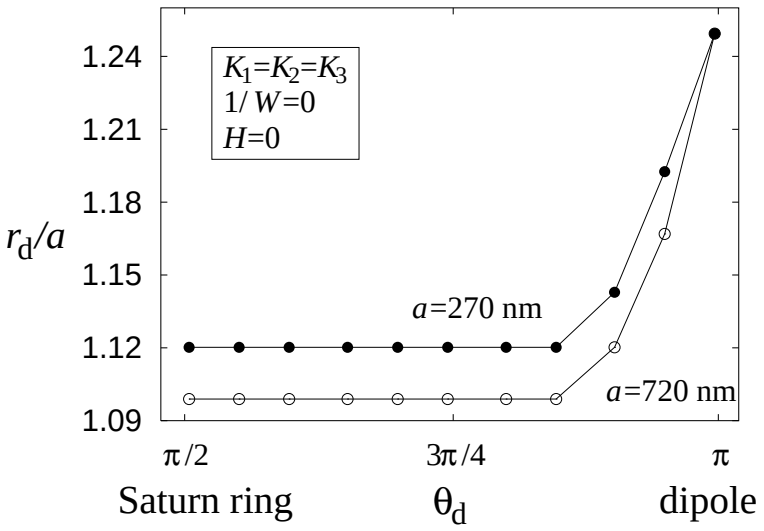


Figure 4.9: The reduced radial coordinate $r_d/a$ of the disclination ring as a function of $\theta_d$ for two particle sizes. Further parameters are indicated in the inset.

ring is open, $r_d$ does not depend on $\theta_d$ within an error of $\pm 0.01$. Only in the region where it closes to the hyperbolic hedgehog, does $r_d$ increase sharply. The figure also illustrates that the ring sits closer to larger particles. The radial position of $r_d/a = 1.10$ for 720 nm particles agrees very well with analytical results obtained by using an ansatz function (see Refs. [216]) and with numerical calculations based on a Monte-Carlo minimization [304].

### Effect of a magnetic field

A magnetic field applied along the symmetry axis of the dipole can induce a transition to the Saturn-ring configuration. This can be understood from a simple back-of-the-envelope calculation. Let us consider high magnetic fields, *i.e.*, magnetic coherence lengths much smaller than the particle size $a$. The magnetic coherence length $\xi_H$ was introduced in Eq. (1.9) as the ratio of elastic and magnetic torques on the director. For $\xi_H \ll a$, the directors are basically aligned along the magnetic field. In the dipole configuration, the director field close to the hyperbolic hedgehog cannot change its topology. The field lines are "compressed" along the $z$ direction, and high densities of the elastic and magnetic free energies occur in a region of thickness $\xi_H$. Since the field lines have to bend around the sphere, the cross section of the region is of the order of $a^2$, and its volume is proportional to $a^2\xi_H$. The Frank free energy density is of the order of $K/\xi_H^2$, where $K$ is a typical Frank constant, and therefore the elastic free energy scales with $Ka^2/\xi_H$. The same holds for the magnetic free energy. In the case of the Saturn-ring configuration, high free energy densities occur in a toroidal region of cross section $\propto \xi_H^2$ around the disclination ring. Hence, the volume scales with $a\xi_H^2$, and the total free energy is of the order of $Ka$, *i.e.*, a factor $a/\xi_H$ smaller than for the dipole.

Fig. 4.10 presents a calculation for a particle size of $a = 0.5\,\mu$m and the liquid crystal compound 5CB. We plot the free energy in units of $\pi K_3 a$ as a function of $\theta_d$ for different magnetic field strengths which we indicate by the reduced inverse coherence length $a/\xi_H$. Without a field ($a/\xi_H = 0$), the dipole is the energetically preferred configuration. The Saturn ring shows metastability. A thermally induced transition between both states cannot happen because of the high potential barrier. At a field strength $a/\xi_H = 0.33$, the Saturn ring becomes the stable configuration. However, there will be no transition until the dipole loses its metastability at a field strength $a/\xi_H = 3.3$, which is only indicated by an arrow in Fig. 4.10. Once the system has changed to the Saturn ring, it will stay there even for zero magnetic field. Fig. 4.11a) schematically illustrates how a dipole can be transformed into a Saturn ring with the help of a magnetic field. If the Saturn ring is unstable at zero field, a hysteresis occurs [see Fig. 4.11b)]. Starting from high magnetic fields, the Saturn ring loses its metastability at $H_{t1}$, and a transition back to the dipole takes place. In Fig. 4.8 we showed that the second situation is realized for particles larger than 720 nm. We also performed calculations for a particle size of $1\mu$m and the liquid crystal compound 5CB and still found the Saturn ring to be metastable at zero field in contrast to the result of the one-constant approximation.

To be more concrete, according to Eq. (1.9), $a/\xi_H = 1$ corresponds to a field strength of 4.6 T when 0.5 $\mu$m particles and the material parameters of 5CB ($K_3 = 0.53 \times 10^{-6}$ dyn,

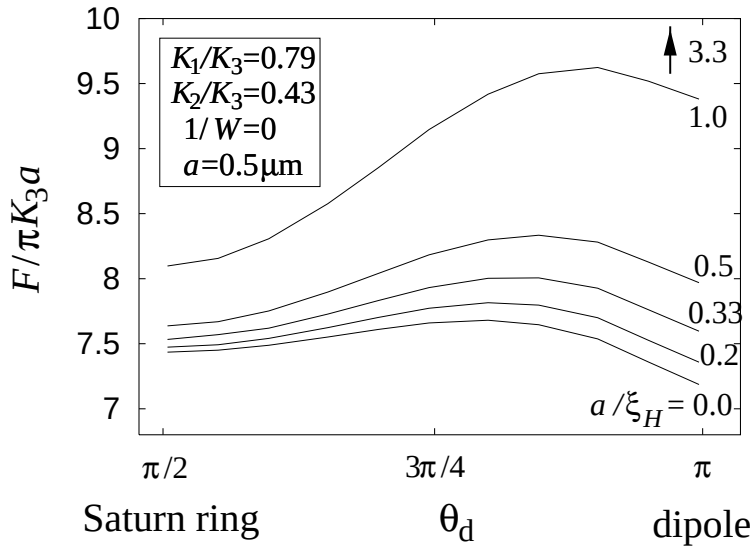


Figure 4.10: The free energy $F$ in units of $\pi K_3 a$ as a function of the angular coordinate $\theta_d$. The parameter of the curves is the reduced inverse magnetic coherence length $a/\xi_H$. Further parameters are indicated in the inset.

$\Delta\chi = 10^{-7}$) are used. Hence, the transition to the Saturn ring in Fig. 4.10 occurs at a rather high field of 15 T. Assuming that there is no dramatic change in $a/\xi_H = 3.3$ for larger particles, this field decreases with increasing particle radius. Alternatively, the transition to the Saturn ring is also induced by an electric field with the advantage that strong fields are much easier to apply. However, the large dielectric anisotropy $\Delta\varepsilon = \varepsilon_\parallel - \varepsilon_\perp$ complicates a detailed analysis because of the difference between applied and local electric fields. Therefore, the electric coherence length $\xi_E = [4\pi K_3/(\Delta\varepsilon E^2)]^{1/2}$, which replaces $\xi_H$, only serves as a rough estimate for the applied field $E$ necessary to induce a transition to the Saturn ring.

### 4.3.4 Influence of Finite Surface Anchoring

In the last subsection we investigate the effect of finite anchoring on the director field around the spherical particle. The saddle-splay term with its elastic constant $K_{24}$ is important now. We always choose a zero magnetic field. In Fig. 4.12 we employ the one-constant approximation and plot the free energy versus the reduced surface extrapolation length $\xi_S/a$ for different reduced saddle-splay constants $K_{24}/K_3$. Recall that $\xi_S$ is inversely proportional to the surface constant $W$ [see Eq. (1.11)]. The straight lines belong to the dipole. Then, for decreasing surface anchoring, there is a first-order transition to the surface-ring structure. We never find the Saturn ring to be the stable configuration although it enjoys some metastability. For $K_{24}/K_3 = 0$, the transition takes place at $\xi_S/a \approx 0.085$. This value is somewhat smaller than the result obtained by Ruhwandl and Terentjev [304]. One could wonder why the surface ring already occurs at such a strong anchoring like $\xi_S/a \approx 0.085$

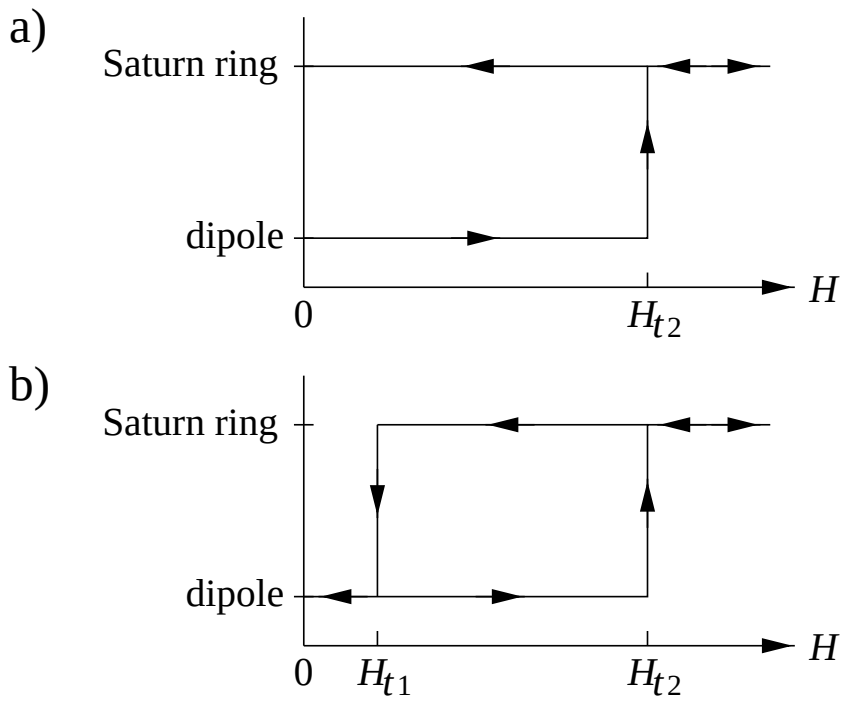


Figure 4.11: a) The Saturn ring is metastable at $H = 0$. The dipole can be transformed into the Saturn ring by increasing the magnetic field $H$ beyond $H_{t2}$ where the dipole loses its metastability. Turning off the field the Saturn ring remains. b) The Saturn ring is unstable at $H = 0$. When the magnetic field is decreased from values above $H_{t2}$, the Saturn ring shrinks back to the dipole at $H_{t1}$ where the Saturn ring loses its metastability. A hysteresis occurs. From Ref. [335].

where any deviation from the homeotropic anchoring costs a lot of energy. However, if $\Delta\theta$ is the angular width of the surface ring where the director deviates from the homeotropic alignment (see inset of Fig. 4.13) then a simple energetical estimate allows $\Delta\theta$ to be of the order of $\xi_S/a$. It is interesting to see that the transition point shifts to higher anchoring strengths, *i.e*, decreasing $\xi_S/a$ when $K_{24}/K_3$ is increased. Obviously, the saddle-splay term favors the surface-ring configuration. To check this conclusion, we plot the reduced saddle-splay free energy $F_{24}$ versus $\xi_S/a$ in Fig. 4.13. The horizontal lines belong to the dipole. They correspond to the saddle-splay energy $4\pi K_{24}a$ which one expects for a rigid homeotropic anchoring at the surface of the sphere. In contrast, for the surface-ring configuration the saddle-splay energy drops sharply. The surface ring at the equator of the sphere introduces a "saddle" in the director field as illustrated in the inset of Fig. 4.13. Such structures are known to be favored by the saddle-splay term. We modeled the surface ring with an angular width $\Delta\theta$ by the following radial and polar director components:

$$n_r = -\tanh\left(\frac{\theta - \pi/2}{\Delta\theta}\right) \qquad \text{and} \qquad n_\theta = -\left[\cosh\left(\frac{\theta - \pi/2}{\Delta\theta}\right)\right]^{-1}, \tag{4.10}$$

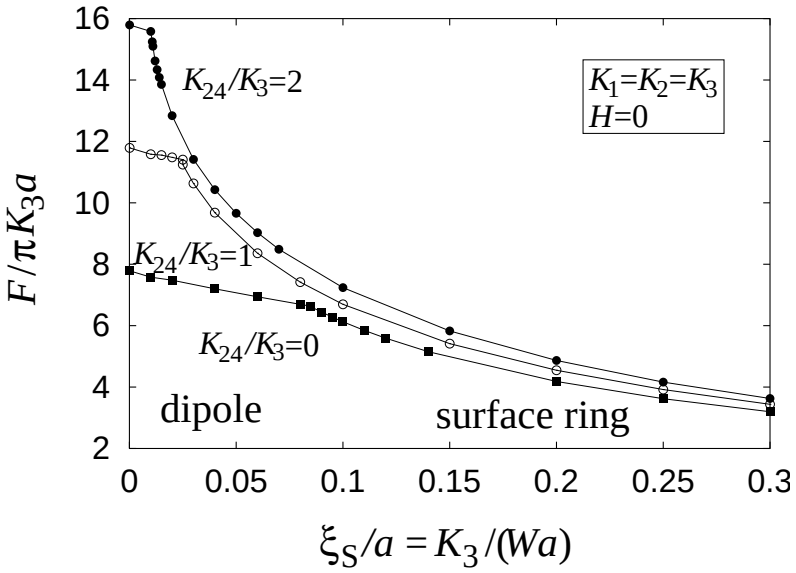


Figure 4.12: The minimum free energy $F$ in units of $\pi K_3 a$ as a function of the reduced surface extrapolation length $\xi_S/a$ for different $K_{24}/K_3$. A first-order phase transition from the dipole to the surface ring occurs. Further parameters are indicated in the inset.

where $\Delta\theta \ll \pi/2$ to ensure that $n_r = 1$ at $\theta = 0, \pi$, and calculated the saddle-splay energy versus $\Delta\theta$ by numerical integration. The result is shown in the inset of Fig. 4.13. It fits very well to the full numerical calculations and confirms again that a narrow "saddle" around the equator can considerably reduce the saddle-splay energy.

For the liquid crystal compound 5CB we determined the stable configuration as a function of $K_{24}/K_3$ and $\xi_S/a$. The phase diagram is presented in Fig. 4.14. With its help, we can derive a lower bound for the surface constant $W$ at the interface of water and 5CB when the surfactant sodium dodecyl sulfate is involved. As the experiments by Poulin *et al.* clearly demonstrate, water droplets dispersed in 5CB do assume the dipole configuration. From the phase diagram we conclude $\xi_S/a < 0.09$ as a necessary condition for the existence of the dipole. With $a \approx 1\,\mu$m, $K_3 = 0.53 \times 10^{-6}\,$dyn, and the definition (1.11) for $\xi_S$ we arrive at

$$W > 0.06\,\mathrm{erg/cm^2} \quad . \tag{4.11}$$

If we assume the validity of the Cauchy-Relation (1.5), which for 5CB gives $K_{24}/K_3 = 0.61$, we conclude that $W > 0.15\,\mathrm{erg/cm^2}$. Recently, Mondain-Monval, Poulin *et al.* were able to observe an equatorial ring structure by changing the composition of a surfactant mixture containing sodium dodecyl sulfate (SDS) and a copolymer of ethylene and propylene oxide (Pluronic F 68) [242]. We conclude from our numerical investigation that they observed the surface-ring configuration.

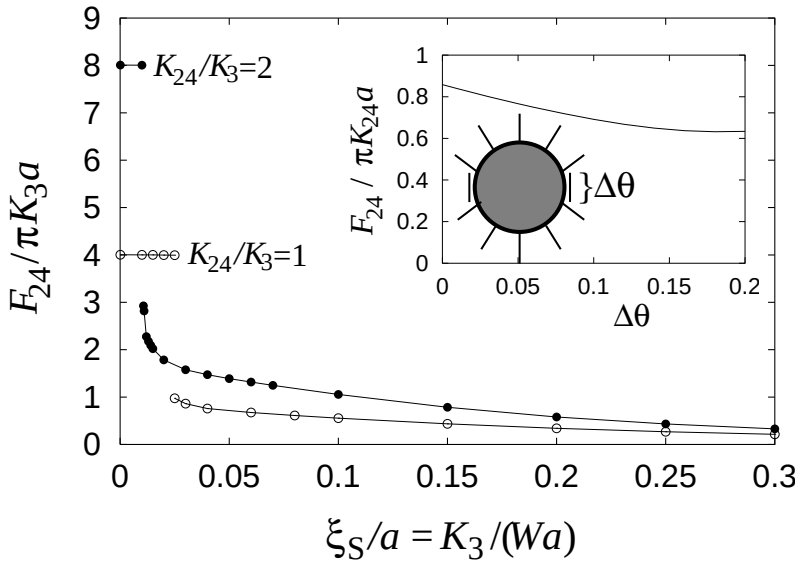


Figure 4.13: The saddle-splay free energy $F_{24}$ in units of $\pi K_3 a$ as a function of $\xi_S/a$ for the same curves as in Fig. 4.12. Inset: $F_{24}$ in units of $\pi K_{24} a$ versus the angular width of the surface ring calculated from the ansatz functions in Eqs. (4.10).

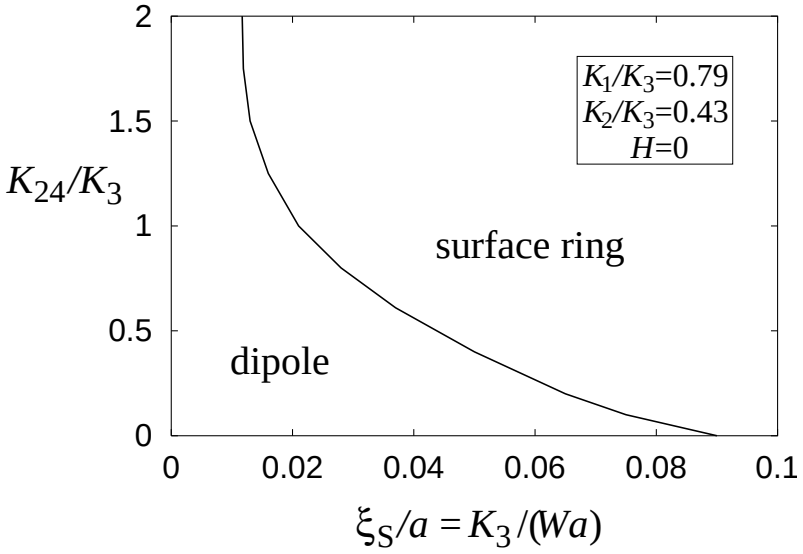


Figure 4.14: Phase diagram of the dipole-surface ring transition as a function of $\xi_S/a$ and $K_{24}/K_3$. Further parameters are indicated in the inset.

## 4.4 Conclusions

In this chapter we presented a detailed study of the three director field configurations around a spherical particle by both analytical and numerical means. We clearly find that for large particles and sufficiently strong surface anchoring, the dipole is the preferred configuration. For conventional calamitic liquid crystals, where $K_2 < K_1$, the dipole should always exhibit a twist around the hyperbolic hedgehog. It should not occur in discotic liquid crystals where $K_2 > K_1$. According to our calculations, the bend constant $K_3$ plays only a minor role in the twist transition. The Saturn ring appears for sufficiently small particles provided that one can realize a sufficiently strong surface anchoring. According to our investigation, for 200 nm particles the surface constant has to be larger than $W = 0.3\,\mathrm{erg/cm^2}$. However, the dipole can be transformed into the Saturn ring by means of a magnetic field if the Saturn ring is metastable at $H = 0$. Otherwise a hysteresis is visible. For the liquid crystal compound 5CB, we find the Saturn ring to be metastable at a particle size $a = 1\,\mu\mathrm{m}$. Increasing the radius $a$, this metastability will vanish in analogy with our calculations within the one-constant approximation (see Fig. 4.8). Lowering the surface-anchoring strength $W$, the surface-ring configuration with a quadrupolar symmetry becomes absolutely stable. We never find a stable structure with dipolar symmetry where the surface ring possesses a general angular position $\theta_d$ or is even shrunk to a point at $\theta_d = 0, \pi$. The surface ring is clearly favored by a large saddle-splay constant $K_{24}$.

The dispersion of spherical particles in a nematic liquid crystal is always a challenge to experimentalists. The clearest results are achieved in inverted nematic emulsions [279, 276, 280, 242]. However, promising experiments with silica or latex spheres do also exist [278, 286, 287, 242, 277]. We hope that the summary of our results stimulates further experiments which probe different liquid crystals as a host fluid [277], manipulate the anchoring strength [242], and investigate the effect of external fields.

# Chapter 5

# Two-Particle Interactions

To understand the properties of, *e.g.*, multi-droplet emulsions, we need to determine the nature of particle-particle interactions. These interactions are mediated by the nematic liquid crystal in which they are embedded and are in general quite complicated. Since interactions are determined by distortions of the director field, there are multi-body as well as two-body interactions. We will content ourselves with calculations of some properties of the effective two-particle interaction. To determine the position-dependent interaction potential between two particles, we should solve the Euler-Lagrange equations, as a function of particle separation, subject to the boundary condition that the director be normal to each spherical object. Solving completely these non-linear equations in the presence of two particles is even more complicated than solving them with one particle, and again we must resort to approximations. Fortunately, interactions at large separations are determined entirely by the far-field distortions and the multipole moments of an individual topological dipole or Saturn ring, which we studied in Section 4.1. The interactions can be derived from a phenomenological free energy. We will present such an approach in this section [288, 279, 216].

## 5.1 Formulating a Phenomenological Theory

In chapter 4, we established that each spherical particle creates a hyperbolic hedgehog to which it binds tightly to create a stable topological dipole. The original spherical inclusion is described by three translational degrees of freedom. Out of the nematic it draws a hedgehog, which itself has three translational degrees of freedom. The two combine to produce a dipole with six degrees of freedom, which can be parametrized by three variables specifying the position of the particle, two angles specifying the orientation of the dipole, and one variable specifying the magnitude of the dipole. As we have seen, the magnitude of the dipole does not fluctuate much and can be regarded as a constant. The direction of the dipole is also fairly strongly constrained. It can, however, deviate from the direction of locally preferred orientation (parallel to a local director to be defined in more detail below) when many particles are present. The particle-defect pair is in addition characterized by its

higher multipole moments. The direction of the principal axes of these moments is specified by the direction of the dipole as long as director configurations around the dipole remain uniaxial. The magnitudes of all the uniaxial moments like the strengths $p$ and $c$ of the dipole and quadrupole moment (see Section 4.1) are energetically fixed, as we have shown in Section 4.2. When director configurations are not uniaxial, the multipole tensors will develop additional components, which we will not consider here. We can thus parametrize topological dipoles by their position and orientation and a set of multipole moments, which we regard as fixed. Let $\boldsymbol{e}^\alpha$ be the unit vector specifying the direction of the dipole moment associated with droplet $\alpha$. Its dipole and quadrupole moments are then $\boldsymbol{p}^\alpha = p\boldsymbol{e}^\alpha$ and $\boldsymbol{c}^\alpha = c(\boldsymbol{e}^\alpha \otimes \boldsymbol{e}^\alpha - \mathbf{1}/3)$, where $p$ and $c$ are the respective magnitudes of the dipole and quadrupole moments calculated, *e.g.*, by analytical means in Section 4.2. The symbol $\otimes$ means tensor product, and $\mathbf{1}$ is the second-rank unit tensor. Note, that this approach also applies to the Saturn-ring and surface-ring configuration but with a vanishing dipole moment $p = 0$. It even applies to particles with tangential boundary conditions where two surfaces defects, called boojums [233, 45, 186], are located at opposite points of the sphere and where the director field possesses a uniaxial symmetry, too. We now introduce dipole- and quadrupole-moment densities, $\boldsymbol{P}(\boldsymbol{r})$ and $\boldsymbol{C}(\boldsymbol{r})$, in the usual way. Let $\boldsymbol{r}^\alpha$ denote the position of droplet $\alpha$, then

$$\boldsymbol{P}(\boldsymbol{r}) = \sum_\alpha \boldsymbol{p}^\alpha \delta(\boldsymbol{r} - \boldsymbol{r}^\alpha) \qquad \text{and} \qquad \boldsymbol{C}(\boldsymbol{r}) = \sum_\alpha \boldsymbol{c}^\alpha \delta(\boldsymbol{r} - \boldsymbol{r}^\alpha) \ . \tag{5.1}$$

In the following, we construct an effective free energy for director and particles valid at length scales large compared to the particle radius. At these length scales, we can regard the spheres as point objects (as implied by the definitions of the densities given above). At each point in space, there is a local director $\boldsymbol{n}(\boldsymbol{r})$ along which the topological dipoles or, *e.g.*, the Saturn rings wish to align. In the more microscopic picture, of course, the direction of this local director corresponds to the far-field director $\boldsymbol{n}_0$. The effective free energy is constructed from rotationally invariant combinations of $\boldsymbol{P}$, $\boldsymbol{C}$, $\boldsymbol{n}$, and the gradient operator $\nabla$ that are also even under $\boldsymbol{n} \to -\boldsymbol{n}$. It can be expressed as a sum of terms

$$F = F_{el} + F_p + F_C + F_{\text{align}}, \tag{5.2}$$

where $F_{el}$ is the Frank free energy, $F_p$ describes interactions between $\boldsymbol{P}$ and $\boldsymbol{n}$, $F_C$ describes interactions between $\boldsymbol{C}$ and $\boldsymbol{n}$ involving gradient operators, and

$$F_{\text{align}} = -D \int d^3r C_{ij}(\boldsymbol{r}) n_i(\boldsymbol{r}) n_j(\boldsymbol{r}) = -DQ \sum_\alpha \left\{ [\boldsymbol{e}^\alpha \cdot \boldsymbol{n}(\boldsymbol{r}^\alpha)]^2 - 1/3 \right\} \tag{5.3}$$

forces the alignment of the axes $\boldsymbol{e}^\alpha$ along the local director $\boldsymbol{n}(\boldsymbol{r}^\alpha)$. The leading contribution to $F_p$ is identical to the treatment of the flexoelectric effect in a nematic [235, 76]

$$F_p = 4\pi K \int d^3r [-\boldsymbol{P} \cdot \boldsymbol{n}(\nabla \cdot \boldsymbol{n}) + \beta \boldsymbol{P} \cdot (\boldsymbol{n} \times \nabla \times \boldsymbol{n})], \tag{5.4}$$

where $\beta$ is a material-dependent unitless parameter. The leading contribution to $F_C$ is

$$F_C = 4\pi K \int d^3r[(\nabla \cdot \boldsymbol{n})\boldsymbol{n} \cdot \nabla(n_i C_{ij} n_j) + \nabla(n_i C_{ij} n_j) \cdot (\boldsymbol{n} \times \nabla \times \boldsymbol{n})] \ . \tag{5.5}$$

There should also be terms in $F_C$ like $C_{ij}\nabla_k n_i \nabla_k n_j$. These terms can be shown to add contributions to the effective two-particle interaction that are higher order in separation than those arising from Eq. (5.5). One coefficient in $F_p$ and all coefficients in $F_C$ are fixed by the requirement that the phenomenological theory yields the far field of one particle given by Eq. (4.2) (see next section). Equation (5.5) is identical to that introduced in Ref. [288] to discuss interactions between Saturn rings, provided $n_i C_{ij} n_j$ is replaced by a scalar density $\rho(\boldsymbol{r}) = \sum_\alpha \delta(\boldsymbol{r} - \boldsymbol{r}^\alpha)$. The two energies are absolutely equivalent to leading order in the components $n_\mu$ of $\boldsymbol{n}$ perpendicular to $\boldsymbol{n}_0$ provided all $\boldsymbol{e}^\alpha$ are restricted to be parallel to $\boldsymbol{n}_0$.

Since $\boldsymbol{P}$ prefers to align along the local director $\boldsymbol{n}$, the dipole-bend coupling term in Eq. (5.4) can be neglected to leading order in deviations of the director from uniformity. The $-\boldsymbol{P} \cdot \boldsymbol{n}(\nabla \cdot \boldsymbol{n})$ term in Eq. (5.4) shows that dipoles aligned along $\boldsymbol{n}$ create local splay as is evident from the dipole configuration depicted in Fig. 4.1. In addition, this term says that dipoles can lower their energy by migrating to regions of maximum splay while remaining aligned with the local director. Experiments on multiple nematic emulsions [279, 280] support this conclusion. Indeed, the coupling of the dipole moment to a strong splay distortion explains the chaining of water droplets in a large nematic drop whose observation we reported in Section 3.3. We return to this observation in Chapter 7.

## 5.2 Effective Pair Interactions

In the following we assume that the far-field director $\boldsymbol{n}_0$ and all the multipole moments of the particles point along the $z$ axis, *i.e.*, $\boldsymbol{e}^\alpha = \boldsymbol{e}_z = \boldsymbol{n}_0$. Hence, we are able to write the dipole and quadrupole densities as

$$\boldsymbol{P}(\boldsymbol{r}) = P(\boldsymbol{r})\boldsymbol{n}_0 \qquad \text{and} \qquad \boldsymbol{C}(\boldsymbol{r}) = \tfrac{3}{2}C(\boldsymbol{r})(\boldsymbol{n}_0 \otimes \boldsymbol{n}_0 - \mathbf{1}/3) \ , \tag{5.6}$$

where $P(\boldsymbol{r})$ and $C(\boldsymbol{r})$ can be both positive and negative. We are interested in small deviations from $\boldsymbol{n}_0$, $\boldsymbol{n} = (n_x, n_y, 1)$, and formulate the effective energy of Eq. (5.2) up to harmonic order in $n_\mu$:

$$F = K \int d^3r \, [\tfrac{1}{2}(\nabla n_\mu)^2 - 4\pi P \partial_\mu n_\mu + 4\pi(\partial_z C)\partial_\mu n_\mu] \ . \tag{5.7}$$

The dipole-bend coupling term of Eq. (5.4) does not contribute because $\boldsymbol{P}$ is aligned along the far-field director. The Euler-Lagrange equations for the director components are

$$\nabla^2 n_\mu = 4\pi \partial_\mu [P(\boldsymbol{r}) - \partial_z C(\boldsymbol{r})], \tag{5.8}$$

which possess the solution

$$n_\mu(\boldsymbol{r}) = -\int d^3r' \, \frac{1}{|\boldsymbol{r}-\boldsymbol{r}'|} \, \partial'_\mu [P(\boldsymbol{r}') - \partial'_z C(\boldsymbol{r}')] \ . \tag{5.9}$$

For a single droplet at the origin, $P(\boldsymbol{r}) = p\,\delta(\boldsymbol{r})$ and $C(\boldsymbol{r}) = \frac{2}{3}c\,\delta(\boldsymbol{r})$, and the above equation yields exactly the far field of Eq. (4.2). This demonstrates the validity of our phenomenological approach.

Particles create far-field distortions of the director, which to leading order at large distances are determined by Eq. (5.8). These distortions interact with the director fields of other particles which leads to an effective particle-particle interaction that can be expressed to leading order as pairwise interactions between dipole and quadrupole densities. Using Eq. (5.9) in Eq. (5.7), we obtain

$$\begin{aligned} \frac{F}{4\pi K} &= \frac{1}{2}\int d^3r d^3r' \, [P(\boldsymbol{r})V_{PP}(\boldsymbol{r}-\boldsymbol{r}')P(\boldsymbol{r}') + C(\boldsymbol{r})V_{CC}(\boldsymbol{r}-\boldsymbol{r}')C(\boldsymbol{r}') \\ &\quad + V_{PC}(\boldsymbol{r}-\boldsymbol{r}')[C(\boldsymbol{r})P(\boldsymbol{r}') - P(\boldsymbol{r})C(\boldsymbol{r}')] \ , \end{aligned} \tag{5.10}$$

with

$$\begin{aligned} V_{PP}(\boldsymbol{r}) &= \partial_\mu\partial_\mu \frac{1}{r} = \frac{1}{r^3}\,(1-3\cos^3\theta) \\ V_{CC}(\boldsymbol{r}) &= -\partial_z^2\partial_\mu\partial_\mu \frac{1}{r} = \frac{1}{r^5}\,(9-90\cos^2\theta+105\cos^4\theta) \\ V_{PC}(\boldsymbol{r}) &= \partial_z\partial_\mu\partial_\mu \frac{1}{r} = \frac{\cos\theta}{r^4}\,(15\cos^2\theta-9) \ , \end{aligned} \tag{5.11}$$

where $\theta$ is the angle enclosed by the separation vector $\boldsymbol{r}$ and $\boldsymbol{n}_0$. The interaction energy between droplets at positions $\boldsymbol{r}$ and $\boldsymbol{r}'$ with respective dipole and quadrupole moments $p$, $p'$, $c$, and $c'$ is thus

$$U(\boldsymbol{R}) = 4\pi K \left[ p\,p' V_{PP}(\boldsymbol{R}) + \frac{4}{9} c\,c' V_{CC}(\boldsymbol{R}) + \frac{2}{3}(c\,p' - c'\,p) V_{PC}(\boldsymbol{R}) \right] \ , \tag{5.12}$$

where $\boldsymbol{R} = \boldsymbol{r} - \boldsymbol{r}'$. The leading term in the potential $U(\boldsymbol{R})$ is the dipole-dipole interaction which is identical to the analogous problem in electrostatics. Minimizing it over the angle $\theta$, one finds that the dipoles prefer to form chains along their axes, *i.e.*, $p\,p' > 0$, $\theta = 0, \pi$. Such a chain of dipoles is illustrated in Fig. 5.1. It is similar to configurations seen in other dipolar systems such as magnetorheological fluids and in magnetic emulsions under the influcence of an external field [135, 210]. The chaining was observed by Poulin *et al.* in inverted emulsions [276, 280] or in a suspension of micron-size latex particles in a lyotropic discotic nematic [277]. Both systems were placed in a thin rectangular cell of approximate dimensions $20\,\mu\text{m} \times 1\,\text{cm} \times 1\,\text{cm}$. The upper and lower plates were treated to produce tangential boundary conditions. Thus the total topological charge in the cell was zero. The dipolar forces were measured recently by a method introduced by Poulin *et al.* [276]. When small droplets are filled with a magnetorheological fluid instead of pure water,

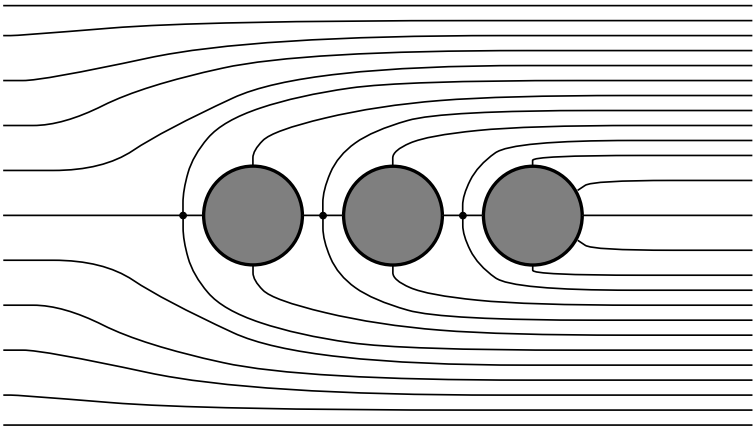

Figure 5.1: A chain of three topological dipoles formed due to their dipolar interaction.

a small magnetic field of about 100 G, applied perpendicular to the chain axis, induces parallel magnetic dipoles. Since they repel each other, the droplets in the chain are forced apart. When the magnetic field is switched off, the droplets move towards each other to reach the equilibrium distance. In a chain of two moving droplets, the dipolar force on one droplet has to be balanced by the Stokes drag,

$$24\pi K \frac{p\,p'}{R^4} = 6\pi\eta_{\text{eff}} a v \ , \tag{5.13}$$

where $v$ is the velocity of one particle, and $\eta_{\text{eff}}$ is an effective viscosity, which we will address in Chapter 6. Intertial effects can be neglected since the movement is overdamped. By measuring the velocity as a function of $R$, Poulin *et al.* could show that the origin of the attractive force is indeed of dipolar nature down to a separation of approximately $4a$. Furthermore, they found that the prefactor of the dipolar force scales as $a^4$, as expected since both the dipole moments $p$ and $p'$ scale as $a^2$ (see Section 4.1). In Chapter 6 we will calculate the Stokes drag of a spherical particle.

If $p, p' = 0$, the quadrupolar interaction is dominant. A minimization over $\theta$ predicts that the quadrupoles should chain under an angle of $\theta = 49°$ [288]. In experiments with tangential boundary conditions at the droplet surface, where a quadrupolar structure with two opposite surface defects (boojums) forms, the chaining occurred under an angle of $\theta = 30°$, probably due to short-range effects [280]. A similar observation was made in a suspension of 50 nm latex particles in a lyotropic discotic nematic [242], where one expects a surface-ring configuration because of the homeotropic surface anchoring (see Section 4.3.4).

Finally, we discuss the coupling between dipoles and quadrupoles in Eq. (5.12). Their moments scale, respectively, as $a^2$ or $a^3$. The coupling is only present when the particles have different radii. Furthermore, for fixed angle $\theta$, the sign of the interaction depends on whether the small particle is on the right or left side of the large one. With this rather subtle effect, which is not yet measured, we close the chapter about two-particle interactions.

# Chapter 6

# Stokes Drag of Spherical Particles

In Section 1.3 we introduced the Ericksen-Leslie equations that govern the hydrodynamics of a nematic liquid crystal. Due to the director as a second hydrodynamic variable besides the fluid velocity, interesting new dynamical phenomena arise. With the Mięsowicz viscosities and Helfrich's permeation, we presented two of them in Section 1.3. Here we deal with the flow of a nematic around a spherical particle in order to calculate its Stokes drag, which is a well-known quantity for an isotropic liquid [330, 306][1]. Via the celebrated Stokes-Einstein relation [96, 97, 98], it determines the diffusion constant of a Brownian particle, and it is, therefore, crucial for a first understanding of the dynamics of colloidal suspensions [306].

In Section 6.1 the existing work on the Stokes drag, which has a long-standing tradition in liquid crystals, is reviewed. Starting from the Ericksen-Leslie equations, we introduce the theoretical concepts for its derivation in Section 6.2. We calculate the Stokes drag for three director configurations; a uniform director field, the topological dipole, and the Saturn-ring structure. Since a full analytical treatment is not possible, we have perfomed a numerical investigation. A summary of its details is presented in Section 6.3. Finally, we discuss the results and open problems in Section 6.4.

## 6.1 Motivation

Due to the complexity of the Ericksen-Leslie equations, only few examples with an analytical solution exist, *e.g.*, the flow between two parallel plates, which defines the different Mięsowicz viscosities [69], the Couette flow [16, 68], the Poiseuille flow [15], which was first measured by Cladis *et al.* [383], or the back flow [269]. Besides the exploration of new effects, resulting from the coupling between the velocity and director field, solutions to the Ericksen-Leslie equations are also of technological interest. They are necessary to determine the switching times of liquid crystal displays.

A common way to measure viscosities of liquids is the falling-ball method, where the

[1] We cite here on purpose the excellent course of Sommerfeld on continuum mechanics. An english edition of his lectures on theoretical physics is available.

velocity of the falling particle is determined by a balance of the gravitational, the buoyancy, and Stokes's friction force. Early experiments in nematic liquid crystals measured the temperature and pressure dependence of the effective viscosity $\eta_{\text{eff}}$ in the Stokes drag [383, 188]. Cladis *et al.* [383] argued that $\eta_{\text{eff}}$ is close to the Mięsowicz shear viscosity $\eta_b$, *i.e.*, to the case where the fluid is flowing parallel to the director (see Fig. 1.3 in Section 1.3). Nearly twenty years later, Poulin *et al.* used the Stokes drag to verify the dipolar force between two topological dipoles in inverted nematic emulsions [276]. Böttger *et al.* observed the Brownian motion of particles above the nematic-isotropic phase transition [37]. Measuring the diffusion constant with the help of dynamic light scattering, they could show that close to the phase transition the effective viscosity in the Stokes drag increases due to surface-induced nematic order close to the particle.

It is obvious, that the hydrodynamic solution for the flow of a nematic liquid crystal around a particle at rest, which is equivalent to the problem of a moving particle, presents a challenge to theorists. Diogo [84] assumed the velocity field to be the same as the one for an isotropic fluid and calculated the drag force for simple director configurations. He was interested in the case where the viscous forces largely exceed the elastic forces of director distortions, *i.e*, Ericksen numbers much larger than one, as we shall explain in the next section. Roman and Terentjev, concentrating on the opposite case, obtained an analytical solution for the flow velocity in a spatially uniform director field, by an expansion in the anisotropy of the viscosity [295]. Heuer *et al.* presented analytical and numerical solutions for both the velocity field and Stokes drag again assuming a uniform director field [177, 155]. They were first investigating a cylinder of infinite length [154]. Ruhwandl and Terentjev allowed for a non-uniform but fixed director configuration, and they numerically calculated the velocity field and Stokes drag of a cylinder [302] or a spherical particle [303]. The particle was surrounded by the Saturn-ring configuration (see Fig. 4.1 of Section 4.1), and the cylinder was accompanied by two disclination lines. The experiments on inverted nematic emulsions [279, 276] motivated us to perform analogous calculations for the topological dipole [370], which we present in the next sections. Recently, Chono and Tsuji performed a numerical solution of the Ericksen-Leslie equations around a cylinder determining both the velocity and director field. They could show that the director field strongly depends on the Ericksen number. However, for homeotropic anchoring their director fields do not show any topological defects required by the boundary conditions.

The Stokes drag of a particle surrounded by a disclination ring strongly depends on the presence of line defects. There exist a few studies, which determine both experimentally [56] and theoretically [162, 74, 307] the drag force of a moving disclination. In the multi-domain cell, a novel liquid crystal display, the occurence of twist disclinations is forced by boundary conditions [311, 310, 290]. It is expected that the motion of these line defects strongly determines the switching time of the display.

## 6.2 Theoretical Concepts

We first review the Stokes drag in an isotropic liquid and then introduce our approach for the nematic environment.

### 6.2.1 Stokes Drag in an Isotropic Fluid

The Stokes drag in an isotropic fluid follows from a solution of the Navier-Stokes equations. Instead of considering a moving sphere, one solves the equivalent problem of the flow around a sphere at rest [330]. An incompressible fluid ($\mathrm{div}\,\boldsymbol{v} = \boldsymbol{0}$) and a stationary velocity field ($\partial\boldsymbol{v}/\partial t = 0$) are assumed, so that the final set of equations reads

$$\mathrm{div}\,\boldsymbol{v} = 0 \qquad \text{and} \qquad -\nabla p' + \mathrm{div}\,\boldsymbol{T}' = \boldsymbol{0}\ . \tag{6.1}$$

In an isotropic fluid the viscous stress tensor $\boldsymbol{T}'$ is proportional to the symmetrized velocity gradient $\boldsymbol{A}$, $\boldsymbol{T}' = 2\eta\boldsymbol{A}$, where $\eta$ denotes the usual shear viscosity. We have subdivided the pressure $p = p_0 + p'$ in a static ($p_0$) and a hydrodynamic ($p'$) part. The static pressure only depends on the constant mass density $\varrho$ and, therefore, does not appear in the momentum-balance equation of the set (6.1). The hydrodynamic contribution $p'$ is a function of the velocity. It can be chosen zero at infinity. Furthermore, under the assumption of creeping flow, we have neglected the non-linear velocity term in the momentum-balance equation resulting from the convective part of the total time derivative $\mathrm{d}\boldsymbol{v}/\mathrm{d}t$. That means, the ratio of inertial ($\varrho v^2/a$) and viscous ($\eta v/a^2$) forces, which defines the *Reynolds number* $Re = \varrho v a/\eta$, is much smaller than one. To estimate the forces, all gradients are assumed to be of the order of the inverse particle radius $a^{-1}$, the characteristic length scale of our problem. Eqs. (6.1) are solved analytically for the non-slip condition at the surface of the particle [$\boldsymbol{v}(r = a) = \boldsymbol{0}$], and for a uniform velocity $\boldsymbol{v}_\infty$ at infinity. Once the velocity and pressure fields are known, the drag force $F_S$ follows from an integration of the total stress tensor $-p\boldsymbol{1} + \boldsymbol{T}'$ over the particle surface. An alternative method demands that the dissipated energy per unit time, $\int(\boldsymbol{T}' \cdot \boldsymbol{A})\, d^3r$, which we introduced in Eq. (1.27) of Section 1.3, should be $F_S\, v_\infty$ [25]. The final result is the famous Stokes formula for the drag force:

$$F_S = \gamma\, v_\infty \qquad \text{with} \qquad \gamma = 6\pi\eta a\ . \tag{6.2}$$

The symbol $\gamma$ is called the friction coefficient. The Einstein-Stokes relation relates it to the diffusion constant $D$ of a Brownian particle [96, 97, 98]:

$$D = \frac{k_\mathrm{B}T}{6\pi\eta a}\ , \tag{6.3}$$

where $k_\mathrm{B}$ is the Boltzmann constant and $T$ is temperature.

We can also calculate the Stokes drag for a finite spherical region of radius $r = a/\varepsilon$ with the particle at its center [370]. The result is

$$F_S = \gamma_\varepsilon\, v_\varepsilon \qquad \text{with} \qquad \gamma_\varepsilon = 6\pi\eta a\, \frac{1 - 3\varepsilon/2 + \varepsilon^3 - \varepsilon^5/2}{(1 - 3\varepsilon/2 + \varepsilon^3/2)^2}\ , \tag{6.4}$$

where $v_\varepsilon$ denotes the uniform velocity at $r = a/\varepsilon$. The correction term is a monotonously increasing function in $\varepsilon$ on the interesting intervall $[0, 1]$. Hence, the Stokes drag increases when the particle is confined to a finite volume. For $\varepsilon = 1/32$ the correction is about 5%.

### 6.2.2 Stokes Drag in a Nematic Environment

To calculate the Stokes drag in a nematic environment, we have to deal with the Ericksen-Leslie equations, which couple the flow of the fluid to the director motion. We do not attempt to solve these equations in general. Analogous to the Reynolds number, we define the *Ericksen number* [74] as the ratio of viscous ($\eta v_\infty/a^2$) and elastic ($K/a^3$) forces in the momentum balance of Eq. (1.18):

$$Er = \frac{\eta v_\infty a}{K} \quad . \tag{6.5}$$

The elastic forces are due to distortions in the director field, where $K$ stands for an average Frank constant. In the following, we assume $Er \ll 1$, *i.e.*, the viscous forces are too weak to distort the director field, and we will always use the static director field for $\boldsymbol{v} = \mathbf{0}$ in our calculations. The condition $Er \ll 1$ constrains the velocity $v_\infty$. Using typical values of our parameters, *i.e.*, $K = 10^{-6}\,\mathrm{dyn}$, $\eta = 0.1\,\mathrm{P}$, and $a = 10\,\mu\mathrm{m}$, we find

$$v_\infty \ll 100\,\frac{\mu\mathrm{m}}{\mathrm{s}} \quad . \tag{6.6}$$

Before we proceed, let us check for three cases if this constraint is fulfilled. First, in the measurements of the dipolar force by Poulin *et al.*, the velocities of the topological dipole are always smaller than $10\,\mu\mathrm{m/s}$ [276]. Secondly, in a falling-ball experiment the velocity $v$ of the falling particle is determined by a balance of the gravitational, the buoyancy, and Stokes's friction force, *i.e.*, $6\pi\eta_{\mathrm{eff}} a v = \frac{4\pi}{3} a^3 (\varrho - \varrho_{\mathrm{fl}}) g$, and we obtain:

$$v = \frac{2}{9}\,\frac{(\varrho - \varrho_{\mathrm{fl}}) a^2 g}{\eta_{\mathrm{eff}}} \quad \longrightarrow \quad 10\,\frac{\mu\mathrm{m}}{\mathrm{s}} \quad . \tag{6.7}$$

To arrive at the estimate, we choose $\eta_{\mathrm{eff}} = 0.1\,\mathrm{P}$ and $a = 10\,\mu\mathrm{m}$. We take $\varrho = 1\,\mathrm{g/cm^3}$ as the mass density of the particle and $\varrho - \varrho_{\mathrm{fl}} = 0.01\,\mathrm{g/cm^3}$ as its difference to the surrounding fluid [306]. Thirdly, we consider the Brownian motion of a suspended particle. With the time $t = a^2/6D$ that the particle needs to diffuse a distance equal to the particle radius $a$ [306], we define an averaged velocity

$$v = \frac{a}{t} = \frac{6D}{a} \quad \longrightarrow \quad 10^{-3}\,\frac{\mu\mathrm{m}}{\mathrm{s}} \quad . \tag{6.8}$$

The estimate was calculated using the Stokes-Einstein relation of Eq. (6.3) with thermal energy $k_{\mathrm{B}}T = 4 \cdot 10^{-14}\,\mathrm{erg}$ at room temperature and the same viscosity and particle radius as above.

After we have shown that $Er \ll 1$ is a reasonable assumption, we proceed as follows. We first calculate the static director field around a sphere from the balance of the elastic

torques, $\boldsymbol{n} \times \boldsymbol{h}^0 = \boldsymbol{0}$ [see Eqs. (1.19) and (1.25)]. It corresponds to a minimization of the free energy. For $\boldsymbol{v} = \boldsymbol{0}$, the static director field defines a static pressure $p_0$ via the momentum balance, $-\nabla p_0 + \operatorname{div} \boldsymbol{T}^0 = 0$, where the elastic stress tensor $\boldsymbol{T}^0$ depends on the gradient of $\boldsymbol{n}$ [see Eqs. (1.18) and (1.11)]. If we again divide the total pressure into its static and hydrodynamic part, $p = p_0 + p'$, the velocity field is determined from the same set of equations as in (6.1), provided that we employ the viscous stress tensor $\boldsymbol{T}'$ of a nematic liquid crystal [see Eq. (1.22)]. In the case of an inhomogeneous director field, both the different shear viscosities and the rotational viscosity $\gamma_1$, discussed in Section 1.3, contribute to the Stokes drag.

In general, the friction force $\boldsymbol{F}_S$ does not point along $\boldsymbol{v}_\infty$, and the friction coefficient is now a tensor $\boldsymbol{\gamma}$. In the following, all our configurations are rotationally symmetric about the $z$ axis, and the Stokes drag assumes the form

$$\boldsymbol{F}_S = \boldsymbol{\gamma} \boldsymbol{v}_\infty \qquad \text{with} \qquad \boldsymbol{\gamma} = \gamma_\perp \boldsymbol{1} + (\gamma_\parallel - \gamma_\perp)\, \boldsymbol{e}_z \otimes \boldsymbol{e}_z \ . \tag{6.9}$$

There only exist two independent components $\gamma_\parallel$ and $\gamma_\perp$ for a respective flow parallel or perpendicular to the symmetry axis. In these two cases, the Stokes drag is parallel to $\boldsymbol{v}_\infty$. Otherwise, a component perpendicular to $\boldsymbol{v}_\infty$, called *lift force*, appears. In analogy with the isotropic fluid, we introduce effective viscosities $\eta_{\text{eff}}^{\parallel}$ and $\eta_{\text{eff}}^{\perp}$ via

$$\gamma_\parallel = 6\pi \eta_{\text{eff}}^{\parallel} a \qquad \text{and} \qquad \gamma_\perp = 6\pi \eta_{\text{eff}}^{\perp} a \ . \tag{6.10}$$

It is sufficient to determine the velocity and pressure fields for two particular geometries with $\boldsymbol{v}_\infty$ either parallel or perpendicular to the $z$ axis. Then, the friction coefficients are calculated with the help of the dissipated energy per unit time [see Eq. (1.27)] [25, 84]:

$$F_S^{\parallel/\perp}\, v_\infty = \int (\boldsymbol{T}' \cdot \boldsymbol{A} + \boldsymbol{h}' \cdot \boldsymbol{N})\, d^3 r \ . \tag{6.11}$$

It turns out that the alternative method via an integration of the stress tensor at the surface of the particle is numerically less reliable. Note that the velocity and pressure fields for an arbitrary angle between $\boldsymbol{v}_\infty$ and $\boldsymbol{e}_z$ follow from superpositions of the solutions for the two selected geometries. This is due to the linearity of our equations.

It is clear that the Brownian motion in an environment with an overall rotational symmetry is governed again by two independent diffusion constants. The generalized Stokes-Einstein formula of the diffusion tensor $\boldsymbol{D}$ takes the form

$$\boldsymbol{D} = D_\perp\, \boldsymbol{1} + (D_\parallel - D_\perp)\, \boldsymbol{e}_z \otimes \boldsymbol{e}_z \qquad \text{with} \qquad D_{\parallel/\perp} = \frac{k_{\text{B}} T}{\gamma_{\parallel/\perp}} \ . \tag{6.12}$$

At the end, we add some critical remarks about our approach which employs the static director field. From the balance equation of the elastic and viscous torques [see Eqs. (1.19), (1.25), and (1.26)], we derive that the change $\delta \boldsymbol{n}$ of the director due to the velocity $\boldsymbol{v}$ is of the order of the Ericksen number: $\delta n \sim Er$. This adds a correction $\delta \boldsymbol{T}^0$ to the elastic stress tensor $\boldsymbol{T}^0$ in the momentum balance equation. In the case of a spatially uniform

director field, the correction $\delta \boldsymbol{T}^0$ is by a factor $Er$ smaller than the viscous forces, and it can be neglected. However, for a non-uniform director field, it is of the same order as the viscous term, and, strictly speaking, should be taken into account. Since our problem is already very complex, even when the directors are fixed, we keep this approximation for a first approach to the Stokes drag. How the friction force changes when the director field is allowed to relax, must be investigated by even more elaborate calculations. Two remarks support the validity of our approach. First, far away from the sphere, $\delta \boldsymbol{n}$ has to decay at least linearly in $1/r$, and $\delta \boldsymbol{T}_0$ is negligible against the viscous forces. Secondly, the non-linear term in the Navier-Stokes equations usually is omitted for $Re \ll 1$. However, whereas the friction and the pressure force for the Stokes problem decay as $1/r^3$, the non-linear term is proportional to $1/r^2$, exceeding the first two terms in the farfield. Nevertheless, performing extensive calculations, Oseen could prove that the correction of the non-linear term to the Stokes drag is of the order of $Re$ [330]. One might speculate that the full relaxation of the director field introduces a correction of the order of $Er$ to the Stokes drag.

## 6.3 Summary of Numerical Details

In this section we only review the main ideas of our numerical method. A detailed account will be given in Ref. [370].

The numerical investigation is performed on a grid which is defined by modified spherical coordinates. Since the region outside the spherical particle is infinitely extended, we employ a reduced radial coordinate $\xi = a/r$. The velocity and director fields are expressed in the local spherical coordinate basis. With this choice of coordinates, the momentum balance of Eqs. (6.1) with the viscous stress tensor of a nematic becomes very complex. We, therefore, used the algebraic program Maple to formulate it.

The two equations in (6.1) are treated by different numerical techniques. Given an initial velocity field, the momentum balance including the inertial term $\partial \boldsymbol{v}/\partial t$ can be viewed as a relaxation equation towards the stationary velocity field, which we aim to determine. The Newton-Gauss-Seidel method, introduced in Section 1.2, provides an effective tool to implement this relaxation. Employing the discretized version of the momentum balance equation, the velocity at the grid point $\boldsymbol{r}$ relaxes according to

$$v_i^{\text{new}}(\boldsymbol{r}) = v_i^{\text{old}}(\boldsymbol{r}) - \frac{[-\nabla p' + \operatorname{div} \boldsymbol{T}']_i}{[\partial(-\nabla p' + \operatorname{div} \boldsymbol{T})]_i / \partial v_i(\boldsymbol{r})} \quad . \tag{6.13}$$

Note that the denominator can be viewed as the inverse of a variable time step for the fictitious temporal dynamics of $\boldsymbol{v}$.

A relaxation equation for the pressure involving $\operatorname{div} \boldsymbol{v} = 0$ is motivated by the method of artificial compressibility [52]. Let us consider the complete mass-balance equation. For small variations of the density, we obtain:

$$\frac{\partial p}{\partial t} = -\frac{\varrho}{c^2} \operatorname{div} \boldsymbol{v} \qquad \text{with} \qquad c = \sqrt{\frac{\partial p}{\partial \varrho}} \quad . \tag{6.14}$$

The quantity $c$ denotes the sound velocity for constant temperature, and $c^2/\varrho$ is the isothermal compressibility. In discretized form we have

$$p^{\text{new}} = p^{\text{old}} - \frac{\varrho}{c^2}\,\Delta t\,\text{div}\,\boldsymbol{v} \quad . \tag{6.15}$$

Note that the reduced fictitious time step $\varrho\Delta t/c^2$ cannot be chosen according to the Newton-Gauss-Seidel method since $\text{div}\,\boldsymbol{v}$ does not contain the pressure $p$. Instead, it should be as large as possible to speed up the calculations. In Ref. [284] upper bounds are given beyond which the the numerical scheme becomes unstable.

To obtain the friction coefficient $\gamma_\parallel$, an effective two-dimensional problem has to be solved due to the rotational symmetry of the director configurations about the $z$ axis. In the case of $\gamma_\perp$ ($\boldsymbol{v}_\infty \perp \boldsymbol{e}_z$), the velocity field possesses at least two mirror planes which are perpendicular to each other and whose line of intersection is the $z$ axis. As a result, the necessary three-dimensional calculations can be reduced to one quadrant of the real space. A description of all the boundary conditions will be presented in Ref. [370].

The director fields for the topological dipole and the Saturn ring are provided by the respective ansatz functions of Eqs. (22) and (33) in Ref. [216]. The parameters of minimum free energy are chosen. In Chapter 4 we showed that these ansatz functions give basically the same results as the numerical investigation.

We checked our program in the isotropic case. It turned out that it is not stable for an infinitely extended integration area. We therefore solved Eqs. (6.1) in a finite region of reduced radius $r/a = 1/\varepsilon = 32$. For $\varepsilon = 1/32$, our program reproduced the isotropic Stokes drag, calculated from Eq. (6.4), with an error of 1%.

## 6.4 Results, Discussion, and Open Problems

We begin with an investigation of the stream line patterns, discuss the effective viscosities, and formulate some open problems at the end.

### 6.4.1 Stream Line Patterns

In Fig. 6.1 we compare the stream line patterns around a spherical particle for an isotropic liquid and a spatially uniform director field parallel to $\boldsymbol{v}_\infty$. A uniform $\boldsymbol{n}$ can be achieved by weak surface anchoring and application of a magnetic field with a magnetic coherence length smaller than the particle radius. In the isotropic fluid the bent stream lines occupy more space around the particle, whereas for a uniform director configuration they seem to follow the vertical director field lines as much as possible. This can be understood from a minimum principle. In Section 1.3 we explained that a shear flow along the director possesses the smallest shear viscosity, called $\eta_b$. Hence, in such a geometry the smallest amount of energy is dissipated. Indeed, for a uniform director field, one can derive the momentum balance from a minimization of the dissipation function stated in Eq. (1.27) [154]. A term $-2p\,\text{div}\,\boldsymbol{v}$ has to be added because of the incompressibility of the fluid. It turns out that the Lagrange multiplier $-2p$ is determined by the pressure $p$.

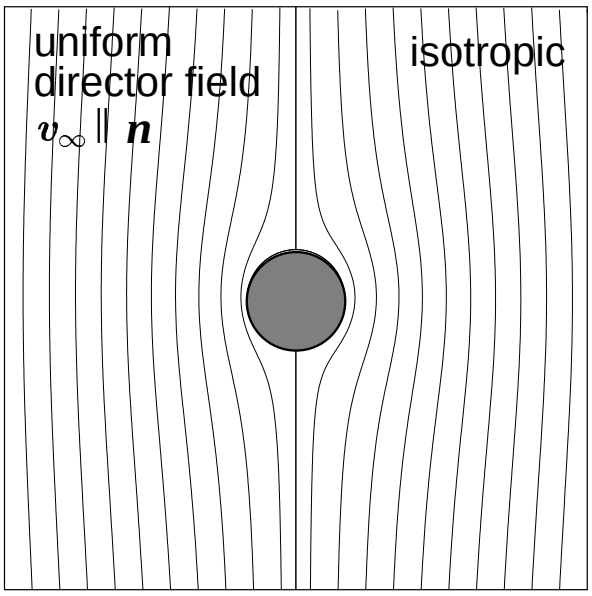


Figure 6.1: Stream line pattern around a spherical particle for an isotropic liquid (right) and a uniform director field parallel to $\boldsymbol{v}_\infty$ (left).

In the case of the topological dipole parallel to $\boldsymbol{v}_\infty$, we observe a clear asymmetry in the stream lines as illustrated in Fig. 6.2. The dot indicates the position of the point defect. It breaks the mirror symmetry of the stream line pattern, which exists, *e.g.*, in an isotropic liquid relative to a plane perpendicular to the vertical axis. In the farfield of the velocity, the splay deformation in the dipolar director configuration is clearly recognizable. Since we use the linearized momentum balance in $\boldsymbol{v}$, the velocity field is the same no matter if the fluid flows upward or downward. The stream line pattern of the Saturn ring [see Fig. 6.3 (right)] exhibits the mirror symmetry, and the position of the ring disclination is visible by a dip in the stream line close to the equator of the sphere.

If $\boldsymbol{v}_\infty$ is perpendicular to the dipole axis, the missing mirror plane of the dipole configuration is even more pronounced in the stream line pattern. It is illustrated in Fig. 6.4, where the point defect is indicated by a dip in the stream line. Although the pattern resembles the one of the Magnus effect [330], symmetry dictates that $F_S^\perp \| \boldsymbol{v}_\infty$. A lift force perpendicular to $\boldsymbol{v}_\infty$ does not exist. We find a non-zero viscous torque acting on the particle whose direction for a fluid flow from left to right is indicated in Fig. 6.4. Symmetry allows such a torque $\boldsymbol{M}$ since the cross product of the dipole moment $\boldsymbol{p}$ and $\boldsymbol{v}_\infty$ gives an axial or pseudovector $\boldsymbol{M} \propto \boldsymbol{p} \times \boldsymbol{v}_\infty$. In the Saturn-ring configuration a non-zero dipole moment and, therefore, a non-zero torque cannot occur.

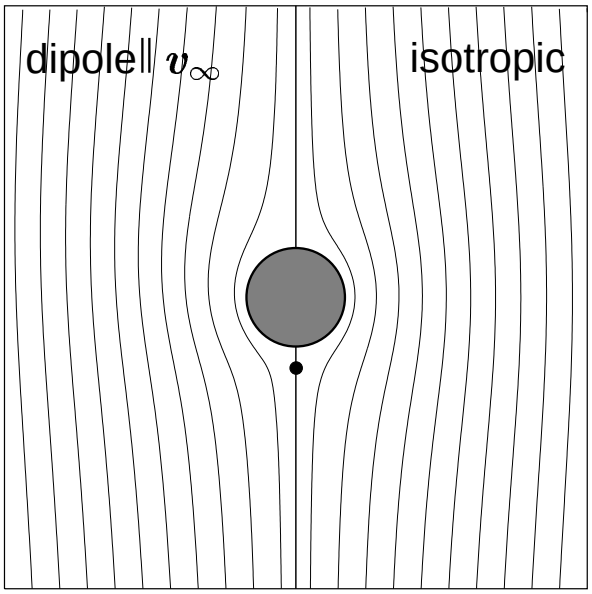


Figure 6.2: Stream line pattern around a spherical particle for an isotropic liquid (right) and the topological dipole parallel to $\boldsymbol{v}_\infty$ (left).

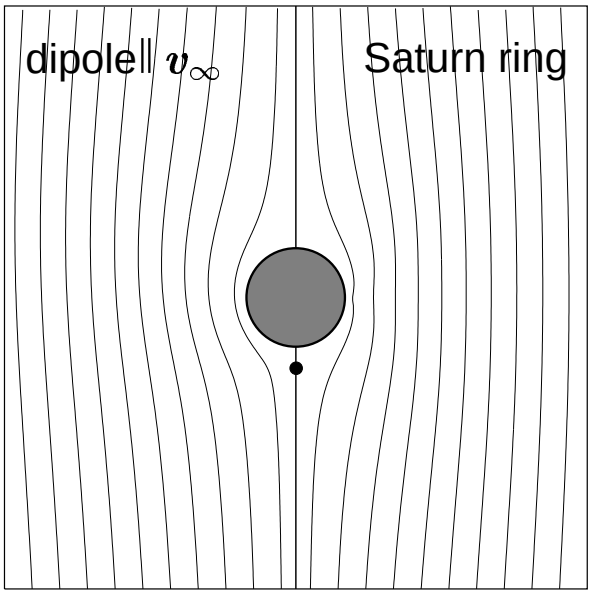


Figure 6.3: Stream line pattern around a spherical particle for the Saturn ring (right) and the topological dipole (left) with their respective symmetry axis parallel to $\boldsymbol{v}_\infty$.

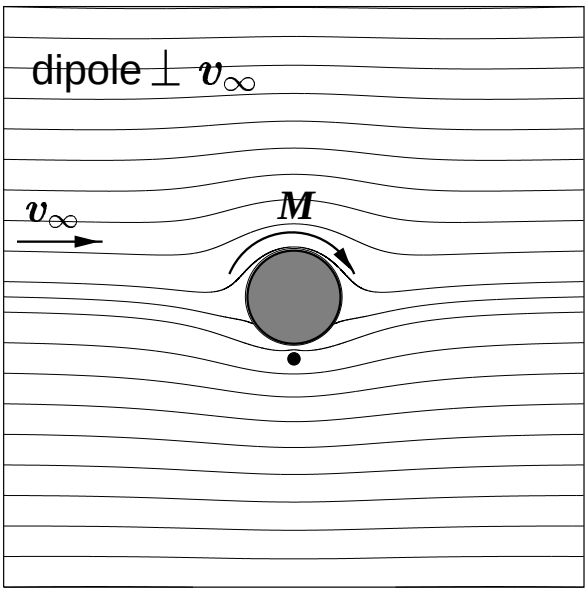


Figure 6.4: Stream line pattern around a spherical particle for the topological dipole perpendicular to $\boldsymbol{v}_\infty$.

### 6.4.2 Effective Viscosities

In Table 6.1 we summarize the effective viscosities of the Stokes drag, defined in Eq. (6.10), for a uniform director field, the dipole and the Saturn-ring configuration. The values are calculated for the two compounds MBBA and 5CB. For a reference, we include the three Mięsowicz viscosities. In the case of $\boldsymbol{v}_\infty$ parallel to the symmetry axis of the three configurations, we might expect that $\eta_{\text{eff}}^{\parallel}$ is close to $\eta_b$ as argued by Cladis *et al.* [383]. For a uniform director field, $\eta_{\text{eff}}^{\parallel}$ exceeds $\eta_b$ by 30% or 60% respectively. The increase originates in the stream lines bending around the particle. The effective viscosity $\eta_{\text{eff}}^{\parallel}$ of the dipole and the Saturn ring are larger than $\eta_b$ by an approximate factor of two. In additon to the bent stream lines, there exist strong director distortions close to the particle which the fluid has to flow through constantly changing the local direction of the moving molecules. Recalling our discussion of the permeation in Section 1.3, a contribution from the rotational viscosity $\gamma_1$ arises which does not exist in a uniform director field. In all three cases, we find $\eta_{\text{eff}}^{\parallel}$ either close to or larger than $\eta_a$, so that $\eta_b$ is not the only determining quantity of $\eta_{\text{eff}}^{\parallel}$, as argued by Cladis *et al.* [383]. For $\boldsymbol{v}_\infty$ perpendicular to the symmetry axis, $\eta_{\perp}^{\text{eff}}$ assumes a value between $\eta_a$ and $\eta_c$, which is understandable since the flow velocity is mainly perpendicular to the director field.

The ratio $\eta_{\text{eff}}^{\perp}/\eta_{\text{eff}}^{\parallel}$ for the uniform director field is the largest since the extreme cases of a respective flow parallel or perpendicular to the director field is realized the best in this configuration. Furthermore, both the dipole and the Saturn ring exhibit nearly the same anisotropy, and we conclude that they cannot be distinguished from each other in a

Table 6.1: Effective viscosities of the Stokes drag for the two compounds MBBA and 5CB and for three different director configurations. As a reference, the three Mięsowicz viscosities are included.

| | MBBA: $\eta_a = 0.416\,\mathrm{P}$, $\eta_b = 0.283\,\mathrm{P}$, $\eta_c = 1.035\,\mathrm{P}$ | | | 5CB: $\eta_a = 0.374\,\mathrm{P}$, $\eta_b = 0.229\,\mathrm{P}$, $\eta_c = 1.296\,\mathrm{P}$ | | |
|---|---|---|---|---|---|---|
| | uniform $\boldsymbol{n}$ | dipole | Saturn ring | uniform $\boldsymbol{n}$ | dipole | Saturn ring |
| $\eta_{\mathrm{eff}}^{\parallel}$ [P] | 0.380 | 0.517 | 0.493 | 0.381 | 0.532 | 0.501 |
| $\eta_{\mathrm{eff}}^{\perp}$ [P] | 0.684 | 0.767 | 0.747 | 0.754 | 0.869 | 0.848 |
| $\eta_{\mathrm{eff}}^{\perp}/\eta_{\mathrm{eff}}^{\parallel}$ | 1.80 | 1.48 | 1.51 | 1.98 | 1.63 | 1.69 |

falling-ball experiment. The ratio $\eta_{\mathrm{eff}}^{\perp}/\eta_{\mathrm{eff}}^{\parallel}$ that we determine for the Saturn ring and the uniform director field in the case of the compound MBBA agree well with the results of Ruhwandl and Terentjev who find $\eta_{\mathrm{eff}}^{\perp}/\eta_{\mathrm{eff}}^{\parallel}|_{\mathrm{uniform}} = 1.69$ and $\eta_{\mathrm{eff}}^{\perp}/\eta_{\mathrm{eff}}^{\parallel}|_{\mathrm{Saturn}} = 1.5$ [303].

In the ansatz function of the dipolar configuration, we vary the separation $r_d$ between the hedgehog and the center of the particle. Both the effective viscosities increase with $r_d$ since the non-uniform director field with its strong distortions occupies more space. However, the ratio $\eta_{\mathrm{eff}}^{\perp}/\eta_{\mathrm{eff}}^{\parallel}$ basically remains the same. For the Saturn ring, $\eta_{\mathrm{eff}}^{\parallel}$ increases stronger with the radius $r_d$ than does $\eta_{\mathrm{eff}}^{\perp}$. This seems to be reasonable since a flow perpendicular to the plane of the Saturn ring experiences more resistance than a flow parallel to the plane. As a result, $\eta_{\mathrm{eff}}^{\perp}/\eta_{\mathrm{eff}}^{\parallel}$ decreases when the ring radius $r_d$ is enlarged.

### 6.4.3 Open Problems

One should try to perform a complete solution of the Ericksen-Leslie equations including a relaxation of the static director field for $\boldsymbol{v} \neq \boldsymbol{0}$. In the case of $Er \ll 1$, a linearization in the small deviation $\delta\boldsymbol{n}$ from the static director field would suffice. Such a procedure helps to gain insight into several open problems. First, it verifies or falsifies the hypothesis that the correction to the Stokes drag is of the order of $Er$. Secondly, the Stokes drag of the topological dipole is the same whether the flow is parallel or anti-parallel to the dipole moment. This is also true for an object with a dipolar shape in an isotropic fluid. If such an object is slightly turned away from its orientation parallel to $\boldsymbol{v}_\infty$, it will experience a viscous torque and either relax back or reverse its direction to find its absolute stable orientation. The topological dipole will not turn around since it experiences an elastic torque towards its initial direction, as explained in Section 5.1. Nevertheless, a full solution of the Ericksen-Leslie equations would show how much the dipole deviates from its preferred direction under the influence of a velocity field. It would also clarify its orientation when $\boldsymbol{v}_\infty$ is perpendicular to the dipolar axis. Furthermore, we expect the non-zero viscous torque,

discussed in Subsection 6.4.1, to be cancelled by elastic torques.

The Stokes drag of particles in a nematic environment still presents a challenging problem to theorists. On the other hand, clear measurements of, *e.g.*, the anisotropy in Stokes's friction force are missing.

# Chapter 7

# Colloidal Dispersions in Complex Geometries

In this chapter we present a numerical investigation of water droplets in a spherically confined nematic solvent. It is motivated by experiments on multiple nematic emulsions which we reported in Section 3.3. However, it also applies to solid spherical particles. Our main purpose is to demonstrate that the topological dipole provides a key unit for the understanding of multiple emulsions. In Sections 7.1-7.3 we first state the questions and main results of our investigation. Then we define the geometry of our problem and summarize numerical details. In particular, we employ the numerical method of finite elements [354] which is most suitable for non-trivial geometries. Finally we present our results in detail and discuss them. The last section contains an analytical treatment of the twist transition of a radial director field enclosed between two concentric spheres. It usually occurs when the inner sphere is not present. We perform a linear stability analysis and thereby explain the observation that a small water droplet at the center of a large nematic drop suppresses the twisting.

## 7.1 Questions and Main Results

In our numerical investigation we demonstrate that the dipolar configuration formed by one spherical particle and its companion hyperbolic point defect also exists in more complex geometries, *e.g.*, nematic drops. This provides an explanation for the chaining reported in Section 3.3 and in Refs. [279, 280]. One water droplet fits perfectly into the center of a large nematic drop, which has a total topological charge +1. Any additional water droplet has to be accompanied by a hyperbolic hedgehog in order not to change the total charge. If the dipole forms (see Fig. 7.1, left), it is attracted by the strong splay deformation in the center, as predicted by the phenomenological theory of Section 5.1 and in Refs. [279, 216], until the short-range repulsion mediated by the defect sets in (see Fig. 7.1, middle). Any additional droplet seeks the region of maximum splay and forms a linear chain with the two other droplets. In the following we present a detailed study of the dipole formation in

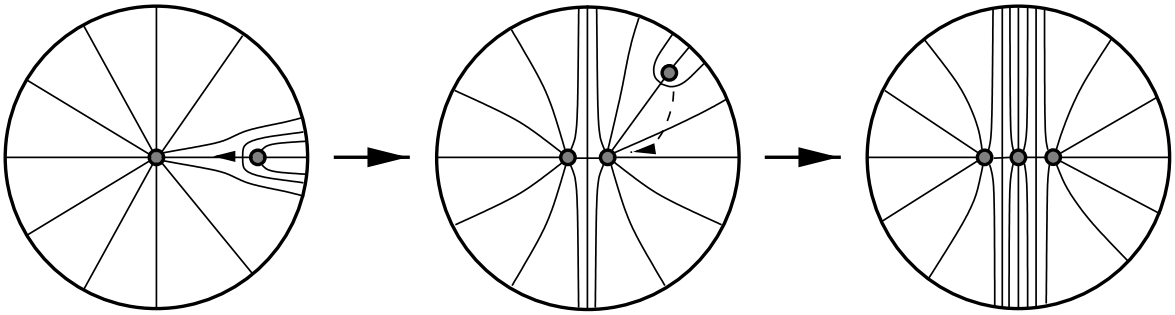

Figure 7.1: Scenario to explain the chaining of water droplets in a large nematic drop. The right water droplet and its companion hyperbolic hedgehog form a dipole, which is attracted by the strong splay deformation around the droplet in the center (left picture). The dipole moves towards the center until at short distances the repulsion mediated by the point defect sets in (middle picture). A third droplet moves to the region of maximum splay to form a linear chain with the two other droplets.

spherical geometries. For example, when the two water droplets in the middle picture of Fig. 7.1 are moved apart symmetrically about the center of the large drop, the dipole forms via a second order phase transition. We also identify the dipole in a bipolar configuration which occurs for planar boundary conditions at the outer surface of the nematic drop. Two boojums, *i.e.*, surface defects appear [233, 45, 186], and the dipole is attracted by the strong splay deformation in the vicinity of one of them [279, 280, 216]. Besides the dipole we find another stable configuration in this geometry, where the hyperbolic hedgehog sits close to one of the boojums, which leads to a hysteresis in the formation of the dipole.

In the experiment it was found that the distance $d$ of the point defect from the surface of a water droplet scales with the radius $r$ of the droplet like $d \approx 0.3\,r$ [279, 280]. In the following we will call this relation the scaling law. By our numerical investigations, we confirm this scaling law within an accuracy of ca. 15%, and we discuss the influence of the outer boundary of the large drop. Finally, we show that water droplets can repel each other without a hyperbolic defect placed between them.

## 7.2 Geometry and Numerical Details

We numerically investigate two particular geometries of axial symmetry. The first problem is defined in Fig. 7.2a). We consider two spherical water droplets with respective radii $r_1$ and $r_2$ in a large nematic drop with radius $r_3$. The whole system possesses axial symmetry, so that the water droplets and the hyperbolic hedgehog, indicated by a cross, are located always on the $z$ axis. We employ a cylindrical coordinate system. The coordinates $z_1$, $z_2$, and $z_d$ denote, respectively, the positions of the centers of the droplets and of the hyperbolic hedgehog on the $z$ axis. The distances of the hedgehog from the surfaces of the two water droplets are, respectively, $d_1$ and $d_2$. Then, the quantity $d_1 + d_2$ means the distance of the two small spheres, and the point defect is situated in the middle between them if $d_1 = d_2$.

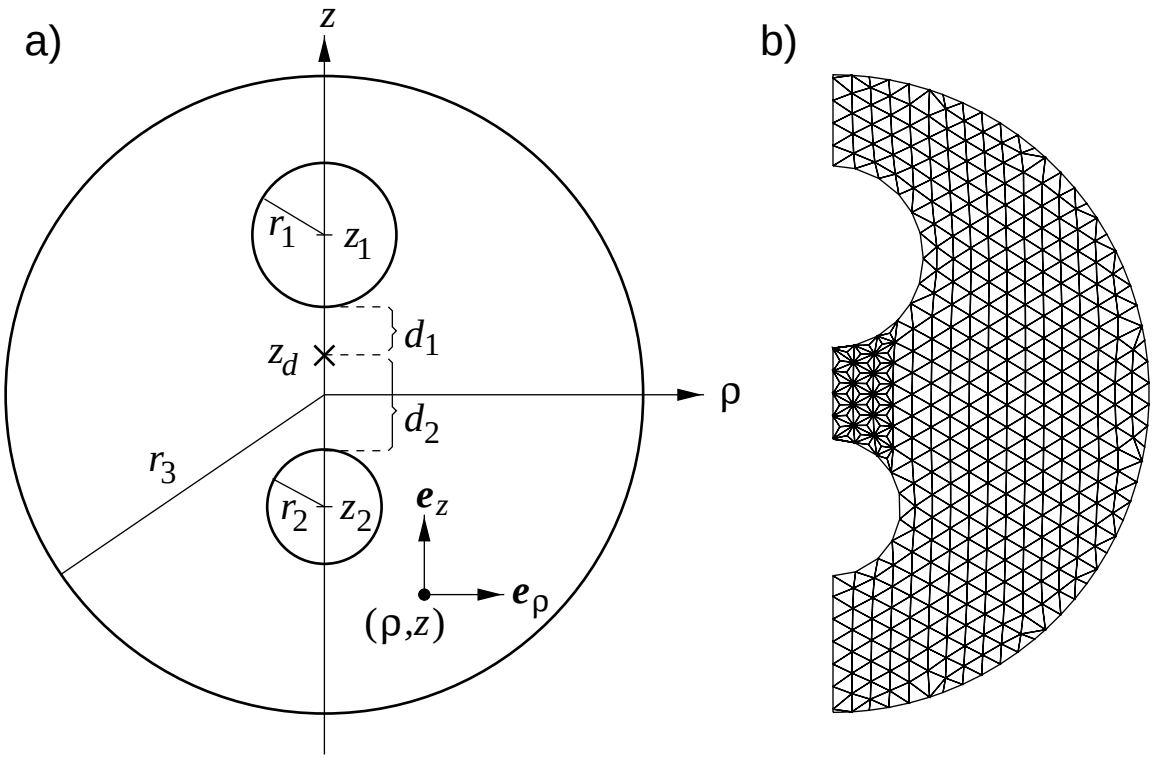


Figure 7.2: a) Geometry parameters for two water droplets with respective radii $r_1$ and $r_2$ in a large nematic drop with radius $r_3$. The system is axially symmetric about the $z$ axis, and cylindrical coordinates $\rho, z$ are used. The coordinates $z_1$, $z_2$, and $z_d$ are the respective positions of the two droplets and the hyperbolic hedgehog. The two distances of the hedgehog from the surfaces of the droplets are $d_1$ and $d_2$. From Ref. [339]. b) Triangulation of the integration area (lattice constant: $b = 0.495$). Between the small spheres a refined net of triangles is chosen. From Ref. [339].

We, furthermore, restrict the nematic director to the $(\rho, z)$ plane, which means that we do not allow for twist deformations[1]. The director is expressed in the local coordinate basis of the cylindrical coordinate system, $\boldsymbol{n}(\rho, z) = \sin\Theta(\rho, z)\boldsymbol{e}_\rho + \cos\Theta(\rho, z)\boldsymbol{e}_z$, where we introduced the *tilt angle* $\Theta$. It is always restricted to the range $[-\pi/2, \pi/2]$ to ensure the $\boldsymbol{n} \to -\boldsymbol{n}$ symmetry of the nematic phase. At all the boundaries we assume a rigid homeotropic anchoring of the director, which allows us to omit any surface term in the free energy. In Ref. [216] it was shown that rigid anchoring is justified in our system and that

[1]In nematic droplets with homeotropic anchoring a twist in the director field is usually observed (see [45] and Section 7.4). In Section 4.3.2 we demonstrated that it even appears in the dipole configuration close to the hyperbolic hedgehog. However, for the Frank elastic constants of 5CB, the distance of the defect from the surface of the water droplet differs only by 10 % if the director field is not allowed to twist. We do not expect a different behavior in the geometry under consideration in this chapter. Here, we want to concentrate, as a first step, on the principal features of the system. Therefore, we neglect twist deformations to simplify the numerics. The same simplification to catch the main behavior of nematic drops in a magnetic field was used by other authors, see, *e.g.*, [179, 178].

any deformation of the water droplets can be neglected.

In the second problem we have only one water droplet inside a large nematic drop. We use the same coordinates and lengths as described in Fig. 7.2a), but omit the second droplet. The anchoring of the director at the outer surface of the large nematic sphere is rigid planar. At the surface of the small sphere we again choose a homeotropic boundary condition.

Because of the nontrivial geometry of our problem, we decided to employ the method of finite elements [354], where the integration area is covered with triangles. We construct a net of triangles by covering our integration area with a hexagonal lattice with lattice constant $b$. Vertices of triangles that only partially belong to the integration area are moved onto the boundary along the radial direction of the appropriate sphere. As a result, extremely obtuse triangles occur close to the boundary. We use a relaxation mechanism to smooth out these irregularities. The final triangulation is shown in Fig. 7.2b). In the area between the small spheres, where the hyperbolic hedgehog is situated, the grid is further subdivided to account for the strong director deformations close to the point defect. The local refinement helps us to locate the minimum position of the defect between the spheres within a maximum error of 15 % by keeping the computing time to a reasonable value [339].

In the following, we express the Frank free energy, introduced in Section 1.1, in units of $K_3 a$ and denote it by the symbol $\overline{F}$. The quantity $a$ is the characteristic length scale of our system, typically several microns. The saddle-splay term, a pure surface term, is not taken into account. The Frank free energy is discretized on the triangular net. For details, we refer the reader to Ref. [339]. To find a minimum of the free energy, we start with a configuration that already possesses the hyperbolic point defect at a fixed position $z_d$ and let it relax via the standard Newton-Gauss-Seidel method [284], which we illustrate in Eq. 1.16 of Section 1.2.

Integrating the free energy density over one triangle yields a line energy, *i.e.*, an energy per unit length. As a rough estimate for its upper limit we introduce the line tension $F_l = (K_1 + K_3)/2$ of the isotropic core of a disclination [76]. Whenever the numerically calculated local line energy is larger than $F_l$, we replace it by $F_l$. Note that $F_l$ differs from Eq. (2.3). However, its main purpose is to stabilize the hyperbolic point defect against opening up to a disclination ring whose radius would be unphysical, *i.e.*, larger than the values discussed in 2.2.

All our calculations are preformed for the nematic liquid crystal pentylcyanobiphenyl (5CB), for which the experiments were done [279, 280]. Its respective bend and splay elastic constants are $K_3 = 0.53 \cdot 10^{-6}$ dyn and $K_1 = 0.42 \cdot 10^{-6}$ dyn. The experimental ratio $r_3/r_{1/2}$ of the radii of the large and small drops is in the range $10 - 50$ [279, 280]. The difficulty is that we want to investigate details of the director field close to the small spheres which requires a fine triangulation on the length scale given by $r_{1/2}$. To keep the computing time to a reasonable value we choose the following lengths: $r_3 = 7$, $r_{1/2} = 0.5 \ldots 2$, and $b = 0.195$ for the lattice constant of the grid. In addition, we normally use one step of grid refinement between the small spheres (geometry 1) or between the small sphere and the south pole of the large nematic drop (geometry 2). With such parameters we obtain a

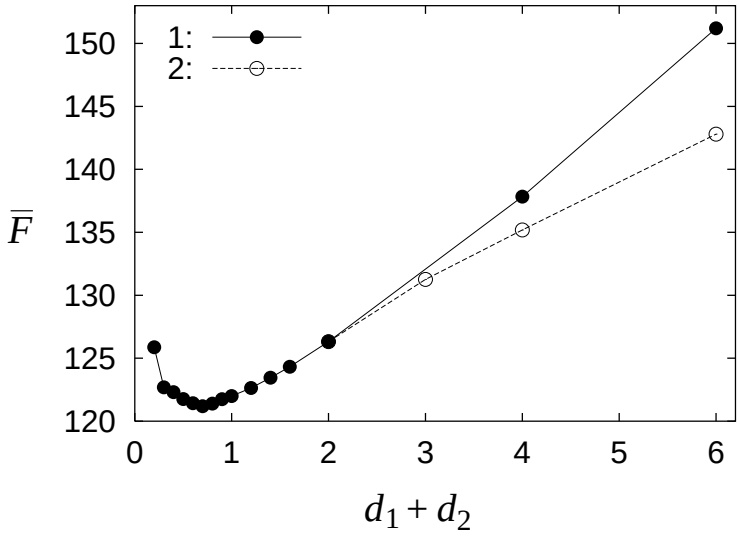


Figure 7.3: The free energy $\overline{F}$ as a function of the distance $d_1 + d_2$ between the small spheres which are placed symmetrically about $z = 0$ ($r_1 = r_2 = 1$). Curve 1: $z_d = 0$, curve 2: position $z_d$ of the defect can relax along the $z$ axis. From Ref. [339].

lattice with 2200-2500 vertices.

## 7.3 Results and Discussion of the Numerical Study

In this section we discuss the results from our numerical investigation. First, we confirm the scaling law $d_{1/2} \approx 0.3\, r_{1/2}$, which was observed in experiment, by varying the different lengths in our geometry. Secondly, we demonstrate that the topological dipole is also meaningful in complex geometries. Finally, we show that the hyperbolic hedgehog is not necessary to mediate a repulsion between the water droplets.

### 7.3.1 Scaling Law

In Fig. 7.3 we plot the reduced free energy $\overline{F}$ as a function of the distance $d_1 + d_2$ between the surfaces of the small spheres, which are placed symmetrically about the center, *i.e.*, $z_2 = -z_1$. Their radii are $r_1 = r_2 = 1$. Curve 1 shows a clear minimum at $d_1 + d_2 \approx 0.7$, the defect stays in the middle between the two spheres at $z_d = 0$. In curve 2 we move the defect along the $z$ axis and plot the minimum free energy for each fixed distance $d_1 + d_2$. It is obvious that beyond $d_1 + d_2 = 2$ the defect moves to one of the small spheres. We will investigate this result in more detail in the following subsection.

In Fig. 7.4 we take three different radii for the small spheres, $r_1 = r_2 = 0.5, 1, 2$, and plot the free energy versus $d_1/r_1$ close to the minimum. Recall that $d_1$ is the distance of the hedgehog from the surface of sphere 1. Since for such small distances $d_1 + d_2$ the defect

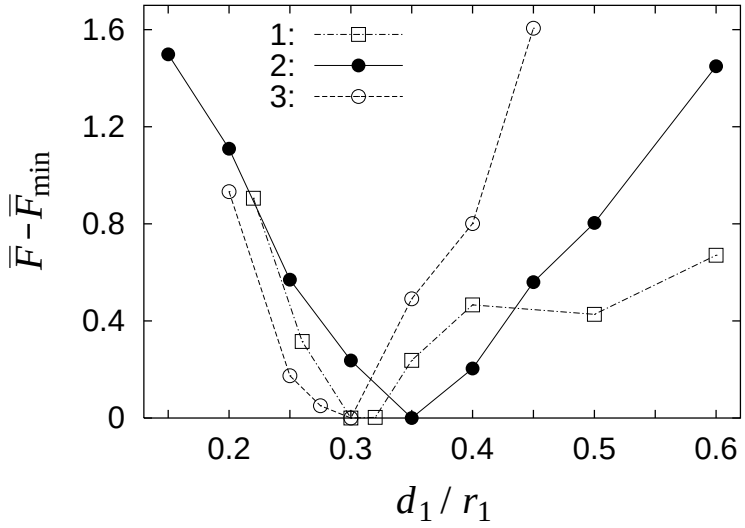


Figure 7.4: The free energy $\overline{F} - \overline{F}_{\min}$ as a function of $d_1/r_1 = d_2/r_2$. The small spheres are placed symmetrically about $z = 0$. Curve 1: $r_1 = r_2 = 0.5$, curve 2: $r_1 = r_2 = 1$, and curve 3: $r_1 = r_2 = 2$. From Ref. [339].

always stays at $z_d = 0$, *i.e.*, in the middle between the two spheres, we have $d_1/r_1 = d_2/r_2$. The quantity $\overline{F}_{\min}$ refers to the minimum free energy of each curve. For each of the three radii we obtain an energetically preferred distance $d_1/r_1$ in the range of [0.3,0.35], which agrees well with the experimental value of 0.3. Why does a scaling law of the form $d_{1/2} = (0.325 \pm 0.025)\, r_{1/2}$ occur? When the small spheres are far away from the surface of the large nematic drop, its finite radius $r_3$ should hardly influence the distances $d_1$ and $d_2$. Then, the only length scale in the system is $r_1 = r_2$, and we expect $d_{1/2} \propto r_{1/2}$. However, in Fig. 7.4 the influence from the boundary of the large sphere is already visible. Let us take curve 2 for spheres with radii $r_{1/2} = 1$ as a reference. It is approximately symmetric about $d_1/r_1 = 0.35$. The slope of the right part of curve 3, which corresponds to larger spheres of radii $r_{1/2} = 2$, is steeper than in curve 2. Also, the location of the minimum clearly tends to values smaller than 0.3. We conclude that the small spheres are already so large that they are strongly repelled by the boundary of the nematic drop. On the other hand, the slope of the right part of curve 1, which was calculated for spheres of radii $r_{1/2} = 0.5$, is less steep than in curve 2. This leads to the conclusion that the boundary of the nematic drop has only a minor influence on such small spheres.

When we move the two spheres with radii $r_{1/2} = 1$ together in the same direction along the $z$ axis, the defect always stays in the middle between the droplets and obeys the scaling law. We have tested its validity within the range $[0, 3]$ for the defect position $z_d$. Of course, the absolut minimum of the free energy occurs in the symmetric position of the two droplets, $z_2 = -z_1$.

We further check the scaling law for $r_1 \neq r_2$. We investigate two cases. When we choose $r_1 = 2$ and $r_2 = 0.6$, we obtain $d_{1/2} \approx 0.3\, r_{1/2}$. In the second case, $r_1 = 2$ and

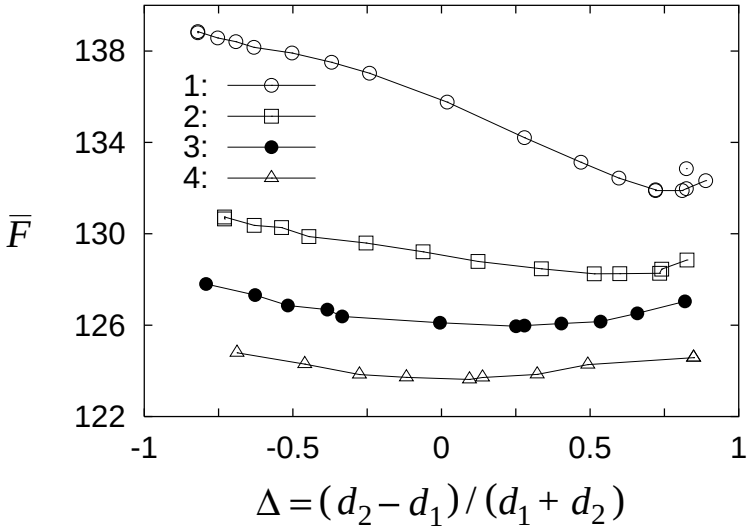


Figure 7.5: The free energy $\overline{F}$ as a function of $\Delta = (d_2 - d_1)/(d_1 + d_2)$. Sphere 2 is placed at $z_2 = 0$. The position $z_1$ of sphere 1 is the parameter. Curve 1: $z_1 = 5$, curve 2: $z_1 = 4$, curve 3: $z_1 = 3.5$, and curve 4: $z_1 = 3$. The radii are $r_1 = r_2 = 1$. From Ref. [339].

$r_2 = 1$, we find $d_1 \approx 0.37\, r_1$ and $d_2 \approx 0.3\, r_2$. As observed in the experiment, the defect sits always closer to the smaller sphere. There is no strong deviation from the scaling law $d_{1/2} = (0.325 \pm 0.025)\, r_{1/2}$, although we would allow for it, since $r_1 \neq r_2$.

### 7.3.2 Identification of the Dipole

In this subsection we demonstrate that the topological dipole is meaningful in our geometry. We place sphere 2 with radius $r_2 = 1$ in the center of the nematic drop at $z_2 = 0$. Then, we determine the energetically preferred position of the point defect for different locations $z_1$ of sphere 1 ($r_1 = 1$). The position of the hedgehog is indicated by $\Delta = (d_2 - d_1)/(d_1 + d_2)$. If the defect is located in the middle between the two spheres, $\Delta$ is zero since $d_1 = d_2$. On the other hand, if it sits at the surface of sphere 1, $d_1 = 0$, and $\Delta$ becomes one. In Fig. 7.5 we plot the free energy $\overline{F}$ versus $\Delta$. In curve 1, where the small spheres are farthest apart from each other ($z_1 = 5$), we clearly find the defect close to sphere 1. This verifies that the dipole is existing. It is stable against fluctuations since a rough estimate of the thermally induced mean displacement of the defect yields 0.01. The estimate is performed in full analogy to Eq. (4.6) of Section 4.2. When sphere 1 is approaching the center (curve 2: $z_1 = 4$ and curve 3: $z_1 = 3.5$), the defect moves away from the droplet until it nearly reaches the middle between both spheres (curve 4: $z_1 = 3$). This means, the dipole vanishes gradually until the hyperbolic hedgehog is shared by both water droplets.

An interesting situation occurs when sphere 1 and 2 are placed symmetrically about $z = 0$. Then, the defect has two equivalent positions on the positive and negative part of the $z$ axis. In Fig. 7.6 we plot again the free energy $\overline{F}$ versus the position $\Delta$ of the

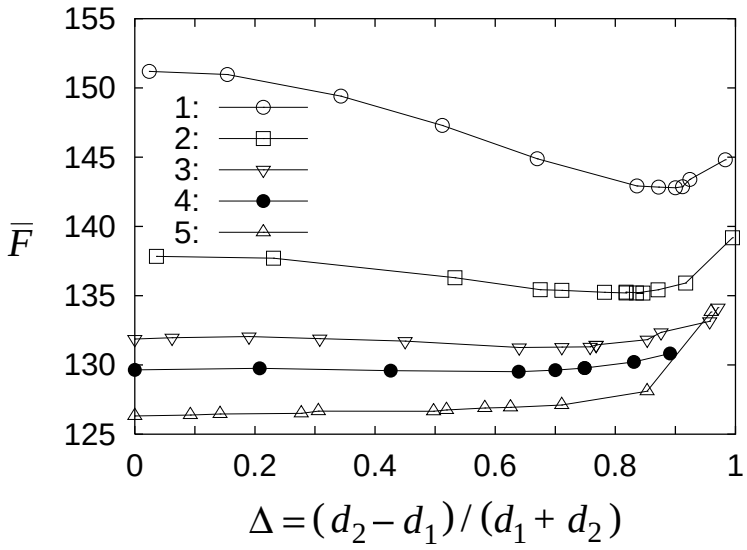


Figure 7.6: The free energy $\overline{F}$ as a function of $\Delta = (d_2 - d_1)/(d_1 + d_2)$. The small spheres are placed symmetrically about $z = 0$. Curve 1: $z_1 = -z_2 = 4$, curve 2: $z_1 = -z_2 = 3$, curve 3: $z_1 = -z_2 = 2.5$, curve 4: $z_1 = -z_2 = 2.3$, curve 5: $z_1 = -z_2 = 2$. The radii are $r_1 = r_2 = 1$. From Ref. [339].

defect. From curve 1 to 3 ($z_1 = z_2 = 4$, 3, 2.5) the minimum in $\overline{F}$ becomes broader and more shallow. The defect moves closer towards the center until at $z_1 = -z_2 \approx 2.3$ (curve 4) it reaches $\Delta = 0$. This is reminiscent to a symmetry-breaking second order phase transition [46, 195] which occurs when, in the course of moving the water droplets apart, the dipole starts to form. We take $\Delta$ as an order parameter, where $\Delta = 0$ and $\Delta \neq 0$ describe, respectively, the high- and the low-symmetry phase. A Landau expansion of the free energy yields

$$\overline{F}(\Delta) = \overline{F}_0(z_1) + a_0[2.3 - z_1]\Delta^2 + c(z_1)\Delta^4 \ , \tag{7.1}$$

where $z_1 = -z_2$ plays the role of the temperature. Odd powers in $\Delta$ are not allowed because of the required symmetry, $\overline{F}(\Delta) = \overline{F}(-\Delta)$. This free energy qualitatively describes the curves in Fig. 7.6. It should be possible to observe such a "second order phase transition"[2] with a method introduced recently by Poulin *et al.* [276] to measure dipolar forces in inverted nematic emulsion. We already explained the method in Section 5.2 after Eq. (5.12). Two small droplets filled with a magnetorheological fluid are forced apart when a small magnetic field of about 100 G is applied perpendicular to the $z$ axis. When the magnetic field is switched off, the two droplets move towards each other to reach the equilibrium distance. In the course of this process the phase transition for the dipole should be observable.

[2]There is strictly speaking no true phase transition since our investigated system has finite size. However, we do not expect a qualitative change in Fig. 7.6 when the nematic drop is much larger than the enclosed water droplets ($r_3 \gg r_1, r_2$), *i.e.*, when the system reaches the limit of infinite size.

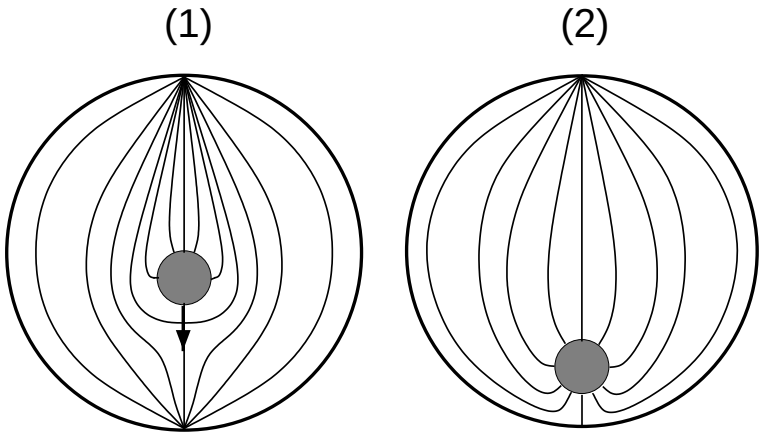


Figure 7.7: Planar boundary conditions at the outer surface of the large sphere create boojums, *i.e.*, surface defects at the north and the south pole. A water droplet with homeotropic boundary conditions nucleates a hyperbolic hedgehog. Two configurations exist that are either stable or metastable depending on the position of the water droplet; (1) the dipole, (2) the hyperbolic hedgehog sitting at the surface. From Ref. [339].

### 7.3.3 The Dipole in a Bipolar Configuration

It is possible to change the anchoring of the director at the outer surface of the large nematic drop from homeotropic to planar by adding some amount of glycerol to the surrounding water phase [279]. Then the bipolar configuration for the director field appears [45, 186], where two boojums [233], *i.e.*, surface defects of charge 1 are situated at the north and south pole of the large nematic drop (see configuration (1) in Fig. 7.7). The topological point charge of the interior of the nematic drop is zero, and every small water droplet with homeotropic boundary condition has to be accompanied by a hyperbolic hedgehog. In the experiment the hedgehog sits close to the water droplet, *i.e.*, the dipole exists and it is attracted by the strong splay deformation close to the south pole [279], as predicted by the phenomenological theory of Chapter 5 and Refs. [279, 216].

A numerical analysis of the free energy $\overline{F}$ is in agreement with experimental observations but also reveals some interesting details which have to be confirmed. In Fig. 7.8 we plot $\overline{F}$ as a function of the position $z_1$ of the small water droplet with radius $r_1 = 1$. The diagram consists of curves (1) and (2), which correspond, respectively, to configurations (1) and (2) in Fig. 7.7. The free energy possesses a minimum at around $z_1 = -5.7$. The director field assumes configuration (2), where the hyperbolic hedgehog is situated at the surface of the nematic drop. Moving the water droplet closer to the surface, induces a repulsion due to the strong director deformations around the point defect. When the water droplet is placed far away from the south pole, *i.e.*, at large $z_1$, the dipole of configuration (1) forms and represents the absolute stable director field. At $z_1 = -3.5$ the dipole becomes metastable but the system does not assume configuration (2) since the energy barrier the system has to overcome by thermal activation is much too high. By numerically calculating the free

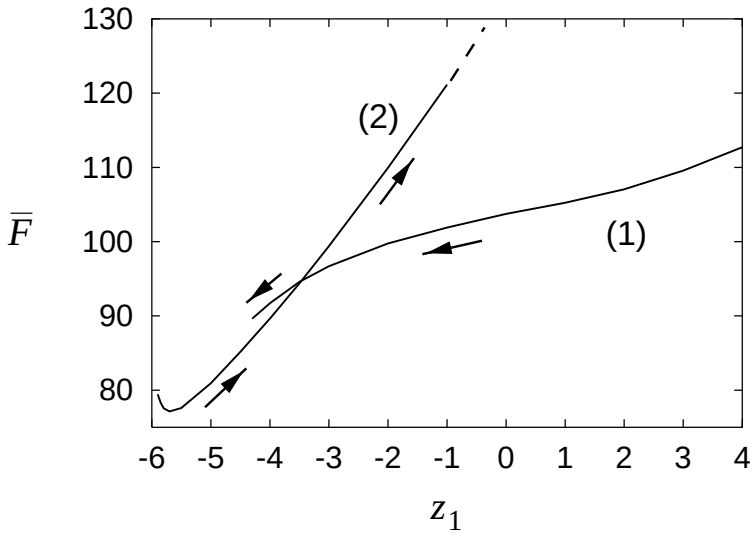


Figure 7.8: The free energy $\overline{F}$ as a function of the position $z_1$ of the water droplet for the configurations (1) and (2). For $z_1 > -3.5$, (1) is stable, and (2) is metastable. The situation is reversed for $-4.3 < z_1 < -3.5$. Configuration (1) loses its metastability at $z_1 = -4.3$. From Ref. [339].

energy for different positions of the hedgehog, we have, *e.g.*, at $z_1 = -4.0$, determined an energy barrier of $K_3 a \approx 1000\, k_\mathrm{B}T$, where $k_\mathrm{B}$ is the Boltzmann constant, $T$ the room temperature, and $a \approx 1\,\mu$m. At $z_1 = -4.3$, the dipole even loses its metastability, the hyperbolic defect jumps to the surface at the south pole and the water droplet follows until it reaches its energetically preferred position. On the other hand, if it were possible to move the water droplet away from the south pole, the hyperbolic hedgehog would stay at the surface, since configuration (2) is always metastable for $z_1 \geq -3.5$. The energy barrier for a transition to the dipole is again at least 1000 $k_\mathrm{B}T$. We have also investigated the distance $d_1$ of the defect from the surface of the water droplet. For $z_1 \in [-2, 4]$, $d_1$ fluctuates between 0.3 and 0.35. For $z_1 < -2$, it increases up to 0.5 at $z_1 = -4.3$, where the dipole loses its metastability.

### 7.3.4 Repulsion without Defect

We return to the first geometry with two water droplets and homeotropic boundary conditions at all the surfaces. When we take either a uniform director field or randomly oriented directors as a starting configuration, our system always relaxes into the configuration sketched in Fig. 7.9. Both water droplets are surrounded in their equatorial plane by a $-1/2$ disclination ring which compensates the point charge $+1$ carried by each droplet. That means, each droplet creates a Saturn-ring configuration around it, which we introduced in Section 4.1 (see also Refs. [349, 185]). To obtain the total point charge $+1$ of the nematic drop there has to be an additional topological defect with a point charge

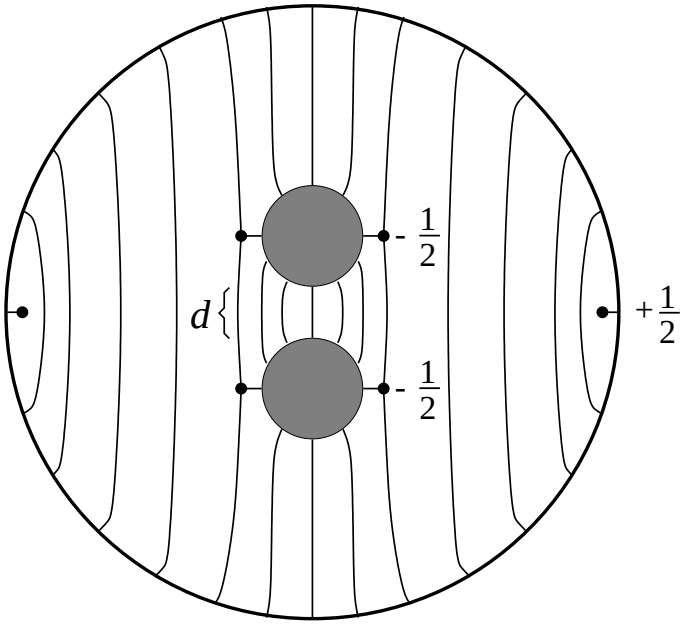


Figure 7.9: An alternative, metastable configuration. Both droplets are surrounded by a $-1/2$ disclination ring which compensates the topological charge $+1$ of each droplet. An additional $+1/2$ disclination ring close to the surface of the nematic drop satisfies the total topological charge $+1$. From Ref. [339].

$+1$. In the numerically relaxed director field, we find a $+1/2$ disclination ring close to the outer surface. This configuration has a higher energy than the one with the hyperbolic hedgehog. It is only metastable. Since a transition to the stable configuration needs a complete rearrangement of the director field, the energy barrier is certainly larger than $K_{33}a \approx 1000\, k_{\mathrm{B}}T$. We, therefore, expect the configuration of Fig. 7.9 to be stable against thermal fluctuations. It would be interesting to search for it in an experiment.

We use the configuration to demonstrate that even without the hyperbolic hedgehog the two water droplets experience some repulsion when they come close to each other. In Fig. 7.10 we plot the free energy $\overline{F}$ versus the separation $d$ of the two spheres. For large $d$, the free energy oscillates which we attribute to numerical artifacts. For decreasing $d$, the free energy clearly increases, and the water droplets repel each other due to the strong deformation of the director field lines connecting the two droplets.

## 7.4 Coda: Twist Transition in Nematic Drops

Already thirty years ago, in connection with nematic emulsions, the two main director configurations in a nematic drop were discussed both experimentally and theoretically [235, 89]: for homeotropic boundary conditions, a radial hedgehog at the center of the drop appears, whereas tangential surface anchoring leads to the bipolar structure already discussed above. The simple picture had to be modified when it was found that nematic

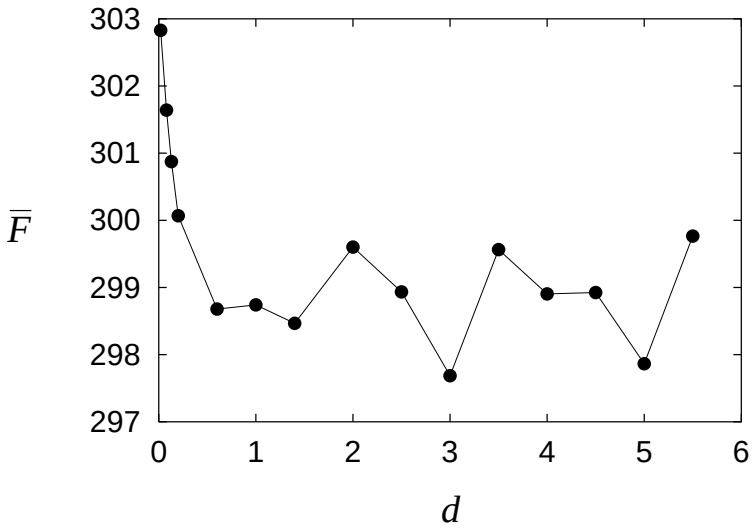


Figure 7.10: The free energy $\overline{F}$ as a function of the distance $d$ of the droplets. A repulsion for $d < 0.6$ is clearly visible. From Ref. [339].

drops in both cases also exhibit a twisted structure [45]. For the bipolar configuration, a linear stability analysis of the twist transition was performed [391]. A numerical study of the twisting in the radial structure of capillaries was presented in Refs. [282, 283]. Lavrentovich and Terentjev proposed that the twisted director field in a nematic drop with homeotropic surface anchoring is given by a combination of a hyperbolic hedgehog at the center of the drop and a radial one at its periphery [199] as illustrated in Fig. 2.3 of Section 2.1. This configuration was analysed by means of an ansatz function, and a criterion for the twist transition was given [199].

In this section we focus on the director field between two concentric spheres with perpendicular anchoring at both the surfaces and present a stability analysis for the radial configuration against axially symmetric deformations. In particular, we will derive a criterion for the twist transition, and we will show that even small spheres inside a large one are sufficent to avoid twisted configurations. This has been recently observed in the experiments on multiple nematic emulsions [279, 280].

Throughout the paper we assume rigid surface anchoring of the molecules. In nematic emulsions it can be achieved by a special choice of the surfactant [279, 280]. For completeness we note that in a single droplet for sufficiently weak anchoring strength an axial structure with an equatorial disclination ring appears [101, 88].

In the following three subsections, we first expand the Frank free energy into small deviations from the radial configuration up to second order. Then, we formulate and solve the corresponding eigenvalue equation arising from a linear stability analysis. The lowest eigenvalue leads to a criterion for the twist transition. The section closes with a discussion of our results.

### 7.4.1 Expansion of the Elastic Energy

We consider the defect-free radial director configuration between two concentric spheres of radii $r_{\min}$ and $r_{\max}$ and assume rigid radial surface anchoring at all the surfaces. If the smaller sphere is missing, the radial director configuration exhibits a point defect at the center. We will argue below that this situation, $r_{\min} = 0$, is included in our treatment.

The twist transition reduces the $SO(3)$ symmetry of the radial director configuration to an axial $C_\infty$ symmetry. In order to investigate the stability of the radial configuration $\boldsymbol{n}_0 = \boldsymbol{e}_r$ against a twist transition, we write the local director in a spherical coordinate basis, allowing for small deviations along the polar ($\theta$) and the azimuthal ($\phi$) direction:

$$\boldsymbol{n}(r,\theta) = \left(1 - \frac{1}{2}b^2 f^2 - \frac{1}{2}a^2 g^2\right)\boldsymbol{e}_r + ag\,\boldsymbol{e}_\theta + bf\,\boldsymbol{e}_\phi \ . \tag{7.2}$$

$f(r,\theta)$ and $g(r,\theta)$ are general functions which do not depend on $\phi$ due to our assumption of axial symmetry. The amplitudes $a$ and $b$ describe the magnitude of the polar and azimuthal deviation from the radial configuration. The second-order terms in $a$ and $b$ result from the normalization of the director.

The radial director field between the spheres only involves a splay distortion, and its Frank free energy is

$$F_{\text{radial}} = 8\pi K_{11}(r_{\max} - r_{\min}) \ , \tag{7.3}$$

where we did not include the saddle-splay energy. If an azimuthal ($b \neq 0$) or a polar component ($a \neq 0$) of the director is introduced, the splay energy can be reduced at costs of non-zero twist and bend contributions depending on the values of the Frank elastic constants $K_1$, $K_2$, and $K_3$. We expand the Frank free energy of the director field in Eq. (7.2) up to second order in $a$ and $b$ and obtain

$$\begin{aligned}\Delta F \ = \ & 2\pi b^2 \int dr \int d\cos\theta \,[-4K_1(f^2 + r f_r f) + K_2(\cot\theta f + f_\theta)^2 + K_3(f + r f_r)^2] \\ & + 2\pi a^2 \int dr \int d\cos\theta \,[-4K_1(g^2 + r g_r g) + K_1(\cot\theta g + g_\theta)^2 + K_3(g + r g_r)^2] \end{aligned} \tag{7.4}$$

as the deviation from $F_{\text{radial}}$. The respective subsripts $_r$ and $_\theta$ denote partial derivatives with respect to the corresponding coordinates. Note that there are no linear terms in $a$ or $b$, *i.e.*, the radial director field is always an extremum of the Frank free energy. Furthermore, there is no cross-coupling term $a\,b$ in Eq. (7.4), and the stability analysis for polar and azimuthal perturbations can be treated separately. For example, for any function $f(r,\theta)$ leading to a negative value of the first integral in Eq. (7.4), the radial configuration ($a = b = 0$) is unstable with respect to a small azimuthal deformation ($b \neq 0$), which introduces a twist into the radial director field. Therefore, we will call it the twist deformation in the following. An analogous statement holds for $g(r,\theta)$ which introduces a pure bend into the radial director field. We are now determining the condition the elastic constants have to fulfill in order to allow for such functions $f(r,\theta)$ and $g(r,\theta)$. As we will demonstrate in the next section, the solution of this problem is equivalent to solving an eigenvalue problem.

### 7.4.2 Formulating and Solving the Eigenvalue Problem

In a first step, we focus on the twist deformation ($b \neq 0$). We are facing the problem to determine for which values of $K_1$, $K_2$, and $K_3$ the functional inequality

$$\int dr \int dx \, \{K_2(1-x^2)[xf/(1-x^2) - f_x]^2 + (K_3 - 4K_1)f^2 \\ + (2K_3 - 4K_1)r f_r f + K_3 r^2 f_r^2\} < 0 \tag{7.5}$$

possesses solutions $f(r,x)$. The left-hand side of the inequality is the first integral of Eq. (7.4) after substituting $x = \cos\theta$. After some manipulations (see Ref. [301]), we obtain

$$\frac{\int dr \int dx \left(K_2 \, f \, \mathcal{D}^{(x)} f + K_3 \, f \, \mathcal{D}^{(r)} f\right)}{\int dr \int dx \, f^2} < 2K_1 \ , \tag{7.6}$$

where the second order differential operators $\mathcal{D}^{(x)}$ and $\mathcal{D}^{(r)}$ are given by

$$\mathcal{D}^{(x)} = (1-x^2)\frac{\partial^2}{\partial x^2} + 2x\frac{\partial}{\partial x} + \frac{1}{1-x^2} \qquad \text{and} \qquad \mathcal{D}^{(r)} = -r^2\frac{\partial^2}{\partial r^2} - 2r\frac{\partial}{\partial r} \ . \tag{7.7}$$

The inequality in Eq. (7.6) is fulfilled the best when the left-hand side assumes a minimum. According to the Ritz principle in quantum mechanics, this minimum is given by the lowest eigenvalue of the operator

$$K_2 \, \mathcal{D}^{(x)} + K_3 \, \mathcal{D}^{(r)} \tag{7.8}$$

on the space of square-integrable functions with $f(r_{\min},\theta) = f(r_{\max},\theta) = 0$ for $0 \leq \theta \leq \pi$ (fixed boundary condition) and $f(r,0) = f(r,\pi) = 0$ for $r_{\min} \leq r \leq r_{\max}$.

The eigenvalue equation of the operator $K_{22}\mathcal{D}^{(x)} + K_{33}\mathcal{D}^{(r)}$ separates into a radial and an angular part. The radial part is an Eulerian differential equation [38] with the lowest eigenvalue

$$\lambda_0^{(r)} = \frac{1}{4} + \left(\frac{\pi}{\ln(r_{\max}/r_{\min})}\right)^2 \tag{7.9}$$

and the corresponding eigenfunction

$$f^{(r)}(r) = \frac{1}{\sqrt{r}} \sin\left(\pi \frac{\ln(r/r_{\min})}{\ln(r_{\max}/r_{\min})}\right) . \tag{7.10}$$

The angular part of the eigenvalue equation is solved by the associated Legendre functions $P_n^{m=1}$. The lowest eigenvalue is $\lambda_0^{(x)} = 2$, and the corresponding eigenfunction is $f^{(x)}(\theta) = P_1^1(\theta) = \sin\theta$.

With both these results, we obtain the instability condition for a twist deformation:

$$\frac{1}{2}\frac{K_3}{K_1}\left[\frac{1}{4} + \left(\frac{\pi}{\ln(r_{\max}/r_{\min})}\right)^2\right] + \frac{K_2}{K_1} < 1 \ . \tag{7.11}$$

This inequality is the main result of the paper. If it is fulfilled, the radial director field no longer minimizes the Frank free energy. Therefore it is a sufficient condition for the radial configuration to be unstable against a twist deformation. It is not a necessary condition since we have restricted ourselves to second-order terms in the free energy, not allowing for large deformations of the radial director field. Hence, we cannot exclude the existence of further configurations which, besides the radial, produce local minima of the free energy.

To clarify our last statement, we take another view. The stability problem can be viewed as a phase transition. Let us take $K_3$ as the "temperature". Then condition (7.11) tells us that for large $K_3$ the radial state is the (linearly) stable one. If the phase transition is second order-like, the radial state loses its stability exactly at the linear stability boundary, while for a first order-like transition the system can jump to the new state (due to nonlinear fluctuations) even well inside the linear stability region. Thus, as long as the nature of the transition is not clear, linear stability analysis cannot predict for sure that the radial state will occur in the linear stability region. Furthermore, if the transition line is crossed, the linear stability analysis breaks down, and there could be a transition from the twisted to a new configuration. However, there is no experimental indication for such a new structure. Keeping this in mind, we will discuss the instability condition (7.11) in the next section.

We finish this section by noting that the elastic energy for a bend deformation ($a \neq 0$) has the same form as the one for the twist deformation ($b \neq 0$), however, with $K_2$ replaced by $K_1$. Therefore, we immediately conclude from (7.11) that the instability condition for a polar component ($a \neq 0$) in the director field (7.2) cannot be fulfilled for positive elastic constants. A director field with vanishing polar component is always stable in second order.

### 7.4.3 Discussion[3]

The instability condition (7.11) indicates for which values of the elastic constants $K_1, K_2$, and $K_3$ the radial configuration is expected to be unstable with respect to a twist deformation. The instability domain is largest for $r_{\max}/r_{\min} \to \infty$ and decreases with decreasing ratio $r_{\max}/r_{\min}$, *i.e.*, a water droplet inside a nematic drop can stabilize the radial configuration.

In Fig. 7.11a) the instability condition (7.11) is shown. If the ratios of the Frank elastic constants define a point in the grey triangles the radial configuration can be unstable depending on the ratio $r_{\max}/r_{\min}$. The dark grey area gives the range of the elastic constants where a twisted structure occurs for $r_{\max}/r_{\min} = 50$. With increasing ratio $r_{\max}/r_{\min}$ the instability domain enlargens until it is limited by $K_3/(8K_1) + K_2/K_1 = 1$ for $r_{\max}/r_{\min} \to \infty$. The light grey triangle is the region where the radial configuration is unstable for $r_{\max}/r_{\min} > 50$ but where it is stable for $r_{\max}/r_{\min} < 50$.

The circles in Fig. 7.11a) represent, respectively, the elastic constants for the liquid crystal compounds MBBA, 5CB, and PAA. For 5CB the elastic constants are in the light

[3]Reprinted with permission from A. Rüdinger and H. Stark, Twist Transition in Nematic Droplets: A Stability Analysis, Liq. Cryst. **26**, 753 (1999). Copyright 1999 Taylor and Francis, http://www.tandf.co.uk.

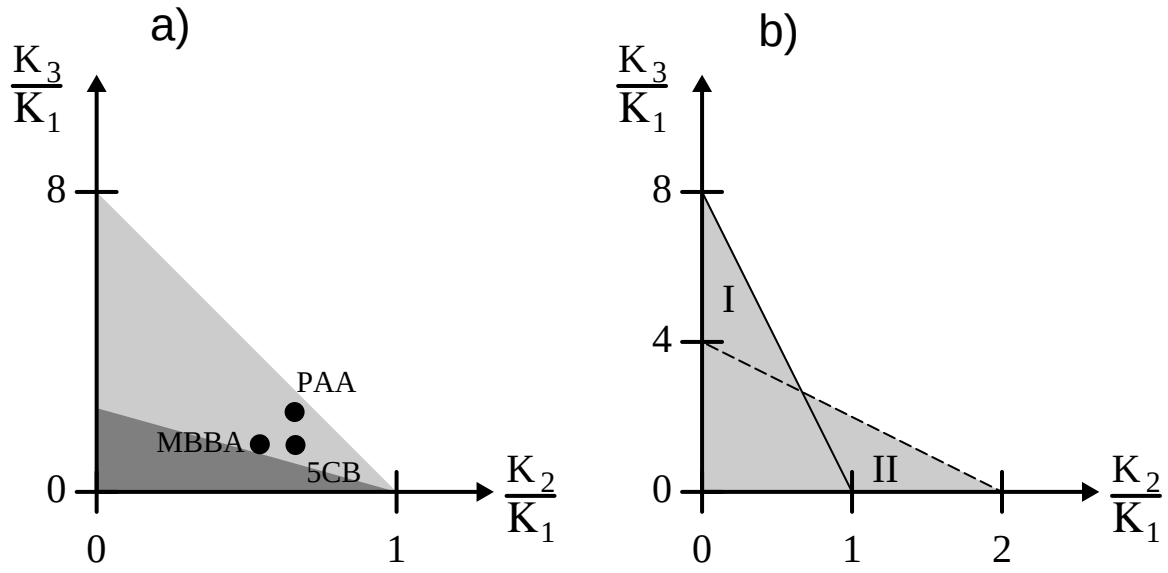


Figure 7.11: a) Stability diagram for the twist transition [cf. Eq. (7.11)]. The dark grey corresponds to the ratios of Frank constants where the radial configuration is unstable for a ratio $r_{\max}/r_{\min} = 50$. The light grey triangle is the region where the radial configuration is unstable for $r_{\max}/r_{\min} \geq 50$. The circles represent the elastic constants for the liquid crystal compounds MBBA, 5CB, and PAA. b) A comparison between the regions of instability for a radial director field against twisting derived in this work (full line) and by Lavrentovich and Terentjev (dashed line) for $r_{\max}/r_{\min} \to \infty$. The regions differ by the areas I and II.

grey domain, *i.e.*, a twisted structure is expected for $r_{\max}/r_{\min} \to \infty$ (no inner sphere) but not for $r_{\max}/r_{\min} < 50$. Such a behavior has been recently observed in multiple nematic emulsions [279]. It has been found that a small water droplet inside a large nematic drop prevents the radial configuration from twisting.

Two examples of nematic drops observed under the microscope between crossed polarizers can be seen in Fig. 7.12. In the left image the director configuration is pure radial, in the right one it is twisted. The left drop contains a small water droplet that stabilizes the radial configuration according to Eq. (7.11). The water droplet is not visible in this image because of the limited resolution. A better image is presented in [279]. We have calculated the polarizing microscope picture of the twisted configuration by means of the $2 \times 2$ Jones matrix formalism [88]. We took the director field of Eq. (7.2) and used the eigenfunction of Eq. (7.10) with an amplitude $b = 0.15$. The result shown in Fig. 7.13 is in qualitative agreement with the experimental image on the right in Fig. 7.12.

In Fig. 7.14 we plot the radial part $f^{(r)}(r)$ [see Eq. (7.10)] of the eigenfunction $f(r,\theta) = f^{(r)}(r)f^{(x)}(\theta)$ governing the twist deformations. For large values of $r_{\max}/r_{\min}$ it is strongly

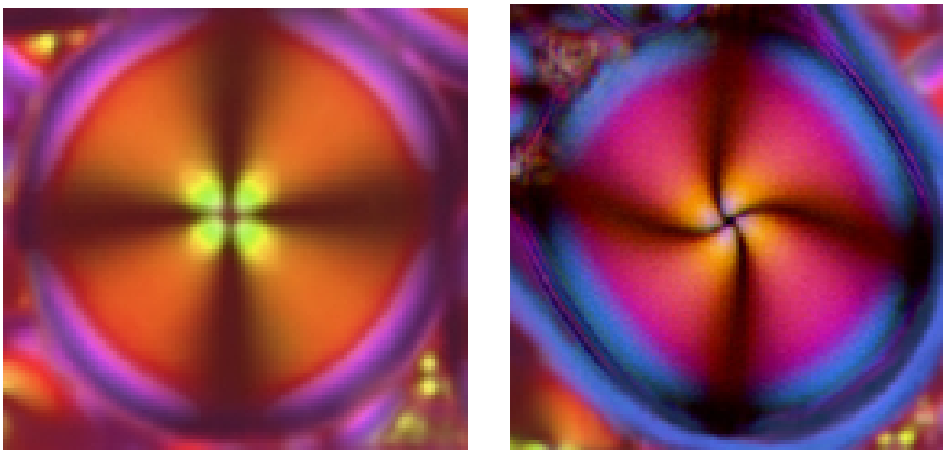

Figure 7.12: Radial (left) and twisted (right) configuration of the director field in a nematic drop (diameter $\approx 20\mu$m) of 5CB observed under the microscope between crossed polarizers. In the radial configuration there is a small isotropic liquid droplet in the center of the nematic drop (invisible in this image). Courtesy of P. Poulin.

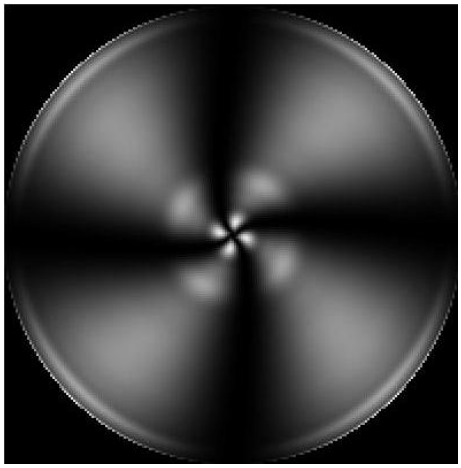

Figure 7.13: Calculated transmission for the twisted configuration of the director field in a nematic drop whose diameter is 20 $\mu$m. The transmission amplitude was obtained by summing over 20 wave lengths between 400 and 800 nm. The amplitude $b$ of the twist deformation was set to 0.15. This figure has to be compared to the rigth image of Fig. 7.12.

peaked near $r_{\min}$. The maximum of $f^{(r)}(r)$ occurs at a radius $r_0$ which is given by

$$\ln \frac{r_0}{r_{\min}} = \frac{\ln(r_{\max}/r_{\min})}{\pi} \arctan \frac{2\pi}{\ln(r_{\max}/r_{\min})} \quad . \tag{7.12}$$

Hence, for $r_{\max}/r_{\min} \gg 1$ the maximal azimuthal component $bf(r_0, \theta)$ of the director field is located at $r_0/r_{\min} = \mathrm{e}^2 \approx 7.39$, *i.e.*, close to the inner sphere. From the polarizing miscroscope pictures it can be readily seen that the twist deformation is largest near the center of the nematic drop. In the opposite limit, $r_{\max}/r_{\min} \approx 1$, the position of maximal twist is at the geometric mean of $r_{\min}$ and $r_{\max}$: $r_0 = (r_{\min} r_{\max})^{1/2}$.

In the limit $r_{\min} \to 0$, where the inner sphere is not existing, a point defect with a core radius $r_c$ is located at $r = 0$. In this case our boundary condition, $f^{(r)}(r_{\min}) = 0$, makes no sense since the director is not defined for $r < r_c$. Fortunately, for $r_{\min} \to 0$ the lowest

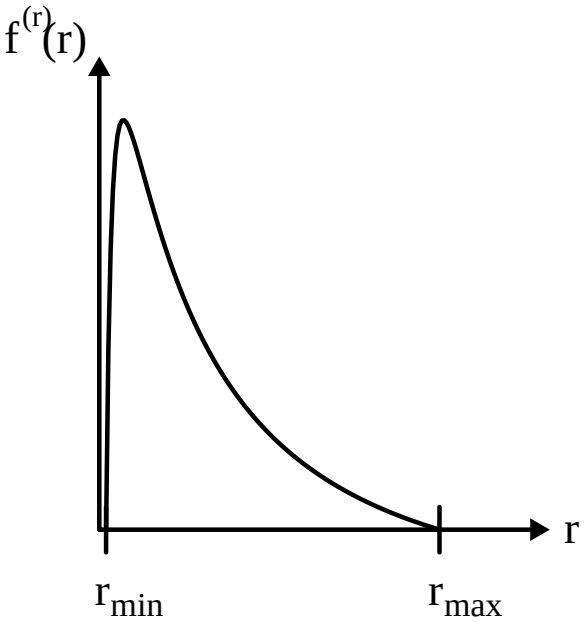


Figure 7.14: Radial dependence of $f^{(r)}(r)$ [cf. Eq. (7.10)] for $r_{\max}/r_{\min} = 50$. The function is strongly peaked close to $r_{\min}$.

eigenvalue of the operator (7.8) and therefore the instability condition is insensitive to a change of the boundary condition. Furthermore, the shape of the eigenfunction is also independent of the boundary condition, in particular its maximum is always located close to $r_{\min}$.

A last comment concerns the work of Lavrentovich and Terentjev [199]. In Fig. 7.11b) we plot as a dashed line the criterion, $K_3/(4K_1)+K_2/(2K_1) = 1$, which the authors of Ref. [199] derived for the twist transition in the case $r_{\max}/r_{\min} \to 0$. They constructed an ansatz function which connects a hyperbolic hedgehog at the center via a twist deformation to a radial director field at the periphery of a nematic drop. Then they performed a stability analysis for an appropriately chosen order parameter. The region of instability calculated in this article and their result differ by the areas I and II. This is due to the complementarity of the two approaches. While the authors of Ref. [199] allow for large deviations with respect to the radial configuration at the cost of fixing an ansatz function, we allow the system to search the optimal configuration (*i.e.*, eigenfunction) for small deformations. We conclude that both results together give a good approximation of the region of instability for the radial configuration against twisting. However, we cannot exclude that a full nonlinear analysis of the problem leads to a change in the stability boundaries.

In conclusion, we have performed a stability analysis of the radial configuration in nematic drops with respect to a twist deformation. Assuming strong perpendicular anchoring at all the surfaces, we have derived an instability condition in terms of the Frank constants. We could show that a small water droplet inside the nematic drop stabilizes the radial configuration.

# Chapter 8

# Temperature-Induced Flocculation above the Nematic-Isotropic Phase Transition

Ping Sheng was the first to study the consequences of surface-induced liquid crystalline order above the nematic-isotropic phase transition [319, 320]. He introduced the notion *paranematic order* in analogy to the paramagnetic phase, in which a magnetic field causes a non-zero magnetization. He realized that the bounding surfaces of a restricted geometry influence the bulk transition temperature $T_c$. In nematic films, *e.g.*, the phase transition even vanishes below a critical thickness [319]. Sheng's work was extended by Poniewierski and Sluckin [274], who studied two plates immersed in a liquid crystal above $T_c$ and who calculated an attractive force between the two plates due to the surface-induced order. This force was investigated in detail by Borštnik and Žumer [36].

The work presented in this chapter explores the liquid crystal mediated interaction between spherical particles immersed into a liquid crystal above $T_c$. It has to be added to the conventional van der Waals, electrostatic, and steric interactions as a new type of interparticle potential. Its strength can be controlled by temperature, and close to the clearing temperature $T_c$, it can induce a flocculation transition in an otherwise stabilized colloidal dispersion.

In Section 8.1 we review the Landau-de Gennes theory, which describes liquid crystalline order close to the phase transition, and we present Euler-Lagrange equations for the director and the Maier-Saupe order parameter to be defined below. Section 8.2 illustrates paranematic order in simple plate geometries and introduces the liquid crystal mediated interaction of two parallel plates. In Section 8.3 we extend it to spherical particles and investigate its consequences when combined with van der Waals and electrostatic interactions.

## 8.1 Theoretical Background

We start with a review of the Landau-de Gennes theory and then formulate the Euler-Lagrange equations for restricted geometries with axial symmetry.

### 8.1.1 Landau-de Gennes Theory in a Nutshell

The director $\boldsymbol{n}$, a unit vector, only indicates the average direction of the molecules. It tells nothing about how well the molecules are aligned. To quantify the degree of liquid crystalline order, we could just vary the magnitude of $\boldsymbol{n}$, *i.e.*, choose a polar vector as an order parameter. However, all nematic properties are invariant under inversion of the director, thus every polar quantity has to be zero. The next choice is any second-rank tensor, *e.g.*, the magnetic susceptibility tensor $\boldsymbol{\chi}$. The order parameter $\boldsymbol{Q}$ is defined by the relation

$$\boldsymbol{Q} = \frac{9}{2\mathrm{tr}\,\boldsymbol{\chi}} \left( \boldsymbol{\chi} - \frac{1}{3}\,\mathbf{1}\,\mathrm{tr}\,\boldsymbol{\chi} \right) \;, \tag{8.1}$$

where $\mathrm{tr}\boldsymbol{\chi} = \chi_{ii}$ stands for the trace of a tensor, and Einstein's summation convention over repeated indices is always assumed in the following. We subtract the isotropic part $\mathbf{1}\mathrm{tr}\boldsymbol{\chi}/3$ from $\boldsymbol{\chi}$, in order that $\boldsymbol{Q}$ vanishes in the isotropic liquid. The prefactor is convention. The order parameter $\boldsymbol{Q}$ describes, in general, biaxial liquid crystalline ordering through its eigenvectors and eigenvalues. The uniaxial symmetry of the nematic phase demands that two eigenvalues of $\boldsymbol{Q}$ are equal, which then assumes the form

$$\boldsymbol{Q} = \frac{3}{2}\,S\Big( \boldsymbol{n} \otimes \boldsymbol{n} - \frac{1}{3}\,\mathbf{1} \Big) \qquad \text{with} \qquad S = \frac{3(\chi_\parallel - \chi_\perp)}{2\chi_\perp + \chi_\parallel} \;. \tag{8.2}$$

The Maier-Saupe or scalar order parameter $S$ indicates the degree of nematic order through the magnetic anisotropy $\Delta\chi = \chi_\parallel - \chi_\perp$. It was first introduced by Maier and Saupe in a microscopic treatment of the nematic phase [222]. The microscopic approach was generalized by Lubensky to describe biaxial order [214].

In his seminal publication (see Ref. [73]) de Gennes was interested in pretransitional effects above the nematic-isotropic phase transition. He constructed a free energy in $\boldsymbol{Q}$ and $\nabla_i Q_{jk}$ in the spirit of Landau and Ginzburg, commonly known as Landau-de Gennes theory:

$$F_{LG} = \int d^3r \, (f_b + f_{\nabla Q}) \;, \tag{8.3}$$

with

$$f_b = \frac{1}{2}\,a_0(T - T^*)\,\mathrm{tr}\,\boldsymbol{Q}^2 - \frac{1}{3}\,b\,\mathrm{tr}\,\boldsymbol{Q}^3 + \frac{1}{4}\,c\,(\mathrm{tr}\,\boldsymbol{Q}^2)^2 \tag{8.4}$$

$$f_{\nabla Q} = \frac{1}{2}\,L_1(\nabla_i Q_{jk})^2 + \frac{1}{2}\,L_2(\nabla_i Q_{ij})^2 \;. \tag{8.5}$$

The quantity $f_b$ introduces a Landau-type free energy density which describes a first-order phase transition, and $f_{\nabla Q}$ is necessary to treat, *e.g.*, fluctuations in $\boldsymbol{Q}$, as noticed by

Ginzburg. Both free energy densities are Taylor expansions in $\boldsymbol{Q}$ and $\nabla_i Q_{jk}$, and each term is invariant under the symmetry group $O(3)$ of the isotropic liquid, *i.e.*, the high-symmetry phase. The Landau parameters of the compound 5CB are $a_0 = 0.087 \cdot 10^7\,\mathrm{erg/cm^3K}$, $b = 2.13 \cdot 10^7\,\mathrm{erg/cm^3}$, $c = 1.73 \cdot 10^7\,\mathrm{erg/cm^3}$, and $T^* = 307.15\,\mathrm{K}$ [57]. The elastic constants $L_1$ and $L_2$ are typically of the order of $10^{-6}\,\mathrm{dyn}$.

It can be shown unambiguously that $f_b$ is minimized by the uniaxial order parameter of Eq. (8.2), for which the free energies $f_b$ and $f_{\nabla Q}$ take the form

$$f_b = \frac{3}{4}\,a_0(T - T^*)S^2 - \frac{1}{4}\,bS^3 + \frac{9}{16}\,cS^4 \tag{8.6}$$

$$f_{\nabla Q} = \frac{3}{4}\,L_1(\nabla_i S)^2 + \frac{9}{4}\,L_1 S^2(\nabla_i n_j)^2 \ . \tag{8.7}$$

To arrive at Eq. (8.7), we set $L_2 = 0$ in order to simplify the free energy as much as possible for our treatment in Sections 8.2 and 8.3. $L_2 \neq 0$ merely introduces some anisotropy, as shown by de Gennes [73]. Assume, *e.g.*, that $S$ is fixed to a non-zero value at a space point $\boldsymbol{r}_s$ in the isotropic fluid, then the nematic order around $\boldsymbol{r}_s$ decays exponentially on a characteristic length scale called nematic coherence length. If $L_2 \neq 0$, the respective coherence lengths along and perpendicular to $\boldsymbol{n}$ are different. In Fig. 8.1 we plot $f_b$ as a function of $S$ using the parameters of 5CB. Above the *superheating* temperature $T^\dagger = T^* + b^2/(24a_0c)$, there exists only one minimum at $S = 0$ for the thermodynamically stable isotropic phase. At $T^\dagger$ a second minimum for the metastable nematic phase evolves, which becomes absolutely stable at the *clearing* temperature $T_c = T^* + b^2/(27a_0c)$. A first-order phase transition occurs, and the order parameter as a function of temperature assumes the form

$$S(T) = \frac{1}{6}\,\frac{b}{c} + \sqrt{\frac{2a}{3c}\,(T^\dagger - T)} \ . \tag{8.8}$$

Finally, at the *supercooling* temperature $T^*$ the curvature of $f_b$ at $S = 0$ changes sign, and the isotropic fluid becomes absolutely unstable. For the compound 5CB, we find $T_c - T^* = 1.12\,\mathrm{K}$ and $T^\dagger - T_c = 0.14\,\mathrm{K}$.

### 8.1.2 Euler-Lagrange Equations for Restricted Geometries

In the following, we determine the surface-induced liquid crystalline order above $T_c$. As usual, it follows from a minimization of the total free energy,

$$F = F_{LG} + F_{sur} \ , \tag{8.9}$$

where we have added a surface term $F_{sur}$ to the Landau-de Gennes free energy $F_{LG}$. We restrict ourselves to uniaxial order and employ a generalization of the Rapini-Papoular potential, introduced in Section 1.1,

$$F_{sur} = \int dA\,\frac{3}{4}\left(W_S(S - S_0)^2 + 3W_{\boldsymbol{n}}SS_0\big[1 - (\boldsymbol{n}\cdot\hat{\boldsymbol{\nu}})^2\big]\right) \ , \tag{8.10}$$

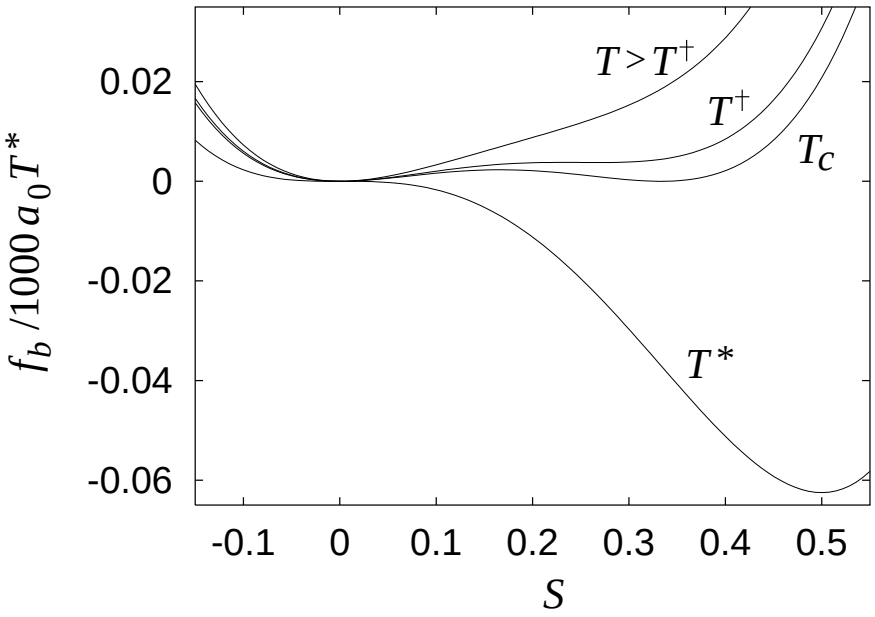


Figure 8.1: The free energy density $f_b$ in units of $1000 a_0 T^*$ as a function of the Maier-Saupe order parameter $S$ vor various temperatures. The Landau coefficients of the compound 5CB are employed. A first-order transition occurs at $T_c$.

where $dA$ is the surface element. The quantity $S_0$ denotes the preferred Maier-Saupe parameter at the surface, and $\hat{\boldsymbol{\nu}}$ is the surface normal since we always assume homeotropic anchoring. The surface-coupling constants $W_S$ and $W_{\boldsymbol{n}}$ penalize a respective deviation of $S$ from $S_0$ and of the director $\boldsymbol{n}$ from $\hat{\boldsymbol{\nu}}$. In recent experiments, anchoring and orientational wetting transitions of liquid crystals, confined to cylindrical pores of alumina membranes, were analyzed [64, 65]. It was found that $W_S$ and $W_{\boldsymbol{n}}$ vary between $10^{-1}\,\mathrm{erg/cm^2}$ and $5\,\mathrm{erg/cm^2}$, with the ratio $W_{\boldsymbol{n}}/W_S$ not being larger than 5. If $W_S = W_{\boldsymbol{n}} = W$, the integrand in Eq. (8.10) is equivalent to the intuitive form $W\mathrm{tr}(\boldsymbol{Q} - \boldsymbol{Q}_0)^2/2$ with the uniaxial $\boldsymbol{Q}$ from Eq. (8.2) and $\boldsymbol{Q}_0 = \frac{3}{2}S_0(\hat{\boldsymbol{\nu}} \otimes \hat{\boldsymbol{\nu}} - \frac{1}{3}\mathbf{1})$. It was introduced by Nobili and Durand [255]. In formulating the elastic free energy density $f_{\nabla Q}$ of Eq. (8.5), one also identifies a contribution which can be written as a total divergence, $\nabla_i(Q_{ij}\nabla_k Q_{jk} - Q_{jk}\nabla_k Q_{ij})$. When transformed into a surface term and when a uniaxial $\boldsymbol{Q}$ is inserted, it results in the saddle-splay energy of Eq. (1.4). To simplify our calculations, we will neglect this term. It is not expected to change the qualitative behavior of our system for strong surface coupling.

In what follows, we assume rotational symmetry about the $z$ axis. We introduce cylindrical coordinates and write the director in the local coordinate basis, $\boldsymbol{n}(\rho, z) = \sin\Theta(\rho, z)\boldsymbol{e}_\rho + \cos\Theta(\rho, z)\boldsymbol{e}_z$, restricting it to the $(\rho, z)$ plane. The same is assumed for the surface normal $\hat{\boldsymbol{\nu}}(\rho, z) = \sin\Theta_0(\rho, z)\boldsymbol{e}_\rho + \cos\Theta_0(\rho, z)\boldsymbol{e}_z$. Expressing and minimizing the total free energy under all these premises, we obtain the Euler-Lagrange equations for $S$

and the tilt angle $\Theta$ in the bulk,

$$\boldsymbol{\nabla}^2 S - \frac{1}{\xi_N^2} S + \frac{b}{2L_1} S^2 - \frac{3c}{2L_1} S^3 - 3S \left( (\boldsymbol{\nabla}\Theta)^2 + \frac{\sin^2\Theta}{\rho^2} \right) = 0 \tag{8.11}$$

$$\boldsymbol{\nabla}^2 \Theta - \frac{\sin\Theta\cos\Theta}{\rho^2} = 0 \ , \tag{8.12}$$

and the boundary equations are

$$(\hat{\boldsymbol{\nu}} \cdot \boldsymbol{\nabla}) S - \frac{1}{\gamma_S \xi_N} (S - S_0) - \frac{3}{2\gamma_{\boldsymbol{n}} \xi_N} S_0 \sin^2(\Theta - \Theta_0) = 0 \tag{8.13}$$

$$(\hat{\boldsymbol{\nu}} \cdot \boldsymbol{\nabla}) \Theta - \frac{1}{2\gamma_{\boldsymbol{n}} \xi_N} \frac{S_0}{S} \sin[2(\Theta - \Theta_0)] = 0 \ . \tag{8.14}$$

The meaning of the nematic coherence length

$$\xi_N = \sqrt{L_1/[a_0(T - T^*)]} \tag{8.15}$$

will be clarified in the next section. At the phase transition, $\xi_{NI} = \xi_N(T_c)$ is of the order of 10 nm, as can be checked by the parameters of 5CB. The surface-coupling strengths $W_S$ and $W_{\boldsymbol{n}}$ are characterized by dimensionless quantities

$$\gamma_S = \frac{1}{\xi_N} \frac{L_1}{W_S} = \frac{\sqrt{a_0(T - T^*) L_1}}{W_S} \quad \text{and} \quad \gamma_{\boldsymbol{n}} = \frac{1}{\xi_N} \frac{L_1}{W_{\boldsymbol{n}}} = \frac{\sqrt{a_0(T - T^*) L_1}}{W_{\boldsymbol{n}}} \ , \tag{8.16}$$

which compare the respective surface extrapolation lengths $L_1/W_S$ and $L_1/W_{\boldsymbol{n}}$ to the nematic coherence length $\xi_N$. For $W = 1\,\mathrm{erg/cm^2}$ and $L_1 = 10^{-6}\,\mathrm{dyn}$, the extrapolation lengths are of the same order as $\xi_N$ at $T_c$, *i.e.*, 10 nm.

## 8.2 Paranematic Order in Simple Geometries

In the first two subsections we study the paranematic order in a liquid crystal compound above $T_c$ for simple plate geometries. It is induced by a coupling between the surfaces and the molecules. We disregard the non-harmonic terms in $S$ in Eq. (8.11) to simplify the problem as much as possible and to obtain an overall view of the system. In Subsection 8.2.3 the effect of the non-harmonic terms is reviewed.

### 8.2.1 One Plate

We assume that an infinitely extended plate, which induces a homeotropic anchoring of the director, is placed at $z = 0$. Its surface normals are $\pm \boldsymbol{e}_z$, and its thickness should be negligibly small. A uniform director field along the $z$ axis obeys Eqs. (8.12) and (8.14), and the Maier-Saupe order parameter $S$ follows from a solution of Eqs. (8.11) and (8.13),

$$S(z) = \frac{S_0}{1 + \gamma_S} \exp[-|z|/\xi_N] \ . \tag{8.17}$$

The order parameter $S$ decays exponentially along the $z$ axis on a characteristic length scale given by the nematic coherence length $\xi_N$. The value of $S$ at $z = 0$ depends on the strength $\gamma_S$ of the surface coupling, *i.e.*, on the ratio of the surface extrapolation length $L_1/W$ and $\xi_N$. The plate is surrounded by a layer of liquid crystalline order whose thickness $\xi_N$ decreases with increasing temperature since $\xi_N \propto (T - T^*)^{-1/2}$. The total free energy per unit surface, $F/A$, consisting of the Landau-de Gennes and the surface free energy, is

$$\frac{F}{A} = \frac{3}{2} W_S S_0^2 \frac{\gamma_S}{1+\gamma_S} \quad . \tag{8.18}$$

Note that the energy increases with temperature since $\gamma_S \propto \sqrt{T - T^*}$. The whole theory certainly becomes invalid when $\xi_N$ approaches molecular dimensions. For 10 K above $T_c$, we find $\xi_N \approx 3$nm, *i.e.*, the theory is valid several Kelvin above $T_c$. Finally, we notice that a nematic wetting layer can be probed by the evanescent wave technique [326].

### 8.2.2 Two Plates

If two plates of the previous subsection are placed at $z = \pm d/2$, the order parameter profile $S(z)$, determined from Eqs. (8.11) and (8.13), is

$$S(z) = S_0 \frac{\cosh(z/\xi_N)}{\cosh(d/2\xi_N) + \gamma_S \sinh(d/2\xi_N)} \quad . \tag{8.19}$$

For separations $d \gg 2\xi_N$, the layers of liquid crystalline order around the plates do not overlap, as illustrated in the inset of Fig. 8.2.[1] If $d \leq 2\xi_N$, the whole volume between the plates is occupied by nematic order, which induces an attraction between the plates. The interaction energy per unit area, $\Delta F/A$, is defined as $\Delta F/A = [F(d) - F(d \to \infty)]/A$. It amounts to

$$\frac{\Delta F}{A} = \frac{F(d) - F(d \to \infty)}{A} = \frac{3}{2} W_S S_0^2 \gamma_S \left[ \frac{\tanh(d/2\xi_N)}{1 + \gamma_S \tanh(d/\xi_N)} - \frac{1}{1+\gamma_S} \right] \quad . \tag{8.20}$$

In Fig. 8.2 we plot $\Delta F/A$ versus the reduced distance $d/2\xi_{NI}$ for different temperatures at $T_c$ and above $T_c$. The material parameters of 5CB are chosen; $W_S = 1\,\mathrm{erg/cm^2}$, and $S_0 = 0.3$. The energy unit $3W_S S_0^2/2 = 10^4\, k_B T$ is determined at room temperature. Note, that $\xi_{NI}$ is the coherence length at $T_c$. If $d \gg \xi_N$, the interaction energy decays exponentially in $d$, $\Delta F/A \propto \exp(d/\xi_N)$. The interaction is always attractive over the whole separation range. This can be understood by a simple argument. Above $T_c$, the nematic order always possesses higher energy than the isotropic liquid. Therefore, the system can reduce its free energy by moving the plates together. The minimum of the interaction energy occurs at $d = 0$, *i.e.*, when the liquid with nematic order between the

[1] Figs. 8.2, 8.3, 8.7, 8.8 reprinted with permission from A. Borštnik, H. Stark, and S. Žumer, Temperature-Induced Flocculation of Colloidal Particles Above the Nematic-Isotropic Phase Transition, Progr. Colloid Polym. Sci **115**, 353 (2000). Copyright 2000 Springer Verlag.

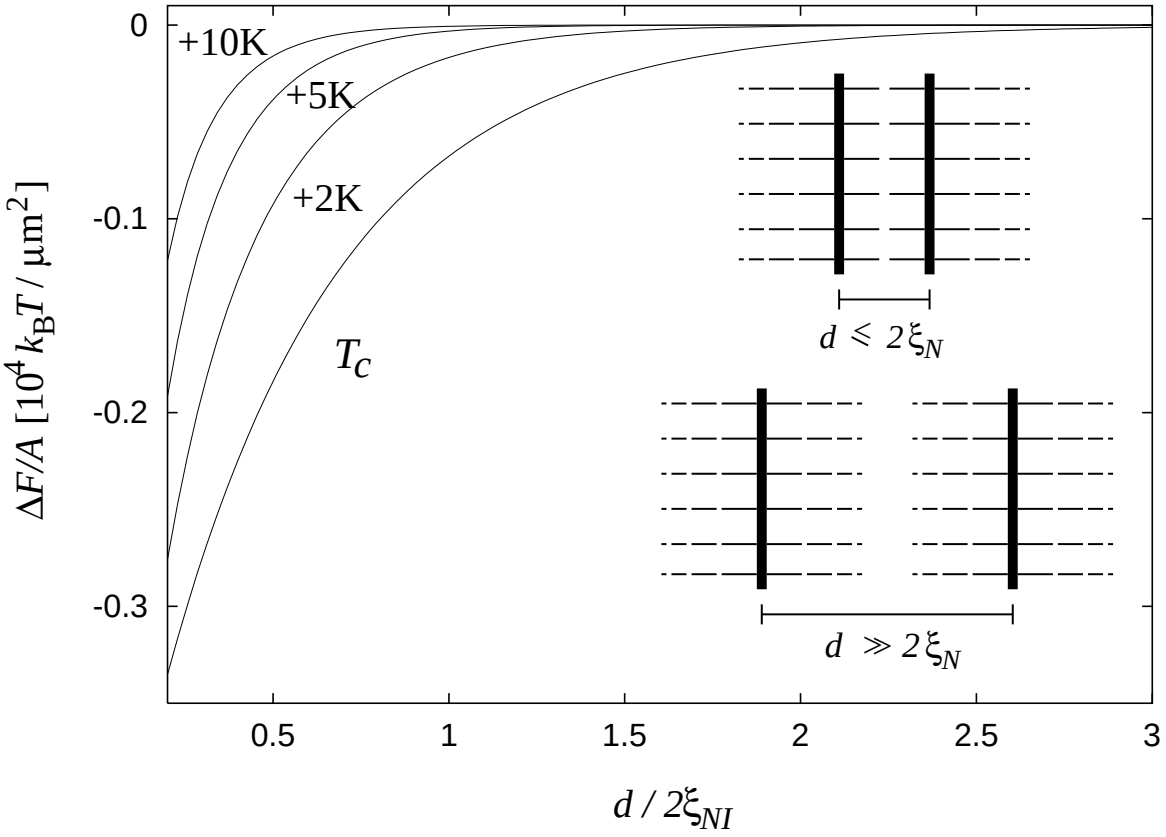


Figure 8.2: Interaction energy per unit area, $\Delta F/A$, as a function of the reduced distance $d/2\xi_{NI}$ for various temperatures. For further explanation see text. From Ref. [35].

plates is completely removed. This simple argument explains the deep potential well in Fig. 8.2. It extends to a separation of $2\xi_N$ where the nematic layers start to overlap. Since $\xi_N \propto (T - T^*)^{-1/2}$, the range of the interaction decreases with increasing temperature, and the depth of the potential well becomes smaller.

### 8.2.3 Effect of Non-Harmonic Terms

In this subsection we review the effects on the two-plate geometry when the complete Landau-de Gennes theory including its non-harmonic terms in $S$ is employed. A wealth of phenomena exists, which we illustrate step by step [319, 320]. Their influence on the interaction of two plates was studied in detail by Borštnik and Žumer [36].

First, we assume rigid anchoring at the nematic-plate interfaces, *i.e.*, $S(\pm d/2)$ is fixed to $S_0$ [319]. For $d \to \infty$, there is a phase transition at the bulk transition temperature $T_{c\infty} = T_c$ from the nematic to the surface-induced paranematic phase, as expected. When the plates are moved together, the transition temperature $T_{cd}$ increases until the first-order transition line in a $d - T$ phase diagram ends in a critical point at $(d_{\rm crit}, T_{cd}^{\rm crit})$.

For $d < d_{\text{crit}}$, no phase transition between the nematic and the paranematic phase is observed anymore. This is similar to the gas-liquid critical point in an isotropic fluid. For $S_0 = S(\pm d/2) = 0.5 - 1$ and typical values of the Landau parameters, $T_{cd}^{\text{crit}}$ is situated approximately 0.2 K above $T_{c\infty} = T_c$ and 0.1 K above the superheating temperature $T^\dagger$.

Secondly, we concentrate on a basically infinite separation, $d \gg \xi_{NI}$, and allow a finite surface-coupling strength $W_S$ [320]. For sufficiently small $W_S$, both the boundary $[S(\pm d/2)]$ and the bulk $[S(0)]$ value of the scalar order parameter exhibit a jump at $T_c$. That means, the surface coupling is so small that $S(\pm d/2)$ follows the bulk order parameter. However, in a finite intervall $W_{S0} < W_S < W_S^{\text{crit}}$, the discontinuity of $S(\pm d/2)$, which Sheng calls a boundary-layer phase transition, occurs at temperatures $T_{\text{bound}}$ above $T_c$. Beyond the critical strength $W_S^{\text{crit}}$, the boundary transition vanishes completely. Sheng just used the linear term $\propto W_S S$ of our surface potential for his investigation. The separate boundary-layer transition occurred in the approximate intervall $0.01\,\text{erg/cm}^2 < W_S < 0.2\,\text{erg/cm}^2$. We do not expect a dramatic change of this intervall for the potential of Eq. (8.10).

Thirdly, we combine the finite separation of the plates with a finite surface-coupling strength $W_S$. The boundary-layer transition temperatures $T_{\text{bound}}$ and the intervall $W_{S0} < W_S < W_S^{\text{crit}}$ are not effected by a finite $d$. In addition, a jump of $S(\pm d)$ occurs at the bulk transition temperature $T_{cd} \leq T_{\text{bound}}$. It evolves gradually with decreasing $d$. When $T_{cd}$ becomes larger than $T_{\text{bound}}$ in the course of moving the plates together, the separate boundary-layer transition disappears. Finally, at a critical thickness $d_{crit}$ the nematic-paranematic transition vanishes altogether.

All these details occur close to $T_{c\infty} = T_c$ within a range of $T_{cd}^{crit} - T_{c\infty} = 0.5\,\text{K}$ [320]. The calculations are non-trivial. Since we do not want to render our investigation in the following section too complicated, we will skip the non-harmonic terms in the Landau-de Gennes theory. Furthermore, we use a relatively high anchoring strength of about $W_S = 1\,\text{erg/cm}^2$, so that $T_{cd}^{crit} - T_{c\infty}$ is even smaller than 0.5 K. The simplifications are sufficient to bring out the main features of our system.

## 8.3 Two-Particle Interactions above the Nematic-Isotropic Phase Transition

In this section we present the liquid crystal mediated interaction above $T_c$ as a new type of two-particle potential. We combine it with the traditional van der Waals and electrostatic interaction and explore its consequences, namely the possibility of a temperature-induced flocculation. We start with a motivation, introduce all three types of interactions, and finally discuss their consequences. Our presentation concentrates on the main ideas and results (see also Ref. [35]). Details of the calculations can be found in Refs. [33] and [34].

### 8.3.1 Motivation

In Chapter 3 we already mentioned that the stability of colloidal systems presents a key issue in colloid science since their characteristics change markedly in the transition from

the dispersed to the aggregated state. There are always attractive van der Waals forces, which have to be balanced by repulsive interactions to prevent a dispersion of particles from aggregating. This is achieved either by electrostatic repulsion, where the particles carry a surface charge, or by steric stabilization, where they are coated with a soluble polymer brush. Dispersed particles approach each other due to their Brownian motion. They aggregate if the interaction potential is attractive, i.e., if it possesses a potential minimum $U_{\min} < 0$ at finite separations. Two situations are possible. In the case of weak attraction, where $|U_{\min}| \approx 1 - 3\,k_{\mathrm{B}}T$, an equilibrium phase separation of a dilute and an aggregated state exists. The higher interaction energy of the dispersed particles is compensated by their larger entropy in comparison to the aggregated phase. Strong attraction, *i.e.*, $|U_{\min}| > 5 - 10\,k_{\mathrm{B}}T$, causes a non-equilibrium phase with all the particles aggregated. They cannot escape the attractive potential in the observation time of interest of, *e.g.*, several hours. Due to Chandrasekhar, the escape time $t_{\mathrm{esc}}$ can be estimated as [47]

$$t_{\mathrm{esc}} = \frac{a^2}{D_0 \exp(-U_{\min}/k_{\mathrm{B}}T)} \qquad \text{with} \qquad D_0 = \frac{k_{\mathrm{B}}T}{6\pi\eta a} \ . \tag{8.21}$$

$D_0$ is the diffusion constant of a non-interacting Brownian particle with radius $a$, and $\eta$ is the shear viscosity of the solvent. The quantity $t_{\mathrm{esc}}$ approximates the time a particle needs to diffuse a distance $a$ in leaving a potential well of depth $U_{\min}$. More refined theories suggest that the complete two-particle potential has to be taken into account when calculating $t_{\mathrm{esc}}$ [208, 147].

Here, we study the influence of liquid crystal mediated interactions on colloidal dispersions above $T_c$, which are stabilized by an electrostatic repulsion. We demonstrate that the main effect of the liquid crystal interaction $U_{LC}$ is an attraction at the length scale of $\xi_N$, whose strength can be controlled by temperature. If the electrostatic repulsion is sufficiently weak, $U_{LC}$ induces a flocculation of the particles within a few Kelvin close to the transition temperature $T_c$. It is completely reversible. A similar situation is found in polymer stabilized colloids. There, the abrupt change from a dispersed to a fully aggregated state within a few Kelvin is called *critical flocculation* [252, 306]. The reversibility of flocculation has interesting technological implications. For example, in "instant" ink, the particles of dried ink redisperse rapidly when put into water [252].

So far, experiments on colloidal dispersions above the clearing temperature $T_c$ are very rare [37, 275]. They would help to explore a new class of colloidal interactions. Furthermore, they could provide insight into wetting phenomena above $T_c$ with all its subtleties close to $T_c$, which we reviewed in Subsection 8.2.3. Also, experiments by Muševič *et al.*, who probe interactions with the help of an atomic force microscope [248, 249], are promising.

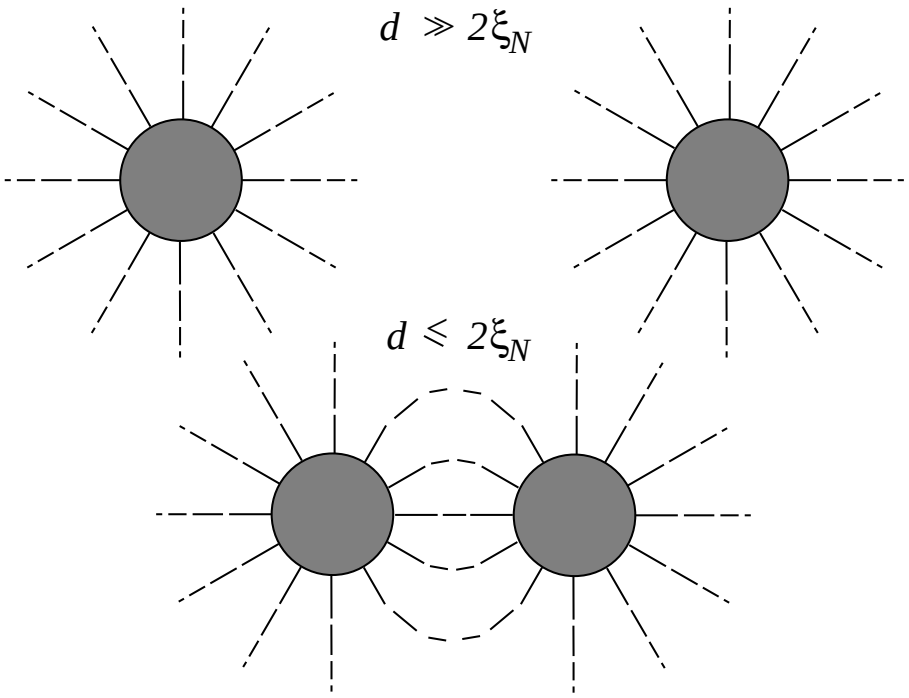


Figure 8.3: Two particles at a separation $d \gg 2\xi_N$ do not interact. At $d \approx 2\xi_N$ both a strong attraction and repulsion set in. From Ref. [35].

### 8.3.2 Liquid Crystal Mediated Interaction

One particle suspended in a liquid crystal above the clearing temperature $T_c$ is surrounded by a layer of surface-induced nematic order whose thickness is of the order of the nematic coherence length $\xi_N$. The director field points radially outward when a homeotropic anchoring at the particle surface is assumed. Two particles with a separation $d \gg 2\xi_N$ do not interact. When the separation is reduced to $d \approx 2\xi_N$, a strong attraction sets in since the total volume of nematic order is decreased as in the case of two plates (see Fig. 8.3). In addition, a repulsion due to the elastic distortion of the director field lines connecting the two particles occur. In this subsection we quantify the two-particle interaction mediated by a liquid crystal.

In principle, the director field and the Maier-Saupe order parameter $S$ follow from a solution of Eqs. (8.11)–(8.14). Since the geometry of Fig. 8.4 a) cannot be treated analytically, we employ two simplifications. First, we approximate each sphere by 72 conical segments, whose cross sections in a symmetry plane of our geometry are illustrated in Fig. 8.4 a). In the following, we assume a particle radius $a = 250\,\mathrm{nm}$, and, therefore, each line segment has a length of 26 nm. Secondly, we construct appropriate ansatz functions for the fields $S(\boldsymbol{r})$ and $\boldsymbol{n}(\boldsymbol{r})$. To arrive at an ansatz for $S(\boldsymbol{r})$, we approximate the bounding surfaces A$i$ and B$i$ of region $i$ by two parallel ring-like plates and employ the order parameter profile of Eq. (8.19), where $d$ is replaced by an average distance $d_i$ of the bounding surfaces. Since the particle radius is an order of magnitude larger than the interesting

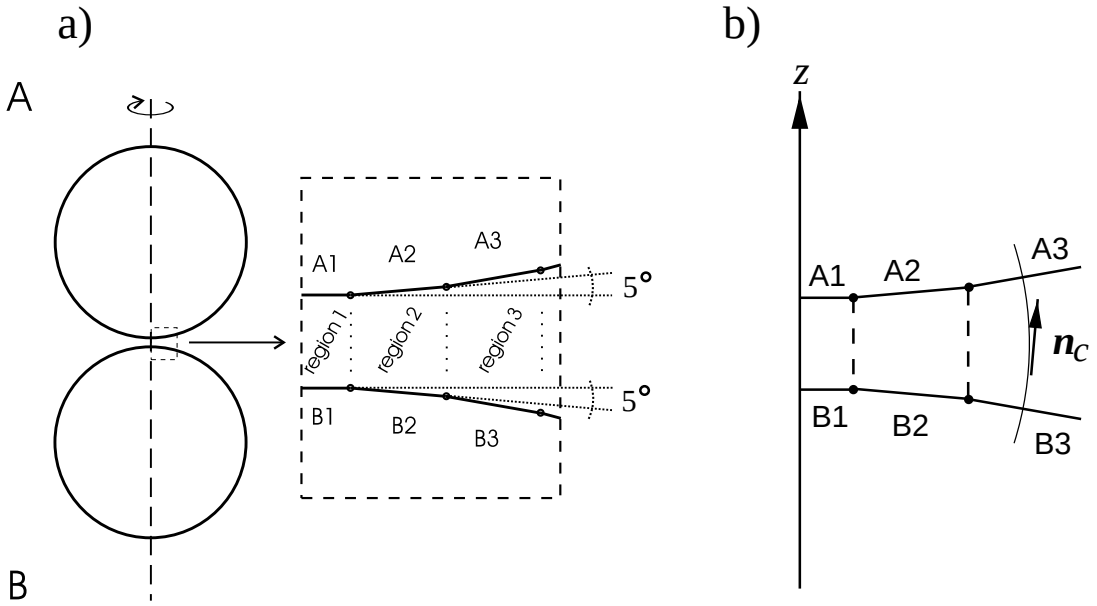


Figure 8.4: a) Two spheres A and B are approximated by conical segments as illustrated in the blowup. b) At separations $d \approx 2\xi_N$, the director is chosen as a tangent vector $\boldsymbol{n}_c$ of a circular segment whose radius is determined by the boundary condition (8.14).

separations, which do not exceed several coherence lengths, the analogy with two parallel plates is justified. Furthermore, we expect that only a few regions close to the symmetry axis are needed to calculate the interaction energy with a sufficient accuracy. In the limit of large separations ($d \gg 2\xi_N$), the director field around each sphere points radially outward. In the opposite limit ($d \approx 2\xi_N$), the director field lines are strongly distorted, and we approximate them by circular segments as illustrated in Fig. 8.4 b) for the third region. The radius of the circle is determined by the boundary condition (8.14) of the director. With decreasing separation of the two particles, the director field should change continuously from $\boldsymbol{n}_\infty$ at $d \gg 2\xi_N$ to the ansatz $\boldsymbol{n}_c$ at small $d$. Hence, we choose $\boldsymbol{n}(\boldsymbol{r})$ as a weighted superposition of $\boldsymbol{n}_c$ and $\boldsymbol{n}_\infty$:

$$\boldsymbol{n}(\boldsymbol{r}) \propto \epsilon_i \, \boldsymbol{n}_c + (1 - \epsilon_i) \, \boldsymbol{n}_\infty \ , \tag{8.22}$$

where the free parameter $\epsilon_i$ follows from a minimization of the free energy in region $i$ with respect to $\epsilon_i$.

As in the case of two parallel plates, the interaction energy is defined relative to the total free energy of infinite separation:

$$U_{LC}(d) = F(d) - F(d \to \infty) \ . \tag{8.23}$$

In calculating $U_{LC}$, we employ the free energy densities of Eqs. (8.6) and (8.7) and the surface potential of Eq. (8.10), neglecting the non-harmonic terms in $S$. The volume integrals

cannot be performed analytically without further approximations which we justified by a comparision with a numerical integration. The final expression of $U_{LC}$ is very complicated, and we refer the reader to Ref. [33] for its explicit form. We checked that regions $i = 1 \ldots 9$ are sufficient to calculate $U_{LC}$. The contribution of region 9 to the interaction energy is less than 5 %. Hence, the orientational order outside these nine regions is not relevant for $U_{LC}$.

We subdivide the interaction energy in an attractive part which results from all terms in the free energy depending on the order parameter $S$ or its gradient, only. The repulsive part is due to the elastic distortion of the director field and a deviation from the homeotropic orientation at the particle surfaces. All the graphs, which we present in the following, are calculated with the Landau parameters of the compound 8CB [57], *i.e.*, $a_0 = 0.12 \cdot 10^{-7}\,\mathrm{erg/cm^3K}$, $b = 3.07 \cdot 10^{-7}\,\mathrm{erg/cm^3}$, $c = 2.31 \cdot 10^{-7}\,\mathrm{erg/cm^3}$, and $L_1 = 1.8 \cdot 10^{-6}\,\mathrm{dyn}$, which gives $T_c - T^* = b^2/(27 a_0 c) = 1.3\,\mathrm{K}$. The surface-coupling constants are $W_S = 1\,\mathrm{erg/cm^2}$ and $W_{\boldsymbol{n}} = 5\,\mathrm{erg/cm^2}$. In the large inset of Fig. 8.5 we plot the attractive and repulsive contribution at the clearing temperature $T_c$ in units of the thermal energy $k_\mathrm{B}T$. As in the case of two parallel plates, the total interaction energy exhibits a deep potential well with an approximate width of $2\xi_{NI}$. At larger separations, it is followed by a weak repulsive barrier whose height is approximately $1.5\,k_\mathrm{B}T$, as indicated by the small inset in Fig. 8.5. If $d \gg 2\xi_N$, $U_{LC}$ decays exponentially: $U_{LC} \propto \exp(-d/\xi_N)$. Figure 8.5 illustrates further that the depth of the potential well, *i.e.*, the liquid crystal mediated attraction of two particles decreases considerably when the dispersion is heated by several Kelvin. That means, the interaction can be controlled by temperature. It is turned off by heating the dispersion well above $T_c$. The same holds for the weak repulsive barrier. As expected, both the depth of the potential well and the hight of the barrier decrease with the surface-coupling constants, where $W_S$ seems to be more important [33].

### 8.3.3 Van der Waals and Electrostatic Interactions

The van der Waals interaction of two thermally fluctuating electric dipoles decays with the sixth power of their inverse distance, $1/r^6$. To arrive at the interparticle potential of two macroscopic objects, a summation over all pairwise interactions of fluctuating charge distributions is performed. In the case of two spherical particles of equal radii $a$, the following, always attractive, van der Waals interaction results [306]:

$$U_W = -\frac{A}{6}\left[\frac{2a^2}{d(d+4a)} + \frac{2a^2}{(d+2a)^2} + \ln\frac{d(d+4a)}{(d+2a)^2}\right] \quad . \tag{8.24}$$

Here $d$ is the distance between the surfaces of the particles, and $A$ is the Hamaker constant. For equal particles made of material 1 embedded in a medium 2, it amounts to [306]

$$A = \frac{3}{4}k_\mathrm{B}T\left(\frac{\epsilon_1 - \epsilon_2}{\epsilon_1 + \epsilon_2}\right)^2 + \frac{3h\nu_\mathrm{uv}}{16\sqrt{2}}\frac{(n_1^2 - n_2^2)^2}{(n_1^2 + n_3^2)^{3/2}} \quad , \tag{8.25}$$

where $\epsilon_1$ and $\epsilon_2$ are the static dielectric constants of the two materials, and $n_1$ and $n_2$ are the corresponding refractive indices of visible light. The relaxation frequency $\nu_\mathrm{uv}$ belongs

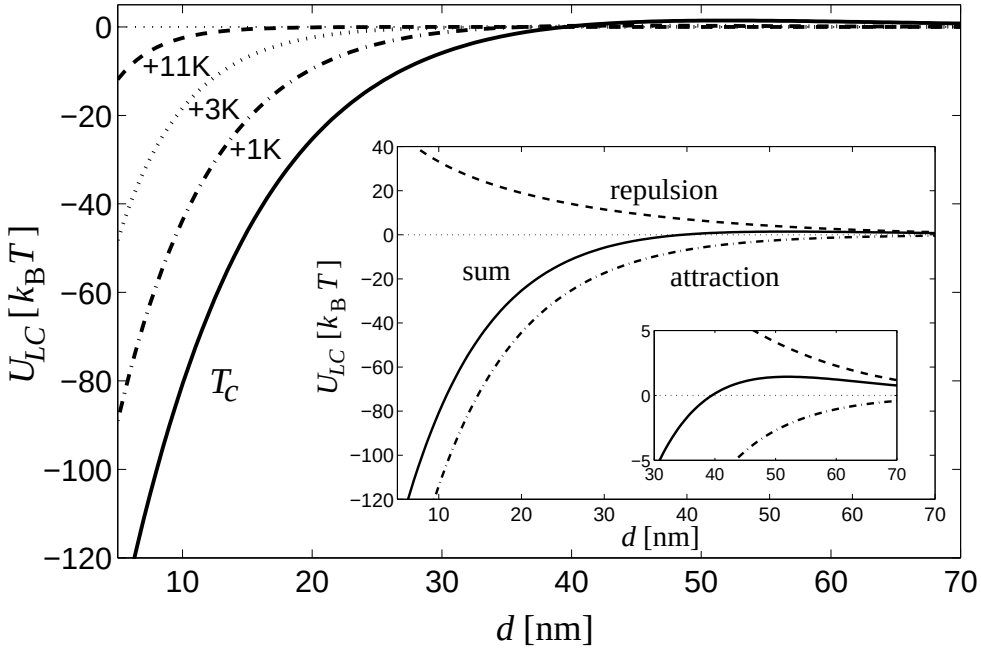


Figure 8.5: The liquid crystal mediated interaction $U_{LC}$ in units of $k_B T$ as a function of the particle separation $d$. The interaction is shown at $T_c$, $T_c + 1\,\mathrm{K}$, $T_c + 3\,\mathrm{K}$, and $T_c + 11\,\mathrm{K}$. It strongly depends on temperature. Large inset: $U_{LC}$ is composed of an attractive and repulsive part. Small inset: A weak repulsive barrier occurs at $d \approx 60\,\mathrm{nm}$.

to the dominant ultraviolet absorption in the dielectric spectrum of the embedding medium 2. Typical values for silica particles immersed into a nematic liquid crystal are $\epsilon_1 = 3.8$, $n_1 = 1.45$, $\epsilon_2 = 11$, $n_2 = 1.57$, and $\nu_{\mathrm{uv}} = 3 \cdot 10^{15}\,\mathrm{s}^{-1}$ [33]. As a result, the Hamaker constant equals $A = 1.1\,k_B T$. Note, that for separations $d \gg a$ the particles are point-like, and the van der Waals interaction decays as $1/d^6$. In the opposite limit, $d \ll a$, it diverges as $a/d$.

We stabilize the colloidal dispersion against the attractive van der Waals forces by employing an electrostatic repulsion. We assume that each particle carries a uniformly distributed surface charge whose density $q_s$ does not change under the influence of other particles. Ionic impurities in the liquid crystal screen the surface charges with which they form the so-called electrostatic double layer. For particles of equal radius $a$ embedded in a medium with dielectric constant $\varepsilon_2$, the electrostatic two-particle potential is described by the following expression [306]:

$$U_E = -\pi\, k_B T\, \frac{a q_s^2}{z^2 e_0^2 n_p}\, \ln(1 - e^{-\kappa d}) \ . \tag{8.26}$$

Here, $e_0$ is the fundamental charge, and $z$ is the valence of the ions in the solvent, which have a concentration $n_p$. The range of the repulsive interaction is determined by the *Debye length*

$$\kappa^{-1} = \sqrt{\varepsilon_2 k_B T / (8\pi e_0^2 z^2 n_p)} \ , \tag{8.27}$$

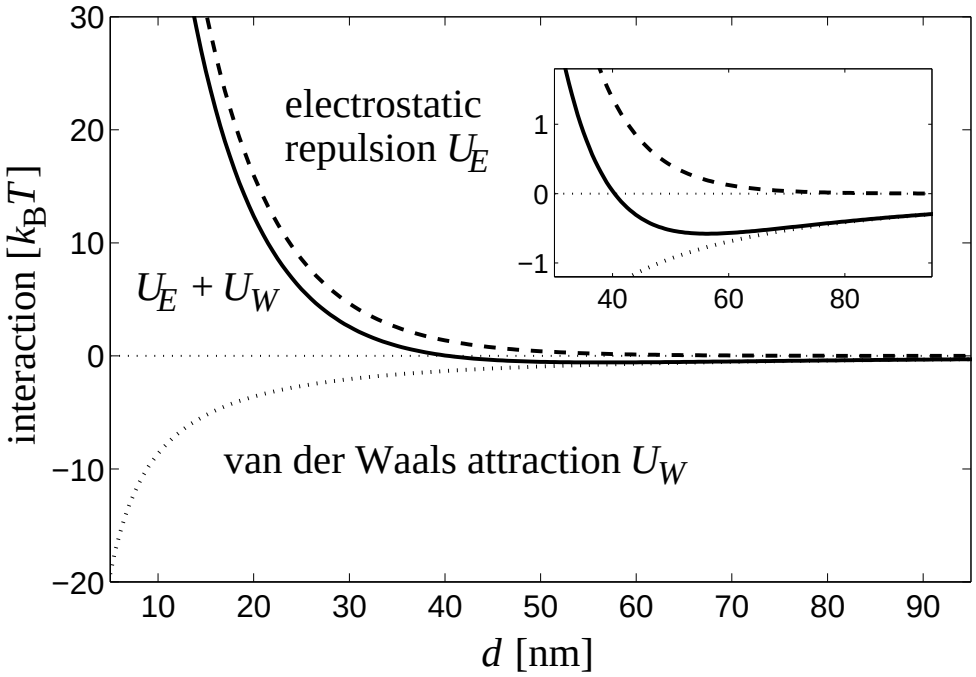


Figure 8.6: The electrostatic (dashed) and van der Waals (dotted) interaction and their sum $U_E + U_W$ (full line) in units of $k_B T$ as a function of particle separation $d$. The parameters are chosen according to the text. Inset: A shallow potential minimum appears at $d \approx 55\,\text{nm}$.

whereas the surface-charge density $q_s$ controls its strength. The potential $U_E$ decays exponentially at $d \gg \kappa^{-1}$. The expression (8.26) is derived via the *Derjaguin approximation* [80, 306], which is only valid for $d, \kappa^{-1} \ll a$. In the following, we take a monovalent salt ($z = 1$), choose $\varepsilon_2 = 11$, and vary $n_p$ between $10^{-4}$ and $10^{-3}\,\text{mol/l}$. Then, at room temperature the Debye length $\kappa^{-1}$ ranges from 10 to 3.5 nm. Together with typical separations $d$ not larger than a few coherence lengths $\xi_N$ and $a = 250\,\text{nm}$, the Derjaguin approximation is justified. Furthermore, we adjust the surface-charge density around $10^4\, e_0/\mu\text{m}^2$. The ranges of $n_p$ and $q_s$ are well accessible in an experiment.

In Fig. 8.6 we plot the electrostatic and the van der Waals interactions and their sum in units of $k_B T$. The surface-charge density $q_s$ is $0.5 \cdot 10^4\, e_0/\mu\text{m}^2$ and $\kappa^{-1} = 8.3\,\text{nm}$. All further parameters besides the Hamaker constant $A$ are chosen as mentioned above. We increased $A$ from 1.1 to 5.5. Even then it is clearly visible that the strong electrostatic repulsion determines the interaction for $d < 30\,\text{nm}$, the dispersion of particles is stabilized. At about 55 nm, $U_E + U_W$ exhibits a shallow potential minimum (see inset of Fig. 8.6), and at $d \gg \kappa^{-1}$, the algebraic decay of the van der Waals interaction takes over. In the following subsection, we investigate the combined effects of all three interactions for the Hamaker constant $A = 1.1$.

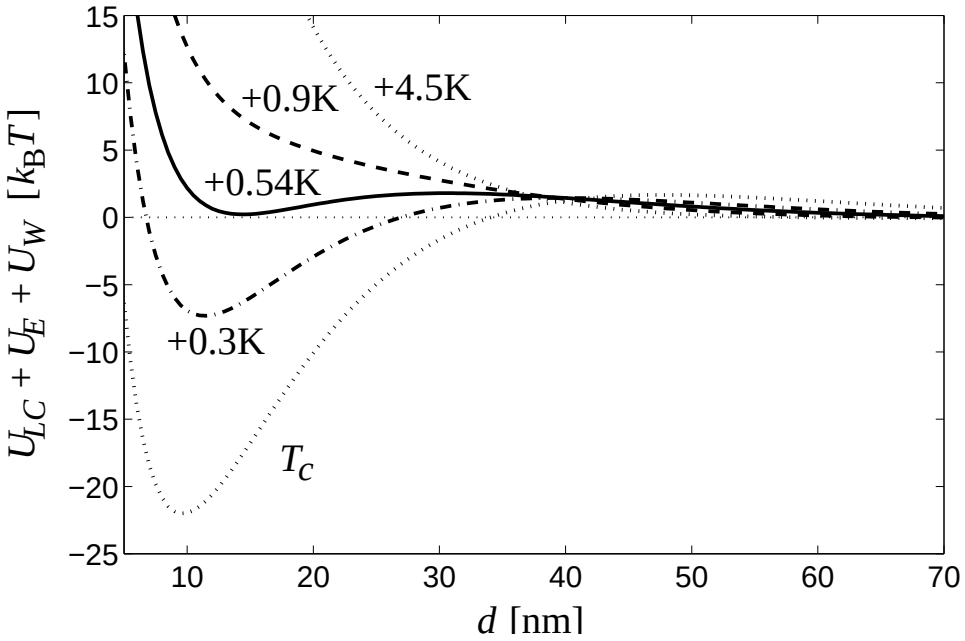


Figure 8.7: The total two-particle interaction $U_{LC} + U_E + U_W$ as a function of particle separation $d$ for various temperatures. A complete flocculation of the particles occurs within a temperature range of about 0.3 K. $q_s = 0.5 \cdot 10^4\, e_0/\mu\text{m}^2$, $\kappa^{-1} = 8.3\,\text{nm}$, and further parameters are chosen according to the text. From Ref. [35].

### 8.3.4 Flocculation versus Dispersion of Particles

In Fig. 8.7 we plot the total two-particle interaction $U_{LC} + U_E + U_W$ as a function of particle separation $d$ for various temperatures. We choose $q_s = 0.5 \cdot 10^4\, e_0/\mu\text{m}^2$ and $\kappa^{-1} = 8.3\,\text{nm}$. At 4.5 K above the transition temperature $T_c$, the dispersion is stable. With decreasing temperature, a potential minimum at finite separation develops. At $T_{FD} = T_c + 0.54\,\text{K}$, the particle doublet or aggregated state becomes energetically preferred. We call $T_{FD}$ the temperature of *flocculation transition*. Below $T_{FD}$, the probability of finding the particles in the aggregated state is larger than the probability that they are dispersed. Already at $T_c + 0.3\,\text{K}$ the minimum is $7\,k_B T$ deep, and all particles are condensed in aggregates. That means, within a temperature range of about 0.3 K there is an abrupt change from a completely dispersed to a fully aggregated system, reminiscent to the critical flocculation transition in colloidal dispersions employing polymeric stabilization [252, 306]. Between $d = 30\,\text{nm}$ and 50 nm, the two-particle interaction exhibits a small repulsive barrier of about $1.5\,k_B T$. Such barriers slow down the aggregation of particles, and one distinguishes between *slow* and *rapid flocculation*. The dynamics of rapid flocculation was first studied by Smoluchowski [328]. Fuchs extended the theory to include arbitrary interaction potentials [125]. However, only after Derjaguin and Landau [81] and Verwey and Overbeek [371] incorporated van der Waals and electrostatic interactions into the theory, became a comparison with experiments possible. In our case, the repulsive barrier

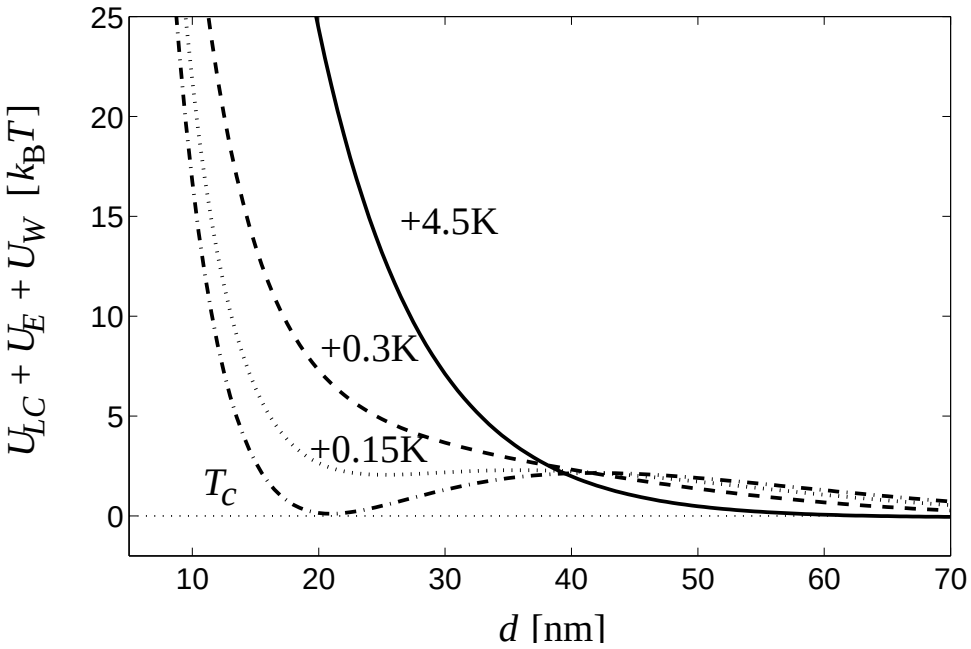


Figure 8.8: In comparison to Fig. 8.7 the surface-charge density is increased to $0.63 \cdot 10^4\, e_0/\mu\text{m}^2$. As a result, flocculation does not occur. From Ref. [35].

of $1.5\, k_\text{B}T$ slows down the doublet formation by a factor of three, *i.e.*, it does not change very dramatically if the barrier is reduced to zero.

If the surface-charge density $q_s$ is increased to $0.63 \cdot 10^4\, e_0/\mu\text{m}^2$, the dispersed state is thermodynamically stable at all temperatures above $T_c$, as illustrated in Fig. 8.8. An increase of the Debye length $\kappa^{-1}$, *i.e.*, the range of the electrostatic repulsion has the same effect. We define the "flocculation end line" as the border line in a $\kappa^{-1} - q_s$ diagram beyond which the dispersed state is thermodynamically stable for all temperatures above $T_c$.

In Fig. 8.9 we present flocculation phase diagrams as a function of temperature and surface-charge density for various Debye lengths $\kappa^{-1}$. The inset shows one such diagram for $\kappa^{-1} = 8.3\,\text{nm}$. The full line represents the flocculation temperature $T_{FD}$ as a function of $q_s$. For temperatures above $T_{FD}$, the particles stay dispersed while for temperatures below $T_{FD}$ the system is flocculated. To characterize the aggregated state further, we have determined lines in the phase diagram of $\kappa^{-1} = 8.3\,\text{nm}$, where the escape time $t_\text{esc}$ of Eq. (8.21) is, respectively, ten (dash-dotted) or hundred (dotted) times larger than in the case of zero interaction. These lines are close to the transition temperature $T_{FD}$, and indicate again that the transition from the dispersed to a completely aggregated state takes place within less than one Kelvin. The large plot of Fig. 8.9 illustrates the flocculation temperature $T_{FD}$ as a function of $q_s$ for various Debye lengths $\kappa^{-1}$. $T_{FD}$ increases when the strength ($q_s$) or the range ($\kappa^{-1}$) of the electrostatic repulsion is reduced. The intersections of the transition lines with the $T = T_c$ axis define the flocculation end line beyond which the system is always dispersed.

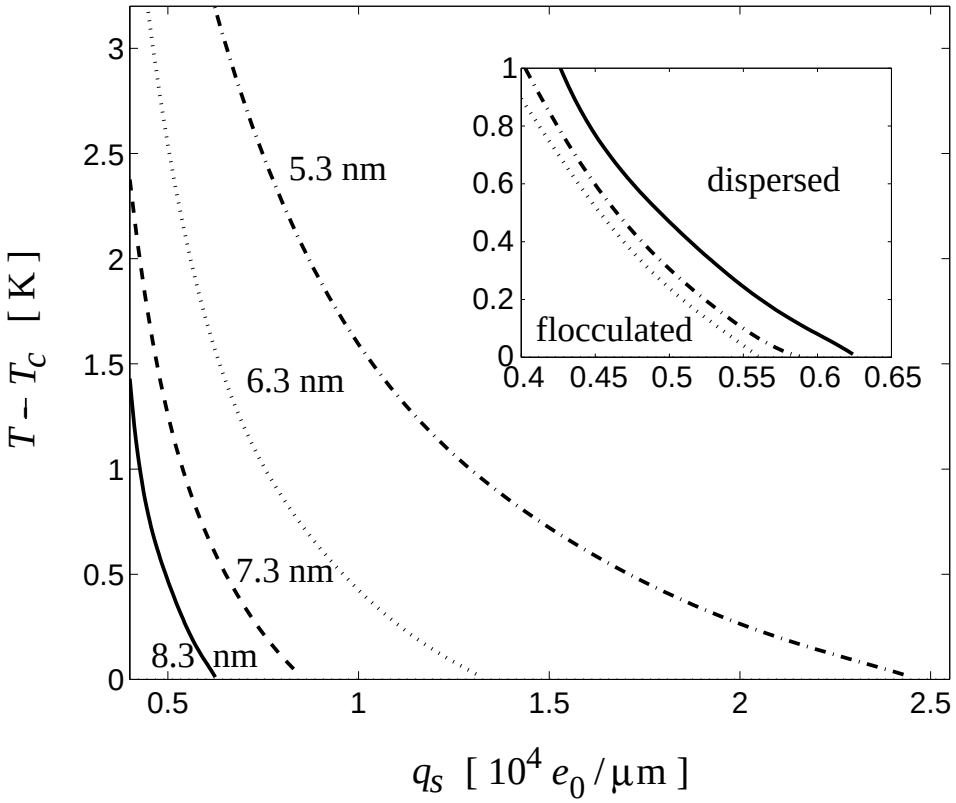


Figure 8.9: Flocculation phase diagrams as a function of temperature and surface-charge density for various Debye lengths $\kappa^{-1}$. Inset: Phase diagram for $\kappa^{-1} = 8.3\,\mathrm{nm}$. The full line represents the flocculation temperature $T_{FD}$ as a function of $q_s$. The dash-dotted and dotted lines indicate escape times from the minimum of the interparticle potential which are, respectively, ten or hundred times larger than in the case of zero interaction.

# Part III

# Multiple Light Scattering from Director Fluctuations

# Chapter 9

# Why Multiple Scattering of Light?

Transport processes in random media are essential for the understanding of many physical phenomena such as the scattering of electrons from impurities in a metal, the propagation of heat in solids, or the moderation of neutrons in a nuclear reactor. The transmission of sun light through clouds, the white appearance of milk, or basically all the visual perception of our natural environment is governed by multiply scattered light. Observable interference effects of light in random media, well-known as Anderson localization of electrons in disordered metals, are a fascinating topic which spawned a new research area for physicists dealing with light transport in disordered media. In Section 9.1 we review this area to give an impression about the variety of the physical ideas developed in recent years. Our presentation stresses the importance of diffusive light transport, which takes place in the limit of many scattering events disregarding any interference between light waves. In Section 9.2 we introduce the theory of radiative transfer to treat multiply scattered light and review the basic concepts of diffusing light in isotropic systems including its important application known as *diffusing-wave spectroscopy*. Section 9.2 serves as an introduction to the next chapter, where we generalize diffusive light transport to nematic liquid crystals.

## 9.1 Motivation

Fifteen years ago the discovery of coherent backscattering or weak localization of light in colloidal suspensions [184, 392, 358, 109] initiated a tremendous research activity on multiple scattering of light [321, 169, 223, 224, 322, 118]. Physicists were attracted by the possibility of achieving the equivalent to the Anderson localization of electrons in disordered solids [12]. Electrons diffusing through the solid are scattered by impurities. A coherent superposition of the electronic wave functions of a closed electron path and its time-reversed counterpart is always constructive [1, 202, 11]. This enhances the probability of the electron to return to its starting point, which in turn decreases the diffusion constant. In three dimensions, it takes a sufficient amount of disorder to finally localize the electronic wave function. Light that is exactly backscattered from a turbid medium constructively interferes with its time-reversed partner as well. Therefore the backscattered light inten-

sity is enhanced by a factor of two relative to the diffusive background. Soon after its discovery, weak localization of light was explained theoretically [141, 6, 353, 7] after some first approaches [78, 352]. Detailed studies of the backscattering cone, both theoretically and experimentally, followed [224]. They concentrated on the effect of polarization of light [342, 393, 297, 8], on a finite thickness of the scattering slab [110, 361], on absorption in the scattering medium [110, 393, 8], on broken time-reversal symmetry due to the Faraday effect in a magnetic field [219, 100, 203, 227, 368], and on chiral systems, which are optically active media [219]. In the case of finite thickness or absorption, long light paths are terminated, and as a result the backscattering intensity is decreased. The same happens for broken time-reversal or parity symmetry, where the phase relation between light paths and their time-reversed counterparts are gradually lost due to different phase velocities of left and right-circularly polarized light. The consequences of recurrent multiple scattering events [387] and amplifying random media [386] on the backscattering cone were published recently. A self-consistent theory for its enhancement factor exists [350]. The theoretical treatment of all these cases is mainly based on point-like scatterers and was performed within a diagrammatic approach to the two-particle electric Green function.

Strong localization of light was addressed theoretically by S. John in two elegant papers [167, 168], by P. W. Anderson [13], and others [324, 14, 333, 322]. After approaching the Anderson localization transition [130], it was first observed for microwaves in two [70] and three [136] dimensions, and it was recently reported in the near-visible range of light in semiconductor powders [384]. However, the latter experiment is controversial [313, 385].

The theoretical description of coherent backscattering employs the diffusion limit for multiply scattered light [141, 6, 7]. Photons are treated as classical random walkers with a random walk step $\ell^*$ indicating the path length a photon has to travel to randomize its initial direction. Once the diffusive light paths are known, their time-reversed counterparts can be included straightforwardly. The width of the backscattering cone turns out to be of the order of $\lambda/\ell^*$, where $\lambda$ is the wavelength of light. The onset of Anderson localization is given by the Ioffe-Regel criterion [164]: $2\pi\ell^*/\lambda \approx 1$.

In 1987 Wolf and Maret discovered that diffusing light in colloidal suspensions could be used for spectroscopy [226], which was later called diffusing-wave spectroscopy (DWS) by Pine *et al.* [270]. This was an important step forward since so far turbid systems could not be investigated with conventional single dynamic light scattering (DLS) [21]. In DWS temporal correlations of the detected light intensities decay much faster than in single scattering since phase shifts in the electric field waves, originating from many scattering events, are accumulated. Therefore, DWS detects dynamic phenomena at much shorter time scales than single light scattering does. This was also recognized in Ref. [298]. Within a diagrammatic approach, the principle of DWS was formulated by Golubentsev [141], Stephen [341], and by MacKintosh and John [220]. Reviews can be found in Refs. [271, 381, 224, 225]. For a collection of recent work see Ref. [400]. First measurements with DWS in a temporal range from 10 to 1000 $\mu$s detected the Brownian motion of suspended particles [226, 270]. Their sizes can be determined via the Stokes-Einstein formula (6.3) [272]. At very short time scales in dilute suspensions, the particles display hydrodynamic interactions with the surrounding fluid. Measuring at times smaller than 1 $\mu$s, a time-dependent self-

diffusion coefficient $D_B = D_{\rm B}^0\,(1 - c/\sqrt{t})$ was found [382] in agreement with theory. In concentrated colloids hydrodynamic interactions between the particles become important [404]. Their effect on the diffusion constant $D_{\rm B}^0$ was studied in Refs. [120, 285, 395]. Finally, the time dependence of $D_B(t)$ in concentrated suspensions was investigated [403, 171, 192]. A glass transition [232] and crystallization [308] in colloidal suspensions were recognized in DWS through a long-time tail in the electric field correlations. It was shown both theoretically and experimentally that DWS can be used to monitor laminar shear [394, 22, 23] and turbulent flow [24] in colloidal dispersions. Even ultrasonic modulation is visible [206]. Beyond colloids, DWS was applied to investigate bubble dynamics in foams [90, 91, 92, 144, 93, 94, 157, 158], shape fluctuations of emulsion droplets [129], viscoelasticity of complex fluids [229, 228], the dynamics of colloidal gels [180], magnetorheological fluids [126], and actin networks [137].

Diffusing light stimulated further fundamental and applied research, which we report in order. It can be employed to image objects in a turbid medium since the diffusing photon density wave is refracted at inhomogeneities in the diffusion constant [257, 31, 79]. Medical applications are explored to locate, *e.g.*, tumors in human tissue [399]. Dynamic correlations, too, are sensitive to the location of objects with different temporal response than the surrounding medium [30, 148, 150, 149, 32]. Finally, a more general approach to imaging through correlations in the intensity profile of transmitted light, called speckle pattern, was formulated by Berkovits and Feng [20].

The classical relation for the diffusion constant, $D = v_E \ell^*/3$, involves a velocity $v_E$. It normally coincides with the group velocity $v_g$ since it governs the transport of light pulses. However, it was shown that the energy transport velcocity $v_E$ deviates considerably from $v_g$ when strong resonant scattering, *e.g.*, in Mie scatterers occurs [359, 365, 366, 193]. The same effect for accoustic waves was discussed in Refs. [262, 317]. There, the authors argue that the energy and group velocity are very similar.

Tiggelen conjectured that light diffusion in Faraday-active media gives rise to a transversal light current under the action of a magnetic field [362]. This Photonic Hall effect was soon verified experimentally [294].

When a slab of turbid material is illuminated by a laser, the intensity profile of transmitted light exhibits a speckle pattern. A very fascinating topic are intensity-intensity correlations $C = \langle\, I(0)\, I(x)\,\rangle / \langle\, I(0)\,\rangle^2$ in this pattern, where $x$ refers to time, space, frequency shift, angle of incidence and detection, or magnetic field [343, 113, 112, 114]. Within the diffusion approximation, this correlation function is called $C_1$. It factorizes into electric field correlations, $C_1 = [\langle\, E(0)\, E(x)\,\rangle]^2 / \langle\, I(0)\,\rangle^2$, which decay exponentially. If one takes into account one crossing of the light paths, a correction $C_2$ smaller by a factor of $g$ occurs. However, $C_2$ is of longer range than $C_1$. The factor $g = N\ell^*/L \gg 1$ is denoted Thouless number, where $L$ is the thickness of the slab, $\ell^*$ is the transport mean free path, and $N$ is the number of possible light channels. $C_2$ was observed by several groups [357, 71, 344, 312]. Finally, two crossings in the light paths generate the so-called universal conductance fluctuations of light, abbreviated by $C_3$, which again is a factor of $g$ smaller than $C_2$ but decays on a longer range. These universal fluctuations are independent of the exact geometry of illumination and detection. They have their equivalent in electron

transport in disordered metals. Recently, Scheffold and Maret detected $C_3$ in an elegant experiment [314].

Photonic crystals are periodic dielectric structures, for which photonic bands can be calculated from Maxwell's theory in complete analogy to electrons in conventional crystals [166, 332, 26]. In 1987 Yablonovitch suggested that a photonic crystal with a complete band gap inhibits the spontaneous emission of excited atoms when the light frequency is situated in the band gap [396]. This opened up an exciting new field in quantum optic. At the same time, S. John argued that moderate disorder in such bandgap materials helps to localize light [168]. In the space around a point defect, light is constantly Bragg reflected and cannot leave the crystal. The existence of a photonic band gap in an fcc lattice was verified in calculations by Soukoulis *et al.* [156], and then fabricated by drilling holes in a slab of material following an idea of Yablonovitch [397]. This produced a band gap in the micro-wave regime. To shift the gap into the visible range of light, inverse opals, *i.e*, air spheres in a high dielectric like Titania are promising [388]. Possible applications [166] of photonic band gap materials are dielectric mirrors. Furthermore, the light mode of a single point defect might be used as a resonant cavity for laser systems, and a row of defects serves as a waveguide of micron-size.

So far we have been concentrating on isotropic systems. There are, however, many turbid materials such as thermotropic and lyotropic liquid crystals, liquid crystalline colloids [119, 174] and emulsions, and also muscle tissue that are anisotropic. In the following chapter it is our aim to develop a formalism that treats diffusive light transport and DWS in anisotropic media with special emphasis on nematic liquid crystals. Our work was inspired by recent experiments which measured coherent backscattering first in multi-domain nematics [373] and then in uniformly aligned samples [372]. Light diffusion and DWS was generalized by Lubensky and Stark [337, 338, 336, 334] and simultaneously by Tiggelen, Maynard, and Heiderich [367, 364, 151, 363]. For a review see Ref. [369]. Anisotropic light diffusion and correlation transport in nematic liquid crystals was demonstrated experimentally by Kao, Jester, Yodh, and Collings [170, 336]. An early formulation of radiative transfer theory in nematics, whose meaning will become clear in the following section, dates back to Romanov and Shalaginov [296]. A calculation of coherent backscattering from anisotropic scatterers, which might serve as a very crude approximation for multi-domain nematics, appeared recently [190]. We mention further studies of liquid crystals in the context of multiply scattered light. Bellini and Clark applied diffusing light to probe liquid crystal ordering in silica aerogels [18]. Čopič and Mertelj used DWS to analyze the orientational diffusion of nematic droplets in polymer dispersed liquid crystals [59]. Collings *et al.* reported the importance of multiple scattering in the exotic blue phase III [327]. Already several years ago photonic band calculations were presented for the cubic cholesteric blue phases by Hornreich, Shtrikman, and Sommers [160]. However, the dielectric contrast was too small to achieve a complete band gap. Self-assembling cubic emulsions, made from an isotropic fluid and a cholesteric nematic, were suggested as a candidate for a band gap material [161], and Busch and John presented band calculations in the inverse opal structure, where the voids are filled by a nematic [43].

## 9.2 Basic Principles of Diffusing Light

In this section we introduce the basic principles and main ideas of diffusing light in isotropic systems. We begin with a review of single dynamic scattering. It serves as an input for the radiative transfer theory which models the transport of light in turbid media. We illustrate how the diffusion approximation is extracted from the equation of radiative transfer. Finally, we explain the concept of DWS. It can be interpreted as "dynamic" absorption in the diffusive transport of temporal correlations in the electric light field. Simple examples help to work out the basic principles.

### 9.2.1 Single Scattering of Light

Light is scattered from inhomogeneities in the dielectric constant. For example, in colloidal dispersions a mismatch between the respective refractive indices of the dispersed particles and the solvent exists. In dynamic light scattering experiments one measures temporal autocorrelations in the scattered electric field, $\langle\, E_s(t)\, E_s(t')\,\rangle$, through time correlations in the light intensity. For simplicity, we treat the electric light field as a scalar quantity. Let $\boldsymbol{k} = (n\omega/c)\hat{\boldsymbol{k}}$ be the wave vector of the incoming light wave $E_0 \exp[i(\boldsymbol{k}\cdot\boldsymbol{r} - \omega t)]$, where $c$ denotes the vacuum speed of light, and $n$ is the average refractive index. Light is scattered once from an inhomogeneous medium of volume $V$ and observed at a distance $r \gg V^{1/3}$. The direction of the scattered light is specified by the wave vector $\boldsymbol{q} = (n\omega/c)\hat{\boldsymbol{q}}$. According to the weak-scattering or the first Born approximation, which treats the inhomogeneities $\delta\varepsilon(\boldsymbol{r}, t)$ in the dielectric constant as a perturbation, the temporal autocorrelations in the scattered electric field becomes

$$\langle\, E_s(t)\, E_s^*(0)\,\rangle = \frac{|E_0|^2 V}{(4\pi r)^2}\, B(\boldsymbol{q}_s, t) \;\;, \tag{9.1}$$

where $\boldsymbol{q}_s = \boldsymbol{q} - \boldsymbol{k}$ stands for the scattering vector. We have introduced the temporal autocorrelation function $B(\boldsymbol{q}_s, t)$ for the fluctuating part $\delta\varepsilon(\boldsymbol{r}, t)$ of the dielectric constant,

$$B(\boldsymbol{q}_s, t) = \frac{\omega^4}{c^4}\, \langle\, \delta\varepsilon(\boldsymbol{q}_s, t)\, \delta\varepsilon^*(\boldsymbol{q}_s, 0)\,\rangle \;\;, \tag{9.2}$$

and used the Fourier transform

$$\langle\, \delta\varepsilon(\boldsymbol{q}, t)\, \delta\varepsilon^*(\boldsymbol{q}, 0)\,\rangle = \int d^3r\, \langle\, \delta\varepsilon(\boldsymbol{r}, t)\, \delta\varepsilon(\boldsymbol{0}, 0)\,\rangle\, \exp(-i\boldsymbol{q}\cdot\boldsymbol{r}) \;\;. \tag{9.3}$$

We will often call $B(\boldsymbol{q}, t)$ the dynamic structure factor since it is directly related to the static and dynamical properties of the scattering medium. In dilute colloidal dispersions of identical particles, *e.g.*, $B(\boldsymbol{q}, t) = \frac{\omega^4}{c^4}\, F(\boldsymbol{q})\, S(\boldsymbol{q})\, \exp(-D_{\mathrm{B}} q^2 t)$. Here, the form factor $F(\boldsymbol{q})$ describes the scattering from a single particle, the static structure factor $S(\boldsymbol{q})$ is due to correlations between the scatterers, and the exponential factor results from Brownian motion characterized by the diffusion constant $D_{\mathrm{B}}$.

To derive an important length scale, we first introduce the *differential scattering cross section*

$$\frac{d\sigma}{d\Omega_{\boldsymbol{q}}} = \frac{V}{(4\pi)^2}\, B(\boldsymbol{q}-\boldsymbol{k},0) \ , \tag{9.4}$$

which provides the scattered light energy per unit time, per solid angle element $d\Omega_{\boldsymbol{k}}$, and per incident intensity $I_0 \propto |E_0|^2$. Given $I_0$, the total loss of energy per unit time follows from an angular integral of the last expression, called the *total scattering cross section* $\sigma$. Hence the loss per unit surface is,

$$\Delta I = -\frac{\sigma}{A}\, I_0 = -\frac{\sigma}{V}\, \Delta z\, I_0 \ , \tag{9.5}$$

where we have written $V = A \times \Delta z$. This formula suggests that the incident intensity decays exponentially with the thickness of the sample, $I = I_0 \, \exp(-\Delta z/\ell_S)$. The *scattering mean free path* or *extinction length* follows from

$$\frac{1}{\ell_S} = \frac{\sigma}{V} = \int \frac{d\Omega_{\boldsymbol{q}}}{(4\pi)^2}\, B(\boldsymbol{q}-\boldsymbol{k},0) \ . \tag{9.6}$$

Note that it does not take into account any multiply scattered light propagating along the initial direction. In the photon picture $\ell_S$ denotes the average path length a photon can travel without being scattered.

So far we did not specify the dynamic structure factor further. Since in isotropic systems all directions in space are equivalent, it can only depend on the *scattering angle* $\vartheta_s$ enclosed by $\boldsymbol{k}$ and $\boldsymbol{q}$. Therefore, we are allowed to replace the integration $\int d\Omega_{\boldsymbol{q}}/(4\pi)^2\, B(\boldsymbol{q}-\boldsymbol{k},t)$ by $\int d\cos\vartheta_s/(8\pi)\, B(\boldsymbol{q}-\boldsymbol{k},t)$. Furthermore, when expanded into spherical harmonics $Y_{lm}(\hat{\boldsymbol{k}})$ and $Y_{lm}(\hat{\boldsymbol{q}})$, the structure factor $B(\boldsymbol{q}-\boldsymbol{k},t)$ takes the form

$$B(\boldsymbol{q}-\boldsymbol{k},t) = \sum_l B_l(t) \sum_{l=-m}^{m} Y^*_{lm}(\hat{\boldsymbol{k}})\, Y_{lm}(\hat{\boldsymbol{q}}) \ . \tag{9.7}$$

### 9.2.2 Radiative Transfer Theory

In principle, multiple light scattering in a random medium can be treated rigorously. To do so, one starts from Maxwell's theory and calculates the averaged two-particle Green function of the electric light field with the help of diagrammatic techniques [124]. The diagrams include light paths which do not "interact" with each other, represented by the so-called *ladder diagrams*, and light paths which intersect that means which share some scattering events. These *crossed diagrams* involve a coherent superposition of the electric light field. The summation over all the diagrams can be performed by solving the Bethe-Salpeter equation for the two-particle Green function.

In the weak-scattering approximation, which we employ here, the most important contribution comes from light paths which do not intersect, *i.e.*, any coherent superposition is omitted. Then, the Bethe-Salpeter equation is equivalent to the radiative transfer theory

for the specific light intensity [48, 165, 360]. It models light transport in random or turbid media at length and time scales much larger than the wave length and period of light. It has a long-standing history, and dates back to the year 1905 when the astrophysicist Schuster [318] tried to understand light transport through the atmosphere of the earth.

We formulate the equation of radiative transfer for the following quantity:

$$W_{\hat{\boldsymbol{k}}}(\boldsymbol{R},T,t) = \langle\, E_{\hat{\boldsymbol{k}}}(\boldsymbol{R},T-t/2)\, E_{\hat{\boldsymbol{k}}}(\boldsymbol{R},T+t/2)\,\rangle \ . \tag{9.8}$$

For $t=0$, it stands for the energy density of a light wave at time $T$ and space point $\boldsymbol{R}$ travelling into a space direction specified by the unit vector $\hat{\boldsymbol{k}}$. The light frequency $\omega$ is omitted. Mathematically, $W_{\hat{\boldsymbol{k}}}(\boldsymbol{R},T,t)$ follows from a Wigner distribution of the electric light field, and our interpretation of $W_{\hat{\boldsymbol{k}}}(\boldsymbol{R},T,t)$ only makes sense when the variables $\boldsymbol{R}$ and $T$ refer to respective variations at length and time scales much larger than the wavelength and period of light. For $t\neq 0$, $W_{\hat{\boldsymbol{k}}}(\boldsymbol{R},T,t)$ describes the temporal autocorrelations in the electric light field. The equation of radiative transfer treats light as a classical particle without phase. It is a balance equation for $W_{\hat{\boldsymbol{k}}}(\boldsymbol{R},T,0)$, and it formally corresponds to the Boltzmann equation which balances the phase space distribution $f(\boldsymbol{r},\boldsymbol{p},T)$ of classical particles [291]. Generalized to the transport of temporal correlations, the equation of radiative transfer takes the form:

$$\left(\frac{n}{c}\,\frac{\partial}{\partial T} + \hat{\boldsymbol{k}}\cdot\boldsymbol{\nabla} + \frac{1}{\ell_S}\right) W_{\hat{\boldsymbol{k}}}(\boldsymbol{R},T,t) = \int \frac{d\Omega_{\boldsymbol{q}}}{(4\pi)^2}\, B(\boldsymbol{k}-\boldsymbol{q},t)\, W_{\hat{\boldsymbol{q}}}(\boldsymbol{R},T,t) + S_{\hat{\boldsymbol{k}}}(\boldsymbol{R},T) \ . \tag{9.9}$$

For $t\neq 0$ it does not appear in standard textbooks [48, 165, 360] but it is a straightforward outcome of the Bethe-Salpeter equation when restricted to the ladder diagrams. It is mentioned, *e.g.*, in Refs. [3, 87, 30]. The first term describes temporal variations of $W_{\hat{\boldsymbol{k}}}(\boldsymbol{R},T,t)$ due to time dependent light sources indicated by the source term $S_{\hat{\boldsymbol{k}}}(\boldsymbol{R},T)$. The second term involves the divergence of the Poynting vector $(c/n)\hat{\boldsymbol{k}}W_{\hat{\boldsymbol{k}}}(\boldsymbol{R},T,t)$ [194]. The correlation function $W_{\hat{\boldsymbol{k}}}(\boldsymbol{R},T,t)$ changes when there is a net flow of energy ($t=0$) or correlation ($t\neq 0$) out of the volume element around $\boldsymbol{R}$. The third and the fourth term refer to losses and gains due to scattering. The dynamical structure factor $B(\boldsymbol{k}-\boldsymbol{q},t)$ and the scattering mean free path have been introduced in Eqs. (9.2) and (9.6), respectively. There is one major difference compared to the Boltzmann equation. Since scattering of light takes place from inhomogeneities in $\varepsilon(\boldsymbol{r},t)$, the scattering terms are linear in $W_{\hat{\boldsymbol{k}}}(\boldsymbol{R},T,t)$. In the Boltzmann equation, however, the collision terms introduce non-linearities in $f(\boldsymbol{r},\boldsymbol{p},T)$. The solution of the equation of radiative transfer is very complicated. Even the famous *Milne problem*, *i.e.*, the transport of light through a slab of scalar point scatterers can only be solved numerically, even when reduced to a semi-infinite geometry [246, 360]. The radiative transfer theory applies to single scattering from a thin sample as well as to multiply scattered light. In the limit of a sufficiently large number of scattering events, it turns into a simple and familiar diffusion equation, to which a *dynamic absorption term* is added when temporal correlations are treated. The physical picture behind this equation is the following. After being scattered many times, a single photon has lost its memory for the initial direction. It therefore performs a classical random walk, whose distribution function obeys a diffusion equation. We will derive it in the next subsection.

We stress that the diffusion equation is a hydrodynamic limit of rigorous transport theory. Its validity is not restricted to radiative transfer. In principle, it can be derived from the Bethe-Salpeter equation in the presence of crossed diagrams, *i.e*, the coherent superposition of electric fields. Vollhard and Wölfle [374, 376] presented a self-consistent theory for the diffusion constant including the *most-crossed* diagrams, that means, the coherent superposition of electric-field paths and their time-reversed companions. They reduce the ability of the photon to diffuse around. The self-consistent theory was applied to the localization transition of electrons.

### 9.2.3 Diffusion Approximation

In this subsection we set $t = 0$ and concentrate on the transport of the energy density of light. The diffusion approximation is valid when the initial direction of single photons is randomized. That means, the angular dependence of $W_{\hat{\boldsymbol{k}}}(\boldsymbol{R}, T, 0)$ deviates only slightly from the equilibrium distribution of the photons which in isotropic system is not a function of $\hat{\boldsymbol{k}}$ (for anisotropic media see Section 10.2.1). We, therefore, write down an angular expansion of $W_{\hat{\boldsymbol{k}}}(\boldsymbol{R}, T, 0)$, keeping only the first two orders,

$$W_{\hat{\boldsymbol{k}}}(\boldsymbol{R}, T, 0) = \frac{1}{4\pi} W_0(\boldsymbol{R}, T, 0) + \frac{3}{4\pi} \frac{n}{c} \hat{\boldsymbol{k}} \cdot \boldsymbol{J}(\boldsymbol{R}, T, 0) + \dots \quad . \tag{9.10}$$

The first term on the right-hand side introduces the total energy density

$$W_0(\boldsymbol{R}, T, 0) = \int d\Omega_{\boldsymbol{k}} \, W_{\hat{\boldsymbol{k}}}(\boldsymbol{R}, T, 0) \quad , \tag{9.11}$$

for which we will establish the diffusion equation. The second term is fixed by the requirement that an angular integration over the Poynting vector $(c/n)\hat{\boldsymbol{k}} W_{\hat{\boldsymbol{k}}}(\boldsymbol{R}, T, 0)$ must yield the total energy current density $\boldsymbol{J}(\boldsymbol{R}, T, 0)$,

$$\boldsymbol{J}(\boldsymbol{R}, T, 0) = \int d\Omega_{\boldsymbol{k}} \, \frac{c}{n} \, \hat{\boldsymbol{k}} \, W_{\hat{\boldsymbol{k}}}(\boldsymbol{R}, T, 0) \quad . \tag{9.12}$$

From a mathematical point of view, Eq. (9.10) corresponds to an expansion into spherical harmonics of angular momentum $l = 0$ and 1. The latter are represented by $\hat{\boldsymbol{k}} = (\sin\vartheta_{\boldsymbol{k}} \cos\varphi_{\boldsymbol{k}}, \sin\vartheta_{\boldsymbol{k}} \sin\varphi_{\boldsymbol{k}}, \cos\vartheta_{\boldsymbol{k}})$.

If we integrate the transport equation (9.9) for $t = 0$ over all directions of $\hat{\boldsymbol{k}}$, the continuity equation for the total energy density $W_0(\boldsymbol{R}, T, 0)$ results,

$$\frac{\partial}{\partial T} W_0(\boldsymbol{R}, T, 0) + \boldsymbol{\nabla} \cdot \boldsymbol{J}(\boldsymbol{R}, T, 0) = \text{source} \quad . \tag{9.13}$$

Furthermore, Fick's first law can be extracted from the equation of radiative transfer. It relates $\boldsymbol{J}(\boldsymbol{R}, T, 0)$ to the gradient of $W_0(\boldsymbol{R}, T, 0)$,

$$\boldsymbol{J}(\boldsymbol{R}, T, 0) = -D \, \boldsymbol{\nabla} W_0(\boldsymbol{R}, T, 0) \quad . \tag{9.14}$$

Any $\hat{\boldsymbol{k}}$ dependence in the source term $S_{\hat{\boldsymbol{k}}}(\boldsymbol{R},T)$ is omitted since it should already provide diffusing light. The diffusion constant obeys the classical relation

$$D = \frac{1}{3}\,\frac{c}{n}\,\ell^* \qquad \text{with} \qquad \frac{1}{\ell^*} = \int \frac{d\cos\vartheta_s}{8\pi}\,(1-\cos\vartheta_s)\,B(\boldsymbol{k}-\boldsymbol{q},0)\ . \tag{9.15}$$

The length $\ell^*$ denotes the *transport mean free path*. In isotropic systems $D$ must be a scalar quantity. It is calculated when the transport equation is projected on $\cos\vartheta_{\boldsymbol{k}} = \cos(\hat{\boldsymbol{k}}\cdot\boldsymbol{J})/J$.[1] Combining Eqs. (9.13) and (9.14), we finally arrive at the diffusion equation for $W_0(\boldsymbol{R},T,0)$:

$$\left[\frac{\partial}{\partial T} - D\,\boldsymbol{\nabla}^2\right] W_0(\boldsymbol{R},T,0) = \text{source}\ . \tag{9.16}$$

It is an exact outcome of the transport equation. As a result of the isotropic symmetry, only the zeroth and first angular moments of $B(\boldsymbol{k}-\boldsymbol{q},0)$ contribute to the diffusion constant of Eq. (9.15). The transport mean free path is often referred to the scattering mean free path:

$$\frac{\ell_S}{\ell^*} = \frac{\int d\cos\vartheta_s\,(1-\cos\vartheta_s)\,B(\boldsymbol{k}-\boldsymbol{q},0)}{\int d\cos\vartheta_s\,B(\boldsymbol{k}-\boldsymbol{q},0)} \equiv \langle\,1-\cos\vartheta_s\,\rangle\ . \tag{9.17}$$

The brackets denote an average over all possible scattering events, which is performed with the help of a normalized structure factor $B(\boldsymbol{k}-\boldsymbol{q},0)/\int d\cos\vartheta_s\,B(\boldsymbol{k}-\boldsymbol{q},0)$ called *phase function* [165, 360]. The transport mean free path is the average step length of a random walker. That means, it is the path length a photon has to travel before its direction is completely randomized. For isotropic scattering, $B(\boldsymbol{k}-\boldsymbol{q},0) = \text{const.}$, and $\ell^* = \ell_S$. On the other hand, for anisotropic scattering the photons have to be scattered several times to randomize their inital direction, and $\ell^* > \ell_S$. The quantity $c/n$ in the diffusion constant normally refers to the group velocity. However, if the fluctuations in the dielectric constant become larger or if resonances in Mie scatterers occur, an *energy velocity* $v_E$ has to be introduced in $D$ which deviates from the group velocity [359].

Alternatively, the diffusion approximation is identified as a diffusion pole in the two-particle Green function, and the diffusion constant is expressed by means of the Kubo-Greenwood formula [221].

The formulation of the boundary condition for diffusing light poses an interesting problem [246, 165]. The transition to diffusing light takes place *in* the turbid medium. Hence, it makes sense to demand that it does not enter the system from outside, *i.e.*, $W_{\hat{\boldsymbol{k}}}(\boldsymbol{R},T,0) = 0$ for all directions $\hat{\boldsymbol{k}}$ pointing into the medium. Since the angular profile of $W_{\hat{\boldsymbol{k}}}(\boldsymbol{R},T,0)$ is fixed by Eq. (9.10), this condition cannot be fulfilled for all $\hat{\boldsymbol{k}}$ simultaneously. Therefore we content ourselves with the approximate condition that the total diffusive energy flux

[1] To arrive at the expression of $\ell^*$, one has to evaluate $\int d\Omega_{\boldsymbol{k}} d\Omega_{\boldsymbol{q}}\,\cos\vartheta_{\boldsymbol{k}} B(\boldsymbol{k}-\boldsymbol{q},0)\cos\vartheta_{\boldsymbol{q}}$. This can be done with the help of Eq. (9.7) and the addition theorem $\sum_{m=-l}^{m=l} Y^*_{lm}(\hat{\boldsymbol{k}})\,Y_{lm}(\hat{\boldsymbol{q}}) = 4\pi P_l(\hat{\boldsymbol{k}}\cdot\hat{\boldsymbol{q}})/(2l+1)$ or, alternatively, by applying a trick. Note that in an isotropic system $\int d\Omega_{\boldsymbol{k}} d\Omega_{\boldsymbol{q}}\,\hat{\boldsymbol{k}}\otimes\hat{\boldsymbol{q}}\,B(\boldsymbol{k}-\boldsymbol{q},0)$ must be proportional to the unit tensor. Then one can write $\int d\Omega_{\boldsymbol{k}} d\Omega_{\boldsymbol{q}}\,\cos\vartheta_{\boldsymbol{k}} B(\boldsymbol{k}-\boldsymbol{q},0)\cos\vartheta_{\boldsymbol{q}} = \mathrm{tr}[\int d\Omega_{\boldsymbol{k}} d\Omega_{\boldsymbol{q}}\,\hat{\boldsymbol{k}}\otimes\hat{\boldsymbol{q}}\,B(\boldsymbol{k}-\boldsymbol{q},0)]/3 = 8\pi^2\int d\cos\vartheta_s\,\cos\vartheta_s\,B(\boldsymbol{k}-\boldsymbol{q},0)/3$.

into the medium is zero,

$$\int_{-1}^{0} \frac{c}{n}\,(\hat{\boldsymbol{\nu}}\cdot\hat{\boldsymbol{k}})\;W_{\hat{\boldsymbol{k}}}(\boldsymbol{R},T,0)\;d(\hat{\boldsymbol{\nu}}\cdot\hat{\boldsymbol{k}})=0\;, \tag{9.18}$$

where $\hat{\boldsymbol{\nu}}$ denotes the surface normal directed outward. Evaluating the integral with the help of the angular profile of $W_{\hat{\boldsymbol{k}}}(\boldsymbol{R},T,0)$, one arrives at the following boundary condition:

$$W_0(\boldsymbol{R},T,0)=-\frac{2}{3}\,\ell^*\,\hat{\boldsymbol{\nu}}\cdot\boldsymbol{\nabla}W_0(\boldsymbol{R},T,0)\;. \tag{9.19}$$

Close to the surface within a layer of thickness $\ell^*$, light is not in the diffusion limit, and the angular profile of Eq. (9.11) cannot really be applied. However, calculations involving the exact transport equation (9.9) only reveal small deviations from Eq. (9.11), and as a result the factor 2/3 in the boundary condition is replaced by 0.7104. If we assume further that $W_0(\boldsymbol{R},T,0)$ is a linear function in $\boldsymbol{R}$, we arrive at the alternative boundary condition, $W_0(\boldsymbol{R},T,0)=0$ at a distance of $2\ell^*/3$ from the surface of the medium.

Let us illustrate the diffusion approximation for a simple but instructive geometry. We assume a slab of turbid medium whose bounding surfaces are located at $z=0$ and $L$ and which is infinitely extended in the $x$ and $y$ direction. The incident light at $z=0$ is a plane wave. Its initial direction will be randomized at a location $z_0\approx\ell^*$ inside the slab, and in the simplest approximation the plane wave produces a delta shaped source for diffusing light at $z_0\approx\ell^*$. Hence, in the stationary case we have to fulfill the following equation together with the boundary conditions at $z=0,L$:

$$\frac{\partial^2}{\partial z^2}\,W_0(z)=-S_0\delta(z-z_0)\qquad\text{and}\qquad W_0(z)|_{z=0,L}=\pm\frac{2}{3}\,\ell^*\,\frac{\partial}{\partial z}\,W_0(z)\bigg|_{z=0,L}\;, \tag{9.20}$$

where the upper/lower sign in the boundary condition corresponds to $z=0/L$. As usual, Eq. (9.20) is solved by a sum of a particular solution (*i.e.*, the Green function in our case) and a general solution of the homogeneous equation:

$$W_0(z)=-\frac{S_0}{2}\,|z-z_0|+C_1z+C_2\;. \tag{9.21}$$

The free parameters $C_1$ and $C_2$ are determined by the boundary conditions:

$$C_1=\frac{S_0}{2}\,\frac{L-2z_0}{L+4\ell^*/3}\qquad\text{and}\qquad C_2=S_0\left(\frac{\ell^*}{3}+\frac{z_0}{2}\right)+\frac{S_0\ell^*}{3}\,\frac{L-2z_0}{L+4\ell^*/3}\;. \tag{9.22}$$

For the energy densities at $z=L$ and 0, we find

$$W_0(L)=\frac{2S_0}{3}\left(z_0+\frac{2}{3}\,\ell^*\right)\frac{\ell^*}{L}\qquad\text{and}\qquad W_0(0)=\frac{2}{3}\,S_0\,\ell^*-W_0(L)\;. \tag{9.23}$$

Note that $W_0(L)$ fulfills an Ohmic law. That means, the transmitted energy density decreases with the inverse slab thickness $L^{-1}$. The length scale is set by $\ell^*$. For a semi-infinite system ($L\to\infty$), all the light is backscattered. Finally, together with the angular

distribution (9.11) and the boundary condition, we obtain the universal transmission profile through a slab of turbid medium,

$$T(\theta, L) = \frac{c}{n} W_{\hat{\boldsymbol{k}}}(L) = \frac{c}{n} \frac{W_0(L)}{4\pi} \left(1 + \frac{3}{2} \cos\theta\right) \quad , \tag{9.24}$$

where $\cos\theta = \hat{\boldsymbol{k}} \cdot \hat{\boldsymbol{\nu}}$. The Ohmic law of Eq. (9.23) is a universal feature of light transmission and not restricted to special light sources. To see that we approximate $\partial W_0/\partial z$ by $[W_0(L) - W_0(0)]/L$ and use the boundary condition of Eqs. (9.20) to arrive at $W_0(L)/W_0(0) \approx 2\ell^*/(3L)$.

We finish the discussion of the diffusion approximation with an estimate. We are interested in the average number $N$ of scattering events of a photon that diffuses through a slab of thickness $L$. On average, a photon needs the time $t = L^2/(2D)$ to diffuse a distance $L$ along the $z$ axis. With $D = \frac{1}{3}\frac{c}{n}\ell^*$ and $t = N\ell_S/\frac{c}{n}$, we arrive at $N \approx L^2/(\ell^*\ell_S)$, which corresponds to an average path length of $L^2/\ell^*$.

### 9.2.4 Diffusing-Wave Spectroscopy

We now explain how diffusing light is used for spectroscopy. We allow $t \neq 0$ in the equation of radiative transfer, *i.e.*, we consider the transport of electric field correlations. The relative time $t$ should be smaller than the typical time scale $\tau_c$ of the dynamics of the investigated system, so that the dynamic structure factor satisfies

$$\frac{B(\boldsymbol{k} - \boldsymbol{q}, 0) - B(\boldsymbol{k} - \boldsymbol{q}, t)}{B(\boldsymbol{k} - \boldsymbol{q}, 0)} \ll 1 \qquad \text{for} \qquad t \ll \tau_c \ . \tag{9.25}$$

Analogous to Eq. (9.10), we formulate an angular expansion for $t \neq 0$ and introduce the total autocorrelation function $W_0(\boldsymbol{R}, T, t)$ and total current $\boldsymbol{J}(\boldsymbol{R}, T, t)$ of electric field correlations. Repeating the derivation of the continuity equation (9.13), we obtain

$$\left[\frac{\partial}{\partial T} + \mu(t)\right] W_0(\boldsymbol{R}, T, t) + \boldsymbol{\nabla} \cdot \boldsymbol{J}(\boldsymbol{R}, T, t) = \text{source} \ . \tag{9.26}$$

A *dynamic absorption* term $\mu(t)\, W_0(\boldsymbol{R}, T, t)$ is added which means that temporal correlations are not conserved quantities because they decay to zero. The *dynamic absorption coefficient* $\mu(t)$ generally follows from an angular average over all dynamic modes of the system,

$$\mu(t) = \frac{c}{n} \frac{1}{8\pi} \int d\cos\vartheta_s \, [B(\boldsymbol{k} - \boldsymbol{q}, 0) - B(\boldsymbol{k} - \boldsymbol{q}, t)] \ . \tag{9.27}$$

For dilute colloidal suspensions with $B(\boldsymbol{q}, t) = \frac{\omega^4}{c^4} F(\boldsymbol{q})\, S(\boldsymbol{q}) \exp(-D_{\mathrm{B}} q^2 t)$, we find $\mu(t) = 2D_B t\omega^2/(\ell^* \frac{c}{n})$. Fick's law of Eq. (9.14) is still valid with neglible corrections of the order of $[B(\boldsymbol{k} - \boldsymbol{q}, 0) - B(\boldsymbol{k} - \boldsymbol{q}, t)]/B(\boldsymbol{k} - \boldsymbol{q}, 0) \ll 1$, and we arrive at a diffusion approximation with "dynamic" absorption,

$$\left[\frac{\partial}{\partial T} - D\, \boldsymbol{\nabla}^2 + \mu(t)\right] W_0(\boldsymbol{R}, T, t) = \text{source} \ . \tag{9.28}$$

Let us discuss the contents of this equation by comparing it to a dynamic single scattering experiment. There, the electric field correlations decay on the characteristic time scale $\tau_c$ of the dynamic structure factor [see Eq. (9.1)] determined by the dynamic modes of the system. For a dilute suspension of colloidal particles, $\tau_c^{-1} = D_{\rm B}\omega^2/(c/n)^2$, which is the average time a Brownian particle needs to diffuse one wavelength of light. Due to the motion of the particles, the scattered electric fields $E_s(0)$ and $E_s(\tau_c)$ of one particular light path obtain a relative phase shift of the order of $\pi$. By averaging over an ensemble of light paths, this leads to a significant decay of the autocorrelation function $\langle E_s(0)\, E_s(\tau_c)\rangle$. When light is diffusing through a slab of turbid material of thickness $L$, it experiences approximately $N = L^2/(\ell^*\ell_S)$ scattering events which all contribute to the relative phase shift of $E_s(0)$ and $E_s(t)$. Therefore, we expect the autocorrelation function $\langle E_s(0)\, E_s(t)\rangle$ to decay exponentially at a time scale of the order of $\tau_c/N$. We will improve this estimate in the next paragraph. To summarize, we realize that diffusing-wave spectroscopy allows to study the dynamics of systems at much smaller time scales than single scattering does.

The physical picture of diffusing-wave spectroscopy, reviewed in the last paragraph, was developed by Maret and Wolf [226]. To arrive at the time correlation function $W_0(\boldsymbol{R}, T, t)$, they summed up all the correlation functions for different light paths. We now demonstrate that their final expression follows directly from Eq. (9.28). We assume a continuous light source which does not vary in time $T$. Hence, a steady-state light field with a temporal correlation function $W_0(\boldsymbol{R}, t)$ develops. The stationary diffusion equation, $[-D\,\boldsymbol{\nabla}^2 + \mu(t)]\, W_0(\boldsymbol{R}, t) = \text{source}$, can be considered as the Laplace transform of

$$\left[-D\,\boldsymbol{\nabla}^2 + \frac{\partial}{\partial\tau}\right] P(\boldsymbol{R}, \tau) = \delta(\tau) \times \text{source} \ , \tag{9.29}$$

where the normalized autocorrelation function is the Laplace transform of $P(\boldsymbol{R}, \tau)$,

$$\frac{W_0(\boldsymbol{R}, t)}{W_0(\boldsymbol{R}, 0)} = \int_{-0}^{\infty} P(\boldsymbol{R}, \tau)\, \exp[-\mu(t)\tau]\, d\tau \ . \tag{9.30}$$

The lower limit $-0$ means a small negative time $\tau$ in order to pick up the $\delta$ function. The meaning of $P(\boldsymbol{R}, \tau)$ is clarified by Eq. (9.29). At $\tau = 0$ a light pulse initiates different diffusive light paths. Then, $P(\boldsymbol{R}, \tau)$ represents the probability for a photon to arrive at a space point $\boldsymbol{R}$ after travelling through the turbid medium during a time $\tau$ along a path of length $s = \tau c/n$. The normalized correlation function (9.30) is a superposition of all light paths ending at $\boldsymbol{R}$ and having different path lengths $\tau c/n$. Each light path influences the correlation function according to its length. The inverse absorption coefficient, $\mu(t)^{-1}$, defines a characteristic travel time for the photons, beyond which the dephasing in the scattered electric fields contributes to the decay of the electric field correlations. Note that the *dephasing time* $\mu(t)^{-1}$ is infinite for $t = 0$ and decreases for increasing $t$. That means, the longer light paths probe the dynamics of the system at shorter time scales while shorter light paths are more sensitive to longer time scales, but still within $t \ll \tau_c$. When applied to dilute colloidal suspensions, we can write the exponent in Eq. (9.30) as $\mu(t)\tau = 2t/\tau_c \times \frac{c}{n}\tau/\ell^*$. We realize that the number $\frac{c}{n}\tau/\ell^*$ of random-walk steps in a light

path determines the decay of the electric field correlations and not the number of scattering events, as crudely estimated in the preceding paragraph. The correlation function decays, on average, by $\exp(-2t/\tau_c)$ per step.

The exact correlation function for a slab of thickness $L$ in either transmission or reflection requires the solution of Eq. (9.28) under the boundary condition of the previous section, which are still valid. Different steady-state light sources are used; plane waves, point sources, and an incident beam with Gaussian cross-section. A good review is given in Ref. [381]. The solution for plane waves in transmission is

$$\frac{W_0(L,t)}{W_0(L,0)} = \frac{L/L_\phi}{\sinh(L/L_\phi)} \qquad \text{with} \qquad L_\phi = \sqrt{D\mu(t)^{-1}} \ . \tag{9.31}$$

It is only valid for $t \ll \tau_c$ in agreement with the constraint (9.25). As long as $L < L_\phi$, we obtain $\log[W_0(L,t)/W_0(L,0)] \sim L^2/l_\phi^2 \sim -t/t_T$, going over into $\log[W_0(L,t)/W_0(L,0)] \sim \frac{1}{2}\log(t/t_T) - \sqrt{t/t_T}$ as $L > L_\phi$. Here we have introduced the typical time scale for transmission $t_T \approx \tau_c/(L/\ell^*)^2 \ll \tau_c$, *i.e.*, $\tau_c$ divided by the number of random walk steps. The last function is approximately linear in $t/t_T$, exhibiting a slightly positive curvature. In reflection from a semi-infinite slab, one finds again for $t \ll \tau_c$

$$\frac{W_0(L,t)}{W_0(L,0)} = \exp(z_0/L_\phi) \sim \exp\left(-\sqrt{t/t_R}\right) \qquad \text{with} \qquad t_R \sim \tau_c \ . \tag{9.32}$$

There is no characteristic path length of the light. Instead, the stretched exponential form in Eq. (9.32) reflects the wide distribution of decay times, which, in turn, results from the wide distribution of path lengths inherent in the backscattering geometry. The length $z_0 \approx \ell^*$ was introduced in the previous subsection in connection with the plane-wave light source. If the slab has a finite thickness, light on very long paths cannot return. As a result, for $t \to 0$ the normalized correlation function $W_0(L,t)/W_0(L,0)$ decays more weakly than indicated in Eq. (9.32).

# Chapter 10

# Light Diffusion in Nematic Liquid Crystals

The spontaneously broken rotational symmetry in liquid crystals has two important consequences compared to isotropic systems. It leads to birefringence in light propagation, with the optical axis given by the director, and it implies the existence of hydrodynamic Goldstone modes, which we introduced in Section 1.4 as director modes. In this chapter we develop the concept of diffusing light for a uniformly aligned nematic crystal. It scatters light due to thermal fluctuations of the local optical axis which introduces a rather different scattering mechanism in comparison with colloidal suspensions. Our final result is a generalization of the diffusion equation with dynamic absorption expressed in Eq. (9.28). We obtain two independent diffusion constants $D_\parallel$ and $D_\perp$ for light diffusing, respectively, parallel and perpendicular to the equilibrium director. The diffusion constants are connected to the elastic and dielectric properties of the nematic phase. The dynamic absorption coefficient is still a scalar, and it appears as an angular average over the inverse viscosities of all director modes. Our presentation is analogous to the previous chapter. We first explain light propagation and single scattering in Section 10.1. Then we derive the diffusion approximation with the help of the radiative transfer theory in Section 10.2.

## 10.1 Light Propagation and Single Scattering in Nematic Liquid Crystals

To treat multiple scattering of light, we have to understand single scattering events and how light propagates between them. We discuss both issues for nematics in the next two subsections. Propagation of light and its scattering is governed by the dielectric properties of a system. In a nematic liquid crystal the local dielectric tensor takes the form

$$\boldsymbol{\varepsilon}(\boldsymbol{r},t) = \varepsilon_\perp \mathbf{1} + \Delta\varepsilon[\boldsymbol{n}(\boldsymbol{r},t) \otimes \boldsymbol{n}(\boldsymbol{r},t)] \ , \tag{10.1}$$

in complete analogy to the tensor of magnetic susceptibility of Eq. (1.7). We have introduced the dielectric anisotropy $\Delta\varepsilon = \varepsilon_\parallel - \varepsilon_\perp$, where $\varepsilon_\parallel$ and $\varepsilon_\perp$ denote dielectric constants

for electric fields applied, respectively, parallel or perpendicular to the director. Scattering takes place from inhomogeneities in the dielectric tensor. As we discussed in Section 1.4, in a uniformly aligned sample thermally induced fluctuations of the director about its equilibrium value $\boldsymbol{n}_0$ exist. They give rise to fluctuations in the local dielectric tensor which in turn scatter light. This is the physical process for which we will formulate the theory of multiple scattering. Since director fluctuations are long-range correlated and characterized by sinusoidal variations in space, light is scattered from some sort of grating rather than single particles like in colloidal suspensions. However, we will identify some analogy between both scattering mechanisms in the course of this section.

### 10.1.1 Light Propagation in a Homogeneous Nematic

A homogeneous nematic is a uniaxial medium and therefore birefringent for light travelling inside. Light propagates through such a system in two characteristic modes. The ordinary light ray behaves as in an isotropic system. However, the extraordinary light mode possesses a direction-dependent index of refraction, its phase and group velocities differ from each other, and the electric field wave is not transverse. In the following we review these facts, look at the energy density and the Poynting vector, and introduce some notation for further use.

We consider the nematic liquid crystal as a dielectric medium characterized by the constitutive equations,

$$\boldsymbol{D}(\boldsymbol{r},t) = \boldsymbol{\varepsilon}(\boldsymbol{r},t)\boldsymbol{E}(\boldsymbol{r},t) \qquad \text{and} \qquad \boldsymbol{B}(\boldsymbol{r},t) = \boldsymbol{H}(\boldsymbol{r},t) \ . \tag{10.2}$$

The time dependence in these equations refers to slow (micro-second) temporal variations of the director and not to the fast (femto-second) cycles of the electromagnetic field. The magnetic permeability is basically unity in liquid crystals, and its effect can be totally neglected against the induced polarization described by the dielectric tensor. If electric charge and current densities are absent, light propagation is determined by the Maxwell wave equation for the electric light field $\boldsymbol{E}(\boldsymbol{r},t)$:

$$\left[\boldsymbol{\nabla}\times\boldsymbol{\nabla}\times + \frac{1}{c^2}\frac{\partial^2}{\partial t^2}\,\boldsymbol{\varepsilon}(\boldsymbol{r},t)\right]\boldsymbol{E}(\boldsymbol{r},t) = \boldsymbol{0} \ . \tag{10.3}$$

We first ignore fluctuations of the dielectric tensor to discuss light propagation in a homogeneous nematic. We adopt Eq. (10.1) with the equilibrium Frank director $\boldsymbol{n}_0$ and obtain the dielectric tensor $\boldsymbol{\varepsilon}_0$. Employing a plane-wave ansatz for the electric field,

$$\boldsymbol{E}(\boldsymbol{r},t) = E^{\alpha}\boldsymbol{e}_{\alpha}(\hat{\boldsymbol{k}})\exp[i(\boldsymbol{k}\cdot\boldsymbol{r}-\omega t)] \ , \tag{10.4}$$

the wave equation (10.3) is transformed into a generalized eigenvalue equation [194, 201, 338]

$$\left[(\mathbf{1}-\hat{\boldsymbol{k}}\otimes\hat{\boldsymbol{k}}) - \frac{1}{n_{\alpha}^2}\,\boldsymbol{\varepsilon}_0\right]\boldsymbol{e}_{\alpha}(\hat{\boldsymbol{k}}) = \boldsymbol{0} \ . \tag{10.5}$$

It determines the electric-polarization vector $\boldsymbol{e}_\alpha(\hat{\boldsymbol{k}})$ and a direction-dependent index of refraction

$$n_\alpha(\hat{\boldsymbol{k}}) = ck/\omega \tag{10.6}$$

for the three possible electric field modes. Due to Eq. (10.6), their wave number $k$ changes with the direction of propagation $\hat{\boldsymbol{k}}$ for fixed $\omega$. We refer to the field modes as ordinary ($\alpha = 2$), extraordinary ($\alpha = 1$), and longitudinal ($\alpha = 3$). The third solution corresponds to a non-propagating mode with $n_3 = \infty$ and $\boldsymbol{e}_3(\hat{\boldsymbol{k}})$ parallel to the wave vector $\boldsymbol{k}$. It will hardly be important for scattering at optical frequencies. We also define polarization vectors $\boldsymbol{d}^\alpha(\hat{\boldsymbol{k}})$ for the displacement field by

$$\boldsymbol{d}^\alpha(\hat{\boldsymbol{k}}) = \varepsilon_0 \boldsymbol{e}_\alpha(\hat{\boldsymbol{k}}) \ . \tag{10.7}$$

The dot product of the eigenvalue equation (10.5) with $\boldsymbol{k}$ results in $\boldsymbol{k}\cdot\boldsymbol{d}^\alpha(\hat{\boldsymbol{k}}) = 0$ confirming the transversality of the displacement field as it should be. With the help of Eq. (10.5), one proves a duality relation between the polarization vectors $\boldsymbol{d}^\alpha(\hat{\boldsymbol{k}})$ and $\boldsymbol{e}_\beta(\hat{\boldsymbol{k}})$. That means, their magnitudes can be chosen to satisfy the biorthogonality relation [201]

$$\boldsymbol{d}^\alpha(\hat{\boldsymbol{k}}) \cdot \boldsymbol{e}_\beta(\hat{\boldsymbol{k}}) = \delta^\alpha_\beta \ , \tag{10.8}$$

in complete analogy to the basis vectors of the real and reciprocal lattice in a crystal. From the last two relations it is obvious that neither $\boldsymbol{d}^\alpha$ nor $\boldsymbol{e}_\alpha$ are unit vectors. They scale, respectively, with the index of refraction or its inverse. This is convenient for expressing energy densities and intensities of light modes in terms of field amplitudes $E^\alpha$, as we will see below. Also, the theory of multiple light scattering involves several tensor quantities for which the two sets of polarization vectors proved to be very useful [338].

A first solution to the eigenvalue equation (10.5) is obvious and gives the ordinary light ray. It possesses an index of refraction

$$n_2 = \sqrt{\varepsilon_\perp} \tag{10.9}$$

and polarization vectors

$$\boldsymbol{e}_2(\hat{\boldsymbol{k}}) = \frac{1}{n_2}\hat{\boldsymbol{u}}_2(\hat{\boldsymbol{k}}) \qquad \text{and} \qquad \boldsymbol{d}^2(\hat{\boldsymbol{k}}) = n_2\hat{\boldsymbol{u}}_2(\hat{\boldsymbol{k}}) \ , \tag{10.10}$$

where the unit vector $\hat{\boldsymbol{u}}_2(\hat{\boldsymbol{k}})$ is perpendicular to both the Frank director $\boldsymbol{n}_0$ and the wave vector $\boldsymbol{k}$, enclosing the angle $\vartheta$ (see Fig. 10.1). Then the second solution, the extraordinary light ray, can be constructed. The polarization vectors are situated in the plane spanned by $\boldsymbol{n}_0$ and $\boldsymbol{k}$:

$$\boldsymbol{d}^1(\hat{\boldsymbol{k}}) = n_1(\hat{\boldsymbol{k}})\,[-\sin\vartheta\boldsymbol{n}_0 + \cos\vartheta\hat{\boldsymbol{u}}_1(\hat{\boldsymbol{k}})] \tag{10.11}$$

and

$$\boldsymbol{e}_1(\hat{\boldsymbol{k}}) = n_1(\hat{\boldsymbol{k}})\left[-\frac{\sin\vartheta}{\varepsilon_\parallel}\boldsymbol{n}_0 + \frac{\cos\vartheta}{\varepsilon_\perp}\hat{\boldsymbol{u}}_1(\hat{\boldsymbol{k}})\right] \ , \tag{10.12}$$

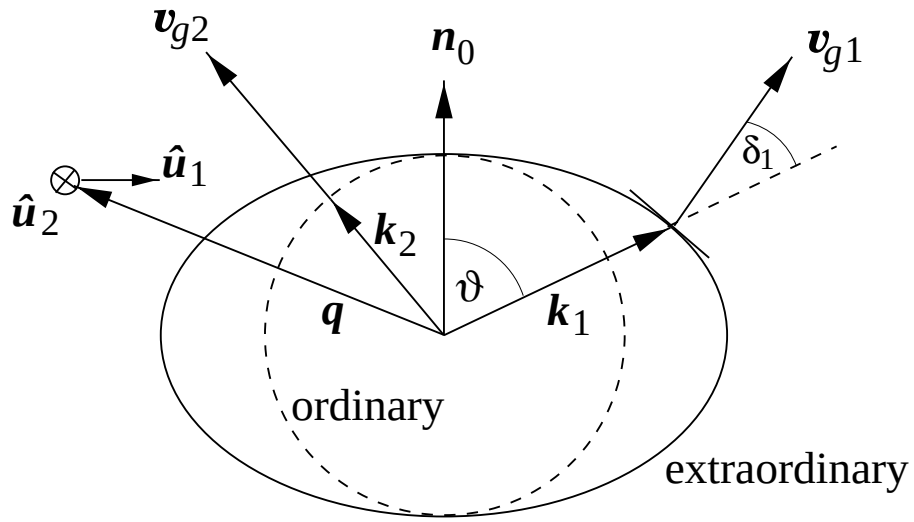


Figure 10.1: Constant-frequency surface for ordinary and extraordinary light rays, seen in the plane spanned by the optical axis ($\boldsymbol{n}_0$) and the wave vector. The ordinary light ray has a constant index of refraction $\sqrt{\varepsilon_\perp}$. The wave vector $\boldsymbol{k}_2$ and the group velocity $\boldsymbol{v}_{g2}$ are parallel to each other. The extraordinary wave has an ellipsoidal index of refraction which equals $\sqrt{\varepsilon_\perp}$ only along the optical axis; $\boldsymbol{k}_1$ and $\boldsymbol{v}_{g1}$ enclose an angle $\delta_1$. The figure corresponds to a positive dielectric anisotropy ($\Delta\varepsilon > 0$), so that the extraordinary ellipsoid is located outside the ordinary sphere. In diffusing light ordinary waves therefore have the minority (see Subsection 10.2.1). The two unit vectors $\hat{\boldsymbol{u}}_1$ and $\hat{\boldsymbol{u}}_2$ characterize the two director modes of wave vector $\boldsymbol{q}$ as introduced in Section 1.4.

where we used the unit vector $\hat{\boldsymbol{u}}_1(\hat{\boldsymbol{k}}) = \boldsymbol{n}_0 \times \hat{\boldsymbol{u}}_2(\hat{\boldsymbol{k}})$ perpendicular to $\boldsymbol{n}_0$. The refractive index $n_1(\hat{\boldsymbol{k}})$ is given by the relation

$$\frac{1}{n_1^2(\hat{\boldsymbol{k}})} = \frac{\sin^2\vartheta}{\varepsilon_\parallel} + \frac{\cos^2\vartheta}{\varepsilon_\perp} \quad . \tag{10.13}$$

Finally, the angle $\delta_1$ between $\boldsymbol{e}_1$ and $\boldsymbol{d}^1$ satisfies

$$\cos\delta_1 = \frac{1}{n_1^2(\hat{\boldsymbol{k}})}\left(\frac{\sin^2\vartheta}{\varepsilon_\parallel^2} + \frac{\cos^2\vartheta}{\varepsilon_\perp^2}\right)^{-1/2} \quad . \tag{10.14}$$

For the ordinary light wave, $\delta_2 = 0$.

Two velocities exist, phase and group velocity, associated with wave propagation. We need to discuss them in more detail. Light modes are characterized by a dispersion relation $\omega(\boldsymbol{k}_\alpha) = v_{p\alpha}k$ for each polarization $\alpha$, where $v_{p\alpha} = c/n_\alpha$ denotes the phase velocity. For given frequency $\omega$, the wave vector is represented by $\boldsymbol{k}_\alpha = \omega\hat{\boldsymbol{k}}/v_{p\alpha}(\hat{\boldsymbol{k}})$, whose magnitude, in the case of the extraordinary ray, depends on the direction $\hat{\boldsymbol{k}}$. If $\omega$ is constant, the wave vector $\boldsymbol{k}_\alpha$ lies on the *constant-frequency surface*, which is a circle of radius $n_2\omega/c$ for the

ordinary ray ($\alpha = 2$) and, as shown in Fig. (10.1), an ellipse with semi-axes $\sqrt{\varepsilon_\perp}\omega/c$ and $\sqrt{\varepsilon_\parallel}\omega/c$ for the extraordinary light wave ($\alpha = 1$). For each polarization, electromagnetic energy is transported along the direction of the group velocity defined by

$$\boldsymbol{v}_{g\alpha} = \boldsymbol{\nabla}_{\boldsymbol{k}}\omega_\alpha(\boldsymbol{k}) \ . \tag{10.15}$$

In the ordinary ray phase and group velocity are identical, *i.e.*, $\boldsymbol{v}_{g2} = \boldsymbol{v}_{p2} = \hat{\boldsymbol{k}}c/n_2$. The group velocity of the extraordinary wave,

$$\boldsymbol{v}_{g1} = cn_1(\hat{\boldsymbol{k}})\left(\frac{\cos\vartheta}{\varepsilon_\perp}\boldsymbol{n}_0 + \frac{\sin\vartheta}{\varepsilon_\parallel}\hat{\boldsymbol{u}}_1\right) \ , \tag{10.16}$$

is normal to the constant-frequency surface, as illustrated in Fig. 10.1. Together with the phase velocity $\boldsymbol{v}_{p1}$ it encloses the same angle $\delta_1$ [see Eq. (10.14)] as the polarization vectors $\boldsymbol{e}_1$ and $\boldsymbol{d}^1$. Furthermore, we find $v_{p1} = \cos\delta_1 v_{g1}$, and it can be checked that the magnitude of $\boldsymbol{e}_\alpha$ equals $v_{g\alpha}/c$.

The energy density of a dielectric medium is expressed by the formula $(\boldsymbol{E}\cdot\boldsymbol{\varepsilon}_0\boldsymbol{E} + \boldsymbol{H}\cdot\boldsymbol{H})/8\pi$. For a plane wave with polarization $E^\alpha\boldsymbol{e}_\alpha$, the cycle-averaged energy density turns out to be

$$W^\alpha = |E^\alpha|^2/(8\pi) \ . \tag{10.17}$$

That means, the amplitude $E^\alpha$ does not determine the strength of the electric field but rather stands for the square root of the energy density of one light mode. This is very convenient since experiments measure energy densities or intensities. In a homogeneous medium without absorption, the Poynting vector $c(\boldsymbol{E}\times\boldsymbol{H})/4\pi$ determines the energy transport. For one light mode, it equals the group velocity times energy density [194]

$$\boldsymbol{S}^\alpha = W^\alpha\boldsymbol{v}_{g\alpha} \ . \tag{10.18}$$

Energy density, group velocity, and Poynting vector will play an important role in what follows.

### 10.1.2 Single Light Scattering from Director Fluctuations

In a homogeneously aligned sample the director fluctuates around its equilibrium value $\boldsymbol{n}_0$, so that $\boldsymbol{n}(\boldsymbol{r},t) = \boldsymbol{n}_0 + \delta\boldsymbol{n}(\boldsymbol{r},t)$. This induces fluctuations $\delta\boldsymbol{\varepsilon}(\boldsymbol{r},t)$ of the dielectric tensor, which are calculated from Eq. (10.1) to first order in $\delta\boldsymbol{n}(\boldsymbol{r},t)$:

$$\delta\boldsymbol{\varepsilon}(\boldsymbol{r},t) = \Delta\varepsilon\left[\delta\boldsymbol{n}(\boldsymbol{r},t)\otimes\boldsymbol{n}_0 + \boldsymbol{n}_0\otimes\delta\boldsymbol{n}(\boldsymbol{r},t)\right] \ . \tag{10.19}$$

In the following we consider a characteristic scattering event where an incoming electric field mode with wave vector $\boldsymbol{k}_\alpha = \omega n_\alpha\hat{\boldsymbol{k}}/c$ and electric polarization vector $\boldsymbol{e}_\alpha(\hat{\boldsymbol{k}})$ is scattered from such fluctuations into an outgoing light mode with wave vector $\boldsymbol{q}_\beta = \omega n_\beta\hat{\boldsymbol{q}}/c$ and polarization vector $\boldsymbol{e}_\beta(\hat{\boldsymbol{q}})$. In the weak-scattering or Born approximation the scattered

electric field is proportional to the Fourier component of $\delta\boldsymbol{\varepsilon}(\boldsymbol{r},t)$ projected on the initial and final polarization:

$$\delta\varepsilon_{\alpha\beta}(\boldsymbol{q}_s,t) = \boldsymbol{e}_\beta(\hat{\boldsymbol{q}}) \cdot \delta\boldsymbol{\varepsilon}(\boldsymbol{q}_s,t)\boldsymbol{e}_\alpha(\hat{\boldsymbol{k}}) \ . \tag{10.20}$$

The quantity

$$\boldsymbol{q}_s = \omega(n_\beta\hat{\boldsymbol{q}} - n_\alpha\hat{\boldsymbol{k}})/c \tag{10.21}$$

denotes the scattering vector. Note that in comparison to our isotropic and scalar treatment of light scattering in Subsection 9.2.1, the polarization of light is now important since we deal with a birefringent medium. The normalization of $\boldsymbol{e}_\alpha(\hat{\boldsymbol{k}})$ and $\boldsymbol{e}_\beta(\hat{\boldsymbol{q}})$ has been chosen as discussed in the preceding subsection. In dynamic light scattering experiments one probes the temporal autocorrelation function of the scattered electric field. In single scattering this autocorrelation function is proportional to the matrix element

$$B_{\alpha\beta}(\hat{\boldsymbol{k}},\hat{\boldsymbol{q}},t) = \frac{\omega^4}{c^4}\left\langle\, \delta\varepsilon_{\alpha\beta}(\boldsymbol{q}_s,t)\, \delta\varepsilon^*_{\alpha\beta}(\boldsymbol{q}_s,0)\,\right\rangle \ . \tag{10.22}$$

Analogous to Subsection 9.2.1, we call $B_{\alpha\beta}(\hat{\boldsymbol{k}},\hat{\boldsymbol{q}},t)$ the dynamic structure factor because it contains information about the elastic and dynamic properties of the director modes. Using $\delta\boldsymbol{\varepsilon}(\boldsymbol{r},t)$ from Eq. (10.19) and the director autocorrelation function specified by Eqs. (1.50) and (1.51) in Section 1.4, we obtain

$$B_{\alpha\beta}(\hat{\boldsymbol{k}},\hat{\boldsymbol{q}},t) = (\Delta\epsilon)^2 k_\mathrm{B}T\,\frac{\omega^4}{c^4}\sum_{\delta=1}^{2}\frac{N(\boldsymbol{e}_\alpha,\boldsymbol{e}_\beta,\hat{\boldsymbol{u}}_\delta)}{K_\delta(\boldsymbol{q}_s)}\,\exp\Big[-\frac{K_\delta(\boldsymbol{q}_s)}{\eta_\delta(\boldsymbol{q}_s)}\,t\Big] \tag{10.23}$$

with a geometry factor

$$N(\boldsymbol{e}_\alpha,\boldsymbol{e}_\beta,\hat{\boldsymbol{u}}_\delta) = [(\boldsymbol{n}_0\cdot\boldsymbol{e}_\beta)(\hat{\boldsymbol{u}}_\delta\cdot\boldsymbol{e}_\alpha) + (\hat{\boldsymbol{u}}_\delta\cdot\boldsymbol{e}_\beta)(\boldsymbol{n}_0\cdot\boldsymbol{e}_\alpha)]^2 \ . \tag{10.24}$$

The elastic constant $K_\delta(\boldsymbol{q}_s)$ and the exponential factor in Eq. (10.23) originate, respectively, from the static and dynamic properties of director fluctuations and were discussed in Section 1.4. The strength of light scattering decreases with the square of the dielectric anisotropy $\Delta\varepsilon$. Adopting that the material parameters are linked to the Maier-Saupe parameter $S$ as follows, $K_\delta, \eta_\delta \propto S^2$ and $\Delta\varepsilon \propto S$ [76], the matrix element $B_{\alpha\beta}(\hat{\boldsymbol{k}},\hat{\boldsymbol{q}},t)$ hardly depends on $S$. Since the front factor $k_\mathrm{B}T$ changes only slightly within the nematic phase, single light scattering hardly depends on temperature $T$. Such independence has indeed been observed [49]. From the last equation it is possible to deduce the allowed scattering events. We infer that ordinary-to-ordinary transitions are not possible since $N(\boldsymbol{e}_2,\boldsymbol{e}_2,\hat{\boldsymbol{u}}_\delta)$ is zero as $\boldsymbol{e}_2$ is always perpendicular to $\boldsymbol{n}_0$. Such a scattering may nevertheless be produced by fluctuations in the isotropic part of the dielectric tensor which, however, are much smaller than the director-induced scattering, and so we will ignore it. Furthermore, one realizes that Eq. (10.24) does not allow forward scattering along the director.

Generalizing Eq. (9.4), the structure factor is related to the differential scattering cross section giving the scattered energy per unit of time, solid angle element, and incident intensity in a medium of volume $V$ [196, 197]:

$$\frac{d\sigma^{\alpha\beta}}{d\Omega_{\boldsymbol{q}}^{\beta}} = \frac{V}{(4\pi)^2}\, n_\alpha(\hat{\boldsymbol{k}}) \cos\delta_\alpha\, B_{\alpha\beta}(\hat{\boldsymbol{k}}, \hat{\boldsymbol{q}}, t=0)\, n_\beta^3(\hat{\boldsymbol{q}}) \ . \tag{10.25}$$

We have used here the solid angle element $d\Omega_{\boldsymbol{q}}^{\beta}$ associated with the outgoing wave vector. For extraordinary light, it differs from the solid angle element $d\Omega_R^{\beta}$ associated with the Poynting vector, being more relevant experimentally and in numerical simulations. The relation between the two is given by $d\Omega_R^1 \,/\, d\Omega_q^1 = [n_1^6(\hat{\boldsymbol{q}}) \cos^3\delta_1] \,/\, (\epsilon_\perp^2 \epsilon_\parallel)$ [336].

Summing over all directions and polarizations of the scattered light in Eq. (10.25) defines the total scattering cross section. In complete analogy to Subsection 9.2.1, we obtain the loss $\Delta S^\alpha$ of the incident intensity $S^\alpha$ per travelled distance $\Delta z$ as

$$\Delta S^\alpha = -\frac{\cos\delta_\alpha}{\ell_\alpha(\hat{\boldsymbol{k}})} \Delta z\, S^\alpha \ , \tag{10.26}$$

which defines the "physical" scattering mean free path $\ell_\alpha(\hat{\boldsymbol{k}})/\cos\delta_\alpha$ in terms of the "bare" scattering mean free path $\ell_\alpha(\hat{\boldsymbol{k}})$:

$$\frac{1}{\ell_\alpha(\hat{\boldsymbol{k}})} = n_\alpha(\hat{\boldsymbol{k}}) \sum_\beta \int \frac{d\Omega_q}{(4\pi)^2} B_{\alpha\beta}(\hat{\boldsymbol{k}}, \hat{\boldsymbol{q}}, t=0) n_\beta^3(\hat{\boldsymbol{q}}) \ . \tag{10.27}$$

The length $\ell_\alpha(\hat{\boldsymbol{k}})/\cos\delta_\alpha$ determines the exponential decay of the incident light intensity along the direction of the Poynting vector $\boldsymbol{S}^\alpha = W^\alpha \boldsymbol{v}_{g\alpha}$ due to scattering. If this decay is measured along the direction of $\hat{\boldsymbol{k}}$, then, for extraordinary light, it is determined by the smaller path length $\ell_1(\hat{\boldsymbol{k}})$ since Poynting vector and $\hat{\boldsymbol{k}}$ enclose just the angle $\delta_1$. The "bare" length appears when multiple light scattering is treated in $\boldsymbol{k}$ space.

The scattering mean free path $\ell_\alpha(\hat{\boldsymbol{k}})$ was studied in detail by two groups [197, 356, 191]. Its explicit dependence on $\hat{\boldsymbol{k}}$ and polarization $\alpha$ was calculated by Romanov *et al.* [356, 191]. It is also pictured in Ref. [369]. In Fig. 10.2 we plot the inverse scattering mean free path, $l_\alpha^{-1}$, in arbitrary units as a function of $\cos\vartheta$, where $\vartheta$ denotes the angle enclosed by the director $\boldsymbol{n}_0$ and $hat\boldsymbol{k}$. In the left picture all Frank constants are equal and $\Delta\varepsilon = 0$. The angular dependence in $l_\alpha$ is purely due to thermal fluctuations perpendicular to the optical axis, expressed in the geometry factor of Eq. (10.24). This case is academic because for $\Delta\varepsilon = 0$ light scattering does not occur. In the right picture material parameters of the compound 5CB are assumed. Along the optical axis ($\cos\vartheta = \pm 1$) both polarizations degenerate, and the mean free paths coincide. The structure factor $B_{\alpha\beta}(\hat{\boldsymbol{k}}, \hat{\boldsymbol{q}}, t)$ diverges for $H \to 0$ and $\boldsymbol{q}_s \to \boldsymbol{0}$. However, such a situation can only occur for extraordinary-to-extraordinary scattering, and we obtain the unphysical result that the scattering mean free path $\ell_1(\hat{\boldsymbol{k}})$ tends to zero for $H \to 0$. This is due to the fact that the weak-scattering approximation, employed to calculate $\ell_\alpha(\hat{\boldsymbol{k}})$, is no longer valid. It assumes that a propagating plane wave is only slightly disturbed by scattering. Therefore, the scattering mean free path has to be much larger than the wavelength of light, $l_\alpha(\hat{\boldsymbol{k}}) n_\alpha \omega/c \gg 1$.

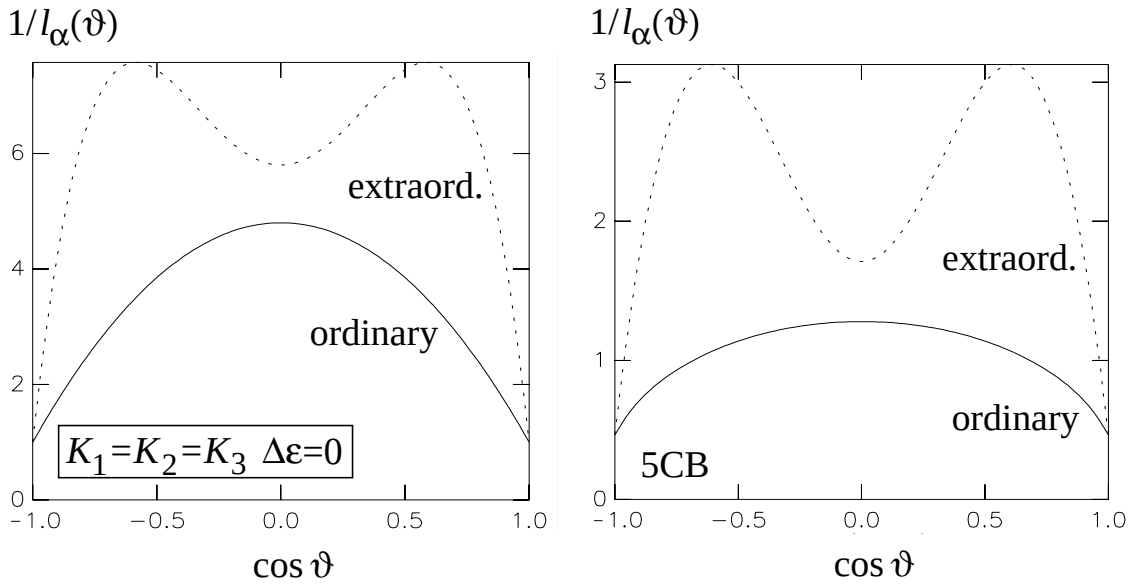


Figure 10.2: Inverse "bare" scattering mean free path, $l_\alpha^{-1}$, in arbitrary units as a function of $\cos\vartheta$, where $\vartheta$ denotes the angle enclosed by the director $\boldsymbol{n}_0$ and $\hat{\boldsymbol{k}}$; $\xi_H = 5\,\mu$m. In the left picture all Frank constants are equal, and $\Delta\varepsilon = 0$. In the right picture material parameters of the compound 5CB are assumed.

To derive a better criterion for the validity of the Born approximation, we adopt a completely isotropic model of the nematic structure factor,

$$B(\boldsymbol{q}-\boldsymbol{k}) = 2(\Delta\varepsilon)^2\,\frac{\omega^4}{c^4}\,\frac{k_\mathrm{B}T}{K(q_s^2+1/\xi_H^2)}\quad , \tag{10.28}$$

where $\xi_H$ is the magnetic coherence length defined in Eq. (1.9), and the factor 2 is due to the two possible director modes for each wave vector. The scattering mean free path $\ell_S$ assumes the form

$$\frac{1}{\ell_S} = 2\int\frac{d\Omega_{\boldsymbol{q}}}{(4\pi)^2}\,B(\boldsymbol{q}-\boldsymbol{k}) = \frac{1}{4\pi}\,\frac{(\Delta\varepsilon)^2}{\varepsilon^2}\,\frac{k_\mathrm{B}T}{K}\,\frac{\omega^2\varepsilon}{c^2}\,\ln\left(1+4\,\frac{\omega^2\varepsilon}{c^2}\,\xi_H^2\right)\quad ; \tag{10.29}$$

now the factor 2 takes into account the two polarizations of light. Employing typical liquid crystal parameters and a magnetic field of one Tesla, where $\xi_H$ is several microns, we find $\ell_S \approx 0.1\,$mm. However, since $\xi_H \propto 1/H$, the scattering mean free path goes to zero logarithmically in $H$. Director fluctuations are correlated within a volume $V = \xi_H^3$. Let $\delta P$ denote the amount of energy per unit time scattered from such a volume. Refering it to the total incoming energy per unit time $P_0$, we obtain

$$\frac{\delta P}{P_0} = \frac{V}{\xi_H^2}\int\frac{d\Omega_{\boldsymbol{q}}}{(4\pi)^2}\,B(\boldsymbol{q}-\boldsymbol{k}) = \frac{\xi_H}{\ell_S}\quad . \tag{10.30}$$

The weak-scattering approximation is valid as long as $\xi_H \ll \ell_S$, which then suggests the popular picture of subsequent scattering from different director fluctuations, which are well

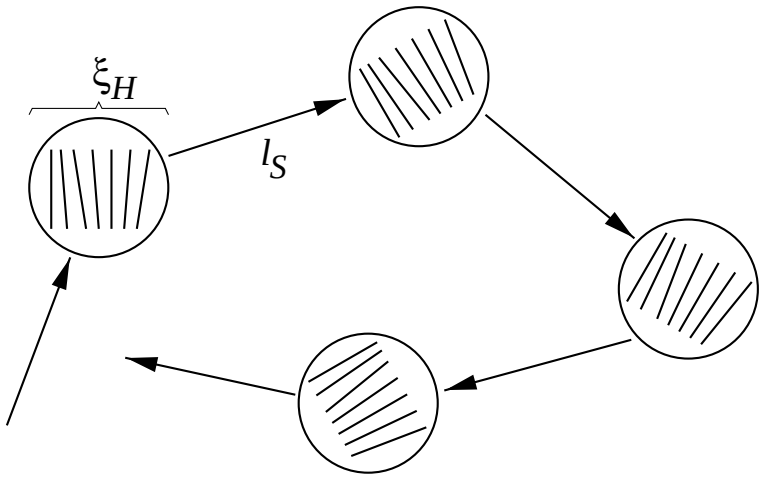


Figure 10.3: As long as $\xi \ll \ell_S$, subsequent scattering from different director fluctuations, which are well separated in space, occurs. If $\xi \approx \ell_S$, the regions overlap, and the weak-scattering approximation is no longer valid.

separated in space as illustrated in Fig. 10.3. This is reminiscent of subsequent scattering from single particles in dilute colloids. If the magnetic field is lowered to approximately $10^{-2}\,\mathrm{T}$ (100 Gauss), $\xi_H$ is of the order of 0.1 mm and approaches $\ell_S$. The weak-scattering approximation is no longer applicable. At the same time, the familiar picture of subsequent scattering from well separated regions of director fluctuations is lost since they start to overlap. To understand light scattering in a nematic with $\ell_S \approx \xi_H$, one has to go beyond the weak-scattering approximation.

Our last remark concerns the symmetry of the dynamic structure factor. In isotropic systems, it is completely diagonal when expanded into spherical harmonics as illustrated in Eq. (9.7). The structure factor for director modes just possesses the rotational symmetry about the equilibrium director $\boldsymbol{n}_0$. Hence, it can be written as a function of the relative azimuthal angle $\varphi = \varphi_{\boldsymbol{q}} - \varphi_{\boldsymbol{k}}$ between $\hat{\boldsymbol{q}}$ and $\hat{\boldsymbol{k}}$. Using the additional symmetry $B_{\alpha\beta}(\hat{\boldsymbol{k}}, \hat{\boldsymbol{q}}, 0) = B_{\alpha\beta}(-\hat{\boldsymbol{k}}, -\hat{\boldsymbol{q}}, 0)$, the following expansion holds:

$$B_{\alpha\beta}(\hat{\boldsymbol{k}}, \hat{\boldsymbol{q}}, 0) = \sum_{m\geq 0} B^m_{\alpha\beta}(\vartheta_{\boldsymbol{k}}, \vartheta_{\boldsymbol{q}}) \cos[m(\varphi_{\boldsymbol{q}} - \varphi_{\boldsymbol{k}})] \ , \tag{10.31}$$

where $\vartheta_{\boldsymbol{k}}$ and $\vartheta_{\boldsymbol{q}}$ are polar angles of $\hat{\boldsymbol{k}}$ and $\hat{\boldsymbol{q}}$ with respect to $\boldsymbol{n}_0$. In Subsection 10.2.3 we will write $B_{\alpha\beta}(\hat{\boldsymbol{k}}, \hat{\boldsymbol{q}}, 0)$ in terms of modified spherical harmonics $\widetilde{Y}^{\alpha}_{lm}(\hat{\boldsymbol{k}})$ and $\widetilde{Y}^{\beta}_{lm}(\hat{\boldsymbol{q}})$. Then, Eq. (10.31) expresses the fact that the matrix element $\langle lm|B_{\alpha\beta}(\hat{\boldsymbol{k}}, \hat{\boldsymbol{q}}, 0)|l'm'\rangle \propto \delta_{mm'}$ is diagonal in the azimuthal quantum number $m$ but not in the angular momentum $l$.

## 10.2 Anisotropic Light Diffusion in Nematics

We are prepared to derive the diffusion approximation of light in a homogeneous nematic liquid crystal. We will closely follow the procedure outlined in Section 9.2 for isotropic systems starting from a radiative transfer equation. In our presentation we will stress the differences between nematics and isotropic systems, and we start with such a difference.

### 10.2.1 Equipartition of Light Energy

Diffusing light of a given frequency $\omega$ tends to equipartition the electromagnetic energy among all available photon states. That means, in an isotropic system the energy is equally distributed on all light modes with polarization $\alpha$ propagating along the direction $\hat{\boldsymbol{k}}$. In an anisotropic system this is no longer true as can be seen by a simple argument. The number of photon states is proportional to the volume element $k^2 dk d\Omega_{\boldsymbol{k}}$ in the phase space of wave vectors $\boldsymbol{k}$. However, in an experiment the frequency $\omega$ of light is fixed. Therefore, employing the dispersion relation $\omega = ck/n_\alpha(\hat{\boldsymbol{k}})$, we find for the number $N_\alpha(\omega, \hat{\boldsymbol{k}}) d\omega d\Omega_{\boldsymbol{k}}$ of photon states with given polarization $\alpha$, frequency $\omega$, and direction $\hat{\boldsymbol{k}}$:

$$N_\alpha(\omega, \hat{\boldsymbol{k}}) d\omega d\Omega_{\boldsymbol{k}} \propto k^2 dk d\Omega_{\boldsymbol{k}} = n_\alpha^3(\hat{\boldsymbol{k}})\, \omega^2 d\omega d\Omega_{\boldsymbol{k}}/c^3 \ . \tag{10.32}$$

We realize that the number of photon states is proportional to the cube of the refractive index, $n_\alpha^3(\hat{\boldsymbol{k}})$. In the case of extraordinary light this leads to an anisotropic distribution of energy density in real space. For a fixed direction $\hat{\boldsymbol{k}}$, the ratio of energy densities in the ordinary and extraordinary mode is given by $N_2(\omega, \hat{\boldsymbol{k}})/N_1(\omega, \hat{\boldsymbol{k}}) = n_2^3(\hat{\boldsymbol{k}})/n_1^3(\hat{\boldsymbol{k}})$. For positive dielectric anisotropy $\Delta\varepsilon > 0$, extraordinary waves are in the majority since $n_1 \geq n_2$. When integrating over the whole solid angle $[N_\alpha(\omega) = \int N_\alpha(\omega, \hat{\boldsymbol{k}}) d\Omega_{\boldsymbol{k}}]$, we find $N_2(\omega)/N_1(\omega) = \varepsilon_\perp/\varepsilon_\parallel$. Despite the heuristic argument, these results are an *exact* outcome of transport theory [367, 337]. They also have an equivalent for elastic waves in solid media [379]. Note that our reasoning holds *regardless* the details of the scattering process and its selection rules for polarization transitions.

### 10.2.2 Radiative Transfer Theory

Analogous to Subsection 9.2.2, we deal with the temporal auto correlation function of the electric field,

$$n_\alpha^3(\hat{\boldsymbol{k}}) W_{\hat{\boldsymbol{k}}}^\alpha(\boldsymbol{R}, T, t) = \langle\, E_{\hat{\boldsymbol{k}}}^\alpha(\boldsymbol{R}, T - t/2)\, E_{\hat{\boldsymbol{k}}}^{\alpha *}(\boldsymbol{R}, T + t/2) \,\rangle \ . \tag{10.33}$$

For $t = 0$, it stands for the energy density of a light wave at time $T$ and space point $\boldsymbol{R}$ travelling into direction $\hat{\boldsymbol{k}}$ with polarization $\alpha$. The light frequency $\omega$ is omitted. We pulled out the factor $n_\alpha^3(\hat{\boldsymbol{k}})$ due to the equipartition of energy on all available photon states in the diffuse regime.

In complete analogy to Eq. (9.9), the radiative transfer equation for correlation transport in anisotropic media takes the form

$$\left(\frac{\partial}{\partial T} + \boldsymbol{v}_{g\alpha}\cdot\boldsymbol{\nabla} + \frac{1}{l_\alpha}\frac{c}{n_\alpha}\right) W^\alpha_{\hat{\boldsymbol{k}}}(\boldsymbol{R},T,t) = c\sum_\beta \int \frac{d\Omega_{\boldsymbol{q}}}{(4\pi)^2} B_{\alpha\beta}(\hat{\boldsymbol{k}},\hat{\boldsymbol{q}},t) n^3_\beta(\hat{\boldsymbol{q}}) W^\beta_{\hat{\boldsymbol{q}}}(\boldsymbol{R},T,t) + S^\alpha_{\hat{\boldsymbol{k}}}(\boldsymbol{R},T) \quad . \tag{10.34}$$

Its interpretation is the same as for isotropic systems. However, its handling is further complicated by the fact that the Poynting vector $\boldsymbol{v}_{g\alpha} W^\alpha_{\hat{\boldsymbol{k}}}(\boldsymbol{R},T,t)$ [see Eq. 10.18] and the scattering mean free path $l_\alpha(\hat{\boldsymbol{k}})$ [see Eq. 10.27] heavily depend on $\hat{\boldsymbol{k}}$. Furthermore, the structure factor $B_{\alpha\beta}(\hat{\boldsymbol{k}},\hat{\boldsymbol{q}},t)$ is more complex due to the reduced symmtry.

The transport equation (10.34) is applicable to general anisotropic random media. Its validity is restricted to length and time scales much longer than the wavelength and time period of light. We are able to derive the equation of radiative transfer from first principles. Starting from Maxwell's theory, it follows in a straightforward way from the Bethe-Salpeter equation for the averaged "two-particle" Green function when only ladder diagrams are taken into account [337, 338, 367, 364, 369, 296]. For nematic liquid crystals, the transport equation was first formulated by Romanov and Shalaginov [296] and solved in the small-angle approximation. We concentrate here on the particularly attractive regime of the much simpler diffusion limit.

### 10.2.3 Diffusion Approximation

To derive the diffusion approximation from Eq. (10.34), we set $t = 0$ and assume that the source term is independent of $\hat{\boldsymbol{k}}$ thus representing a source for diffusing light. We first study the equilibrium solution of Eq. (10.34), where $W^\alpha_{\hat{\boldsymbol{k}}}(\boldsymbol{R},T,0)$ equals a constant $W_0$. As a result, expression (10.27) for the scattering mean free path $\ell_\alpha(\hat{\boldsymbol{k}})$ is reproduced. The energy density $n^3_\alpha(\hat{\boldsymbol{k}})W_0$ depends on the direction $\hat{\boldsymbol{k}}$ and polarization $\alpha$ of light, due to the equipartition of the light energy on all available photon states, as argued in Subsection (10.2.1). So far, this is not confirmed experimentally.

The diffusion approximation follows when $n^3_\alpha(\hat{\boldsymbol{k}})W^\alpha_{\hat{\boldsymbol{k}}}(\boldsymbol{R},T,0)$ deviates only slightly from the equilibrium angular distribution. Let us therefore study an angular expansion of $W^\alpha_{\hat{\boldsymbol{k}}}(\boldsymbol{R},T,0)$,

$$W^\alpha_{\hat{\boldsymbol{k}}}(\boldsymbol{R},T,0) = \frac{1}{8\pi} W_0(\boldsymbol{R},T) + \frac{3}{4\pi}\frac{1}{c\overline{n^3_\alpha}} n_\alpha\, \hat{\boldsymbol{k}}\cdot\boldsymbol{J}^\alpha(\boldsymbol{R},T,0) + \sum_{l>1,m} W^\alpha_{lm}(\boldsymbol{R},T,0)\widetilde{Y}^\alpha_{lm}(\hat{\boldsymbol{k}}) \quad , \tag{10.35}$$

where we wrote the total energy density

$$\overline{n^3}W_0(\boldsymbol{R},T,0) = \sum_\alpha \int d\Omega_{\boldsymbol{k}}\, n^3_\alpha(\hat{\boldsymbol{k}})\, W^\alpha_{\hat{\boldsymbol{k}}}(\boldsymbol{R},T,0) \tag{10.36}$$

as $W_0$ times an angular average over the cubes of both refractive indices:

$$\overline{n^3} = (\overline{n_1^3} + \overline{n_2^3})/2 = \int d\Omega_{\boldsymbol{k}} [n_1^3(\hat{\boldsymbol{k}}) + n_2^3(\hat{\boldsymbol{k}})]/8\pi = (\varepsilon_\perp^{1/2}\varepsilon_\parallel + \varepsilon_\perp^{3/2})/2 \ . \tag{10.37}$$

Our aim is to establish a diffusion equation for $W_0(\boldsymbol{R}, T, 0)$. Furthermore, we introduced the total energy density current $\boldsymbol{J}^\alpha(\boldsymbol{R}, T, 0)$ associated with polarization $\alpha$, by integrating over the Poynting vector of Eq. (10.18):

$$\boldsymbol{J}^\alpha(\boldsymbol{R}, T, 0) = \int d\Omega_{\boldsymbol{k}}\, n_\alpha^3\, \boldsymbol{v}_{g\alpha}\, W_{\hat{\boldsymbol{k}}}^\alpha(\boldsymbol{R}, T, 0) \ . \tag{10.38}$$

The angular expansion (10.35) is written in complete analogy to Eq. (9.10). However, for uniaxial systems, it is useful to choose modified spherial harmonics $\widetilde{Y}_{lm}^\alpha(\hat{\boldsymbol{k}})$. They are defined via the weight function $n_\alpha^3(\hat{\boldsymbol{k}})$ in the orthogonality relation

$$\int d\cos\vartheta d\varphi\ n_\alpha^3(\hat{\boldsymbol{k}}) \widetilde{Y}_{lm}^\alpha(\hat{\boldsymbol{k}})\, \widetilde{Y}_{l'm'}^\alpha(\hat{\boldsymbol{k}}) = \overline{n_\alpha^3}\delta_{ll'}\delta_{mm'} \ , \tag{10.39}$$

where $\hat{\boldsymbol{k}} = (\sin\vartheta\cos\varphi, \sin\vartheta\sin\varphi, \cos\vartheta)$. We will see below that this choice establishes an approximation scheme for the diffusion constants of light. We still obtain the conventional spherical harmonics in the case of ordinary waves. To derive $\widetilde{Y}_{lm}^1(\hat{\boldsymbol{k}})$ for extraordinary modes, we introduce a new coordinate $C = n_1(\hat{\boldsymbol{k}})\cos\vartheta/n_2$. It is equivalent to $\boldsymbol{n}_0 \cdot \hat{\boldsymbol{k}} = \cos\vartheta$ since it also ranges from $-1$ to 1. With this transformation, the weight function becomes a constant:

$$\int d\cos\vartheta n_1^3(\hat{\boldsymbol{k}}) \ldots = \overline{n_1^3} \int dC \ldots . \tag{10.40}$$

Hence, the basis functions $\widetilde{Y}_{lm}^1(\hat{\boldsymbol{k}})$ simply follow from spherical harmonics when $\cos\vartheta$ is replaced by $C$. Employing the abbreviation $C = \cos\vartheta$ in the case of ordinary light, the modified spherical harmonics are the same for $\alpha = 1$ and 2. Their real representation for $l = 1$ reads

$$\widetilde{Y}_{10}^\alpha(\hat{\boldsymbol{k}}) = \sqrt{\frac{3}{4\pi}}\, C \qquad \text{and} \qquad \frac{\widetilde{Y}_{11}^\alpha(\hat{\boldsymbol{k}}) \pm \widetilde{Y}_{1-1}^\alpha(\hat{\boldsymbol{k}})}{2} = \sqrt{\frac{3}{4\pi}}\sqrt{1-C^2} \begin{cases} \cos\varphi \\ \sin\varphi \end{cases} . \tag{10.41}$$

In expansion (10.35) we have already used them explicitly in the second term taking into account Eq. (10.16) of the group velocity. Also note the modified "trigonometric" relation $n_1(\hat{\boldsymbol{k}})\sin\vartheta/n_2 = \sqrt{\varepsilon_\parallel/\varepsilon_\perp}\sqrt{1-C^2}$.

We are prepared to extract the diffusion approximation from the transport equation (10.34). Multiplying Eq. (10.34) by $n_\alpha^3(\hat{\boldsymbol{k}})$ and summing over all directions of $\hat{\boldsymbol{k}}$ and the two polarizations, yields the continuity equation of the energy density:

$$\frac{\partial}{\partial T}\,\overline{n^3} W_0 + \boldsymbol{\nabla}\cdot\boldsymbol{J} = \text{source} \ . \tag{10.42}$$

The vector $\boldsymbol{J} = \boldsymbol{J}^1 + \boldsymbol{J}^2$ denotes the total energy density current. Via Fick's law, it is related to the gradient of the energy density:

$$\boldsymbol{J} = -\boldsymbol{D}\boldsymbol{\nabla}\overline{n^3}W_0 \ . \tag{10.43}$$

We will derive Fick's law below. We introduced the diffusion tensor

$$\boldsymbol{D} = D_\perp \mathbf{1} + (D_\parallel - D_\perp)\boldsymbol{n}_0 \otimes \boldsymbol{n}_0 \tag{10.44}$$

with its two independent light diffusion constants $D_\parallel$ and $D_\perp$, respectively, parallel and perpendicular to the director $\boldsymbol{n}_0$. Eliminating the current $\boldsymbol{J}$, finally results in the diffusion equation for $W_0(\boldsymbol{R}, T, 0)$,

$$\left(\frac{\partial}{\partial T} - D_\parallel \nabla_\parallel^2 - D_\perp \boldsymbol{\nabla}_\perp^2\right) W_0(\boldsymbol{R}, T, 0) = \text{source} \ , \tag{10.45}$$

where $\boldsymbol{\nabla} = (\boldsymbol{\nabla}_\perp, \nabla_\parallel)$.

To derive Fick's law (10.43), we first concentrate on components parallel to the director $\boldsymbol{n}_0$. Due to symmetry, the resulting expression for $D_\parallel$ only involves the azimuthal quantum number $m = 0$. We project the transport equation (10.34) on all modified spherical harmonics $\widetilde{Y}_{l0}^\alpha(\hat{\boldsymbol{k}})$ with odd[1] angular momentum $l \geq 1$ and obtain a set of equations which couple the energy density $W_0$, the components $J_\parallel^1$ and $J_\parallel^2$, and all further expansion coefficients $W_{l0}^\alpha$ ($l \geq 3$). We employ a symbolic matrix notation to formulate the set of equations:

$$\begin{pmatrix} \frac{(4\pi)^3}{18}\frac{c}{n_2^2}\nabla_\parallel \begin{bmatrix} 1 \\ 1 \end{bmatrix} & \begin{matrix} \mathcal{B}_{11}^\parallel & \mathcal{B}_{12}^\parallel \\ \mathcal{B}_{12}^\parallel & \mathcal{B}_{22}^\parallel \end{matrix} & \begin{bmatrix} \langle 10|\boldsymbol{B}|l'0\rangle \end{bmatrix} \\ \begin{matrix} 0 \\ 0 \\ \vdots \end{matrix} & \begin{bmatrix} \langle l0|\boldsymbol{B}|10\rangle \end{bmatrix} & \begin{bmatrix} \langle l0|\boldsymbol{B}|l'0\rangle \end{bmatrix} \end{pmatrix} \begin{pmatrix} W_0 \\ J_\parallel^1 \\ J_\parallel^2 \\ W_{30}^1 \\ W_{30}^2 \\ \vdots \end{pmatrix} = \mathbf{0} \ . \tag{10.46}$$

The quantitites $\mathcal{B}_{\alpha\beta}^\parallel$ are extended matrix elements of $B_{\alpha\beta}(\hat{\boldsymbol{k}}, \hat{\boldsymbol{q}})$ only involving $l = 1$ spherical harmonics:

$$\begin{aligned} \mathcal{B}_{11}^\parallel &= \int_{\hat{\boldsymbol{k}}}\int_{\hat{\boldsymbol{q}}} [(C_{\boldsymbol{k}}^2 - C_{\boldsymbol{k}}C_{\boldsymbol{q}})B_{11}(\hat{\boldsymbol{k}}, \hat{\boldsymbol{q}}) + C_{\boldsymbol{k}}^2 \frac{\varepsilon_\perp}{\varepsilon_\parallel} B_{12}(\hat{\boldsymbol{k}}, \hat{\boldsymbol{q}})] \\ \mathcal{B}_{22}^\parallel &= \int_{\hat{\boldsymbol{k}}}\int_{\hat{\boldsymbol{q}}} [(C_{\boldsymbol{k}}^2 - C_{\boldsymbol{k}}C_{\boldsymbol{q}})B_{22}(\hat{\boldsymbol{k}}, \hat{\boldsymbol{q}}) + C_{\boldsymbol{k}}^2 \frac{\varepsilon_\perp}{\varepsilon_\parallel} B_{21}(\hat{\boldsymbol{k}}, \hat{\boldsymbol{q}})] \\ \mathcal{B}_{12}^\parallel &= -\int_{\hat{\boldsymbol{k}}}\int_{\hat{\boldsymbol{q}}} C_{\boldsymbol{k}}C_{\boldsymbol{q}} B_{12}(\hat{\boldsymbol{k}}, \hat{\boldsymbol{q}}) \ , \end{aligned} \tag{10.47}$$

[1] Only spherical harmonics with odd $l$ describe a directed flow of energy in the angular expansion (10.35).

where we use the abbreviation $\int_{\hat{\boldsymbol{k}}} = \int dC_{\boldsymbol{k}} d\varphi_{\boldsymbol{k}}$. The symbol $[\,\langle l0|\boldsymbol{B}|l'0\rangle\,]$ in Eq. (10.46) stands for a matrix of objects similar to $\mathcal{B}^{\parallel}_{ij}$, however involving at least one higher spherical harmonic. Terms proportional to $\partial J^{\alpha}_{\parallel}/\partial T$ are neglected in Eq. (10.46). Concentrating on the upper left part in Eq. (10.46), we realize a relation between $\nabla_{\parallel} W_0$ and the energy density currents $J^{\alpha}_{\parallel}$. Due to our special choice of the modified spherical harmonics, there is no such direct connection between $W_0$ and the higher expansion coefficients $W^{\alpha}_{l0}$ ($l \geq 3$). If the matrix elements $\langle 10|\boldsymbol{B}|l'0\rangle$ are zero, we can directly solve for the two currents $J^{1}_{\parallel}$ and $J^{2}_{\parallel}$, and we obtain the parallel component of Fick's law (10.43),

$$J_{\parallel} = J^{1}_{\parallel} + J^{2}_{\parallel} = -D_{\parallel} \nabla_{\parallel} \overline{n^3} W_0 \ , \tag{10.48}$$

with the diffusion constant

$$D_{\parallel} = \frac{(4\pi)^3}{18} \frac{c}{n_2^2 \overline{n^3}} \frac{\mathcal{B}^{\parallel}_{11} + \mathcal{B}^{\parallel}_{22} - 2\mathcal{B}^{\parallel}_{12}}{\mathcal{B}^{\parallel}_{11}\mathcal{B}^{\parallel}_{22} - (\mathcal{B}^{\parallel}_{12})^2} \ . \tag{10.49}$$

Since generally $\langle 10|\boldsymbol{B}|l'0\rangle \neq 0$, we set up an approximation scheme. Via the lower part of Eq. (10.46), the coefficients $W^{\alpha}_{l0}$ ($l > 1$) can be expressed in terms of $J^{1}_{\parallel}$ and $J^{2}_{\perp}$ and reinserted into the upper part. Depending on the number of spherical harmonics we take into account, the diffusion constant $D_{\parallel}$ of Eq. (10.49) is renormalized. We have checked that corrections from $l = 3$ spherical harmonics are smaller than 1%, so that Eq. (10.49) already gives a good approximation for $D_{\parallel}$.

Due to symmetry reasons, $D_{\perp}$ depends only on spherical harmonics with azimuthal quantum numbers $m = \pm 1$. The perpendicular component $\boldsymbol{J}_{\perp}$ is derived in the same manner as $J_{\parallel}$ projecting the transport equation (10.34) on $[\widetilde{Y}^{\alpha}_{l1}(\hat{\boldsymbol{k}}) + \widetilde{Y}^{\alpha}_{l-1}(\hat{\boldsymbol{k}})] \propto \cos\varphi_{\boldsymbol{k}}$:

$$\boldsymbol{J}_{\perp} = \boldsymbol{J}^{1}_{\perp} + \boldsymbol{J}^{2}_{\perp} = -D_{\perp} \boldsymbol{\nabla}_{\perp} \overline{n^3} W_0 \tag{10.50}$$

with

$$D_{\perp} = \frac{(4\pi)^3}{18} \frac{c}{n_2^2 \overline{n^3}} \frac{\mathcal{B}^{\perp}_{11} + \mathcal{B}^{\perp}_{22}\varepsilon_{\perp}/\varepsilon_{\parallel} - 2\mathcal{B}^{\perp}_{12}\sqrt{\varepsilon_{\perp}/\varepsilon_{\parallel}}}{\mathcal{B}^{\perp}_{11}\mathcal{B}^{\perp}_{22} - (\mathcal{B}^{\perp}_{12})^2} \ . \tag{10.51}$$

The matrix elements $\mathcal{B}^{\perp}_{\alpha\beta}$ are defined as in Eqs. (10.47) but with $C$ replaced by $\sqrt{1-C^2}\cos\varphi$.

The diffusion constants can also be calculated by determining the diffusion pole of the average two-particle Green function of the electric field [337, 338] or by explicitely summing up different light paths in direct space [336]. Both methods lead to the same approximation scheme as derived above. Tiggelen *et al.* generalized the Kubo-Greenwood formula for the diffusion constant [221] to uniaxial media [367, 364]. It involves an integral equation for a tensor $\boldsymbol{\gamma}$, which they determined numerically. The calculated diffusion constants agree with the results reported in the next subsection.

### 10.2.4 Discussion of the Diffusion Constants

To specify the magnitudes of $D_\parallel$ and $D_\perp$, we introduce an "averaged" transport mean free path

$$l_0^* = 9\pi \frac{c_\perp^2}{\omega^2} \frac{K_3}{k_B T} \frac{1}{\alpha^2} \ , \tag{10.52}$$

where $c_\perp$ is the speed of light of the ordinary light ray. We write the diffusion constants in the form

$$D_\parallel = c_\perp l_0^* \widetilde{D}_\parallel / 3 \qquad \text{and} \quad D_\perp = c_\perp l_0^* \widetilde{D}_\perp / 3 \ , \tag{10.53}$$

reminiscent of isotropic systems. The numerical factors $\widetilde{D}_\parallel$ and $\widetilde{D}_\perp$ depend only on the ratios of the Frank elastic constants ($K_1/K_3$ and $K_2/K_3$) and the relative dielectric anisotropy $\Delta\epsilon/\epsilon_\perp$. The factor $9\pi$ in $l_0^*$ is chosen such that $\widetilde{D}_\parallel$ and $\widetilde{D}_\perp$ are approximately 1 in the limit of an "isotropic" nematic with $K_1 = K_2 = K_3$, $\Delta\varepsilon = 0$, and $H = 0$. In this case we find $\widetilde{D}_\parallel = 1.053$ and $\widetilde{D}_\perp = 0.998$ with a small anisotropy of $D_\parallel/D_\perp = 1.06$ because of the inherent anisotropy in the nematic structure factor represented by the geometrical factor $N(\boldsymbol{e}_\alpha, \boldsymbol{e}_\beta, \hat{\boldsymbol{u}}_\delta)$ of Eq. (10.24). We, at least, qualitatively understand why $D_\parallel$ is larger than $D_\perp$. The diffusion constants grow when the ability of the system to scatter light decreases. From Eqs. (10.49) and (10.51) for $D_\parallel$ and $D_\perp$, we recognize that the diffusion constants are determined, respectively, by scattering around the director ($m = 0$) or perpendicular to it ($m = \pm 1$). However, forward and backward scattering along the director is suppressed by the geometrical factor, and we expect $D_\parallel$ to be larger than $D_\perp$. With the completely isotropic structure factor of Eq. (10.28) [$N(\boldsymbol{e}_\alpha, \boldsymbol{e}_\beta, \hat{\boldsymbol{u}}_\delta) = 1$], the transport mean free path is easy to calculate. It is smaller than $l_0^*$ by a factor of 4/9, which again demonstrates the effect of the geometrical factor. With the material parameters of the nematic compound 5CB ($\Delta\varepsilon/\varepsilon_\perp = 0.228$, $n_2 = 1.543$, $K_3 = 5.3 \cdot 10^{-7}$ dyn), green light ($\omega/c = 1.15 \cdot 10^5\,\mathrm{cm}^{-1}$), and a temperature of $T = 300\,\mathrm{K}$, we obtain $l_0^* = 2.3\,\mathrm{mm}$ or $D_0 = c_\perp l_0^*/3 = 1.5 \cdot 10^9\,\mathrm{cm}^2/\mathrm{s}$ in rough agreement with experiments [170, 336].

For 5CB we demonstrate in Fig. 10.4 how the diffusion constants $\widetilde{D}_\parallel$ and $\widetilde{D}_\perp$ and the relative anisotropy $(D_\parallel - D_\perp)/D_\perp$ behave in a magnetic field. $\widetilde{D}_\parallel$ and $\widetilde{D}_\perp$ grow with $H$ because the magnetic field suppresses director fluctuations. The field dependence of the relative anisotropy in the diffusion is weak. For ordinary magnetic fields up to $5 \times 10^4\,\mathrm{G}$, corresponding to a magnetic coherence length $\xi_H$ of approximately $1\,\mu\mathrm{m}$, the changes in $\widetilde{D}_\parallel$ and $\widetilde{D}_\perp$ are small. The values for $H = 0$ read $\widetilde{D}_\parallel = 0.95$ and $\widetilde{D}_\perp = 0.65$ with a ratio $\widetilde{D}_\parallel/\widetilde{D}_\perp = 1.45$. Together with $D_0 = c_\perp l_0^*/3 = 1.5 \cdot 10^9\,\mathrm{cm}^2/\mathrm{s}$, we obtain $D_\parallel = 1.43 \cdot 10^9\,\mathrm{cm}^2/\mathrm{s}$ and $D_\perp = 0.98 \cdot 10^9\,\mathrm{cm}^2/\mathrm{s}$. These numbers are in excellent ageement with numerical simulations, where we studied the temporal development of a photon cloud in the compound 5CB by means of the Monte Carlo method [336]. The ratio $\widetilde{D}_\parallel/\widetilde{D}_\perp$ is also in good agreement with experiments [170, 336]. However, the absolute values of $D_\parallel$ and $D_\perp$ are larger by a factor of two. We attribute this partially to the fact that the experiments used light with a longer wavelength. Note that both diffusion constants are finite for $H \to 0$, although the scattering mean free path for extraordinary-to-extraordinary scattering goes to zero, as discussed in Subsection 10.1.2. In the completely isotropic model

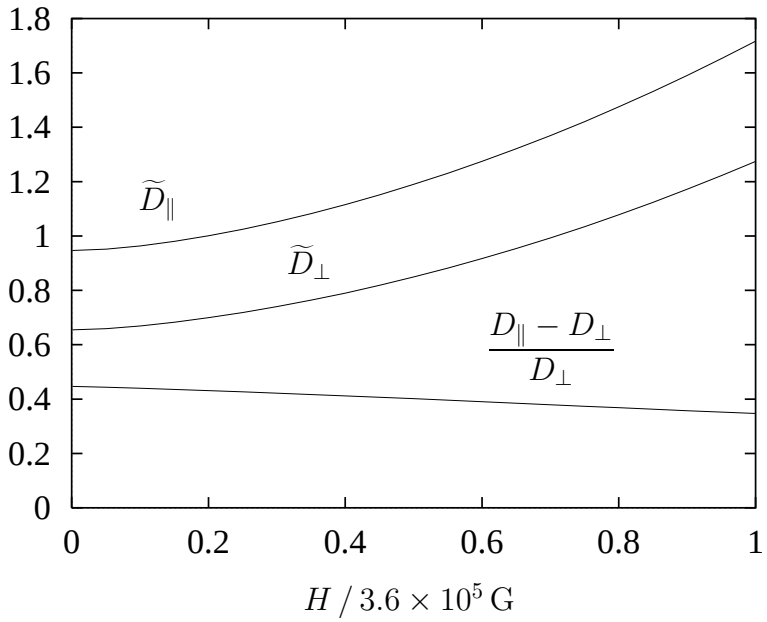


Figure 10.4: Reduced diffusion constants $\widetilde{D}_\parallel$ and $\widetilde{D}_\perp$ and the relative anisotropy $(D_\parallel - D_\perp)/D_\perp$ as a function of the magnetic field strength $H$ for the nematic compound 5CB ($K_1/K_3 = 0.79$, $K_2/K_3 = 0.43$, and $\Delta\epsilon/\epsilon_\perp = 0.228$).

of Eq. (10.28) we understand this fact. The singularity from $\boldsymbol{q}_s^2 \propto 1 - \cos\vartheta_s$ is cancelled by the familiar factor $1 - \cos\vartheta_s$ in the expression (9.15) of the isotropic diffusion constant.

In Fig. 10.5 we explore the anisotropy in the diffusion as a function of the dielectric anisotropy $\Delta\epsilon/\epsilon_\perp$ for $K_1 = K_2 = K_3$. As already discussed, even at $\Delta\epsilon = 0$, the diffusion constants $D_\parallel$ and $D_\perp$ are slightly different because of the inherent anisotropy in the nematic structure factor. The anisotropy in the diffusion grows with $\Delta\epsilon$ because the speed of light of the extraordinary light ray is larger along the director than perpendicular to it. In contrast, when $\Delta\epsilon/\epsilon_\perp < -0.15$, the anisotropy $(D_\parallel - D_\perp)/D_\perp$ changes sign, and light diffuses faster perpendicular to the director. This effect and the inversion point $D_\parallel = D_\perp$ should be observable in discotic nematics where $\Delta\epsilon$ is negative. The approximately linear growth in Fig. (10.5) can be reproduced by a kinematic approach to the diffusion tensor involving the group velocity $\boldsymbol{v}_{g\alpha}$ [369],

$$\boldsymbol{D} \propto \sum_{\alpha=1,2} \int \boldsymbol{v}_{g\alpha}(\hat{\boldsymbol{k}}) \otimes \boldsymbol{v}_{g\alpha}(\hat{\boldsymbol{k}})\, n_\alpha^3(\hat{\boldsymbol{k}})\, d\Omega_{\boldsymbol{k}} \Bigg/ \sum_{\alpha=1,2} \int n_\alpha^3(\hat{\boldsymbol{k}})\, d\Omega_{\boldsymbol{k}} \quad , \tag{10.54}$$

where $n_\alpha^3(\hat{\boldsymbol{k}})$ counts the number of photon states. If the Frank constants $K_i$ differ from each other, the curve in Fig. (10.5) is merely shifted along the vertical axis.

Finally, we discuss how diffusion depends on the reduced elastic constants $K_1/K_3$ and $K_2/K_3$. We show in Fig. 10.6 that $\widetilde{D}_\perp$ decreases with the elastic constants. This is

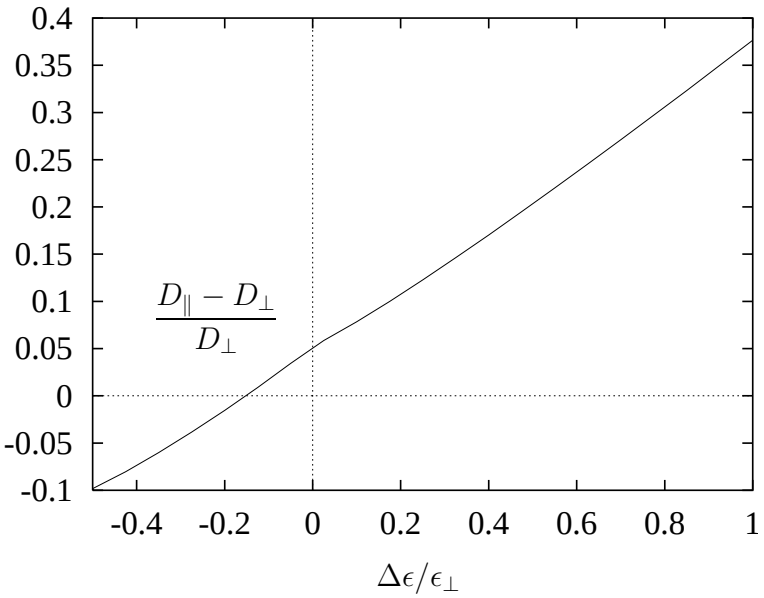


Figure 10.5: Relative anisotropy $(D_\parallel - D_\perp)/D_\perp$ as a function of $\Delta\epsilon/\epsilon_\perp$ for $K_1 = K_2 = K_3$.

obvious since light scattering from director modes increases if they fluctuate stronger. At the extreme values of $K_1/K_3 = K_2/K_3 = 0.01$, we obtain $\widetilde{D}_\perp = 0.07$. The contour lines reveal an asymmetry between the splay ($K_1$) and the twist ($K_2$) distortions. $\widetilde{D}_\perp$ decreases more strongly with $K_2/K_3$. The diffusion constant $\widetilde{D}_\parallel$ exhibits a similar behavior. Fig. 10.7 illustrates the anisotropy $(D_\parallel - D_\perp)/D_\perp$ for the same range. It grows with decreasing elastic constants, demonstrating that $\widetilde{D}_\perp$ is more affected by splay and twist distortions than is $\widetilde{D}_\parallel$. The asymmetry between splay and twist is clearly visible. Figures 10.6 and 10.7 cover the range of conventional thermotropic nematics where usually $K_1/K_3 < 1$ and $K_2/K_3 < 1$. In Fig. 10.8 we extend this range to $K_1/K_3 = K_2/K_3 = 10$, and we observe that the anisotropy $(D_\parallel - D_\perp)/D_\perp$ changes sign. The contour line on the base of the coordinate system indicates where $D_\parallel = D_\perp$. Roughly speaking, $D_\parallel < D_\perp$ if $K_1/K_3 > 0.6$ and $K_2/K_3 > 1.4$. It should be possible to achieve such conditions in discotic nematics, which typically exhibit $K_2 > K_1 > K_3$ (see Section 1.1). In a smectic-$A$ phase (Sm-$A$) twist and bend deformations are expelled by the layered structure [72] hence $K_1/K_3 \ll 1$. Unfortunately, this means also that certain scattering vectors show very weak scattering, and the diffusion approximation cannot be achieved for reasonably sized samples. However, in the vicinity of a Sm-$A$-nematic phase transition, where the layered structure of Sm-$A$ softens or starts to form in the nematic phase, the diffusion approximation of light could be used to study the behavior of the Frank elastic constants close to the transition. A third interesting system is a polymer nematic liquid crystal. For long rigid rods, one expects a large splay constant [238, 86]. Taratuta *et al.* [347] determined the Frank elastic constants for a racemic mixture of poly-$\gamma$-benzyl-glutamate (PBG) in a solvent. They determined the ratios $K_1/K_3 = 0.85$ and $K_2/K_3 = 0.07$ with an absolute value of $K_3 = 4.7 \cdot 10^{-7}$ dyn,

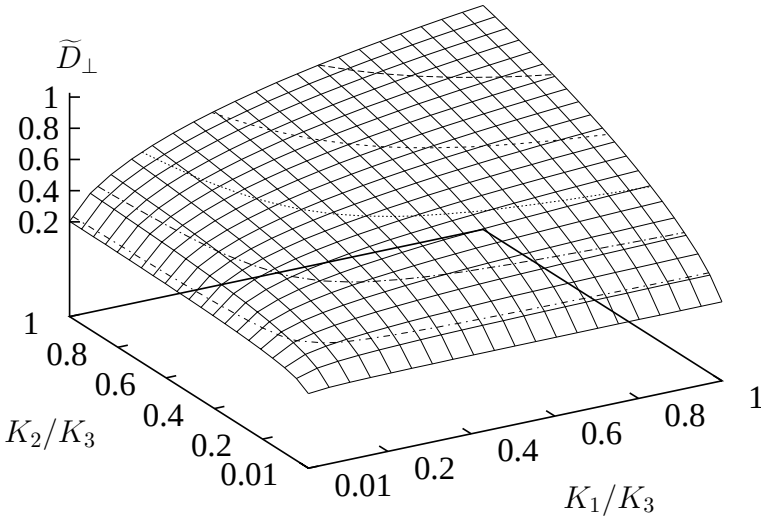


Figure 10.6: Reduced diffusion constant $\widetilde{D}_\perp$ as a function of $K_1/K_3$ and $K_2/K_3$ for $\Delta\epsilon = 0$.

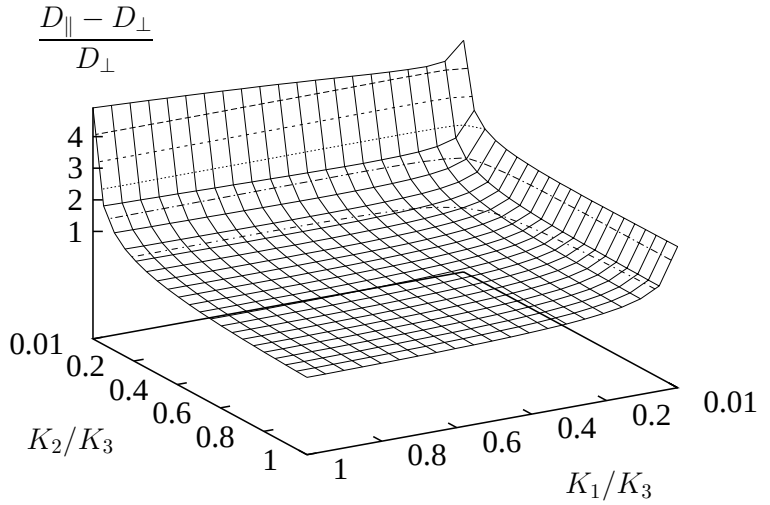


Figure 10.7: Relative anisotropy $(D_\parallel - D_\perp)/D_\perp$ as a function of $K_1/K_3$ and $K_2/K_3$ for $\Delta\epsilon = 0$.

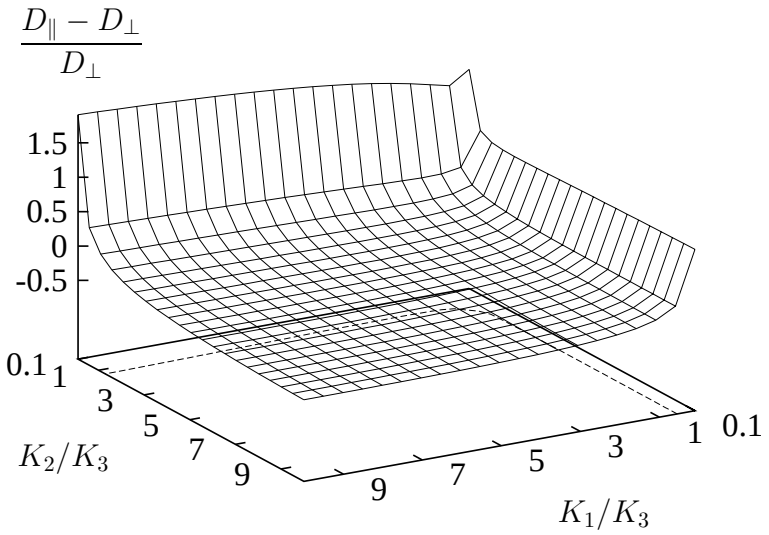


Figure 10.8: Relative anisotropy $(D_\parallel - D_\perp)/D_\perp$ as a function of $K_1/K_3$ and $K_2/K_3$ for $\Delta\epsilon = 0$. Compared to Fig. 10.7 the reduced elastic constants range from 0.1 to 10.

which is suitable for the diffusion approximation of light. From these parameters we predict a "large" ratio of $D_\parallel/D_\perp = 2.8$. The reported system has a very low dielectric anisotropy $\Delta\varepsilon$ and scatters light only weakly. However, it should be possible to find systems which are more favorable regarding $\Delta\varepsilon$.

### 10.2.5 Diffusing-wave spectroscopy

Finally we use the radiative transfer equation (10.34) to study the transport of electric field correlations ($t \neq 0$) extending the idea of DWS to anisotropic media. We have to restrict ourselves to times $t$ much smaller than the characteristic time scales $\tau_c$ of the system under investigation. In nematic liquid crystals $\tau_c$ corresponds to typical director relaxation times $\tau = \gamma/(Kq_s^2)$, as explained in Section 1.4. For wave numbers $q_s = \omega n/c$ of visible light, $\tau_c$ ranges from 10 to 100 $\mu$s. We rewrite the dynamic structure factor,

$$B_{\alpha\beta}(\hat{\boldsymbol{k}}, \hat{\boldsymbol{q}}, t) = B_{\alpha\beta}(\hat{\boldsymbol{k}}, \hat{\boldsymbol{q}}, 0) + [B_{\alpha\beta}(\hat{\boldsymbol{k}}, \hat{\boldsymbol{q}}, t) - B_{\alpha\beta}(\hat{\boldsymbol{k}}, \hat{\boldsymbol{q}}, 0)] \ . \tag{10.55}$$

In nematics the second part on the right-hand side assumes the form

$$B_{\alpha\beta}(\hat{\boldsymbol{k}}, \hat{\boldsymbol{q}}, t) - B_{\alpha\beta}(\hat{\boldsymbol{k}}, \hat{\boldsymbol{q}}, 0) = -(\Delta\varepsilon)^2 k_\mathrm{B} T \frac{\omega^4}{c^4} \sum_{\delta=1}^{2} \frac{N(\boldsymbol{e}_\alpha, \boldsymbol{e}_\beta, \hat{\boldsymbol{u}}_\delta)}{\eta_\delta(\boldsymbol{q}_s)} \, t \quad \text{for} \quad t \ll \tau_c \tag{10.56}$$

where we performed an expansion of the exponential time factor in expression (10.23). All the coefficients in an angular expansion of $W^\alpha_{\hat{\boldsymbol{k}}}(\boldsymbol{R}, T, t)$ similar to Eq. (10.35) now carry the relative time $t$ as an additional argument. In particular, we introduce the total autocorrelation function

$$\overline{n^3} W_0(\boldsymbol{R}, T, t) = \sum_\alpha \int d\Omega_{\boldsymbol{k}} \, n_\alpha^3(\hat{\boldsymbol{k}}) \, W^\alpha_{\hat{\boldsymbol{k}}}(\boldsymbol{R}, T, t) \tag{10.57}$$

and the total current of electric field correlations

$$\boldsymbol{J}(\boldsymbol{R},T,t) = \boldsymbol{J}^1(\boldsymbol{R},T,t) + \boldsymbol{J}^2(\boldsymbol{R},T,t) = \sum_\alpha \int d\Omega_{\boldsymbol{k}}\, n_\alpha^3\, \boldsymbol{v}_{g\alpha}\, W^\alpha_{\hat{\boldsymbol{k}}}(\boldsymbol{R},T,t) \ . \tag{10.58}$$

Repeating the derivation of the continuity equation (10.42), we obtain

$$\left[\frac{\partial}{\partial T} + \mu(t)\right] \overline{n^3} W_0(\boldsymbol{R},T,t) + \boldsymbol{\nabla}\cdot\boldsymbol{J}(\boldsymbol{R},T,t) = \text{source} \ . \tag{10.59}$$

Due to the dynamic absorption term $\mu(t)\,\overline{n^3}W_0(\boldsymbol{R},T,t)$, temporal correlations are not conserved since they decay to zero. Note that the dynamic absorption coefficient $\mu(t)$ is still a scalar quantity. It generally follows from an angular average over all dynamic modes of the system under investigation,

$$\mu(t) = \frac{c}{8\pi\overline{n^3}} \sum_{\alpha\beta} \int\int \frac{d\Omega_{\boldsymbol{k}} d\Omega_{\boldsymbol{q}}}{(4\pi)^2}\, n_\alpha^3(\hat{\boldsymbol{k}})[B_{\alpha\beta}(\hat{\boldsymbol{k}},\hat{\boldsymbol{q}},0) - B_{\alpha\beta}(\hat{\boldsymbol{k}},\hat{\boldsymbol{q}},t)] n_\beta^3(\hat{\boldsymbol{q}}) \ . \tag{10.60}$$

Hence, DWS can only provide a gobal view on the dynamics of an anisotropic system. We neglect additional terms in Eq. (10.59) containing higher coefficients $W^\alpha_{lm}$. Such terms are small due to the assumption that $t \ll \tau_c$. The same applies to Fick's law of Eq. (10.43), so that we finally arrive at the diffusion equation with dynamic absorption,

$$\left[\frac{\partial}{\partial T} - D_\parallel \nabla_\parallel^2 - D_\perp \boldsymbol{\nabla}_\perp^2 + \mu(t)\right] W(\boldsymbol{R},T,t) = \text{source} \ , \tag{10.61}$$

as the basis of DWS.

We calculate the absorption coefficient for director modes by combining Eqs. (10.60) and (10.56):

$$\mu(t) = \mu_0 t \qquad \text{with} \qquad \mu_0 = \frac{2k_BT}{9\pi}\,\frac{\omega^4}{c^3}\,\frac{(\Delta\varepsilon)^2}{\sqrt{\varepsilon_\perp}}\,\frac{\widetilde{\mu}}{\gamma} \ . \tag{10.62}$$

The numerial factor $\widetilde{\mu}$ represents a dimensionless angular average,

$$\widetilde{\mu} = \frac{9}{8(\varepsilon_\perp+\varepsilon_\parallel)} \sum_{\alpha,\beta,\delta} \int\int \frac{d\Omega_{\boldsymbol{k}} d\Omega_{\boldsymbol{q}}}{(4\pi)^2}\, \frac{n_\alpha^3(\hat{\boldsymbol{k}})\, N(\boldsymbol{e}_\alpha,\boldsymbol{e}_\beta,\hat{\boldsymbol{u}}_\delta)\, n_\beta^3(\hat{\boldsymbol{q}})}{\eta_\delta(\boldsymbol{q}_s)} \ , \tag{10.63}$$

which is only a function of reduced Leslie viscosities $\alpha_i/\gamma$ and $\Delta\varepsilon/\varepsilon_\perp$. We haven chosen the factor such that $\widetilde{\mu} = 1$ if $\eta_\delta(\boldsymbol{q}_s) = \gamma$ and $\Delta\varepsilon = 0$. In the case of $\eta_\delta(\boldsymbol{q}_s) = \gamma$, we find $\widetilde{\mu} = [1 + \Delta\varepsilon/(4\varepsilon_\perp]/[1 + \Delta\varepsilon/(2\varepsilon_\perp]$. In conventional thermotropic nematics $\widetilde{\mu}$ is always of the order of one. Note that the absorption coeffient $\mu(t)$ depends on viscosities only and not at all on the Frank elastic constants. They cancel because they determine both the static light scattering as well as the hydrodynamics of director modes. This is in contrast to colloidal suspensions where $\mu_0 = 2D_B\omega^2/(\ell^*\frac{c}{n})$. The mean free path $\ell^*$ characterizes light diffusion and $D_B$ the Brownian motion of colloidal particles.

For the nematic compound 5CB, $\gamma/\widetilde{\mu} = 0.60 \pm .20\,\mathrm{P}$ was determined experimentally by Kao *et al.* using DWS and Eq. (10.62) [170, 336]. This value is in good agreement with the rotational viscosity $\gamma = 0.81\,\mathrm{P}$ of 5CB [58] demonstrating the validity of the theory. The numerical factor amounts to $\widetilde{\mu} = 1.3 \pm 0.3$ and can be verified roughly by Eq. (10.63)

Down to the experimental resolution of $4 \times 10^{-8}\,\mathrm{s}$, no deviation of the director dynamics from the Erickson-Leslie theory was observed. It should show up in a different temporal power law of $\mu(t)$. It would be interesting to study systems with larger viscosities, like polymer liquid crystals, and to search for such a deviation. As reported in Section 9.1, colloidal particles, *e.g.*, do not exhibit a simple diffusive behavior at short time scales.

### 10.2.6 What is the Transport Mean Free Path?

So far, we have not mentioned the transport mean free path at all. The derivation of the diffusion equation just provides the diffusion tensor $\boldsymbol{D}$. There are, at the moment, several suggestions to define transport mean free paths, which we review shortly.

The first suggestion uses the classical relation $D = c\ell^*/(3\overline{n})$. With the help of an appropriately averaged refractive index $\overline{n}$, two transport mean free paths can be introduced according to $\ell^*_\parallel = 3\overline{n}D_\parallel/c$ and $\ell^*_\perp = 3\overline{n}D_\perp/c$ [336].

In Monte Carlo simulations of multiple scattering a large amount of photons are launched along one particular direction specified by the unit vector $\hat{\boldsymbol{\nu}}$. After a sufficient amount of scattering events, the photons are in the diffusion regime. A transport mean free path $\ell^*(\hat{\boldsymbol{\nu}})$ can be defined as the displacement of the center of mass of the diffuse photon cloud with respect to the starting point of the photons [336].

In isotropic diffusion $\ell^*$ enters explicitly via the boundary condition in Eq. (9.20). Its generalization to anisotropic diffusion becomes very complicated, and we do not formulate it here. Tiggelen et al. consider an infinite slab of thickness $L$, whose surface normal points along the unit vector $\hat{\boldsymbol{\nu}}$. They give an expression for the total transmission coefficient of light summed over direction and polarization [364, 369],

$$T(L) = \frac{2\,\hat{\boldsymbol{\nu}} \cdot \boldsymbol{D}\hat{\boldsymbol{\nu}}/v_E(\hat{\boldsymbol{\nu}})}{L} \quad , \tag{10.64}$$

where

$$v_E(\hat{\boldsymbol{\nu}}) = 2 \sum_{\alpha=1,2} \int n^3_\alpha(\hat{\boldsymbol{k}})\,[\boldsymbol{v}_{g\alpha}(\hat{\boldsymbol{k}}) \cdot \hat{\boldsymbol{\nu}}]\,d\Omega^+_{\boldsymbol{k}} \Big/ \sum_{\alpha=1,2} \int n^3_\alpha(\hat{\boldsymbol{k}})\,d\Omega^+_{\boldsymbol{k}} \tag{10.65}$$

defines some weighted average of the group velocities over the solid angle $\Omega^+_{\boldsymbol{k}}$ corresponding to transmitted photons, *i.e.*, photons whose group velocities are directed outward from the slab. We can call $3\,\hat{\boldsymbol{\nu}} \cdot \boldsymbol{D}\hat{\boldsymbol{\nu}}/v_E$ the transport mean free path $\ell^*(\hat{\boldsymbol{\nu}})$, so that Eq. (10.64) takes the form of Ohm's classical law $T = 2\ell^*/3L$.

# Final Remarks

In this work we have demonstrated that inhomogeneous nematic liquid crystals are challenging systems for discovering and studying new physical effects and ideas. They are not only interesting by themselves but they also offer the opportunity to explore different fascinating research fields. As such, we could establish connections both to colloid science and to wave propagation in disordered media.

Colloidal dispersions in a nematic liquid crystal introduce a new class of long-range two-particle interactions mediated by the distorted director field. They are of either dipolar or quadrupolar type depending on whether the single particles exhibit the dipole, Saturn-ring or surface-ring configuration. The dipolar forces were verified in an excellent experiment by P. Poulin *et al.* [276]. Via the well-known flexoelectric effect [235], strong director distortions in the dipole configuration should induce an electric dipole associated with each particle. It would be interesting to study, both theoretically and experimentally, how this electric dipole contributes to the dipolar force. On the other hand, there exists a strong short-range repulsion between particles due to the presence of a hyperbolic point defect which prevents, *e.g.*, water droplets from coalescing. Even above the nematic-isotropic phase transition, liquid crystals mediate an attractive interaction at a length scale of 10 nm. Its strength is easily controlled by temperature, and it produces an observable effect since it can induce flocculation when the system is close to the phase transition.

To understand colloidal dispersions in nematics in detail, we have performed an extensive study of the three possible director configurations around a single particle. These configurations are ideal objects to investigate the properties of topological point and line defects. The dipolar structure should exhibit a twist in conventional calamitic compounds. The transition from the dipole to the Saturn ring can be controlled, *e.g.*, by a magnetic field which presents a means to access the dynamics of topological defects. Furthermore, we have studied how the strength of surface anchoring influences the director configuration. Surface effects are of considerable importance in display technology, and there is fundamental interest in understanding the coupling between liquid crystal molecules and surfaces. In addition, we have clarified the mechanism due to which the saddle-splay term in the Frank free energy promotes the formation of the surface-ring structure. Stokes drag and Brownian motion in nematics have hardly been studied experimentally. Especially the dipole configuration with its vector symmetry presents an appealing object. We have calculated its Stokes drag for a fixed director field. However, we have speculated that for small Ericksen numbers ($Er \ll 1$) flow-induced distortions of the director field result in

corrections to the Stokes drag which are of the order of $Er$. Finally, we have demonstrated that the dipole, consisting of the spherical particle and its companion point defect, also exists in more complex geometries, and we have studied in detail how it forms.

On the other hand, multiply scattered light has a lot of fascinating implications, including the possibility of localizing light in a disordered system, "hidden" correlations in the speckle pattern of strongly scattering media, and photonic band gap materials. The diffusion limit is a very successful regime to describe light transport in random media. Diffusing-wave spectroscopy (DWS), which monitors the dynamics of turbid systems at time scales much shorter than their characteristic times, and the imaging of large-scale inhomogeneities present attractive applications for diffusing light. In this work we have generalized the theory of diffuse correlation transport of light to random anisotropic media, and we have tested our formalism by applying it to director fluctuations in nematics for which single light scattering is well understood. Many new phenomena appear and questions arise which are worthwhile to explore. Is it possible to detect the equipartition of energy on all available photon states in diffusing light? In nematics, it results in an anisotropic distribution of energy on the light modes characterized by polarization and direction of propagation. Can DWS illuminate the short time dynamics of director fluctuations, and can theory predict a deviation from their conventional diffusive behavior? We have thoroughly studied the diffusion constants of light as a function of magnetic field and the three Frank elastic constants. Discotic materials, polymer liquid crystals, and the nematic phase close to the nematic-smectic phase transition exhibit a large variation in the three Frank constants. So far, these systems have not been explored in experiment. All our calculations are performed within the weak-scattering approximation which implies the popular picture of subsequent scattering from regions of director fluctuations well separated in space, reminiscent of scattering in colloidal systems. The question arises what happens, both theoretically and experimentally, if one exceeds the validity of approximation? The coherent backscattering cone in aligned nematics has already been observed, however, its anisotropy still needs to be studied both in experiment and in theory. A numerical approach exists [151].

Beyond the uniformly aligned nematic, liquid crystals offer a wealth of multiply scattering materials which suggest an application of radiative transfer theory and diffusive light transport. We mention porous media filled with nematics [18], polymer dispersed liquid crystals (PDLC) [85, 88], focal conic textures in cholesterics [398], and the Blue Phase III [189, 217, 99, 327]. The last two materials are especially appealing because they are chiral and possess an intrinsic periodic structure from which light is scattered. The scattering cross section heavily depends on the circular polarization of light. It was found recently that the Blue Phase III constitutes an isotropic phase with strong chiral fluctuations. PDLCs have rather dramatic light scattering properties, which can be switched from an opaque to a clear state by an external electric field. Scattering from PDLC films has been investigated mostly in the anomalous diffraction and Rayleigh-Gans approximation [88, 355, 172, 60, 61]. A complete understanding of this transition can only be obtained from the equation of radiative transfer, which covers the regime from single to multiple scattering completely. Also applications to lyotropic and polymeric liquid crystals and to

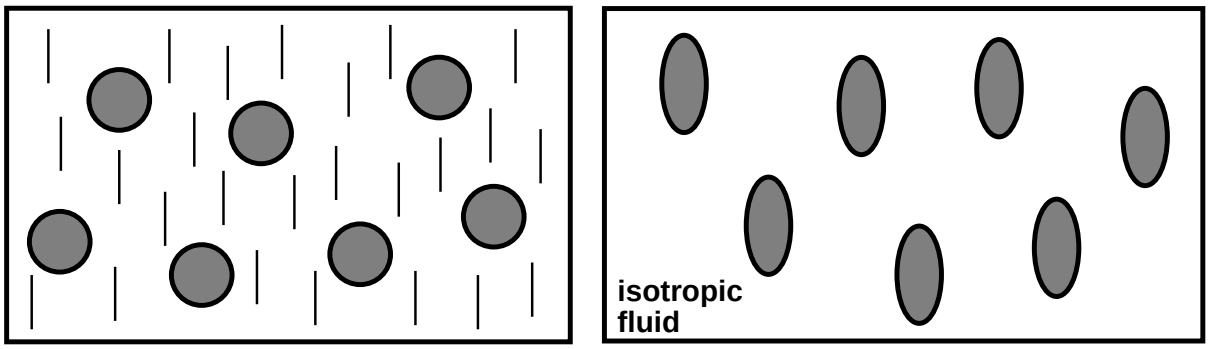


Figure 10.9: (left) Spherical particles dispersed in a uniformly aligned nematic. Anisotropic light diffusion originates in the host medium only. (right) Ellipsoidal particles dispersed in an isotropic liquid. Anisotropic light diffusion originates in the scatterers only.

liquid crystalline colloids could be of interest.

Both topics treated in this work are strongly connected. Colloidal particles dispersed in a nematic liquid crystal offer an appealing possibility to study multiple scattering of light. In the so-called filled nematics [95, 183, 182, 19], silica spheres are clued together by hydrogen and chemical bonds. As a result, they form a gel-like network which causes the formation of domains with different director orientation. These domains strongly scatter light. To test our ideas of diffusing light in an overall anisotropic system, we suggest, however, two ideal situations. In the first one, spherical particles are dispersed in a uniformly aligned nematic, as depicted in Fig. 10.9 (left). The only source for anisotropic light diffusion is the host medium and no longer the weak scattering from director fluctuations which is negligible compared to the scattering from particles. Such a situation can be handled with the formalism presented in Chapter 10. We only have to replace the structure function of director fluctuations by the appropriate quantity for the particles. However, a clear experiment requires the director field around the particles to be undistorted, in order to exclude light scattering from the non-uniform director field. This might be achieved by weak surface anchoring of the directors and by applying a strong magnetic field[2]. The opposite ideal case refers to liquid crystalline colloids. They consist of anisotropic particles uniformly aligned in an isotropic solvent, as illustrated in Fig. 10.9 (right). Here, anisotropic light diffusion completely originates in the scatterers. It has recently been observed in magnetorheological suspensions where paramagnetic particles form long chains under the influence of an applied magnetic field [126].

The two ideal situations demonstrate explicitly that nematic colloidal dispersions and multiple scattering of light provide topics which stimulate a wealth of new physical ideas. A part of these ideas was treated in the present work.

[2]Single scattering from spherical particles with weak surface anchoring dispersed in an oriented nematic was treated in Ref. [273] within the weak-scattering approximation. However, the authors neglect the birefringence of the nematic phase which is crucial in our case.

# Bibliography


[1] E. Abrahams, P. W. Anderson, D. C. Licciardello, and T. V. Ramakrishnan, Scaling Theory of Localization: Absence of Quantum Diffusion in Two Dimensions, Phys. Rev. Lett. **42**(10), 673–676 (March 1979).

[2] A. A. Abrikosov, On the Magnetic Properties of Superconductors of the Second Group, Sov. Phys. JETP **5**(6), 1174–1182 (December 1957), [Zh. Eksp. Teor. **32**, 1442 (1957)].

[3] B. J. Ackerson, R. L. Dougherty, N. M. Reguigui, and U. Nobbmann, Correlation transfer: Application of radiative transfer solution methods to photon correlation problems, J. Thermophys. Heat Transfer **6**, 577–588 (1992).

[4] A. Ajdari, B. Duplantier, D. Hone, L. Peliti, and J. Prost, "Pseudo-Casimir" effect in liquid crystals, J. Phys. II France **2**, 487–501 (March 1992).

[5] A. Ajdari, L. Peliti, and J. Prost, Fluctuation-Induced Long-Range Forces in Liquid Crystals, Phys. Rev. Lett. **66**(11), 1481–1484 (March 1991).

[6] E. Akkermans and R. Maynard, Weak localization of waves, J. Physique Lett. **46**, L1045–L1053 (November 1985).

[7] E. Akkermans, P. E. Wolf, and R. Maynard, Coherent Backscattering of Light by Disordered Media: Analysis of the Peak Line Shape, Phys. Rev. Lett. **56**(14), 1471–1474 (April 1986).

[8] E. Akkermans, P. E. Wolf, R. Maynard, and G. Maret, Theoretical study of the coherent backscattering of light by disordered media, J. Phys. France **49**, 77–98 (January 1988).

[9] E. Allahyarov, I. D'Amico, H. Löwen, Attraction between Like-Charged Macroions by Coulomb Depletion, Phys. Rev. Lett. **81**(6), 1334–1337 (August 1998).

[10] D. W. Allender, G. P. Crawford, and J. W. Doane, Determination of the Liquid-Crystal Surface Elastic Constant $K_{24}$, Phys. Rev. Lett. **67**(11), 1442–1445 (September 1991).

[11] B. L. Al'tshuler and P. A. Lee, Disordered Electronic Systems, Phys. Today **41**(12), 36–44 (December 1988).

[12] P. W. Anderson, Absence of Diffusion in Certain Random Lattices, Phys. Rev. **109**(5), 1492–1505 (March 1958).

[13] P. W. Anderson, The question of classical localization: A theory of white paint?, Philos. Mag. B **52**(3), 505–509 (1985).

[14] K. Arya, Z. B. Su, and J. L. Birman, Anderson Localization of Electromagnetic Waves in a Dielectric Medium of Randomly Distributed Metal Particles, Phys. Rev. Lett. **57**(21), 2725–2728 (November 1986).

[15] R. J. Atkin, Poiseuille Flow of Liquid Crystals of the Nematic Type, Arch. Ratl. Mech. Anal. **38**, 224–240 (1970).

[16] R. J. Atkin and F. M. Leslie, Couette Flow of Nematic Liquid Crystals, Quart. J. Mech. Appl. Math. **23**, S3–S24 (1970).

[17] G. Barbero and C. Oldano, Derivativ-Dependent Surface-Energy Terms in Nematic Liquid Crystals, Nuovo Cimento **6D**(5), 479–493 (November 1985).

[18] T. Bellini and N. A. Clark, *Light Scattering as a Probe of Liquid Crystal Ordering in Silica Aerogels*, in *Liquid Crystals in Complex Geometries*, edited by G. P. Crawford and S. Žumer, pages 381–409, Taylor & Francis, London (1996).

[19] T. Bellini, N. A. Clark, V. Degiorgio, F. Mantegazza, and G. Natale, Light-scattering measurment of the nematic correlation length in a liquid crystal with quenched disorder, Phys. Rev. E **57**(3), 2996–3006 (March 1998).

[20] R. Berkovits and S. Feng, Theory of Speckle-Pattern Tomography in Multiple-Scattering Media, Phys. Rev. Lett. **65**(25), 3120–3123 (December 1990).

[21] B. J. Berne and R. Pecora, *Dynamic Light Scattering – with applications to chemistry, biology, and physics*, John Wiley & Sons, Incorporated, New York (1976).

[22] D. Bicout, E. Akkermans, and R. Maynard, Dynamical correlations for multiple light scattering in laminar flow, J. Phys. I France **1**, 471–491 (April 1991).

[23] D. Bicout and G. Maret, Multiple light scattering in Taylor-Couette flow, Physica A **210**, 87–112 (1994).

[24] D. J. Bicout and R. Maynard, Multiple light scattering in turbulent flow, Physica B **204**, 20–26 (1995).

[25] R. B. Bird, W. E. Stewart, and E. N. Lightfoot, *Transport Phenomena*, John Wiley, New York (1960).

[26] A. Birner, K. Busch, and F. Müller, Photonische Kristalle, Phys. Bl. **55**(4), 27–33 (April 1999).

[27] C. Blanc and M. Kleman, The confinement of smectics with a strong anchoring, submitted to Eur. Phys. J. E.

[28] G. Blatter, M. V. Feigel'mann, V. B. Geshkenbein, A. I. Larkin, and V. M. Vinokur, Vortices in high-temperature superconductors, Rev. Mod. Phys. **66**(4), 1125–1388 (October 1994).

[29] L. M. Blinov, A. Y. Kabayenkov, and A. A. Sonin, Experimental studies of the anchoring energy of nematic liquid crystals, Liq. Cryst. **5**(2), 645–661 (1989).

[30] D. A. Boas, L. E. Campbell, and A. G. Yodh, Scattering and imaging with diffusing temporal field correlations, Phys. Rev. Lett. **75**(9), 1855–1858 (August 1995).

[31] D. A. Boas, M. A. O'Leary, B. Chance, and A. G. Yodh, Scattering and wavelength transduction of diffuse photon density waves, Phys. Rev. E **47**(5), R2999–R3003 (May 1993).

[32] D. A. Boas and A. G. Yodh, Spatially varying dynamic properties of turbid media probed with diffusing temporal light correlation, J. Opt. Soc. Am. A **14**(1), 192–215 (January 1997).

[33] A. Borštnik, H. Stark, and S. Žumer, Interaction of spherical particles dispersed in liquid crystals above the nematic-isotropic phase transition, Phys. Rev. E **60**(4), 4210–4218 (October 1999).

[34] A. Borštnik, H. Stark, and S. Žumer, Temperature-induced flocculation of colloidal particles immersed into the isotropic phase of a nematic liquid crystal, Phys. Rev. E **61**(3), 2831-2839 (March 2000).

[35] A. Borštnik, H. Stark, and S. Žumer, Temperature-Induced Flocculation of Colloidal Particles Above the Nematic-Isotropic Phase Transition, Progr. Colloid Polym. Sci **115**, 353–356 (2000).

[36] A. Borštnik and S. Žumer, Forces in an inhomogeneously ordered nematic liquid crystal, Phys. Rev. E **56**(3), 3021–3027 (September 1997).

[37] A. Böttger, D. Frenkel, E. van de Riet, and R. Zijlstra, Diffusion of Brownian particles in the isotropic phase of a nematic liquid crystal, Mol. Cryst. Liq. Cryst. **2**(4), 539–547 (1987).

[38] W. E. Boyce and R. C. Di Prima, *Elementary Differential Equations*, John Wiley, New York (1992).

[39] A. Bray, Theory of phase-ordering kinetics, Adv. Phys. **43**(3), 357–459 (1994).

[40] F. Brochard and P. G. de Gennes, Theory of Magnetic Suspensions in Liquid Crystals, J. Phys. (Paris) **31**, 691–708 (July 1970).

[41] R. Bubeck, C. Bechinger, S. Neser, and P. Leiderer, Melting and Reentrant Freezing of Two-Dimensional Colloidal Crystals in Confined Geometry, Phys. Rev. Lett. **82**(16), 3364–3367 (April 1999).

[42] S. V. Burylov and Y. L. Raikher, Orientation of a solid particle embedded in a monodomain nematic liquid crystal, Phys. Rev. E **50**(1), 358–367 (July 1994).

[43] K. Busch and S. John, Liquid Crystal Photonic Band Gap Materials: The Tunable Electromagnetic Vacuum, Phys. Rev. Lett. **83**(5), 967–970 (August 1999).

[44] H. B. Callen, *Thermodynamics and an Introduction to Thermostatistics*, John Wiley & Sons, New York, second edition (1985).

[45] S. Candau, P. L. Roy, and F. Debeauvais, Magnetic Field Effects in Nematic and Cholesteric Droplets Suspended in an Isotropic Liquid, Mol. Cryst. Liq. Cryst. **23**, 283–297 (1973).

[46] P. Chaikin and T. C. Lubensky, *Principles of Condensed Matter Physics*, Cambridge University Press, Cambridge (1995).

[47] S. Chandrasekhar, Stochastic problems in physics and astronomy, Rev. Mod. Phys. **15**, 1–89 (1943).

[48] S. Chandrasekhar, *Radiative transfer*, Dover books on intermediate and advanced mathematics, Dover Publications, New York (1960).

[49] S. Chandrasekhar, *Liquid Crystals*, Cambridge University Press, Cambridge, second edition (1992).

[50] S. Chandrasekhar and G. Ranganath, The structure and energetics of defects in liquid crystals, Adv. Phys. **35**(6), 507–596 (1986).

[51] S.-H. Chen and N. M. Amer, Observation of Macroscopic Collective Behavior and New Texture in Magnetically Doped Liquid Crystals, Phys. Rev. Lett. **51**(25), 2298–2301 (December 1983).

[52] A. J. Chorin, A Numerical Method for Solving Incompressible Viscous Flow Problems, J. Comput. Phys. **2**, 12–26 (1967).

[53] I. Chuang, R. Durrer, N. Turok, and B. Yurke, Cosmology in the Laboratory: Defect Dynamics in Liquid Crystals, Science **251**, 1336–1342 (March 1991).

[54] P. E. Cladis and M. Kléman, Non-Singular Disclinations of Strength $S = +1$ in Nematics, J. Phys. (Paris) **33**, 591–598 (May-June 1972).

[55] P. E. Cladis, M. Kléman, and P. Piéranski, Sur une nouvelle méthode de décoration de la mésomorphe du p,n-méthoxybenzilidène p-bétylaniline (MBBA), C. R. Acad. Sci. Ser. B **273**, 275–277 (1971).

[56] P. E. Cladis, W. van Saarloos, P. L. Finn, and A. R. Kortan, Dynamics of Line Defects in Nematic Liquid Crystals, Phys. Rev. Lett. **58**(3), 222–225 (January 1987).

[57] H. J. Coles, Laser and Electric Field Induced Birefringence Studies on the Cyanobiphenyl Homologues, Mol. Cryst. Liq. Cryst. Lett. **49**, 67–74 (1978).

[58] P. Collings (1995), private communication.

[59] M. Čopič and A. Mertelj, Reorientation in Random Potential: A Model for Glasslike Dynamics in Confined Liquid Crystals, Phys. Rev. Lett. **80**(7), 1449–1452 (February 1998).

[60] S. J. Cox, V. Y. Reshetnyak, and T. J. Sluckin, Effective Medium Theory of Light Scattering in PDLC Films, J. Phys. D **31**(14), 1611 (1998).

[61] S. J. Cox, V. Y. Reshetnyak, and T. J. Sluckin, Theory of Dielectric and Optical Properties of PDLC Films, Mol. Cryst. Liq. Cryst. **320**, 301–319 (1998).

[62] G. P. Crawford, D. W. Allender, and J. W. Doane, Surface elastic and molecular-anchoring properties of nematic liquid crystals confined to cylindrical cavities, Phys. Rev. A **45**(12), 8693–8708 (June 1992).

[63] G. P. Crawford, D. W. Allender, J. W. Doane, M. Vilfan, and I. Vilfan, Finite molecular anchoring in the escaped-radial nematic configuration: A $^2$H-NMR study, Phys. Rev. A **44**(4), 2570–2576 (August 1991).

[64] G. P. Crawford, R. Ondris-Crawford, S. Žumer, and J. W. Doane, Anchoring and Orientational Wetting Transitions of Confined Liquid Crystals, Phys. Rev. Lett. **70**(12), 1838–1841 (March 1993).

[65] G. P. Crawford, R. J. Ondris-Crawford, J. W. Doane, and S. Žumer, Systematic study of orientational wetting and anchoring at a liquid-crystal–surfactant interface, Phys. Rev. E **53**(4), 3647–3661 (April 1996).

[66] G. P. Crawford and S. Žumer, editors, *Liquid Crystals in Complex Geometries*, Taylor & Francis, London (1996).

[67] J. C. Crocker and D. G. Grier, When Like Charges Attract: The Effects of Geometrical Confinement on Long-Range Colloidal Interactions, Phys. Rev. Lett. **77**(9), 1897–1900 (August 1996).

[68] P. K. Currie, Couette Flow of a Nematic Liquid Crystal in the Presence of a Magnetic Field, Arch. Ratl. Mech. Anal. **37**, 222–242 (1970).

[69] P. K. Currie, Apparent viscosity during viscometric flow of nematic liquid crystals, J. Phys. (Paris) **40**, 501–505 (May 1979).

[70] R. Dalichaouch, J. P. Armstrong, S. Schultz, P. M. Platzman, and S. L. McCall, Microwave localization by two-dimensional random scattering, Nature **354**, 53–55 (November 1991).

[71] J. F. de Boer, M. C. W. van Rossum, M. P. van Albada, T. M. Nieuwenhuizen, and A. Lagendijk, Probability Distribution of Multiple Scattered Light Measured in Total Transmission, Phys. Rev. Lett. **73**(19), 2567–2570 (November 1994).

[72] P. G. de Gennes, Conjectures sur l'état smectique, J. Phys. (Paris) Coll. C4 **30**(11-12), 65–71 (1969).

[73] P. G. de Gennes, Short Range Order Effects in the Isotropic Phase of Nematics and Cholesterics, Mol. Cryst. Liq. Cryst. **12**, 193–214 (1971).

[74] P. G. de Gennes, *Nematodynamics*, in *Molecular Fluids*, edited by R. Balian and G. Weill, pages 373–400, Gordon and Breach, London (1976).

[75] P. G. de Gennes, Interactions between Solid Surfaces in a Presmectic Fluid, Langmuir **6**(9), 1448–1450 (1990).

[76] P. G. de Gennes and J. Prost, *The Physics of Liquid Crystals*, volume 83 of *International Series of Monographs on Physics*, Oxford Science Publications, Oxford, second edition (1993).

[77] S. R. de Groot, *Thermodynamics of Irreversible Processes*, Selected Topics in Modern Physics, North-Holland Publishing Company, Amsterdam (1951).

[78] D. A. De Wolf, Electromagnetic Reflection from an Extended Turbulent Medium: Cumulative Forward-Scatter Single-Backscatter Approximation, IEEE Trans. Antennas Propag. **AP-19**(2), 254–262 (March 1971).

[79] P. N. den Outer and T. M. Nieuwenhuizen, Location of objects in multiple-scattering media, J. Opt. Soc. Am. A **10**(6), 1209–1218 (June 1993).

[80] B. V. Derjaguin, Friction and adhesion. IV: The theory of adhesion of small particles, Kolloid Z. **69**, 155–164 (1934).

[81] B. V. Derjaguin and L. Landau, Theory of the stability of strongly charged lyophobic sols and the adhesion of strongly charged particles in solutions of electrolytes, Acta Physicochim. URSS **14**, 633–662 (1941).

[82] A. D. Dinsmore, D. T. Wong, P. Nelson, and A. G. Yodh, Hard Spheres in Vesicles: Curvature-Induced Forces and Particle-Induced Curvature, Phys. Rev. Lett. **80**(2), 409–412 (January 1998).

[83] A. D. Dinsmore, A. G. Yodh, and D. J. Pine, Entropic control of particle motion using passive surface microstructures, Nature **383**, 239–244 (September 1996).

[84] A. C. Diogo, Friction Drag on a Sphere Moving in a Nematic Liquid Crystal, Mol. Cryst. Liq. Cryst. **100**, 153–165 (1983).

[85] J. W. Doane, N. A. Vaz, B. G. Wu, and S. Žumer, Field controlled light scattering from nematic microdroplets, Appl. Phys. Lett. **48**, 269–271 (1986).

[86] A. M. Donald and A. H. Windle, *Liquid Crystalline Polymers*, Cambridge Solid State Science Series, Cambridge University Press, Cambridge, first edition (1992).

[87] R. L. Dougherty, B. J. Ackerson, N. M. Reguigui, F. Dorri-Nowkoorani, and U. Nobbmann, Correlation Transfer: Development and Application, J. Quant. Spectrosc. & Radiat. Transfer **52**(6), 713–727 (1994).

[88] P. S. Drzaic, *Liquid Crystal Dispersions*, volume 1 of *Series on Liquid Crystals*, World Scientific Publishing, Singapore (1995).

[89] E. Dubois-Violette and O. Parodi, Émulsions nématiques. Effets de champ magnétiques et effets piézoélectriques, J. Phys. (Paris) Coll. C4 **30**(11-12), 57–64 (1969).

[90] D. J. Durian, D. A. Weitz, and D. J. Pine, Multiple Light-Scattering Probes of Foam Structure and Dynamics, Science **252**, 686–688 (May 1991).

[91] D. J. Durian, D. A. Weitz, and D. J. Pine, Scaling behavior in shaving cream, Phys. Rev. A **44**(12), R7902–R7905 (December 1991).

[92] J. C. Earnshaw and A. H. Jaafar, Diffusing-wave spectroscopy pf a flowing foam, Phys. Rev. E **49**(6), 5408–5411 (June 1994).

[93] J. C. Earnshaw and M. Wilson, Strain-induced dynamics of flowing foam: an experimental study, J. Phys. Cond. Mat. **7**, L49–L53 (1995).

[94] J. C. Earnshaw and M. Wilson, A Diffusing Wave Spectroscopy Study of Constrictive Flow of Foam, J. Phys. II France **6**, 713–722 (May 1996).

[95] R. Eidenschink and W. H. de Jeu, Static scattering in filled nematic: new liquid crystal display technique, Electron. Lett. **27**, 1195 (1991).

[96] A. Einstein, Über die von der molekularkinetischen Theorie der Wärme geforderte Bewegung von in ruhenden Flüssigkeiten suspendierten Teilchen, Ann. Phys. (Leipzig) **17**, 549–560 (1905).

[97] A. Einstein, Eine neue Bestimmung der Moleküldimensionen, Ann. Phys. (Leipzig) **19**, 289–306 (1906).

[98] A. Einstein, Zur Theorie der Brownschen Bewegung, Ann. Phys. (Leipzig) **19**, 371–381 (1906).

[99] J. Englert, L. Longa, H. Stark, and H.-R. Trebin, Fluctuations Dominate the Phase Diagram of Chiral-Nematic Liquid Crystals, Phys. Rev. Lett. **81**(7), 1457–1460 (August 1998).

[100] F. A. Erbacher, R. Lenke, and G. Maret, Multiple Light Scattering in Magneto-optically Active Media, Europhys. Lett. **21**(5), 551–556 (February 1993).

[101] J. H. Erdmann, S. Žumer, and J. W. Doane, Configuration Transition in a Nematic Liquid Crystal Confined to a Small Spherical Cavity, Phys. Rev. Lett. **64**(16), 1907–1910 (April 1990).

[102] J. L. Ericksen, Anisotropic Fluids, Arch. Ratl. Mech. Anal. **4**, 231–237 (1960).

[103] J. L. Ericksen, Theory of Anisotropic Fluids, Trans. Soc. Rheol. **4**, 29–39 (1960).

[104] J. L. Ericksen, Conservation Laws of Liquid Crystals, Trans. Soc. Rheol. **5**, 23–34 (1961).

[105] J. L. Ericksen, Continuum Theory of Liquid Crystals, Appl. Mech, Rev. **20**(11), 1029–1032 (November 1967).

[106] J. L. Ericksen, Continuum Theory of Liquid Crystals of Nematic Type, Mol. Cryst. Liq. Cryst. **7**, 153–164 (1969).

[107] A. C. Eringen, editor, *Continuum Physics: Volume I-IV*, Academic Press, Incorporated, New York (1976).

[108] A. C. Eringen and C. B. Kafadar, *Part I: Polar Field Theories*, in *Continuum Physics: Volume IV – Polar and Nonlocal Field Theories*, edited by A. C. Eringen, pages 1–73, Academic Press, Incorporated, New York (1976).

[109] S. Etemad, R. Thompson, and M. J. Andrejco, Weak Localization of Photons: Universal Fluctuations and Ensemble Averaging, Phys. Rev. Lett. **57**(5), 575–578 (August 1986).

[110] S. Etemad, R. Thompson, M. J. Andrejco, S. John, and F. C. MacKintosh, Weak Localization of Photons: Termination of Coherent Random Walks by Absorption and Confined Geometry, Phys. Rev. Lett. **59**(13), 1420–1423 (September 1987).

[111] J. Fang, E. Teer, C. M. Knobler, K.-K. Loh, and J. Rudnick, Boojums and the shapes of domains in monolayer films, Phys. Rev. E **56**(2), 1859–1868 (August 1997).

[112] S. Feng, *Novel Correlations and Fluctuations in Speckle Patterns*, in *Scattering and Localization of Classical Waves in Random Media*, volume 8 of *World Scientific Series on Directions in Condensed Matter Physics*, edited by P. Sheng, pages 179–206, World Scientific, Singapore (1990).

[113] S. Feng, C. Kane, P. A. Lee, and A. D. Stone, Correlations and Fluctuations of Coherent Wave Transmission through Disordered Media, Phys. Rev. Lett. **61**(7), 834–837 (August 1988).

[114] S. Feng and P. A. Lee, Mesoscopic Conductors and Correlations in Laser Speckle Patterns, Science **251**, 633–639 (February 1991).

[115] A. M. Figueiredo Neto and M. M. F. Saba, Determination of the minimum concentration of ferrofluid required to orient nematic liquid crystals, Phys. Rev. A **34**(4), 3483–3485 (October 1986).

[116] D. Forster, *Hydrodynamic Fluctuations, Broken Symmetry, and Correlation Functions*, volume 47 of *Frontiers in Physics: A Lecture Note and Reprint Series*, W. A. Benjamin, Incorporated, Massachusetts (1975).

[117] D. Forster, T. Lubensky, P. Martin, J. Swift, and P. Pershan, Hydrodynamics of Liquid Crystals, Phys. Rev. Lett. **26**(17), 1016–1019 (April 1971).

[118] J.-P. Fouque, editor, *Diffuse Waves in Complex Media*, volume 531 of *NATO Science Series C: Mathematical and Physical Sciences*, Kluwer Academic Publishers, Dordrecht (1999).

[119] S. Fraden, *Phase Transitions in Colloidal Suspensions of Virus Particles*, in *Observation, Prediction, and Simulation of Phase Transitions in Complex Fluids*, volume 460 of *NATO Advanced Studies Institute Series C: Mathematical and Physical Sciences*, edited by M. Baus, L. F. Rull, and J. P. Ryckaert, pages 113–164, Kluwer Academic Publishers, Dordrecht (1995).

[120] S. Fraden and G. Maret, Multiple Light Scattering from Concentrated, Interacting Suspensions, Phys. Rev. Lett. **65**(4), 512–515 (July 1990).

[121] F. C. Frank, I. Liquid Crystals: On the Theory of Liquid Crystals, Discuss. Faraday Soc. **25**, 19–28 (1958).

[122] G. Friedel and F. Grandjean, Observation géométriques sur les liquides à coniques focales, Bull. Soc. Fr. Mineral **33**, 409–465 (1910).

[123] G. Friedel, *Dislocations*, Pergamon Press, Oxford (1964).

[124] U. Frisch, *Wave Propagation in Random Media*, in volume I of *Probabilistic Methods in Applied Mathematics*, edited by A. T. Barucha-Reid, pages 75–181, Academic Press, New York (1968).

[125] N. Fuchs, Über die Stabilität und Aufladung der Aerosole, Z. Phys. **89**, 736–743 (1934).

[126] E. M. Furst and A. P. Gast, Particle dynamics in magnetorheological suspensions using diffusing-wave spectroscopy, Phys. Rev. E **58**(3), 3372–3376 (September 1998).

[127] C. Gähwiller, Direct Determination of the Five Independent Viscosity Coefficients of Nematic Liquid Crystals, Mol. Cryst. Liq. Cryst. **20**, 301–318 (1973).

[128] P. Galatola and J. B. Fournier, Nematic-Wetted Colloids in the Isotropic Phase, Mol. Cryst. Liq. Cryst. **330**, 535–539 (1999).

[129] H. Gang, A. H. Krall, and D. A. Weitz, Shape Fluctuations of Interacting Fluid Droplets, Phys. Rev. Lett. **73**(25), 3435–3438 (December 1994).

[130] N. Garcia and A. Z. Genack, Anomalous Photon Diffusion at the Threshold of the Anderson Localization Transition, Phys. Rev. Lett. **66**(14), 1850–1853 (April 1991).

[131] A. Garel, Boundary Conditions for Textures and Defects, J. Phys. (Paris) **39**, 225–229 (1978).

[132] E. C. Gartland (1998), private communication.

[133] E. C. Gartland and S. Mkaddem, Instability of radial hedgehog configurations in nematic liquid crystals under Landau–de Gennes free-energy models, Phys. Rev. E **59**(1), 563–567 (January 1999).

[134] A. P. Gast and W. B. Russel, Simple Ordering in Complex Fluids, Phys. Today **51**(12), 24–30 (December 1998).

[135] A. P. Gast and C. F. Zukoski, Electrorheological Fluids as Colloidal Suspensions, Adv. Colloid Interface Science **30**, 153–202 (1989).

[136] A. Genack and N. Garcia, Observation of Photon Localization in a Three-Dimensional Disordered System, Phys. Rev. Lett. **66**(16), 2064–2067 (April 1991).

[137] T. Gisler and D. A. Weitz, Scaling of the Microrheology of Semidilute F-Actin Solutions, Phys. Rev. Lett. **82**(7), 1606–1609 (February 1999).

[138] A. Glushchenko, H. Kresse, V. Reshetnyak, Yu.Reznikov, and O. Yaroshchuk, Memory effect in filled nematic liquid crystals, Liq. Cryst. **23**(2), 241–246 (1997).

[139] J. Goldstone, Field theories with "superconductor" solutions, Nuovo Cimento **19**(1), 154–164 (January 1961).

[140] J. Goldstone, A. Salam, and S. Weinberg, Broken symmetries, Phys. Rev. **127**(3), 965–970 (August 1962).

[141] A. A. Golubentsev, Suppression of interference effects in multiple scattering of light, Sov. Phys. JETP **59**(1), 26–32 (January 1984), [Zh. Eksp. Teor. Fiz. **86**, 47 (1984)].

[142] J. W. Goodby, M. A. Waugh, S. M. Stein, E. Chin, R. Pindak, and J. S. Patel, Characterization of a new helical smectic liquid crystal, Nature **337**, 449–452 (February 1989).

[143] J. W. Goodby, M. A. Waugh, S. M. Stein, E. Chin, R. Pindak, and J. S. Patel, A New Molecular Ordering in Helical Liquid Crystals, J. Am. Chem. Soc. **111**(21), 8119–8125 (1989).

[144] A. D. Gopal and D. J. Durian, Nonlinear Bubble Dynamics in a Slowly Driven Foam, Phys. Rev. Lett. **75**(13), 2610–2613 (September 1995).

[145] E. Gramsbergen, L. Longa, and W. H. de Jeu, Landau Theory of the Nematic–Isotropic Phase Transition, Phys. Rep. **135**(4), 195–257 (1986).

[146] Groupe d'Etude des Cristaux Liquides, Dynamics of Fluctuations in Nematic Liquid Crystals, J. Chem. Phys. **51**(2), 816–822 (July 1969).

[147] P. Hänggi, P. Talkner, and M. Borkovec, Reaction-rate theory: fifty years after Kramers, Rev. Mod. Phys. **62**(2), 251–341 (April 1990).

[148] M. Heckmeier and G. Maret, Visualization of flow in multiple-scattering liquids, Europhys. Lett. **34**(4), 257–262 (May 1996).

[149] M. Heckmeier and G. Maret, Dark speckle imaging of colloidal suspensions in multiple scattering media, Progr. Colloid. Polym. Sci. **104**, 12 (1997).

[150] M. Heckmeier, S. E. Skipetrov, G. Maret, and R. Maynard, Imaging of dynamic heterogeneities in multiple-scattering media, J. Opt. Soc. Am. A **14**(1), 185–191 (January 1997).

[151] A. Heiderich, R. Maynard, and B. A. van Tiggelen, Multiple Light Scattering in Ordered Nematic Liquid Crystals, J. Phys. II France **7**, 765–792 (May 1997).

[152] W. Helfrich, Capillary flow of cholesteric and smectic liquid crystals, Phys. Rev. Lett. **23**(7), 372–374 (August 1969).

[153] G. Heppke, D. Krüerke, and M. Müller, Surface anchoring of the discotic cholesteric phase of chiral pentayne systems, in *Abstract Book* of 24. Freiburger Arbeitstagung Flüssigkristalle, Freiburg, Germany (1995).

[154] H. Heuer, H. Kneppe, and F. Schneider, Flow of a Nematic Liquid Crystal around a Cylinder, Mol. Cryst. Liq. Cryst. **200**, 51–70 (1991).

[155] H. Heuer, H. Kneppe, and F. Schneider, Flow of a Nematic Liquid Crystal around a Sphere, Mol. Cryst. Liq. Cryst. **214**, 43–61 (1992).

[156] K. M. Ho, C. T. Chan, and C. M. Soukoulis, Existence of a Photonic Gap in Periodic Dielectric Structures, Phys. Rev. Lett. **65**(25), 3152–3155 (December 1990).

[157] H. Hoballah, R. Höhler, and S. Cohen-Addad, Time Evolution of the Elastic Properties of Aqueous Foam, J. Phys. II France **7**, 1215–1224 (September 1997).

[158] R. Höhler, S. Cohen-Addad, and H. Hoballah, Periodic Nonlinear Bubble Motion in Aqueous Foam under Oscillating Shear Strain, Phys. Rev. Lett. **79**(6), 1154–1157 (August 1997).

[159] R. G. Horn, J. N. Israelachvili, and E. Perez, Forces due to structure in a thin liquid crystal film, J. Phys. (Paris) **42**, 39–52 (1981).

[160] R. M. Hornreich, S. Shtrikman, and C. Sommers, Photonic bands in simple and body-centered-cubic cholesteric blue phases, Phys. Rev. E **47**(3), 2067–2072 (March 1993).

[161] C.-Y. Huang, J. J. Stott, and R. G. Petschek, Routes to Self-Assembling Stable Photonic Band-Gap Phases in Emulsions of Chiral Nematics with Isotropic Fluids, Phys. Rev. Lett. **80**(25), 5603–5606 (June 1998).

[162] H. Imura and K. Okano, Friction Coefficient for a Moving Disclination in a Nematic Liquid Crystal, Phys. Lett. A **42**(6), 403–404 (January 1973).

[163] A. Jákli, L. Almásy, S. Borbély, and L. Rosta, Memory of silica aggregates dispersed in smectic liquid crystals: Effect of the interface properties, Eur. Phys. J. B **10**, 509–513 (1999).

[164] A. F. Ioffe and A. R. Regel, Non-Crystalline, Amorphous and Liquid Electronic Semiconductors, Prog. Semicond. **4**, 237–291 (1960).

[165] A. Ishimaru, *Wave Propagation and Scattering in Random Media*, volume 1 & 2, Academic Press, New York (1978).

[166] J. D. Joannopoulos, R. D. Meade, and J. N. Winn, *Photonic Crystals: Molding the Flow of Light*, Princeton University Press, Princeton (1995).

[167] S. John, Electromagnetic Absorption in a Disordered Medium near a Photon Mobility Edge, Phys. Rev. Lett. **53**(22), 2169–2172 (November 1984).

[168] S. John, Strong Localization of Photons in Certain Disordered Dielectric Superlattices, Phys. Rev. Lett. **58**(23), 2486–2489 (June 1987).

[169] S. John, Localization of Light, Phys. Today **44**(5), 32–40 (May 1991).

[170] M. H. Kao, K. A. Jester, A. G. Yodh, and P. J. Collings, Observation of Light Diffusion and Correlation Transport in Nematic Liquid Crystals, Phys. Rev. Lett. **77**(11), 2233–2236 (September 1996).

[171] M. H. Kao, A. G. Yodh, and D. J. Pine, Observation of Brownian Motion on the Time Scale of Hydrodynamic Interactions, Phys. Rev. Lett. **70**(2), 242–245 (January 1993).

[172] J. R. Kelly and P. Palffy-Muhoray, The Optical Response of Polymer Dispersed Liquid Crystals, Mol. Cryst. Liq. Cryst. **243**, 11–29 (1994).

[173] G. M. Kepler and S. Fraden, Attractive Potential between Confined Colloids at Low Ionic Strength, Phys. Rev. Lett. **73**(2), 356–359 (July 1994).

[174] Th. Kirchhoff, H. Löwen, and R. Klein, Dynamical correlations in suspensions of charged macromolecules, Phys. Rev. E **53**(5), 5011–5022 (May 1996).

[175] R. Klein, *Interacting Brownian Particles – The Dynamics of Colloidal Suspensions*, in *The Physics of Complex Systems*, edited by F. Mallamace and H. E. Stanley, pages 301–345, IOS Press, Amsterdam (1997).

[176] M. Kléman, *Points, Lines and Walls: In Liquid Crystals, Magnetic Systems, and Various Ordered Media*, John Wiley & Sons, New York (1983).

[177] H. Kneppe, F. Schneider, and B. Schwesinger, Axisymmetrical Flow of a Nematic Liquid Crystal around a Sphere, Mol. Cryst. Liq. Cryst. **205**, 9–28 (1991).

[178] S. Komura, R. J. Atkin, M. S. Stern, and D. A. Dunmur, Numerical analysis of the radial–axial structure transition with an applied field in a nematic droplet, Liq. Cryst. **23**(2), 193–203 (1997).

[179] S. Kralj and S. Žumer, Fréedericksz transitions in supra-$\mu$m nematic droplets, Phys. Rev. A **45**(4), 2461–2470 (February 1992).

[180] A. H. Krall and D. A. Weitz, Internal Dynamics and Elasticity of Fractal Colloidal Gels, Phys. Rev. Lett. **80**(4), 778–781 (January 1998).

[181] M. Krech, *The Casimir Effect in Critical Systems*, World Scientific, Singapore (1994).

[182] M. Kreuzer and R. Eidenschink, *Filled Nematics*, in *Liquid Crystals in Complex Geometries*, edited by G. P. Crawford and S. Žumer, pages 307–324, Taylor & Francis, London (1996).

[183] M. Kreuzer, T. Tschudi, and R. Eidenschink, Erasable optical storage in bistable liquid crystal cells, Mol. Cryst. Liq. Cryst. **223**, 219–227 (1992).

[184] Y. Kuga and A. Ishimaru, Retroreflectance from a dense distribution of spherical particles, J. Opt. Soc. Am. A **1**(8), 831–835 (August 1984).

[185] O. V. Kuksenok, R. W. Ruhwandl, S. V. Shiyanovskii, and E. M. Terentjev, Director structure around a colloid particle suspended in a nematic liquid crystal, Phys. Rev. E **54**(5), 5198–5203 (November 1996).

[186] M. Kurik and O. Lavrentovich, Negative-positive monopole transitions in cholesteric liquid crystals, JETP Lett. **35**(9), 444–447 (May 1982), [Pis'ma Zh. Eksp. Teor. Fiz. **35**, 362 (1982)].

[187] M. V. Kurik and O. D. Lavrentovich, Defects in liquid crystals: homotopy theory and experimental studies, Sov. Phys. Usp. **31**(3), 196–224 (March 1988), [Usp. Fiz. Nauk **154**, 381 (1988)].

[188] E. Kuss, $pVT$-Data and Viscosity-Pressure Behavior of MBBA and EBBA, Mol. Cryst. Liq. Cryst. **47**, 71–83 (1978).

[189] Z. Kutnjak, C. W. Garland, J. L. Passmore, and P. J. Collings, Supercritical Conversion of the Third Blue Phase to the Isotropic Phase in a Highly Chiral Liquid Crystal, Phys. Rev. Lett. **74**(24), 4859–4862 (June 1995).

[190] L. V. Kuz'min, V. P. Romanov, and L. A. Zubkov, Coherent backscattering from anisotropic scatterers, Phys. Rev. E **54**(6), 6798–6801 (December 1996).

[191] V. L. Kuz'min, V. P. Romanov, and L. A. Zubkov, Propagation and scattering of light in fluctuating media, Phys. Rep. **248**(2-5), 71–368 (November 1994).

[192] A. J. C. Ladd, H. Gang, J. X. Zhu, and D. A. Weitz, Temporal and spatial dependence of hydrodynamic correlations: Simulation and experiment, Phys. Rev. E **52**(6), 6550–6572 (December 1995).

[193] A. Lagendijk and B. A. van Tiggelen, Resonant multiple scattering of light, Phys. Rep. **270**, 143–215 (1996).

[194] L. D. Landau and E. M. Lifschitz, *Electrodynamics of Continuous Media*, volume 8 of *Course of Theoretical Physics*, Pergamon Press, Oxford, first englisch edition (1960).

[195] L. D. Landau and E. M. Lifschitz, *Statistische Physik, Teil 1*, volume 5 of *Lehrbuch der Theoretischen Physik*, Akademie-Verlag, Berlin, sixth edition (1984).

[196] D. Langevin, Anisotropy of the Turbidity of a Nematic Liquid Crystal, Solid State Commun. **14**, 435–437 (1974).

[197] D. Langevin and M. A. Bouchiat, Anisotropy of the turbidity of an oriented nematic liquid crystal, J. Phys. (Paris) Coll. C1 **36**(3), 197–202 (March 1975).

[198] A. E. Larsen and D. G. Grier, Like-charge attractions in metastable colloidal crystallites, Nature **385**, 230–233 (January 1997).

[199] O. Lavrentovich and E. Terentév, Phase transition altering the symmetry of topological point defects (hedgehogs) in a nematic liquid crystal, Sov. Phys. JETP **64**(6), 1237–1244 (December 1986), [Zh. Eksp. Teor. Fiz. **91**, 2084 (1986)].

[200] O. D. Lavrentovich, Topological defects in dispersed liquid crystals, or words and worlds around liquid crystal drops, Liq. Cryst. **24**(1), 117–125 (1998).

[201] M. Lax and D. F. Nelson, Linear and nonlinear electrodynamics in elastic anisotropic dielectrics, Phys. Rev. B **4**(10), 3694–3731 (November 1971).

[202] P. A. Lee and T. V. Ramakrishnan, Disordered electronic systems, Rev. Mod. Phys. **57**(2), 287–337 (April 1985).

[203] R. Lenke and G. Maret, Affecting Weak Light Localization by Strong Magnetic Fields, Phys. Scr. **T49**, 605–609 (1993).

[204] F. M. Leslie, Some Constitutive Equations for Anisotropic Fluids, Quart. J. Mech. Appl. Math. **19**, 357–370 (1966).

[205] F. M. Leslie, Some Constitutive Equations for Liquid Crystals, Arch. Ratl. Mech. Anal. **28**, 265–283 (1968).

[206] W. Leutz and G. Maret, Ultrasonic modulation of multiply scattered light, Physica B **204**, 14–19 (1995).

[207] B. I. Lev and P. M. Tomchuk, Interaction of foreign macrodroplets in a nematic liquid crystal and induced supermolecular structures, Phys. Rev. E **59**(1), 591–602 (January 1999).

[208] S. Lifson and J. L. Jackson, On the Self-Diffusion of Ions in a Polyelectrolyte Solution, J. Chem. Phys. **36**(9), 2410–2414 (May 1962).

[209] D. Link and N. Clark (1997), private communication.

[210] J. Liu, E. M. Lawrence, A. Wu, M. L. Ivey, G. A. Flores, K. Javier, J. Bibette, and J. Richard, Field-Induced Structures in Ferrofluid Emulsions, Phys. Rev. Lett. **74**(14), 2828–2831 (April 1995).

[211] H. Löwen, Kolloide – auch für Physiker interessant, Phys. Bl. **51**(3), 165–168 (1995).

[212] H. Löwen, Solvent-Induced Phase Separation in Colloidal Fluids, Phys. Rev. Lett. **74**(6), 1028–1031 (February 1995).

[213] H. Löwen, Phase separation in colloidal suspensions induced by a solvent phase transition, Z. Phys. B **97**, 269–279 (1995).

[214] T. C. Lubensky, Molecular Description of Nematic Liquid Crystals, Phys. Rev. A **2**(6), 2497–2514 (December 1970).

[215] T. C. Lubensky, Hydrodynamics of cholesteric liquid crystals, Phys. Rev. A **6**(1), 452–470 (July 1972).

[216] T. C. Lubensky, D. Pettey, N. Currier, and H. Stark, Topological defects and interactions in nematic emulsions, Phys. Rev. E **57**(1), 610–625 (January 1998).

[217] T. C. Lubensky and H. Stark, Theory of a critical point in the blue-phase-III–isotropic phase diagram, Phys. Rev. E **53**(1), 714–721 (January 1996).

[218] I. F. Lyuksyutov, Topological instability of singularities at small distances in nematics, Sov. Phys. JETP **48**(1), 178–179 (July 1978), [Zh. Eksp. Teor. Fiz. **75**, 358-360 (July 1978)].

[219] F. C. MacKintosh and S. John, Coherent backscattering of light in the presence of time-reversal-noninvariant and parity-nonconserving media, Phys. Rev. B **37**(4), 1884–1897 (February 1988).

[220] F. C. MacKintosh and S. John, Diffusing-wave spectroscopy and multiple scattering of light in correlated random media, Phys. Rev. B **40**(4), 2383–2406 (August 1989).

[221] G. D. Mahan, *Many Particle Physics*, Plenum Press, New York (1981).

[222] W. Maier and A. Saupe, Eine einfache molekular-statistische Theorie der nematischen kristallinflüssigen Phase. Teil I, Z. Naturforsch. Teil A **14**, 882–889 (1959).

[223] G. Maret, Lokalisierung von Licht durch Vielfachstreuung, Phys. Bl. **48**(3), 161–167 (March 1992).

[224] G. Maret, *Recent Experiments on multiple scattering and localization of light*, in *Mesoscopic Quantum Physics*, *Les Houches, Session LXI, 1994*, edited by E. Akkermans, G. Montambaux, J.-L. Pichard, and J. Zinn-Justin, pages 147–180, North-Holland, Amsterdam (1995).

[225] G. Maret, Diffusing-wave spectroscopy, Current Opinion in Colloid & Interface Science **2**, 251–257 (1997).

[226] G. Maret and P. E. Wolf, Multiple light scattering from disordered media: The effect of Brownian motion of scatterers, Z. Phys. B **65**, 409–413 (1987).

[227] A. S. Martinez and R. Maynard, Faraday effect and multiple scattering of light, Phys. Rev. B **50**(6), 3714–3732 (August 1994).

[228] T. G. Mason, H. Gang, and D. A. Weitz, Diffusing-wave-spectroscopy measurements of viscoelasticity of complex fluids, J. Opt. Soc. Am. A **14**(1), 139–149 (January 1997).

[229] T. G. Mason and D. A. Weitz, Optical Measurements of Frequency-Dependent Linear Viscoelastic Moduli of Complex Fluids, Phys. Rev. Lett. **74**(7), 1250–1253 (February 1995).

[230] S. P. Meeker, W. C. K. Poon, J. Crain, and E. M. Terentjev, Colloid-liquid-crystal composites: An unusual soft solid, Phys. Rev. E **61**(6), R6083–R6086 (June 2000).

[231] S. Meiboom, M. Sammon, and W. F. Brinkman, Lattice of disclinations: The structure of the blue phases of cholesteric liquid crystals, Phys. Rev. A **27**(1), 438–454 (January 1983).

[232] A. Meller and J. Stavans, Glass Transition and Phase Diagrams of Strongly Interacting Binary Colloidal Mixtures, Phys. Rev. Lett. **68**(24), 3646–3649 (June 1992).

[233] N. Mermin, *Surface Singularities and Superflow in $^3$He-A*, in *Quantum Fluids and Solids*, edited by S. B. Trickey and E. D. Adams and J. W. Dufty, pages 3–22, Plenum Press, New York (1977).

[234] N. D. Mermin, The topological theory of defects in ordered media, Rev. Mod. Phys. **51**(3), 591–648 (July 1979).

[235] R. B. Meyer, Piezoelectric Effects in Liquid Crystals, Phys. Rev. Lett. **22**(18), 918–921 (May 1969).

[236] R. B. Meyer, Point Disclinations at a Nematic-Isotropic Liquid Interface, Mol. Cryst. Liq. Cryst. **16**, 355–369 (1972).

[237] R. B. Meyer, On the Existence of Even Indexed Disclinations in Nematic Liquid Crystals, Philos. Mag. **27**, 405–424 (1973).

[238] R. B. Meyer, *Mechanical Properties of Nematic Polymers*, in *Polymer Liquid Crystals*, edited by A. Ciferri, W. R. Krigbaum, and R. B. Meyer, pages 133–163, Material Science Series, Academic Press, New York (1982).

[239] M. Mięsovicz, Influence of a Magnetic Field on the Viscosity of Para-Azoxyanisol, Nature **136**, 261 (August 1935).

[240] Mięsowicz, The Three Coefficients of Viscosity of Anisotropic Liquids, Nature **158**, 27 (1946).

[241] V. P. Mineev, *Topologically stable defects and solitons in ordered media*, in volume 2 of *Soviet Scientific Reviews, Section A: Physics Reviews*, edited by I. M. Khalatnikov, pages 173–246, Harwood Academic Publishers, London (1980).

[242] O. Mondain-Monval, J. C. Dedieu, T. Gulik-Krzywicki, and P. Poulin, Weak Surface Energy in Nematic Dispersions: Saturn Ring Defects and Quadrupolar Interactions, Eur. Phys. J. B **12**, 167–170 (1999).

[243] L. Moreau, P. Richetti, and P. Barois, Direct Measurement of the Interaction between Two Ordering Surfaces Confining a Presmectic Film, Phys. Rev. Lett. **73**(26), 3556–3559 (December 1994),

[244] H. Mori and H. Nakanishi, On the Stability of Topologically Non-Trivial Point Defects, J. Phys. Soc. Jpn. **57**(4), 1281–1286 (April 1988).

[245] A. H. Morrish, *The Physical Principles of Magnetism*, Wiley Series on the Science and Technology of Materials, John Wiley & Sons, Incorporated, New York (1965).

[246] P. M. Morse and H. Feshbach, *Methods of Theoretical Physics, Part: I*, McGraw-Hill Book Company, Inc, New York (1953).

[247] V. M. Mostepanenko and N. N. Trunov, *The Casimir effect and its application*, Clarendon Press, Oxford (1997).

[248] I. Muševič, G. Slak, and R. Blinc, Observation of Critical Forces in a Liquid Crystal by an Atomic Force Microscope, in *Abstract Book,* page 91, of 16th International Liquid Crystal Conference, Kent, USA (1996).

[249] I. Muševič, G. Slak, and R. Blinc, Temperature controlled microstage for an atomic force microscope, Rev. Sci. Instrum. **67**(7), 2554–2556 (July 1996).

[250] F. R. N. Nabarro, *Theory of Crystal Dislocations*, The international series of monographs on physics, Clarendon Press, Oxford (1967).

[251] H. Nakanishi, K. Hayashi, and H. Mori, Topological Classification of Unknotted Ring Defects, Commun. Math. Phys. **117**, 203–213 (1988).

[252] D. H. Napper, *Polymeric Stabilization of Colloidal Dispersions*, volume 3 of *Colloid Science*, Academic Press, London (1983).

[253] J. Nehring and A. Saupe, On the Elastic Theory of Uniaxial Liquid Crystals, J. Chem. Phys. **54**(1), 337–343 (1971).

[254] D. R. Nelson, *Defect-mediated Phase Transitions*, volume 7 of *Phase Transitions and Critical Phenomena*, edited by C. Domb and J. Lebowitz, pages 1–99, Academic Press, New York (1983).

[255] M. Nobili and G. Durand, Disorientation-induced disordering at a nematic-liquid-crystal–solid interface, Phys. Rev. A **46**(10), R6174–R6177 (November 1992).

[256] C. Oldano and G. Barbero, An Ab Initio Analysis of the Second-Order Elasticity Effect on Nematic Configurations, Phys. Lett. **110A**, 213–216 (July 1985).

[257] M. A. O'Leary, D. A. Boas, B. Chance, and A. G. Yodh, Refraction of Diffuse Photon Density Waves, Phys. Rev. Lett. **69**(18), 2658–2661 (November 1992).

[258] L. Onsager, Reciprocal relations in irreversible processes. I., Phys. Rev. **37**, 405–426 (February 1931).

[259] C. W. Oseen, The theory of liquid crystals, Trans. Faraday Soc. **29**, 883–899 (1933).

[260] M. A. Osipov and S. Hess, The elastic constants of nematic discotic liquid crystals with perfect local orientational order, Mol. Phys. **78**(5), 1191–1201 (1993).

[261] S. Ostlund, Interactions between topological point singularities, Phys. Rev. E **24**(1), 485–488 (July 1981).

[262] J. H. Page, P. Sheng, H. P. Schriemer, I. Jones, X. Jing, and D. A. Weitz, Group Velocity in Strongly Scattering Media, Science **271**, 634–637 (February 1996).

[263] O. Parodi, Stress Tensor for a Nematic Liquid Crystal, J. Phys. (Paris) **31**, 581–584 (July 1970).

[264] E. Penzenstadler and H.-R. Trebin, Fine structure of point defects and soliton decay in nematic liquid crystals, J. Phys. France **50**, 1027–1040 (May 1989).

[265] V. M. Pergamenshchik, Surfacelike-elasticity-induced spontaneous twist deformations and long-wavelength stripe domains in a hybrid nematic layer, Phys. Rev. E **47**(3), 1881–1892 (March 1993).

[266] V. M. Pergamenshchik, P. I. Teixeira, and T. J. Sluckin, Distortions induced by the $k_{13}$ surfacelike elastic term in a thin nematic liquid-crystal film, Phys. Rev. E **48**(2), 1265–1271 (August 1993).

[267] V. M. Pergamenshchik, $K_{13}$ term and effective boundary condition for the nematic director, Phys. Rev. E **58**(1), R16–R19 (July 1998).

[268] D. Pettey, T. C. Lubensky, and D. Link, Topological inclusions in 2D smectic C films, Liq. Cryst. **25**(5), 579–587 (1998).

[269] P. Pieranski, F. Brochard, and E. Guyon, Static and Dynamic Behavior of a Nematic Liquid Crystal in a Magnetic Field. Part II: Dynamics, J. Phys. (Paris) **34**, 35–48 (January 1973).

[270] D. J. Pine, D. A. Weitz, P. M. Chaikin, and E. Herbolzheimer, Diffusing-wave spectroscopy, Phys. Rev. Lett. **60**(12), 1134–1137 (March 1988).

[271] D. J. Pine, D. A. Weitz, G. Maret, P. E. Wolf, E. Herbolzheimer, and P. M. Chaikin, *Dynamical Correlations of Multiply Scattered Light*, in *Scattering and Localization of Classical Waves in Random Media*, volume 8 of *Directions in Condensed Matter Physics*, edited by P. Sheng, pages 312–372, World Scientific, Singapore (1990).

[272] D. J. Pine, D. A. Weitz, J. X. Zhu, and E. Herbolzheimer, Diffusing-wave spectroscopy: dynamic light scattering in the multiple scattering limit, J. Phys. France **51**, 2101–2127 (September 1990).

[273] I. P. Pinkevich and V. Y. Reshetnyak, Influence of Small Spherical Particles on the Spatial Director Distribution and Light Scattering in a Nematic Cell, Mol. Cryst. Liq. Cryst. **321**, 145–164 (1998).

[274] A. Poniewierski and T. Sluckin, Theory of the nematic-isotropic transition in a restricted geometry, Liq. Cryst. **2**(3), 281–311 (1987).

[275] P. Poulin (1999), private communication.

[276] P. Poulin, V. Cabuil, and D. A. Weitz, Direct Measurement of Colloidal Forces in an Anisotropic Solvent, Phys. Rev. Lett. **79**(24), 4862–4865 (December 1997).

[277] P. Poulin, N. Francès, and O. Mondain-Monval, Suspension of spherical particles in nematic solutions of disks and rods, Phys. Rev. E **59**(4), 4384–4387 (April 1999).

[278] P. Poulin, V. A. Raghunathan, P. Richetti, and D. Roux, On the dispersion of latex particles in a nematic solution. I. Experimental evidence and a simple model, J. Phys. II France **4**, 1557–1569 (September 1994).

[279] P. Poulin, H. Stark, T. C. Lubensky, and D. A. Weitz, Novel Colloidal Interactions in Anisotropic Fluids, Science **275**, 1770–1773 (March 1997).

[280] P. Poulin and D. A. Weitz, Inverted and multiple emulsions, Phys. Rev. E **57**(1), 626–637 (January 1998).

[281] P. Poulin, Novel phases and colloidal assemblies in liquid crystals, Current Opinion in Colloid & Interface Science **4**, 66–71 (1999).

[282] M. J. Press and A. S. Arrott, Theory and Experiment on Configurations with Cylindrical Symmetry in Liquid-Crystal Droplets, Phys. Rev. Lett. **33**(7), 403–406 (August 1974).

[283] M. J. Press and A. S. Arrott, Elastic Energies and Director Fields in Liquid Crystal Droplets, I. Cylindrical Symmetry, J. Phys. (Paris) Coll. C1 **36**(3), 177–184 (March 1975).

[284] W. H. Press, S. A. Teukolsky, W. T. Vetterling, and B. P. Flannery, *Numerical Recipes in Fortran: The Art of Scientific Computing*, Cambridge University Press, Cambridge (1992).

[285] X. Qiu, X. L. Wu, J. Z. Xue, D. J. Pine, D. A. Weitz, and P. M. Chaikin, Hydrodynamic Interactions in Concentrated Suspensions, Phys. Rev. Lett. **65**(4), 516–519 (July 1990).

[286] V. A. Raghunathan, P. Richetti, and D. Roux, Dispersion of latex particles in a nematic solution. II. Phase diagram and elastic properties, Langmuir **12**(16), 3789–3792 (August 1996).

[287] V. A. Raghunathan, P. Richetti, D. Roux, F. Nallet, and A. K. Sood, Colloidal Dispersions in a liquid-crystalline medium, Mol. Cryst. Liq. Cryst. **288**, 181–187 (1996).

[288] S. Ramaswamy, R. Nityananda, V. A. Raghunathan, and J. Prost, Power-law forces between particles in a nematic, Mol. Cryst. Liq. Cryst. **288**, 175–180 (1996).

[289] J. Rault, Sur une méthode nouvelle d'étude de l'orientation moléculaire à la surface d'un cholestérique, C. R. Acad. Sci. Ser. B **272**, 1275–1276 (1971).

[290] M. Reichenstein, T. Seitz, and H.-R. Trebin, Numerical Simulations of Three Dimensional Liquid Crystal Cells, Mol. Cryst. Liq. Cryst. **330**, 549–555 (1999).

[291] F. Reif and W. Muschik, *Statistische Physik und Theorie der Wärme*, Walter de Gruyter, Berlin, third edition (1987).

[292] F. Reinitzer, Beiträge zur Kenntniss des Cholesterins, Monatshefte Chemie **9**, 421 (1888).

[293] S. R. Renn and T. C. Lubensky, Abrikosov dislocation lattice in a model of the cholesteric–to–smectic-A transition, Phys. Rev. A **38**(4), 2132–2147 (August 1988).

[294] G. L. J. A. Rikken and B. A. van Tiggelen, Observation of magnetically induced transverse diffusion of light, Nature **381**, 54–55 (May 1996).

[295] V. G. Roman and E. M. Terentjev, Effective Viscosity and Diffusion Tensor of an Anisotropic Suspension or Mixture, Colloid J. USSR **51**, 435–442 (1989), [Kolloidnyi Zhurnal **51**(3), 507-515 (1989)].

[296] V. P. Romanov and A. N. Shalaginov, Radiation transfer equation in nematic liquid crystals, Opt. Spectrosc. (USSR) **64**(6), 774–778 (June 1988).

[297] M. Rosenbluh, I. Edrei, M. Kaveh, and I. Freund, Precision determination of the line shape for coherently backscattered light from disordered solids: Comparison of vector and scalar theories, Phys. Rev. A **35**(10), 4458–4460 (May 1987).

[298] M. Rosenbluh, M. Hoshen, I. Freund, and M. Kaveh, Time Evolution of Universal Optical Fluctuations, Phys. Rev. Lett. **58**(26), 2754–2757 (June 1987).

[299] R. Rosso and E. G. Virga, Metastable nematic hedgehogs, J. Phys. A **29**, 4247–4264 (1996).

[300] D. Rudhardt, C. Bechinger, and P. Leiderer, Direct Measurement of Depletion Potentials in Mixtures of Colloids and Nonionic Polymers, Phys. Rev. Lett. **81**(6), 1330–1333 (August 1998).

[301] A. Rüdinger and H. Stark, Twist Transition in Nematic Droplets: A Stability Analysis, Liq. Cryst. **26**(5), 753–758 (1999).

[302] R. W. Ruhwandl and E. M. Terentjev, Friction Drag on a Cylinder Moving in a Nematic Liquid Crystal, Z. Naturforsch. Teil A **50**, 1023–1030 (1995).

[303] R. W. Ruhwandl and E. M. Terentjev, Friction drag on a particle moving in a nematic liquid crystal, Phys. Rev. E **54**(5), 5204–5210 (November 1996).

[304] R. W. Ruhwandl and E. M. Terentjev, Long-range forces and aggregation of colloid particles in a nematic liquid crystal, Phys. Rev. E **55**(3), 2958–2961 (March 1997).

[305] R. W. Ruhwandl and E. M. Terentjev, Monte Carlo simulation of topological defects in the nematic liquid crystal matrix around a spherical colloid particle, Phys. Rev. E **56**(5), 5561–5565 (1997).

[306] W. B. Russel, D. A. Saville, and W. R. Schowalter, *Colloidal Dispersions*, Cambridge University Press, Cambridge (1995).

[307] G. Ryskin and M. Kremenetsky, Drag Force on a Line Defect Moving through an Otherwise Undisturbed Field: Disclination Line in a Nematic Liquid Crystal, Phys. Rev. Lett. **67**(12), 1574–1577 (September 1991).

[308] S. Sanyal, A. K. Sood, S. Ramkumar, S. Ramaswamy, and N. Kumar, Novel Polarization Dependence in Diffusing-Wave Spectroscopy of Crystallizing Colloidal Suspensions, Phys. Rev. Lett. **72**(18), 2963–2966 (May 1994).

[309] S. D. Sarma and A. Pinczuk, editors, *Perspectives in Quantum Hall Fluids*, John Wiley and Sons, New York (1997).

[310] M. Schadt, Optisch strukturierte Flüssigkristall-Anzeigen mit großem Blickwinkelbereich, Phys. Bl. **52**(7/8), 695–698 (1996).

[311] M. Schadt, H. Seiberle, and A. Schuster, Optical patterning of multi-domain liquid-crystal displays with wide viewing angles, Nature **318**, 212–215 (May 1996).

[312] F. Scheffold, W. Härtl, G. Maret, and E. Matijević, Observation of long-range correlations in temporal intensity fluctuations of light, Phys. Rev. E **56**(17), 10942–10952 (November 1997).

[313] F. Scheffold, R. Lenke, R. Tweer, and G. Maret, Localization or classical diffusion of light, Nature **398**, 207–208 (March 1999).

[314] F. Scheffold and G. Maret, Universal Conductance Fluctuations of Light, Phys. Rev. Lett. **81**(26), 5800–5803 (December 1998).

[315] N. Schopohl and T. J. Sluckin, Defect Core Structure in Nematic Liquid Crystals, Phys. Rev. Lett. **59**(22), 2582–2584 (1987).

[316] N. Schopohl and T. J. Sluckin, Hedgehog structure in nematic and magnetic systems, J. Phys. France **49**, 1097–1101 (July 1988).

[317] H. P. Schriemer, M. L. Cowan, J. H. Page, P. Sheng, Z. Liu, and D. A. Weitz, Energy Velocity of Diffusing Waves in Strongly Scattering Media, Phys. Rev. Lett. **79**(17), 3166–3169 (October 1997).

[318] A. Schuster, Radiation through a foggy atmosphere, Astrophys. J. **21**(1), 1–22 (January 1905).

[319] P. Sheng, Phase Transition in Surface-Aligned Nematic Films, Phys. Rev. Lett. **37**(16), 1059–1062 (October 1976).

[320] P. Sheng, Boundary-layer phase transition in nematic liquid crystals, Phys. Rev. A **26**(3), 1610–1617 (September 1982).

[321] P. Sheng, editor, *Scattering and Localization of Classical Waves in Random Media*, volume 8 of *World Scientific Series on Directions in Condensed Matter Physics*, World Scientific, Singapore (1990).

[322] P. Sheng, *Introduction to Wave Scattering, Localization, and Mesoscopic Phenomena*, Academic Press, San Diego (1995).

[323] P. Sheng and E. B. Priestly, *The Landau-de Gennes Theory of Liquid Crystal Phase Transition*, in *Introduction to Liquid Crystals*, edited by E. B. Priestly, P. J. Wojtowicz, and P. Sheng, pages 143–201, Plenum Press, New York (1979).

[324] P. Sheng and Z.-Q. Zhang, Scalar-Wave Localization in a Two-Component Composite, Phys. Rev. Lett. **57**(15), 1879–1882 (October 1986).

[325] S. V. Shiyanovskii and O. V. Kuksenok, Structural transitions in nematic filled with colloid particles, Mol. Cryst. Liq. Cryst. **321**, 45–56 (1998).

[326] R. Sigel and G. Strobl, Static and dynamic light scattering from the nematic wetting layer in an isotropic crystal, Progr. Colloid Polym. Sci. **104**, 187–190 (1997).

[327] U. Singh, P. J. Collings, C. J. Booth, and J. W. Goodby, Static and Dynamic Light Scattering near the Liquid Crystalline Blue Phase III – Isotropic Liquid Critical Point, J. Phys. II France **7**, 1683–1691 (November 1997).

[328] M. Smoluchowski, Versuch einer mathematischen Theorie der Koagulationkinetik kolloider Lösungen, Z. Phys. Chem. (Leipzig) **92**, 129–168 (1917).

[329] K. Sokalski and T. W. Ruijgrok, Elastic Constants for Liquid Crystals of Disc-Like Molecules, Physica A **113A**, 126–132 (1982).

[330] A. Sommerfeld, *Vorlesungen über Theoretische Physik II. Mechanik der deformierbaren Medien*, Verlag Harri Deutsch, Frankfurt/M., sixth edition (1978).

[331] A. Sonnet, A. Kilian, and S. Hess, Alignment tensor versus director: Description of defects in nematic liquid crystals, Phys. Rev. E **52**(1), 718–722 (July 1995).

[332] C. M. Soukoulis, editor, *Photonic Band Gap Materials*, Kluwer Academic Publishers, Dordrecht (1996).

[333] C. M. Soukoulis, E. N. Economou, G. S. Grest, and M. H. Cohen, Existence of Anderson Localization of Classical Waves in a Random Two-Component Medium, Phys. Rev. Lett. **62**(5), 575–578 (January 1989).

[334] H. Stark, Radiative Transfer Theory and Diffusion of Light in Nematic Liquid Crystals, Mol. Cryst. Liq. Cryst. **321**, 403–418 (1998).

[335] H. Stark, Director Field Configurations around a Spherical Particle in a Nematic Liquid Crystal, Eur. Phys. J. B **10**, 311-321 (1999).

[336] H. Stark, M. H. Kao, K. A. Jester, T. C. Lubensky, A. G. Yodh, and P. J. Collings, Light diffusion and diffusing-wave spectroscopy in nematic liquid crystals, J. Opt. Soc. Am. A **14**(1), 156–178 (January 1997).

[337] H. Stark and T. C. Lubensky, Multiple Light Scattering in Nematic Liquid Crystals, Phys. Rev. Lett. **77**(11), 2229–2232 (September 1996).

[338] H. Stark and T. C. Lubensky, Multiple light scattering in anisotropic media, Phys. Rev. E **55**(1), 514–533 (January 1997).

[339] H. Stark, J. Stelzer, and R. Bernhard, Water Droplets in a Spherically Confined Nematic Solvent: A Numerical Investigation, Eur. Phys. J. B **10**, 515–523 (1999).

[340] J. Stelzer, M. A. Bates, L. Longa, and G. R. Luckhurst, Computer simulation studies of anisotropic systems. XXVII. The direct pair correlation function of the Gay–Berne discotic nematic and estimates of its elastic constants, J. Chem. Phys. **107**(18), 7483–7492 (November 1997).

[341] M. J. Stephen, Temporal fluctuations in wave propagation in random media, Phys. Rev. B **37**(1), 1–5 (January 1988).

[342] M. J. Stephen and G. Cwilich, Rayleigh scattering and weak localization: Effects of polarization, Phys. Rev. B **34**(11), 7564–7572 (December 1986).

[343] M. J. Stephen and G. Cwilich, Intensity Correlation Functions in Light Scattered from a Random Medium, Phys. Rev. Lett. **59**(3), 285–287 (July 1987).

[344] M. Stoytchev and A. Z. Genack, Measurement of the Probability Distribution of Total Transmission in Random Waveguides, Phys. Rev. Lett. **79**(2), 309–312 (July 1997).

[345] K. J. Strandburg, Two-dimensional melting, Rev. Mod. Phys. **60**(1), 161–207 (January 1988).

[346] B. D. Swanson and L. B. Sorenson, What Forces Bind Liquid Crystal, Phys. Rev. Lett. **75**(18), 3293–3296 (October 1995).

[347] V. G. Taratuta, A. J. Hurd, and R. B. Meyer, Light-scattering study of a polymer liquid crystal, Phys. Rev. Lett. **55**(2), 246–249 (July 1985).

[348] G. I. Taylor, The mechanism of plastic deformation of crystals, Proc. R. Soc. London, Ser. A **145**, 362–415 (1934).

[349] E. M. Terentjev, Disclination loops, standing alone and around solid particles, in nematic liquid crystals, Phys. Rev. E **51**(2), 1330–1337 (February 1995).

[350] B. A. Tiggelen, D. A. Wiersma, and A. Lagendijk, Self-Consistent Theory for the Enhancement Factor in Coherent Backscattering, Europhys. Lett. **30**(1), 1–6 (April 1995).

[351] H.-R. Trebin, The topology of non-uniform media in condensed matter physics, Adv. Phys. **31**(3), 195–254 (1982).

[352] L. Tsang and A. Ishimaru, Backscattering enhancement of random discrete scatterers, J. Opt. Soc. Am. A **1**(8), 836–839 (August 1984).

[353] L. Tsang and A. Ishimaru, Theory of backscattering enhancement of random discrete isotropic scatterers based on the summation of all ladder and cyclical terms, J. Opt. Soc. Am. A **2**(8), 1331–1338 (August 1985).

[354] E. H. Twizell, *Computational methods for partial differential equations*, Chichester, Horwood (1984).

[355] S. Žumer and J. W. Doane, Light scattering from a small nematic droplet, Phys. Rev. A **34**(4), 3373–3385 (October 1986).

[356] A. Y. Val'kov and V. P. Romanov, Characteristics of propagation and scattering of light in nematic liquid crystals, Sov. Phys. JETP **63**(4), 737–743 (April 1986), [Zh. Eksp. Teor. Fiz. **90**, 1264 (1986)].

[357] M. P. van Albada, J. F. de Boer, and A. Lagendijk, Observation of Long-Range Intensity Correlation in the Transport of Coherent Light through a Random Medium, Phys. Rev. Lett. **64**(23), 2787–2790 (June 1990).

[358] M. P. van Albada and A. Lagendijk, Observation of Weak Localization of Light in a Random Medium, Phys. Rev. Lett. **55**(24), 2692–2695 (December 1985).

[359] M. P. van Albada, B. A. van Tiggelen, A. Lagendijk, and A. Tip, Speed of Propagation of Classical Waves in Strongly Scattering Media, Phys. Rev. Lett. **66**(24), 3132–3135 (June 1991).

[360] H. C. van de Hulst, *Multiple Light Scattering: Tables, Formulas and Applications*, volume 1 & 2, Academic Press, New York (1980).

[361] M. B. van der Mark, M. P. van Albada, and A. Lagendijk, Light scattering in strongly scattering media: Multiple scattering and weak localization, Phys. Rev. B **37**(7), 3575–3592 (March 1988).

[362] B. A. van Tiggelen, Transverse Diffusion of Light in Faraday-Active Media, Phys. Rev. Lett. **75**(3), 422–424 (July 1995).

[363] B. A. van Tiggelen, Optics of Diffuse Light in Nematic Liquid Crystals, Mol. Cryst. Liq. Cryst. **321**, 197–212 (1998).

[364] B. A. van Tiggelen, A. Heiderich, and R. Maynard, Light Diffusion in Oriented Nematic Liquid Crystals, Mol. Cryst. Liq. Cryst. **293**, 205–238 (1997).

[365] B. A. van Tiggelen, A. Lagendijk, A. Tip, and G. F. Reiter, Effect of Resonant Scattering on Localization of Waves, Europhys. Lett. **15**(5), 535–540 (July 1991).

[366] B. A. van Tiggelen, A. Lagendijk, M. P. van Albada, and A. Tip, Speed of light in random media, Phys. Rev. B **45**(21), 12233–12243 (June 1991).

[367] B. A. van Tiggelen, R. Maynard, and A. Heiderich, Anisotropic Light Diffusion in Oriented Nematic Liquid Crystals, Phys. Rev. Lett. **77**(4), 639–642 (July 1996).

[368] B. A. van Tiggelen, R. Maynard, and T. M. Nieuwenhuizen, Theory for multiple light scattering from Rayleigh scatterers in magnetic fields, Phys. Rev. E **53**(3), 2881–2908 (March 1996).

[369] B. A. van Tiggelen and H. Stark, Light Diffusion in Nematic Liquid Crystals, Rev. Mod. Phys. **72**(4), (October 2000).

[370] D. Ventzki and H. Stark, Stokes Drag of Particles Suspended in a Nematic Liquid Crystal, in preparation.

[371] E. J. W. Verwey and J. T. G. Overbeek, *Theory of the Stability of Lyophobic Colloids*, Elsevier Science B. V., Amsterdam (1948).

[372] H. K. M. Vithana, L. Asfaw, and D. L. Johnson, Coherent backscattering of light in a nematic liquid crystal, Phys. Rev. Lett. **70**(23), 3561–3564 (June 1993).

[373] D. V. Vlasov, L. A. Zubkov, N. V. Orekhova, and V. P. Romanov, Weak localization due to scattering of light in nonoriented liquid crystals, JETP Lett. **48**(2), 91–94 (July 1988), [Pis'ma Zh. Eksp. Teor. Fiz. **48**, 86 (1988)].

[374] D. Vollhardt and P. Wölfle, Diagrammatic, self-consistent treatment of the Anderson localization problem in $d \leq 2$ dimensions, Phys. Rev. E **22**(10), 4666–4679 (November 1980).

[375] D. Vollhardt and P. Wölfle, *The Phases of Helium 3*, Taylor & Francis, New York (1990).

[376] D. Vollhardt and P. Wölfle, *Selfconsistent Theory of Anderson Localization*, in *Electronic Phase Transitions*, volume 32 of *Modern Problems in Condensed Matter Sciences*, edited by W. Hanke and Y. V. Kopaev, pages 1–78, Elsevier Science, Amsterdam (1992).

[377] G. E. Volovik and O. D. Lavrentovich, Topological dynamics of defects: boojums in nematic drops, Sov. Phys. JETP **58**(6), 1159–1168 (December 1983), [Zh. Eksp. Teor. Fiz. **85**, 1997 (1983)].

[378] T. W. Warmerdam, D. Frenkel, and R. J. J. Zijlstra, Measurements of the ratio of the Frank constants for splay and bend in nematics consisting of disc-like molecules - 2,3,6,7,10,11-hexakis(*p*-alkoxybenzoyloxy)triphenylenes, Liq. Cryst. **3**(3), 369–380 (1988).

[379] R. L. Weaver, On diffuse waves in solid media, J. Acoust. Soc. Am. **71**(6), 1608–1609 (June 1982).

[380] Q.-H. Wei, C. Bechinger, D. Rudhardt, and P. Leiderer, Experimental Study of Laser-Induced Melting in Two-Dimensional Colloids, Phys. Rev. Lett. **81**(12), 2606–2609 (September 1998).

[381] D. A. Weitz and D. J. Pine, *Diffusing-wave spectroscopy*, in *Dynamic Light Scattering*, edited by W. Brown, pages 652–720, Oxford University Press, Oxford (1992).

[382] D. A. Weitz, D. J. Pine, P. N. Pusey, and R. J. A. Tough, Nondiffusive Brownian Motion by Diffusing-Wave Spectroscopy, Phys. Rev. Lett. **63**(16), 1747–1750 (October 1989).

[383] A. E. White, P. E. Cladis, and S. Torza, Study of Liquid Crystals in Flow: I. Conventional Viscometry and Density Measurements, Mol. Cryst. Liq. Cryst. **43**, 13–31 (1977).

[384] D. S. Wiersma, P. Bartolini, A. Lagendijk, and R. Righini, Localization of light in a disordered medium, Nature **390**, 671–673 (December 1997).

[385] D. S. Wiersma, J. G. Rivas, P. Bartolino, A. Lagendijk, and R. Righini, Localization or classical diffusion of light? Reply, Nature **398**, 207 (March 1999).

[386] D. S. Wiersma, M. P. van Albada, and A. Lagendijk, Coherent Backscattering of Light from Amplifying Random Media, Phys. Rev. Lett. **75**(9), 1739–1742 (August 1995).

[387] D. S. Wiersma, M. P. van Albada, B. A. van Tiggelen, and A. Lagendijk, Experimental Evidence for Recurrent Multiple Scattering Events of Light in Disordered Media, Phys. Rev. Lett. **74**(21), 4193–4196 (May 1995).

[388] J. E. G. J. Wijnhoven and W. L. Vos, Preparation of Photonic Crystals Made of Air Spheres in Titania, Science **281**, 802–804 (August 1998).

[389] J. Wilks and D. Betts, *An Introduction to Liquid Helium*, Clarendon Press, Oxford (1987).

[390] C. Williams, P. Pierański, and P. E. Cladis, Nonsingular $S = +1$ Screw Disclination Lines in Nematics, Phys. Rev. Lett. **29**(2), 90–92 (July 1972).

[391] R. D. Williams, Two transitions in tangentially anchored nematic droplets, J. Phys. A **19**, 3211–3222 (1986).

[392] P. E. Wolf and G. Maret, Weak Localization and Coherent Backscattering of Photons in Disordered Media, Phys. Rev. Lett. **55**(24), 2696–2699 (December 1985).

[393] P. E. Wolf, G. Maret, E. Akkermans, and R. Maynard, Optical coherent backscattering by random media: an experimental study, J. Phys. France **49**, 63–75 (January 1988).

[394] X. L. Wu, D. J. Pine, P. M. Chaikin, J. S. Juang, and D. A. Weitz, Diffusing-wave spectroscopy in a shear flow, J. Opt. Soc. Am. B **7**(1), 15–20 (January 1990).

[395] J. Z. Xue, X. L. Wu, D. J. Pine, and P. M. Chaikin, Hydrodynamic interactions in hard-sphere suspensions, Phys. Rev. A **45**(2), 989–993 (January 1992).

[396] E. Yablonovitch, Inhibited Spontaneous Emission in Solid-State Physics and Electronics, Phys. Rev. Lett. **58**(20), 2059–2062 (May 1987).

[397] E. Yablonovitch, T. J. Gmitter, and K. M. Leung, Photonic Band Structure: The Face-Centered-Cubic Case Employing Nonspherical Atoms, Phys. Rev. Lett. **67**(17), 2295–2298 (October 1991).

[398] D.-K. Yang, L.-C. Chien, and Y.-K. Fung, *Polymer-stabilized Cholesteric Textures: Materials and Applications*, in *Liquid Crystals in Complex Geometries*, edited by G. P. Crawford and S. Žumer, pages 103–142, Taylor & Francis, London (1996).

[399] A. G. Yodh and B. Chance, Spectroscopy and Imaging with Diffusing Light, Phys. Today **48**(3), 34–40 (March 1995).

[400] A. Yodh, B. Tromberg, E. Sevick-Muraca, and D. Pine, editors, *Diffusing Photons in Turbid Media*, special issue of J. Opt. Soc. Am. A **14**(1), 136–330 (January 1997).

[401] K. Zahn, R. Lenke, and G. Maret, Two-Stage Melting of Paramagnetic Colloidal Crystals in Two Dimensions, Phys. Rev. Lett. **82**(13), 2721–2724 (March 1999).

[402] M. Zapotocky, L. Ramos, P. Poulin, T. C. Lubensky, and D. A. Weitz, Particle-Stabilized Defect Gel in Cholesteric Liquid Crystals, Science **283**, 209–212 (January 1999).

[403] J. X. Zhu, D. J. Durian, J. Müller, D. A. Weitz, and D. J. Pine, Scaling of Transient Hydrodynamic Interactions in Concentrated Suspensions, Phys. Rev. Lett. **68**(16), 2559–2562 (April 1992).

[404] J. X. Zhu, D. A. Weitz, and R. Klein, *Dynamic Correlations of Multiply Scattered Light from Strongly Interacting Suspensions*, in *Photonic Band Gaps and Localization*, edited by C. M. Soukoulis, pages 115–129, Plenum Press, New York (1993).

[405] P. Ziherl, R. Podgornik, and S. Žumer, Casimir force in liquid crystals close to the nematic-isotropic phase transition, Chem. Phys. Lett. **295**, 99–104 (1998).

[406] J. Zinn-Justin, *Quantum Field Theory and Critical Phenomena*, volume 92 of *International Series of Monographs on Physics*, Oxford Science Publications, Oxford, third edition (1996).

[407] H. Zöcher, The Effect of a Magnetic Field on the Nematic State, Trans. Faraday Soc. **29**, 945–957 (1933).

# Acknowledgement

First, I would like to thank Tom Lubensky at the University of Pennnsylvania in Philadelphia where I held a postdoctoral position from March 94 to August 96. The work presented here was initiated by a close collaboration with him. I profited very much from his experience, and I also owe him a new view of physics.

At the University of Pennsylvania I had the opportunity to collaborate with the experimentalists Philippe Poulin, Arjun Yodh, and Dave Weitz. They contributed enormously to the contents of this work. I also thank Ming H. Kao, Kristen Jester, David Pettey, and Nathan Currier for their collaboration. And of course, thank you Randy Kamien for sharing the office and for all sorts of discussions.

After my return to the Institut für Theoretische und Angewandte Physik (ITAP) at the University of Stuttgart, I worked together with Andreas Rüdinger, Joachim Stelzer, and Dieter Ventzki. The results are presented in this thesis. I thank all of them and especially Joachim Stelzer who improved the style of writing of this thesis.

I enjoy working with Anamarija Borštnik and Slobodan Žumer from the University of Ljubljana; Anamarija spent some time at the ITAP doing her graduate work. Chapter 8 is the outcome of our collaboration.

A lot of thanks to Bart van Tiggelen from Grenoble for collaborating. I profited very much from his deep insight into multiple light scattering. I furthermore acknowledge helpful discussions with Martin Čopič, Eugene Gartland, Thomas Gisler, Michael Heckmeier, Axel Kilian, R. Klein, G. Maret, R. Maynard, Alenka Mertelj, E. Sackmann, and Eugene Terentjev.

At the ITAP, I thank Marta Bachteler, Jochen Englert, Katharina Lieser, and Michael Reichenstein for collaborating on different projects, Thorsten Seitz for discussions about computer codes, Gabi Zeeger for organizing the "Teeseminar", Johannes Roth and Gunther Schaaf for keeping the computer system in good shape, and Michael Reichenstein for taking care of LaTeX and the ITAP website. I am grateful to all other members of the group and to our secretaries Bettina Rank and Dorothee Stammler for the pleasant environment at the ITAP.

This habilitation thesis will be judged by some referees as part of the habilitation procedure. I thank them in advance for their efforts. I also thank my "Mentorengruppe" at the University of Stuttgart, consisting of Profs. Dosch, Muramatsu, Trebin, Weidlich, Weiss, for supporting my habilitation.

Last but not least I am grateful to Prof. Trebin. He encouraged me to pursue a scientific career and always strongly supported this habilitation work. He provided an environment in which I could freely follow my scientific interests. Many thanks.

Finally, I acknowledge financial assistance from the Deutsche Forschungsgemeinschaft through grants Sta 352/2-1/2 and Tr 154/17-1/2.